First Measurement of θ_{13} with the Final Two Detector Setup of the Double Chooz Experiment

Von der Fakultät für Mathematik, Informatik und Naturwissenschaften der RWTH Aachen University zur Erlangung des akademischen Grades eines Doktors der Naturwissenschaften genehmigte Dissertation

vorgelegt von

Dipl.-Phys. Dipl.-Math.
Stefan Schoppmann

aus Herford (Westfalen)

Berichter: Universitätsprofessor Dr.rer.nat. Achim Stahl
Universitätsprofessor Dr.rer.nat. Christopher Wiebusch

Tag der mündlichen Prüfung: 25.10.2016

Abstract

The Double Chooz experiment is a reactor antineutrino disappearance experiment located at the nuclear power plant CHOOZ-B near the village of Chooz, France. The aim of the experiment is a high precision measurement of the neutrino oscillation amplitude $\sin^2(2\theta_{13})$. The experiment is built of two identical liquid scintillator detectors. They measure the neutrino oscillations on two distinct baselines using the flux of electron-antineutrinos originating from two nuclear reactors. After a single detector phase starting in 2011, the second detector has been commissioned in early 2015.

In its first part, this work describes the design, implementation and commissioning of the data handling system responsible for the collection and transfer of the majority of the recorded experiment data. The system replaces the former single detector setup and provides several new fail-safe and diagnostic features. It is a multi-server MySQL-based setup interleaved with the laboratory systems in Chooz on the one end and the central computing facility of the in2p3 institute on the other end. The system is shown to have excellent performance allowing for both, unimpaired data acquisition in the laboratories and data processing in the computing centre. Additionally, the system is basis for an experiment-wide general purpose monitoring tool.

In the second part of this work, a newly developed oscillation analysis approach for the Double Chooz data is presented. It utilises rate and spectral shape information. For the first time, it offers the possibility to include a full three flavour oscillation model into the oscillation analysis. Furthermore, a detailed treatment of energy scale non-linearities in the oscillation analysis is developed. Moreover, the novel adaptive modelling of spectral shape uncertainties reveals better insights to the treatment of the reactor flux uncertainties within the oscillation analysis. With the new approach, the first two detector data of the Double Chooz experiment is analysed in addition to the formerly recorded one-detector data. Due to the extended dataset, the Double Chooz experiment successfully confirms the existence of reactor antineutrino oscillations at the $6\,\sigma$ confidence level. With the improved precision, this analysis presents a value for the oscillation amplitude of $\sin^2(2\theta_{13}) = 0.117 \pm 0.019$ assuming $\Delta m^2_{ee} = (2.44 \pm 0.09) \cdot 10^{-3}\mathrm{eV}^2$ and normal mass hierarchy.

Kurzfassung

Das Double Chooz Experiment ist ein Antineutrino-Disappearance Experiment. Es befindet sich auf dem Gelände des Kernkraftwerkes CHOOZ-B nahe des französischen Dorfs Chooz. Das Ziel des Experiments ist es, die Neutrinooszillationsamplitude $\sin^2(2\theta_{13})$ mit hoher Präzision zu vermessen. Aufgebaut ist das Experiment aus zwei identischen Flüssigszintillatordetektoren, die den Fluss von Antineutrinos aus den zwei Reaktoren des Kernkraftwerkes in unterschiedlichen Entfernungen messen. Nach der in 2011 gestarteten Einzeldetektorphase sind seit Anfang 2015 nun beide Detektoren in Betrieb.

Diese Arbeit beschreibt zunächst den Aufbau und die Inbetriebnahme eines neuen Datenverarbeitungssystems für die Doppeldetektorphase, welches verantwortlich ist für die Aufzeichnung und den Transfer des Großteils der Experimentdaten. Das neue System ersetzt das ursprüngliche System der Einzeldetektorphase. Es bietet gegenüber dem Vorgängersystem eine erweiterte Ausfallsicherheit sowie bessere Diagnosefunktionen. Das Datenverarbeitungssystem ist MySQL-basiert und aus mehreren Servern aufgebaut, die zum einen mit den Laborsystemen, zum anderen mit dem genutzen Rechenzentrum des in2p3-Institutes vernetzt sind. Das neue Datenverarbeitungssystem erzielt ausgezeichnete Leistungswerte und ermöglicht eine ununterbrochene Datennahme in den Laboratorien, sowie gleichzeitig eine unbeeinträchtigte Auswertung der Daten auf Seiten des Rechenzentrums. Weiterhin wird das System als experimentweites Mehrzwecküberwachungssystem genutzt.

Im zweiten Teil dieser Arbeit wird eine neu entwickelte Oszillationsanalyse basierend auf Neutrinorate und Form des Neutrinoenergiespektrums vorgestellt. Erstmals bietet sie die Möglichkeit die Daten des Double Chooz Experiments unter Ausnutzung des vollen Oszillationsformalismus mit seinen drei Neutrinogenerationen auszuwerten. Weiterhin berücksichtigt die neue Analyse die Nichtlinearitäten der Energieskala in einem erweiterten Detailgrad. Ebenso ermöglicht der neuartige Ansatz zur Modellierung von Formunsicherheiten im Reaktorneutrinospektrum ein vertieftes Verständnis der Behandlung von ebendiesen Unsicherheiten in der Oszillationsanalyse. Mithilfe des neuen Verfahrens werden erstmalig Daten aus der Doppeldetektorphase ausgewertet. Durch den so ergänzten Einzeldetektordatensatz gelingt es der Double Chooz Kollaboration erstmals die Existenz von Reaktorantineutrinooszillationen zu bestätigen. Die Nichtexistenz solcher Oszillationen kann mit einem Konfidenzniveau von $6\,\sigma$ ausgeschlossen werden. Entsprechend erzielt die hier vorgestellte Analyse für die Oszillationsamplitude einen Wert von $\sin^2(2\theta_{13}) = 0.117 \pm 0.019$, wobei hierfür $\Delta m^2_{ee} = (2.44 \pm 0.09) \cdot 10^{-3}\mathrm{eV}^2$ und normale Massenhierarchie angenommen wurde.

Contents

List of Figures

List of Tables

Glossary

acc: accidental background
av.: average
β**-n:** double decay process with emitted electron and neutron, see also LiHe
bkgrd: bac**kgr**oun**d**
B: boron
Ba: barium
cand.: candidate
CC: see CC-IN2P3
CC-IN2P3: Centre de **C**alcul de l'**I**nstitut **N**ational de **P**hysique Nucléaire et de **P**hysique des **P**articlues (central computing facility of the Double Chooz experiment hosted by the French national institute for nuclear physics and particle physics)
C.L.: confidence **l**evel
Cf: cali**f**ornium
Co: cobalt
corr: correlated
CPS: Chimney **P**ulse **S**hape
Cs: ceas**i**um
CT: Common **T**runk
C.V.: central **v**alue
DB: data**b**ases
DC: Double **C**hooz
DC-III: 3rd oscillation analysis result of the **D**ouble **C**hooz experiment, can be subdivided into Gd and H analysis
DC-IV: 4th analysis result of the **D**ouble **C**hooz experiment, can be subdivided into Gd and H analysis
DNS: Domain **N**ame **S**ystem
DOGS: Double Chooz **O**ffline **G**roup **S**oftware
DUQ: Digital **U**nit of **Charge**
EDF: Électricité **d**e **F**rance
eff.: efficiency
FD: Far **D**etector
FD1: Far **D**etector during **1**-detector configuration while at least 1 reactor was powered
FD1off: Far **D**etector during **1**-detector configuration while no reactor was powered
FD2: Far **D**etector during **2**-detector configuration while at least 1 reactor was powered (identical with FD-II)
FD-I: Far **D**etector during **1**-detector configuration
FD-II: Far **D**etector during **2**-detector configuration (identical with FD2)

FN: fast **neutrons**
FNSM: correlated background, see FN and see SM
GC: γ-**C**atcher
Gd: ga**d**olinium
Gd-III: see DC-III and see n-Gd
Gd-IV: see DC-IV and see n-Gd
GLG4sim: "**G**eneric**L**AND" **G**eant**4 sim**ulation
GLoBES: General **Lo**ng **B**aseline **E**xperiment **S**imulator
H: hydrogen
He: helium, see also β-n
IBD: inverse β-**d**ecay
ID: Inner **D**etector
IH: inverted neutrino mass **h**ierarchy
IN2P3: l'**I**nstitut **N**ational de **P**hysique Nucléaire et de **P**hysique des **P**articlues (the French national institute for nuclear physics and particle physics)
ineff.: inefficiency
IP: Internet **P**rotocol
IV: Inner **V**eto
Kr: krypton
LAND: Liquid-scintillator **A**nti-**N**eutrino **D**etector
LEP: Large **E**lectron-**P**ositron Collider
Li: lithium, see also β-n
LiHe: see Li and see He
LN: Light **N**oise
μ**: m**uon
MC: Monte **C**arlo
meas.: measured
MultiSim: multiple **sim**ulation
m.w.e.: metre **w**ater **e**quivalent
ν**: n**eutrino
n: neutron
ND: Near **D**etector
n.d.f.: number of **d**egrees of **f**reedom
n-Gd: neutron capture by **g**a**d**olinium, also nGd
n-H: neutron capture by **h**ydrogen, also nH
NH: normal neutrino mass **h**ierarchy
norm.: normalisation
NT: Neutrino **T**arget
OD: Outer **D**etector
OV: Outer **V**eto
p: proton
PE: photo **e**lectron
pdf: probability **d**ensity **f**unction
pred.: predicted
Pu: plutonium
PMNS: Pontecorvo-**M**aki-**N**akagawa-**S**akata-Matrix
PMT: Photo**m**ultiplier **t**ube

RoSS: Read**o**ut **S**imulation **S**oftware
r+s: rate **and s**hape
σ: 68 % C.L.
SM: stopping **m**uon
stat: statistical
sys: systematical
U: uranium
uncert.: uncertainty
vis: visible

“Ich glaub’ ich hab’s!”

Anselm Stüken

Chapter 1

Introduction

In 1968, the Homestake experiment [1], which was aiming for a measurement of the solar neutrino flux, showed a significant discrepancy between the expectation from the solar standard model and the actual measurement. This deficit was soon confirmed by further experiments of same and different detection type. However, there was no clear consent among the experimental data and no explanation for the observed deficit could be experimentally found for decades.

This so called solar neutrino problem could not be solved until 15 years ago. In 1998, the Super-Kamioka **N**eutrino **D**etection **E**xperiment (**S**uper-**K**amiokande/SK[1]) [2] was able to show that muon neutrinos produced in Earth's atmosphere by cosmic rays are changing their flavour depending on the travel length and energy. This observation was clear evidence for the mechanism of neutrino oscillation, i.e. the energy and travel length dependent conversion between neutrinos of different flavours. Moreover, in 2001, the **S**udbury **N**eutrino **O**bservatory (SNO) [3] showed that by measuring neutrinos of all three flavours, the solar standard model expectation holds. The solar neutrino problem was thus caused by neutrino oscillations which lower the flux of initial electron neutrinos.

Several additional experiments were carried out to gain a better understanding of this effect. However, until 2011, it was unclear whether all of the theoretically allowed oscillation channels exist. This was caused by the fact that the last unmeasured oscillation channel has a small amplitude. First indications that this oscillation channel exists were given by the **M**ain **I**njector **N**eutrino **O**scillation **S**earch experiment (MINOS) [4], the **T**okai **to K**amioka experiment (T2K) [5] and the Double Chooz experiment [6]. The Daya Bay [7] and RENO [8] experiments were finally able to measure this oscillation in 2012 with high precision, so were the T2K [9] and Double Chooz [10] experiments in 2013. The experiments continue to increase the precision of their measurements.

The Double Chooz experiment [12; 13] measures the neutrino oscillation parameter θ_{13} by observing the disappearance of electron antineutrinos, i.e. the oscillation of those neutrinos into neutrinos of different flavour. For this purpose, the neutrino flux originating from two nuclear reactors located at the French power plant CHOOZ-B is used. The experiment consists of two liquid scintillator detectors of equal design installed in different distances from the reactor cores. While the far detector measures the neutrino flux near the location of the maximal oscillation effect, the near detector provides a measurement of the approximately

[1] The meaning of the acronym "Kamiokande" as used by the Super-Kamiokande collaboration was altered with respect to the predecessor experiment Kamiokande, were it meant Kamioka **N**ucleon **D**ecay **E**xperiment.

unoscillated neutrino flux.

This thesis describes the latest measurement of the Double Chooz experiment. After the recent commissioning of the near detector, the final two detector setup is used for the first time in this measurement. After a theoretical introduction to neutrino oscillations in chapter 2 and a general introduction to the Double Chooz experiment in chapter 3, this thesis separates into two parts.

The first part in chapter 4 describes the design, implementation, commissioning and performance of a data handling and distribution system. It is newly installed for the two detector phase. This system is used for the transfer, tracking and storage of the majority of data recorded by any part of the experiment. Its performance and reliability is thereby essential for the later analysis of the data. As all recorded data is centrally processed by the system, it is moreover designed to monitor all subsystems of the experiment either as primary layer or as redundant layer in the case of sensitive detector components. The data handling system is also the backbone of the final oscillation analysis presented in the second part of this thesis as it handles the internal data of the analysis.

The second part of the thesis focuses on the oscillation analysis, i.e. the determination of the oscillation parameter θ_{13}. Chapter 5 details the selection of a neutrino candidate sample as well as the construction of the predictions for the signal and backgrounds assuming no oscillations. Moreover, the energy calibration is reviewed. The oscillation analysis which extracts the value of the oscillation parameter from the input model is described in chapter 6. The independently developed novel approach complements the previous oscillation analysis strategy of the Double Chooz collaboration. It is likelihood-based and exploits the spectral shape and rate of neutrino events. The analysis approach uses for the first time an adaptive spectral shape model as well as a non-approximative neutrino oscillation model. In addition, several other systematic effects are treated for the first time as nuisance parameters. By this, the presented oscillation analysis provides high accuracy as well as new insights into the process of the oscillation analysis itself. Using this newly developed approach, the first two detector data of the Double Chooz experiment is analysed. The new data yields a reduced relative uncertainty for $\sin^2(2\theta_{13})$ of 16 % compared to the previously published single detector analysis with a relative uncertainty of 27 %. In consequence, the presented oscillation analysis enables the Double Chooz collaboration for the first time to confirm the existence of reactor antineutrino oscillations.

Chapter 2

Theory of Neutrino Oscillations

The following chapter will introduce the theoretical foundations of neutrino oscillations following reference [14, p. 2 & seqq.]. It will rather focus on introducing aspects of the theory as they are required in the context of this thesis than giving a full account of the complete theory.

2.1 The Neutrinos

The existence of neutrinos was postulated for the first time in 1933 when Wolfgang Pauli suggested the participation of an unknown particle in the β-decay in order to solve the measured violation of energy and angular momentum conservation [15, p. 119]. The suggested particle has to be free of electrical charge and interact only via the weak force and the force of gravity. In 1956, the postulated particle was measured for the first time at the Savannah River Site nuclear power plant [16]. The particle was later called ν_e, the electron neutrino[1]. The measured cross-section of the discovered particle of $10^{-44}\,\mathrm{cm}^2$ [16, p. 104] and the mass of $< 2\,\mathrm{eV/c}^2$ [17] are rather small. This explains why this particle was not detected earlier and confirms Pauli's postulation.

In 1962 the existence of a second type of neutrino, the muon neutrino ν_μ, was discovered at the **A**lternating **G**radient **S**ynchrotron (AGS) at the Brookhaven National Laboratory [18]. A third neutrino type, called tau neutrino ν_τ, was discovered in 2001 at the **F**ermi **N**ational **A**ccelerator **L**aboratory (FNAL) [19]. Data from the **L**arge **E**lectron-**P**ositron Collider (LEP) [17] yields towards the existence of precisely the three discovered neutrino generations. By these results, neutrinos have the same number of generations as other types of elementary particles and confirm the standard model of elementary particles.

2.2 Neutrino Oscillations

While the discoveries of the three neutrino generations confirmed the standard model, the discovery of neutrino oscillations made an extension to the standard model necessary: The effect of neutrino oscillation was theorised for the first time by Bruno Pontecorvo [20; 21]. In 1957 he discussed the possibility of the transformation between neutrinos and antineutrinos. Today, neutrino oscillation is understood as the transformation of neutrinos of a certain flavour

[1] More precisely, not the electron neutrino ν_e, but the electron antineutrino $\bar{\nu}_e$ was discovered in 1956.

into neutrinos of another flavour [24], e.g. muon neutrinos into electron neutrinos. Within the framework of quantum mechanics, this transformation is possible due to the inequality of the neutrino eigenstates of energy and the neutrino eigenstates of the weak force.

Mathematically, a neutrino has to be seen as a vector in a vector space [25, p. 111 & seqq.]. In this vector space, two operators of our interest exist. To each operator three eigenvectors or eigenstates exist. One operator is the Hamilton operator and if a neutrino is in an eigenstate to this operator, i.e. its state is represented by an eigenvector of the Hamilton operator, the neutrino has a certain mass. The second operator is the flavour operator. If a neutrino is in an eigenstate to this operator, the neutrino has a certain flavour.

The eigenvectors of the afore-mentioned operators make up two distinct orthonormal bases of the underlying vector space. The three flavour eigenstates or eigenvectors are labelled as electron neutrino $|\nu_e\rangle$, muon neutrino $|\nu_\mu\rangle$ and tau neutrino $|\nu_\tau\rangle$ and build the first basis. The three mass eigenstates are labelled with integers: $|\nu_1\rangle$, $|\nu_2\rangle$ and $|\nu_3\rangle$. They build the second basis [26, p. 255]. The vector which represents the neutrino in this space $|\nu_x\rangle$ can be represented as a linear combination of the three basis vectors of both bases [17]:

$$|\nu_x\rangle = \sum_{j=1}^{3} \xi_j |\nu_j\rangle, \text{ with } j \in \{1,2,3\} \text{ and } |\nu_x\rangle = \sum_{\alpha=1}^{3} \kappa_\alpha |\nu_\alpha\rangle, \text{ with } \alpha \in \{e,\mu,\tau\}. \tag{2.1}$$

It is possible to change between the two bases by applying a change of basis matrix. This matrix is called **P**ontecorvo-**M**aki-**N**akagawa-**S**akata-Matrix (PMNS) and is denoted as U_{PMNS} [27, p. 2]. For this change of basis, one considers an arbitrary neutrino $|\nu_x\rangle$ as represented by its coordinate vector

$$(\xi_1, \xi_2, \xi_3)^{\mathrm{T}} \tag{2.2}$$

and finds the coordinate vector of this neutrino $|\nu_x\rangle$ in the changed basis as[2]

$$(\kappa_e, \kappa_\mu, \kappa_\tau)^{\mathrm{T}} = U_{PMNS}^{\dagger} \times (\xi_1, \xi_2, \xi_3)^{\mathrm{T}}. \tag{2.3}$$

The principles of quantum mechanics require a neutrino $|\nu_x\rangle$ to be in a certain flavour eigenstate when created, e.g. $|\nu_x\rangle = |\nu_e\rangle$, since it is created in a weak interaction [25, p. 113]. On the other hand, while the neutrino propagates through space (as it would from a source to a detector) the time evolution of the its quantum state is generated by the Hamiltonian according to the Schrödinger equation [26, p. 255]. Thus, in analogy to equation 2.3, the initial neutrino with certain flavour is now to be considered in the basis of mass eigenstates, hence:

$$|\nu_x\rangle = |\nu_\alpha\rangle = \sum_{j=1}^{3} U_{\alpha j}^{*} |\nu_j\rangle, \text{ with } \alpha \in \{e,\mu,\tau\}. \tag{2.4}$$

The time evolution according to the Schrödinger equation reads as

$$|\nu_j(t)\rangle = |\nu_j(0)\rangle e^{-i(Et-pz)}, \text{ with } j \in \{1,2,3\} \tag{2.5}$$

were t denotes the time from the creation, E the energy of the neutrino, p the momentum and z the position along the z-axis, while the neutrino is assumed to travel along this axis.

[2] The usage of the inverse $U_{PMNS}^{\dagger} = U_{PMNS}^{-1}$ instead of the unitary matrix U_{PMNS} itself is convention.

Utilising equation 2.4 we get the time evolution of the initial neutrino[3] as [17]

$$|\nu_\alpha(t)\rangle = \sum_{j=1}^{3} U^*_{\alpha j}|\nu_j(0)\rangle e^{-i(Et-pz)}, \text{ with } \alpha \in \{e,\mu,\tau\}. \tag{2.6}$$

In equation 2.6, assuming ultrarelativistic neutrinos, the time can be substituted by the travel distance L ($c = 1$). By additionally Taylor-expanding the energy to leading order in this equation and dropping phase factors[4], one gets the good approximation of

$$|\nu_\alpha(L)\rangle = \sum_{j=1}^{3} U^*_{\alpha j}|\nu_j(0)\rangle e^{-im_j^2 L/(2E)}, \text{ with } \alpha \in \{e,\mu,\tau\}. \tag{2.7}$$

Due to different mass eigenvalues m_j, $j \in \{1,2,3\}$ of the three mass eigenstates, the time evolution of the three mass eigenstates is slightly different [26, p. 255]. This means that the neutrino $|\nu_\alpha(L)\rangle$ is in general no longer in an eigenstate for $L > 0$. One can see this directly from equation 2.7: for $L > 0$ the ratio of the three coefficients $U^*_{\alpha 1}e^{-im_1^2 L/(2E)}$ / $U^*_{\alpha 2}e^{-im_2^2 L/(2E)}$ / $U^*_{\alpha 3}e^{-im_3^2 L/(2E)}$ is different from the initial ratio for $L = 0$ and hence

$$|\nu_\alpha(L=0)\rangle \neq |\nu_\alpha(L>0)\rangle, \text{ with } \alpha \in \{e,\mu,\tau\} \tag{2.8}$$

in general holds[5].

We assumed that the neutrino travels from a source to a detector. The detection works via the weak force, thus the neutrino has to have a certain flavour in this reaction. Hence, it has to be in a certain flavour eigenstate. The theory of quantum mechanics dictates that the neutrino takes on a certain flavour eigenstate, e.g. $|\nu_\beta\rangle$, with a probability equal to the square of the projection of its current state, e.g. $|\nu_\alpha(L)\rangle$, onto $|\nu_\beta\rangle$ [25, p. 117]. The probability can be expressed as

$$P(\nu_\alpha \to \nu_\beta)(L) = |\langle\nu_\beta|\nu_\alpha(L)\rangle|^2, \text{ with } \alpha,\beta \in \{e,\mu,\tau\}, \tag{2.9}$$

where $\langle\nu_\beta| = |\nu_\beta\rangle^\dagger$ denotes the complex conjugate of $|\nu_\beta\rangle$. The term $\langle\nu_\beta|\nu_\alpha(L)\rangle$ is thus to be understood as a bilinear mapping $\langle\nu_\beta|(|\nu_\alpha(L)\rangle)$, in which $|\nu_\alpha(L)\rangle$ is an element of the original vector space and $\langle\nu_\beta|$ denotes the element of the dual space corresponding unambiguously to $|\nu_\beta\rangle$ by the Riez representation theorem. Equation 2.9 can be understood as the probability to measure the initial neutrino $|\nu_\alpha\rangle$ after a travel distance L as a neutrino of type $|\nu_\beta\rangle$. Applying equations 2.4 and 2.7 and keeping in mind that $\langle\nu_\beta| = |\nu_\beta\rangle^\dagger$, equation 2.9 reads as

$$P(\nu_\alpha \to \nu_\beta)(L) = \left|\sum_{j=1}^{3} U_{\alpha j}U^*_{\beta j}e^{-im_j^2 L/(2E)}\right|^2. \tag{2.10}$$

This probability undergoes periodical changes with the travel time and travel distance, respectively. Figure 2.1 shows this probability graph for the case of the Double Chooz experiment. In order to compute this probability, the actual representation of the PMNS matrix becomes important. The common representation utilises the notion of Euler angles and reads [17]

[3] To be precise, the neutrino is in general no longer in a flavour eigenstate for $t > 0$ (see later) and should better be referred to as $|\nu_x(t)\rangle$. However, since equation 2.6 describes the time evolution of the vector $|\nu_\alpha\rangle = |\nu_\alpha(t=0)\rangle$ the usage of $|\nu_\alpha(t)\rangle$ is mathematically correct.

[4] These factors are irrelevant in the later derived oscillation equation.

[5] More precisely, it even holds in general that $|\nu_\alpha(L=0)\rangle \neq \epsilon|\nu_\alpha(L>0)\rangle$, $\alpha \in \{e,\mu,\tau\}$, $\epsilon \in \mathbb{R}$, i.e. $|\nu_\alpha(L=0)\rangle$ and $|\nu_\alpha(L>0)\rangle$ are in general not linear dependent. Only from this additional inequality follows that the neutrino is no longer in the initial eigenstate.

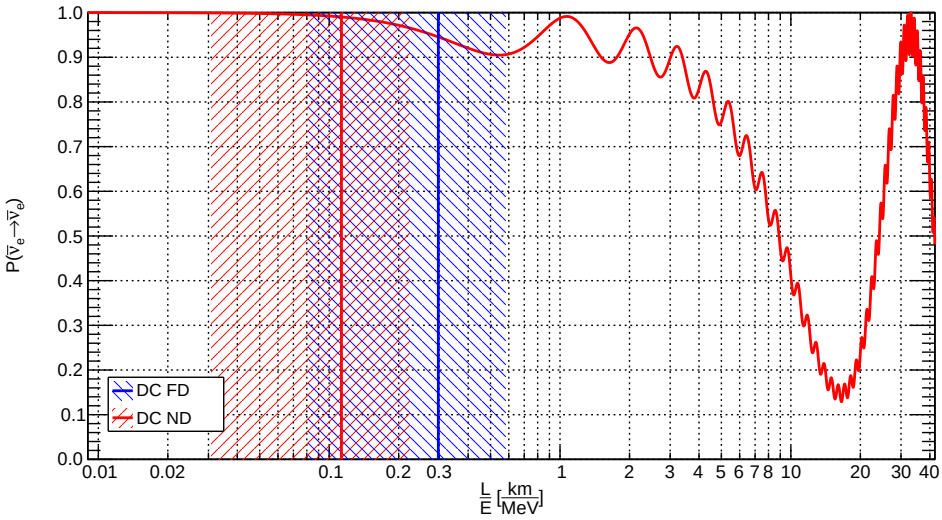

Figure 2.1: Vacuum oscillation probability function of the Double Chooz experiment. The survival probability of electron antineutrinos $P(\bar{\nu}_e \rightarrow \bar{\nu}_e)$ is plotted. The experimentally accessible parts of this graph are highlighted for the DC-far (blue) and DC-near (red) detectors. The $\frac{L}{E}$ with highest expected number of events is denoted by a solid line in the same colour. The oscillation parameter values assumed in this plot are those in table 2.1 for the normal hierarchy.

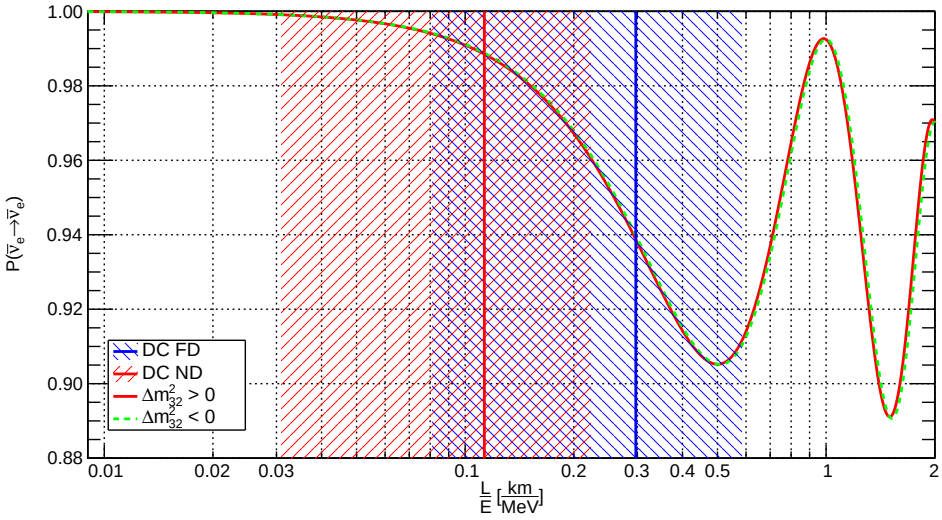

Figure 2.2: Influence of the neutrino mass hierarchy on the vacuum oscillation probability functions of the Double Chooz experiment. The figure is a detailed view of figure 2.1 (see there for explanation). Added is a graph for inverted mass hierarchy (dashed-green) using the corresponding oscillation parameter values as listed in table 2.1.

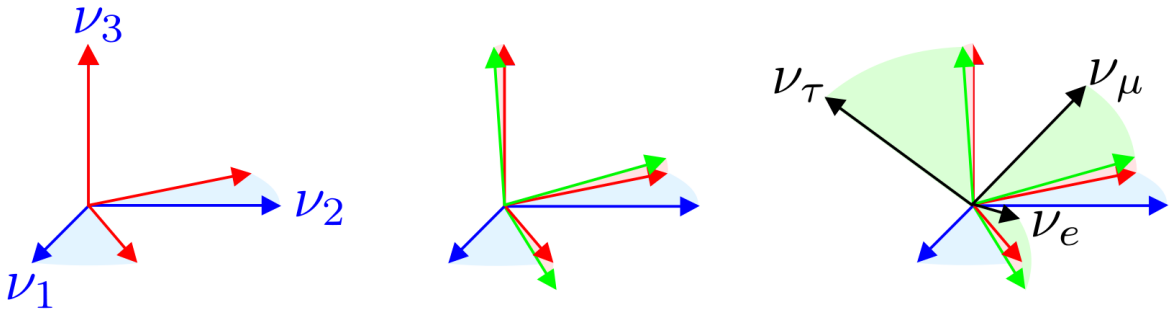

Figure 2.3: Change of basis between the basis of flavour eigenstates and the basis of mass eigenstates. The mixing angles are the Euler angles. The application of the submatrices in equation 2.11 corresponds to the figures from left to right. The angles are drawn approximately realistic. [28, p. 16]

$$U_{PMNS} = \begin{pmatrix} c_{12}c_{13} & s_{12}c_{13} & s_{13}e^{-i\delta} \\ -s_{12}c_{23} - s_{13}s_{23}c_{12}e^{i\delta} & c_{12}c_{23} - s_{12}s_{13}s_{23}e^{i\delta} & s_{23}c_{13} \\ s_{12}s_{23} - s_{13}c_{12}c_{23}e^{i\delta} & -s_{23}c_{12} - s_{12}s_{13}c_{23}e^{i\delta} & c_{13}c_{23} \end{pmatrix} \times \begin{pmatrix} 1 & 0 & 0 \\ 0 & e^{i\alpha_1} & 0 \\ 0 & 0 & e^{i\alpha_2} \end{pmatrix}$$

$$= \begin{pmatrix} 1 & 0 & 0 \\ 0 & c_{23} & s_{23} \\ 0 & -s_{23} & c_{23} \end{pmatrix} \times \begin{pmatrix} c_{13} & 0 & s_{13}e^{-i\delta} \\ 0 & 1 & 0 \\ -s_{13}e^{i\delta} & 0 & c_{13} \end{pmatrix} \times \begin{pmatrix} c_{12} & s_{12} & 0 \\ -s_{12} & c_{12} & 0 \\ 0 & 0 & 1 \end{pmatrix} \times \begin{pmatrix} 1 & 0 & 0 \\ 0 & e^{i\alpha_1} & 0 \\ 0 & 0 & e^{i\alpha_2} \end{pmatrix}$$

$$\text{with } s_{kl} = \sin(\theta_{kl}) \text{ and } c_{mn} = \cos(\theta_{mn}). \tag{2.11}$$

The variables θ_{kl} represent the Euler angles as seen in figure 2.3 and $\delta = \delta_{CP}$ is the CP-violating phase. This accounts for different oscillation probabilities between neutrinos and antineutrinos [29, p. 36]. Its influence on the change of basis matrix can be seen in the mixture of flavour and mass eigenstates in figure 2.4. The variables α_j, $j \in \{1, 2\}$ are the Majorana phases and are only of importance if neutrinos are equal to antineutrinos [17]. In our context, these phases can be neglected since they are on the main diagonal of the PMNS matrix.

Using equations 2.11 and 2.10 together with the unitarity of the PMNS matrix, one can compute the survival probability of reactor antineutrinos as [31, p. 1]

$$P(\bar{\nu}_e \to \bar{\nu}_e) = 1 - \sin^2(2\theta_{13}) \cdot \left(\cos^2(\theta_{12}) \sin^2\left(\frac{\Delta m^2_{31} L}{4E}\right) + \sin^2(\theta_{12}) \sin^2\left(\frac{\Delta m^2_{32} L}{4E}\right)\right) - \cos^4(\theta_{13}) \sin^2(2\theta_{12}) \sin^2\left(\frac{\Delta m^2_{21} L}{4E}\right) \tag{2.12}$$

with

$$\Delta m^2_{jk} := m^2_j - m^2_k \tag{2.13}$$

denoting the differences between the squared mass eigenvalues m_j, $j \in \{1, 2, 3\}$. As argued in [31], it is desirable to formulate equation 2.12 in terms of an effective squared mass splitting

$$\Delta m^2_{ee} := \cos^2(\theta_{12}) \Delta m^2_{31} + \sin^2(\theta_{12}) \Delta m^2_{32} \tag{2.14}$$

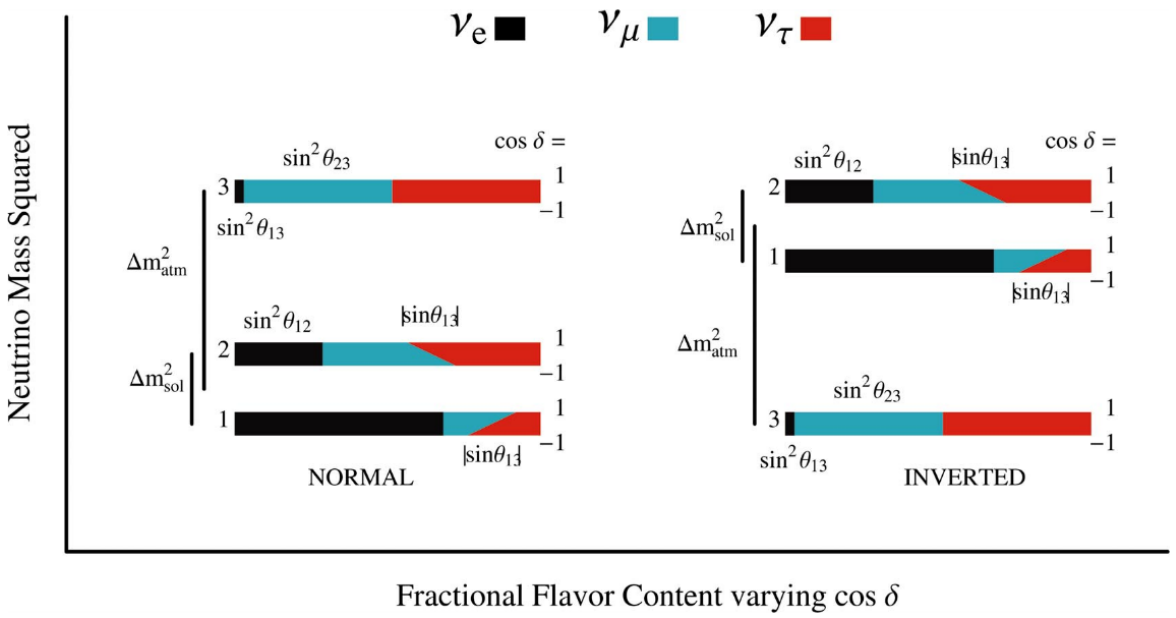

Figure 2.4: View of the two neutrino mass hierarchies and the effect of CP-violation on the mixing between flavour and mass eigenstates. The bottom of the bars corresponds to $\cos(\delta_{CP}) = -1$ the top to $+1$. Fixed in this plot are the mixing angles: $\sin^2(\theta_{12}) = 0.30$, $\sin^2(\theta_{13}) = 0.03$ and $\sin^2(\theta_{23}) = 0.50$. One can see that the variation in the flavour admixture is in the order of $\sin(\theta_{13})$. Reprinted figure with permission from [30, p. 3] ©2004 American Physical Society.

such that equation 2.12 can be written in excellent approximation [31, p. 1] as

$$P(\bar{\nu}_e \to \bar{\nu}_e) \approx 1 - \sin^2(2\theta_{13}) \sin^2\left(\frac{\Delta m^2_{ee} L}{4E}\right) - \cos^4(\theta_{13}) \sin^2(2\theta_{12}) \sin^2\left(\frac{\Delta m^2_{21} L}{4E}\right). \quad (2.15)$$

The graph of the function is given in figure 2.1. The equation yields that the positions of the minima/maxima of the graph are determined by the mass differences, while the amplitudes are determined by the mixing angles. In figure 2.1, the smaller oscillation with higher frequency is due to θ_{13} and Δm^2_{31}, the other due to θ_{12} and Δm^2_{21}.

A further dependency of the oscillation probability is due to the mass hierarchy of the neutrinos. Due to the large uncertainty of Δm^2_{32} compared to the value of Δm^2_{21} (cf. table 2.1) it is up to the present date not possible to determine the ordering of mass states. As a consequence, two possible hierarchies for the neutrino masses exist [30]. In the normal mass hierarchy scenario $m_1 < m_2 < m_3$ holds, in the inverted mass hierarchy scenario $m_3 < m_1 < m_2$ holds. This can be seen in figure 2.4. Although the form of equation 2.12 is unaffected by the mass hierarchy, the values of the probabilities are affected, since the values of the mass differences are affected. Hence, the probability graph splits up in two graphs as shown in figure 2.2.

Since the experiments are not located in vacuum, matter effects have in principle to be considered. However, the effect on equation 2.12 is negligible in the Double Chooz experiment due to the short baselines of 400 m and 1.05 km, respectively [31, p. 1].

parameter	value	hierarchy
Δm^2_{21}	$(7.53 \pm 0.18) \cdot 10^{-5}\,\mathrm{eV}^2$	
Δm^2_{32}	$(2.44 \pm 0.06) \cdot 10^{-3}\,\mathrm{eV}^2$	normal
$-\Delta m^2_{32}$	$(2.52 \pm 0.07) \cdot 10^{-3}\,\mathrm{eV}^2$	inverted
$\sin^2(2\theta_{12})$	0.846 ± 0.021	
$\sin^2(2\theta_{13})$	0.093 ± 0.008	
$\sin^2(2\theta_{23})$	$0.999^{+0.001}_{-0.018}$	normal
$\sin^2(2\theta_{23})$	$1.000^{+0.000}_{-0.017}$	inverted

Table 2.1: Summary of current knowledge on the oscillation parameters. [17]

The current knowledge on all relevant parameters is summarised in table 2.1. One can see a difference of almost two orders of magnitude for the neutrino mass squared splittings. Likewise, the values for the mixing angles show a large spread. While $\sin^2(2\theta_{23})$ is realised around its possible maximum, $\sin^2(2\theta_{13})$ is rather small. The parameters θ_{12} and Δm^2_{21} are mainly determined by results of the **Kam**ioka **L**iquid Scintillator **A**nti**n**eutrino **D**etector (KamLAND) experiment [32], the **S**udbury **N**eutrino **O**bservatory (SNO) [33], the Borexino experiment [34] and other solar neutrino experiments. The parameters θ_{12} and Δm^2_{21} could mainly be determined by atmospheric and long-baseline accelerator oscillation experiments like the Super-Kamiokande [35], the **M**ain **I**njector **N**eutrino **O**scillation **S**earch experiment (MINOS) [36], the **K**EK **to K**amioka experiment (K2K) [37] and the **T**okai **to K**amioka experiment (T2K) [38]. Knowledge on the parameter $\sin^2(2\theta_{13})$ is mainly given by the reactor experiments Daya Bay [7], RENO [8] and Double Chooz [10]. For the parameter $\sin^2(2\theta_{13})$, the analysis presented in chapter 6 will provide a new measurement.

Chapter 3

The Double Chooz Experiment

In this thesis, the handling and analysis of data from the Double Chooz experiment will be discussed. Hence, this chapter gives an overview of the experimental setup built to record this data and the basic characteristics of the data itself. The overview follows mainly reference [14, p. 10 & seqq.].

The idea of a neutrino oscillation experiment is to compare the neutrino flux originating from a neutrino source in different distances. At least one source and two flux measurements or a precise flux prediction and a measurement are required. The average distances from the source(s) to the detectors are called the baselines of the experiment. In a reactor experiment, the difference between the fluxes can have two reasons:

- Since the neutrino flux is isotropic, it decreases inverse proportionally with the distance from the reactors.
- The flux difference can be due to neutrino oscillations.

In the Double Chooz experiment, the effect due to neutrino oscillations is much smaller than the geometrical effect. In addition, detector imprecisions and background contributions can cause discrepancies between the flux measurements. Those imprecisions and backgrounds have to be eliminated or corrected by the design of the experiment and the data analysis strategy.

The **D**ouble **C**hooz (DC) experiment [12; 13] is a reactor experiment. It aims for the measurement of the survival probability of electron antineutrinos and thereby for the measurement of the lepton mixing angle θ_{13}, a parameter of the lepton mixing matrix U_{PMNS} as given in equation 2.11. By its measurement principle it is characterised as a disappearance experiment.

The Double Chooz experiment consists of two detectors measuring the neutrino flux from two nuclear reactors. The near detector has an approximate distance of 400 m to the reactor cores, the far detector has a distance of approximately 1050 m to the cores. The far detector is located near the first oscillation minimum (cf. figure 2.1) such that the maximal effect of the neutrino oscillation can be measured. The exact geometry can be seen in figure 3.1. The far detector started operations in 2011 and since 2015 both detectors are operational.

In the two detector setup, the **n**ear **d**etector (ND) provides a first measurement of the neutrino flux. This is taken as the almost unoscillated reference flux. The **f**ar **d**etector (FD-II) then measures the flux in a greater distance to the cores. This flux is called the oscillated neutrino flux. Assuming that the neutrino flux is isotropic, a prediction of the flux

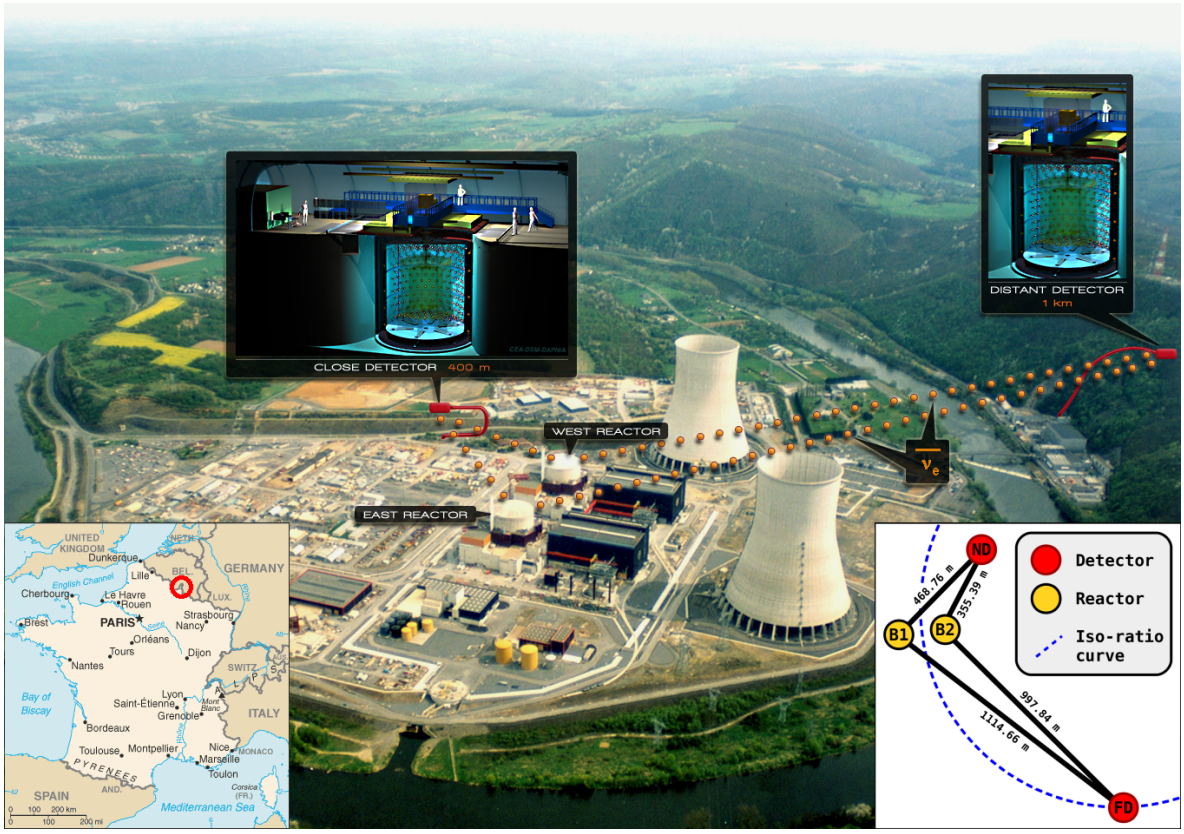

Figure 3.1: Geographical setup of the Double Chooz experiment: The large picture shows the nuclear power plant site [39]. The insert in the lower left corner shows the location of the experiment within France [40]. The insert in the lower right corner shows the precise distances between the reactors (B1 and B2) and the near and far detectors (ND and FD) measured in a dedicated geodetic survey [41]. The iso-ratio curve marks the points for which the ratio between the reactor fluxes is the same as for the far detector.

in the far detector can be made by extrapolating the measured flux of the near detector. The difference between the measured far detector flux and the unoscillated prediction is due to neutrino oscillations and can be transformed in a value for θ_{13} by equation 2.15. In the single detector setup, the prediction of the neutrino flux in the **f**ar **d**etector (FD-I) has to be done by measuring the thermal output of the two reactors and converting it into the primary neutrino flux.

The measurement presented in this work uses data collected during both detector phases. The amount of recorded data with both setups can be seen in figure 3.2. A more detailed presentation of the datasets is given in chapter 5.

3.1 The Reactors

The source of the neutrinos are the two nuclear reactors CHOOZ-B1 and CHOOZ-B2. They belong to the CHOOZ nuclear power plant (Centrale nucléaire de Chooz) of the French electric utility company EDF (**É**lectricité **d**e **F**rance). The plant is located in France near the town of

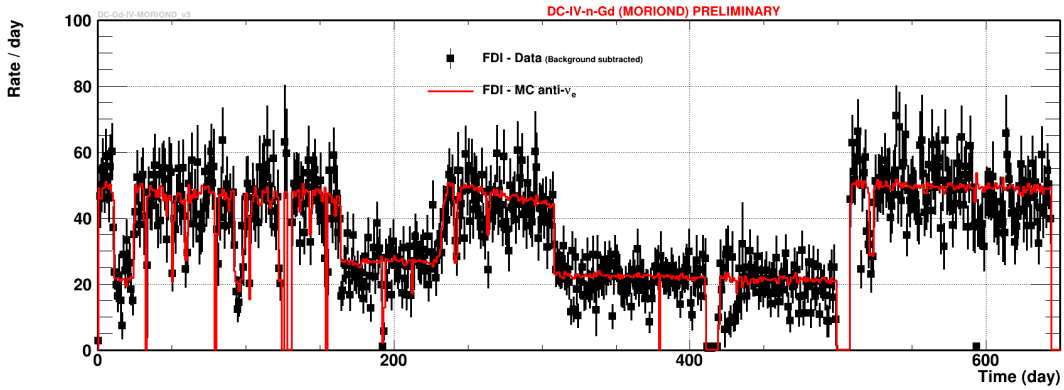

(a)

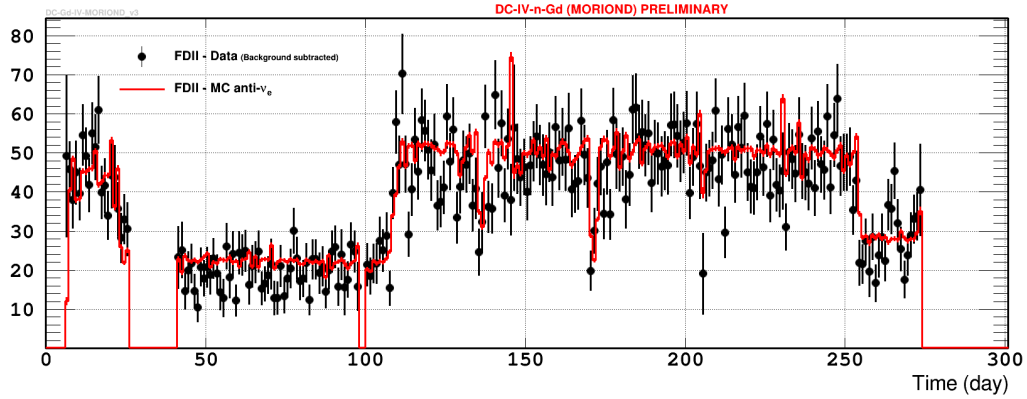

(b)

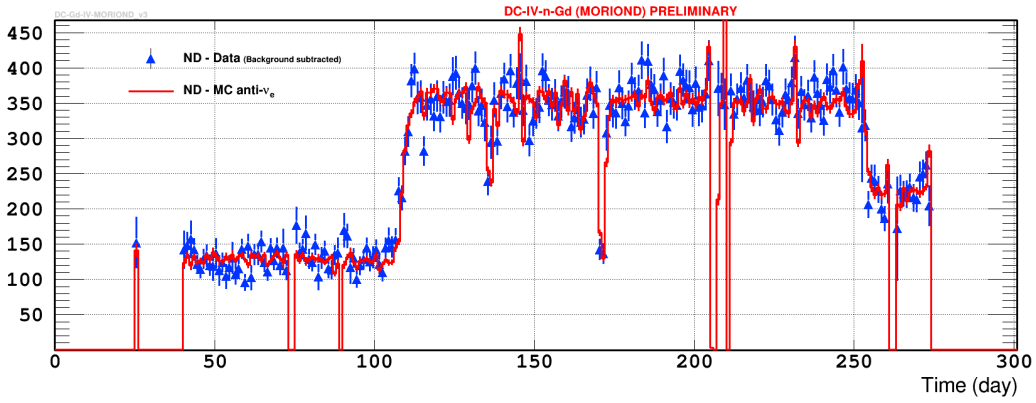

(c)

Figure 3.2: Recorded data (background subtracted) in the single detector and two detector phase compared to the predicted signal rate. The (a) far detector during single detector phase (FD-I), (b) far detector during two detector phase (FD-II) and (c) near detector during two detector phase (ND) is shown. For the FD-I, only the first 490 days have been analysed yet. The large steps are caused by the number of active reactor cores. [42]

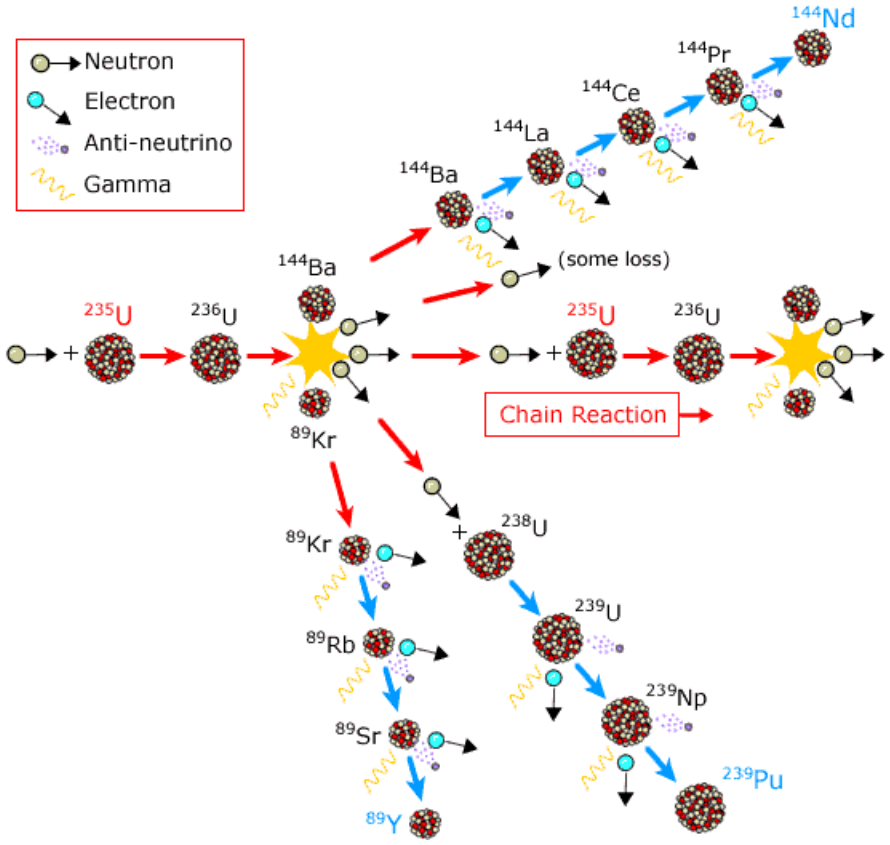

Figure 3.3: Sketch of main reactions in the reactors [44].

Chooz next to the Belgian border (cf. figure 3.1). The reactors are pressure water reactors of the type N4 and have an electrical power output of 2·1500 MW [12, p. 23]. The main process in the reactors is a controlled chain reaction of uranium-235

$$\mathrm{n} + {}^{235}\mathrm{U} \rightarrow {}^{236}\mathrm{U}^{*} \rightarrow {}^{89}\mathrm{Kr} + {}^{144}\mathrm{Ba} + 3\mathrm{n} \tag{3.1}$$

as also shown in figure 3.3. The subsequent decay chains of krypton and barium are then releasing energy via β-decays, which is eventually converted into electrical power. As the breakup into krypton and barium is only the dominant, but not the only process, a variety of over 10.000 β-branches built from around 850 isotopes contribute to the nuclear processes in the reactor cores [43, p. 18]. During each β-decay, electron antineutrinos are produced as shown in figure 3.3. Unlike other fission products, neutrinos can escape the reactor building due to their small cross section and can be measured in a detector outside of the building. Those neutrinos are the signal contribution in the Double Chooz experiment.

The thermal output of the reactors is used to measure the current reaction rate by the minute and to predict consequently the neutrino flux from the reactors. This flux calculation has significant uncertainties due to evolving reactor fuel components and power output regulations. As shown in figure 3.3, the evolution of fuel components is due to the enrichment of plutonium isotopes by neutron capture and subsequent nuclear transformation following the fission of uranium isotopes [12, p. 17]. The reactor prediction will be discussed in greater detail in section 5.3.

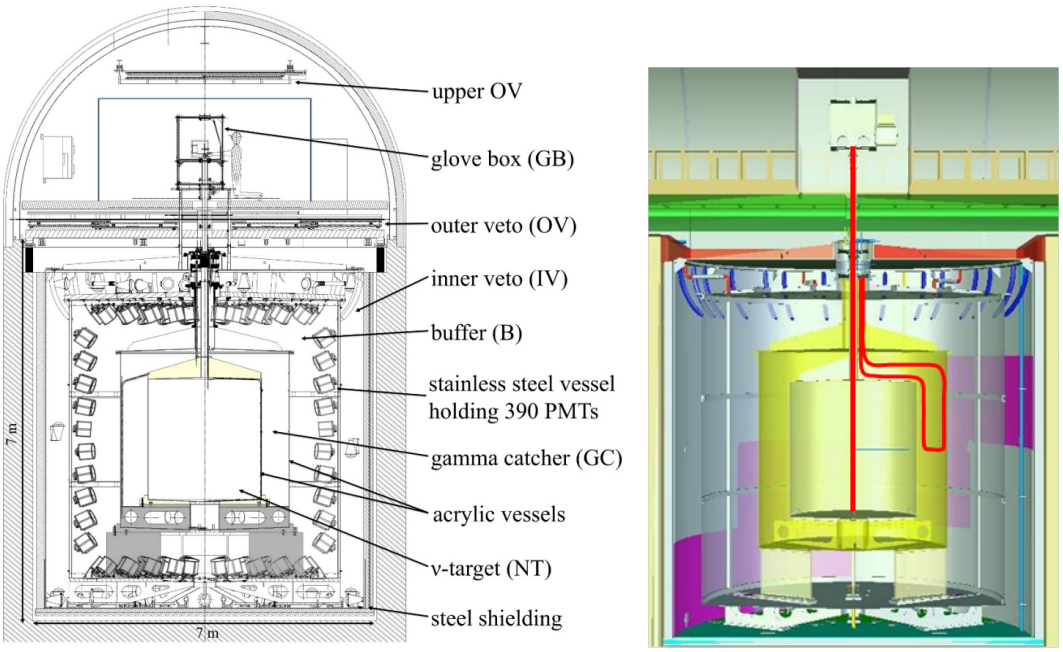

(a) (b)

Figure 3.4: The Double Chooz detectors and their calibration source deployment systems. Figure (a) shows a sectional sketch of the Double Chooz detectors [10, p. 3]. Figure (b) shows the calibration source deployment systems in the scintillator-filled ID volumes. The central red line shows the pathway of the z-axis calibration system used in the target volume, the red loop shows the pathway of the guide-tube calibration system used in the γ-catcher volume [46, p. 16].

3.2 The Detectors

The Double Chooz detectors are liquid scintillator detectors. The far detector is located in the surrounding rock of the nuclear plant (cf. figure 3.1). It was constructed in a cavern built in an access tunnel of the dismantled CHOOZ-A reactor. It has an overburden of 300 **m**etre **w**ater **e**quivalent (m.w.e.) rock. The near detector was built in a new cavern next to the reactors and has an overburden of 140 m.w.e. [45]. The two detectors are designed equal in order to reduce systematic uncertainties between the two neutrino flux measurements. As shown in figure 3.4, the main detector component is cylindrical, has a height and diameter of approximately 7 m and consists of several volumes enclosing each other. The detector components are in detail [13, p. 63 & seqq.]:

▶ **Inner Detector:** The **I**nner **D**etector (ID) consists of the three cylindrical inner volumes of the detector. They are separated by transparent acrylic. To the outside volume, the ID is optically separated by a steel tank. On the inside of this steel tank 390 **p**hoto**m**ultiplier **t**ubes (PMT) are installed. They are all oriented towards the same central volume (cf. figure 3.4a). Further details on the PMTs can be found in reference [47]. The three volumes are from the inside to the outside:

- **Neutrino Target:** The **N**eutrino **T**arget (NT) is filled with liquid scintillator and has a volume of 10.2 m^3. In this volume, the main detection reaction for the neutrinos shall

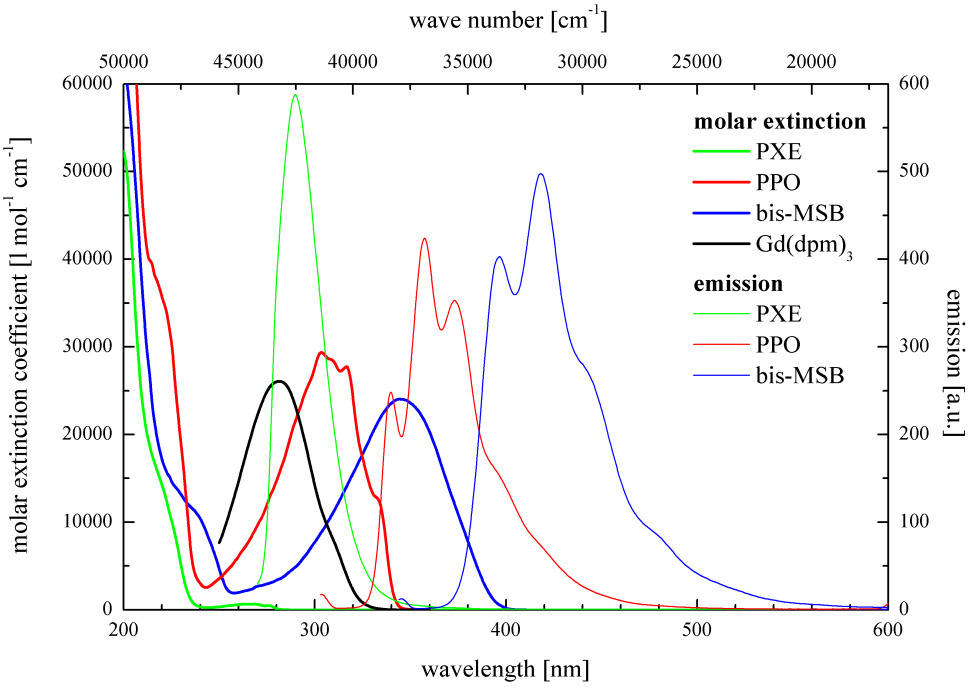

Figure 3.5: Absorption and emission spectra of the scintillator components. The absorption by the gadolinium complex reduces the light yield of the target scintillator. [48, p. 19].

take place. The scintillator, built from 80 %$_{\text{vol}}$ non-scintillating dodecane and 20 %$_{\text{vol}}$ PXE is loaded with 1 g/l gadolinium [49, p. 2], which enhances the neutrino detection. The details of this will be described in section 3.5. The scintillator is responsible for the conversion of the neutrino energy into light visible for the PMTs. Wavelength shifters are mixed with the scintillator to shift the light to a wavelength with higher transparency and better PMT efficiency (cf. figure 3.5). Those acceptor molecules are 20 mg/l bis-MSB and 7 g/l PPO [49, p. 2]. As visible in figure 3.5, the chemical gadolinium complex is acting as a quencher in the neutrino target, reducing the light yield. Details on the scintillator components can be found in reference [48].

• **γ-Catcher:** The γ-**C**atcher (GC) encloses the NT volume. It is a hollow cylinder of 21.5 m^3 volume. It is filled with a similar mixture of liquid scintillator as the NT, but without gadolinium. Non-scintillating 66 %$_{\text{vol}}$ Shell Ondina 909 and 30 %$_{\text{vol}}$ dodecane are mixed with scintillating 4 %$_{\text{vol}}$ PXE [49, p. 2]. Again, wavelength shifters are added to the scintillator. Those are 20 mg/l bis-MSB and 2 g/l PPO [49, p. 2]. The mixture is tuned to match the NT light yield and density. This reduces the mechanical stress on the acrylic vessel separating the two volumes. In the case of a neutrino detection reaction near to the boundary of the NT, the γ-catcher has the purpose to convert escaping photons of this reaction into visible light. Moreover, the GC acts, together with the NT, as fiducial volume for a second detection channel not involving gadolinium. This will be detailed in section 3.5. Further details on the scintillator can be found in reference [48].

• **Buffer:** The Buffer is the outer hollow cylinder of the ID enclosing the γ-catcher. It has a volume of 100 m^3 and is filled with non-scintillating mineral oil. It accommodates the PMTs. Since the mineral oil is non-scintillating, radioactive isotopes in the steel

vessel and the PMTs itself produce less light. By this, only the central volumes are built to produce light. This light is then observed by all PMTs.

▶ **Inner Veto:** The **I**nner **V**eto (IV) volume encloses the ID. It is optically separated from the ID by a steel tank and is of hollow cylindrical geometry. It is filled with liquid scintillator and on the inside of the outer wall 78 PMTs are installed. The PMTs are oriented parallel to the walls as pictured in figure 3.4a. Most of the PMTs observe different volumes of the IV since the central steel tank prevents the PMTs from observing the whole IV volume. The IV has the purpose to detect particles other than neutrinos coming from the outside into the detector. Many of these particles are able to mimic neutrinos and hence need to be rejected in the event selection or tagged for background studies, respectively. The IV in the far detector is enclosed by a 17 cm thick steel shield in order to reduce the flux from atmospheric muons in the detector and to shield it against radioactivity of the surrounding rock. In the near detector, the lateral and bottom shielding is made of water instead of steel, while the top shielding remains unchanged.

▶ **Outer Veto:** The **O**uter **V**eto consists of two double layers of plastic scintillator strips mounted on the floors of the laboratories directly above the steel shielding and underneath the ceiling (cf. figure 3.4a). If covers an area of 91 m^2 in the far detector [10, p. 4] and an area of 47 m^2 in the near detector [50]. The OV outreaches the cylindrical part of the detector. By this, it is possible to detect atmospheric muons penetrating into the surrounding rock of the detector. Such muons can produce secondary particles which can then laterally enter the detector. More details on the OV can be found in reference [51].

▶ **Chimney:** The NT and GC volumes can be accessed for calibration purposes by a vertical shaft located in the centre of the detector (cf. figure 3.4a). This shaft is called chimney. The chimney subvolumes have direct contact with the corresponding subvolumes of the ID and they are filled with the same scintillator mixtures as the ID. At its top, the chimney leads into a glove box installed inside a clean room (cf. figure 3.4a). From this glove box, calibration sources can be deployed into the scintillator volumes. This will be detailed in section 3.3. Since the chimney penetrates the buffer, the IV and the OV layers, the veto systems have an acceptance hole and some background events can enter the ID unseen. This is compensated by a dedicated background rejection strategy in the chimney region as presented in section 5.2.

3.3 Calibration Systems

The detectors are equipped with a variety of calibration systems to determine precisely the conversion constants between visible energy and charge depositions in the PMTs. Furthermore, the evolution of these constants can be monitored over time. Such evolution can either be caused by degradation of the detector components over time or after a power cycle of hardware components. The calibration systems are in detail:

▶ **Inner Veto Light Injection System:** The **I**nner **V**eto **L**ight **I**njection (IVLI) system is built from optical fibres directing light individually and directly onto each single PMT. This system can therefore measure gains and timing of individual PMTs. The intensity and colour of the emitted light can be altered to probe a variety of cases. The IVLI is used as a weekly calibration system. Further details can be found in reference [52].

▶ **Inner Detector Light Injection System:** Like the IVLI, the **I**nner **D**etector **L**ight **I**njection (IDLI) system is built from optical fibres directing light onto the ID PMTs. Intensity

and light colour can be varied. In contrast to the IVLI system, the IDLI system sends light across the detector either in narrow beams or widely spread patterns. It can be used to determine the signal timing of the PMTs and liquid scintillator properties. Like the IVLI, the IDLI is used for weekly calibrations. Further details can be found in reference [53].

▶ **Guide Tube System:** The guide tube system is installed inside the γ-catcher volume and accessed through the chimney. It consists of a steel tube installed in the upper half of the volume. For one fixed polar angle, it reaches along the edges of the γ-catcher starting from the top (cf. figure 3.4b). The guide tube is used to pull radioactive calibration sources by a stepper motor along a wire to dedicated positions. Such calibrations are used to monitor scintillator degradation and to determine the energy scale of the detectors. Further details can be found in reference [54].

▶ **Z-Axis System:** The z-axis system is used to lower calibration sources through the chimney into the NT. The sources are deployed by a stepper motor along a wire to positions along the z-axis, i.e. the symmetry axis, of the detector (cf. figure 3.4b). As calibration sources, radioactive probes as well as a diffuser ball illuminated by a laser via an optical fibre are used. It fulfils a similar purpose as the guide tube system and is additionally used to determine the concentration of gadolinium in the liquid scintillator. Further details can be found in reference [55].

3.4 Simulation and Reconstruction Software

The Double Chooz experiment uses for the analysis of data and the simulation of the experiment custom software written in C++. The **D**ouble Chooz **O**ffline **G**roup **S**oftware (DOGS) is based on the particle physics analysis framework ROOT [56], which is itself written in C++. The simulation package of the DOGS, which is responsible for the physics simulation in the detector, is the Generic Liquid-scintillator Anti-Neutrino Detector "**G**eneric**L**AND" **G**eant**4** **sim**ulation (GLG4sim) and is a Geant4 [57] application based on KGL4sim [58], the simulation software of the KamLAND experiment [32]. Aside of this simulation software, the DOGS simulates the electronics behaviour of the detector using its own electronic simulation package **R**ead**o**ut **S**imulation **S**oftware (RoSS) [59]. After being processed by GLG4sim and RoSS, the simulated events are in the exact same format as the real data. Both data types are then processed by the **C**ommon **T**runk (CT) custom software package [60] which is responsible for the event reconstruction and low level event analysis. By this, the properties of the measured neutrino events can directly be compared with the full detector simulation of the measurement.

3.5 The Neutrino Detection

In section 3.2, the detectors of the Double Chooz experiment have been described. In the central volumes neutrinos are detected by the reaction of the **i**nverse β-**d**ecay (IBD) [13, p. 10]:

$$\bar{\nu}_e + \mathrm{p}^+ \rightarrow \mathrm{e}^+ + \mathrm{n} \tag{3.2}$$

In this reaction, an electron antineutrino $\bar{\nu}_e$ hits a proton of the scintillator and converts into a positron and a neutron. As seen in figure 3.6a, the cross section for this reaction is non-zero only above 1.8 MeV. Below this energy threshold, the total antineutrino energy does not suffice to generate the mass of the positron (511 keV [17]) and the additional mass of the

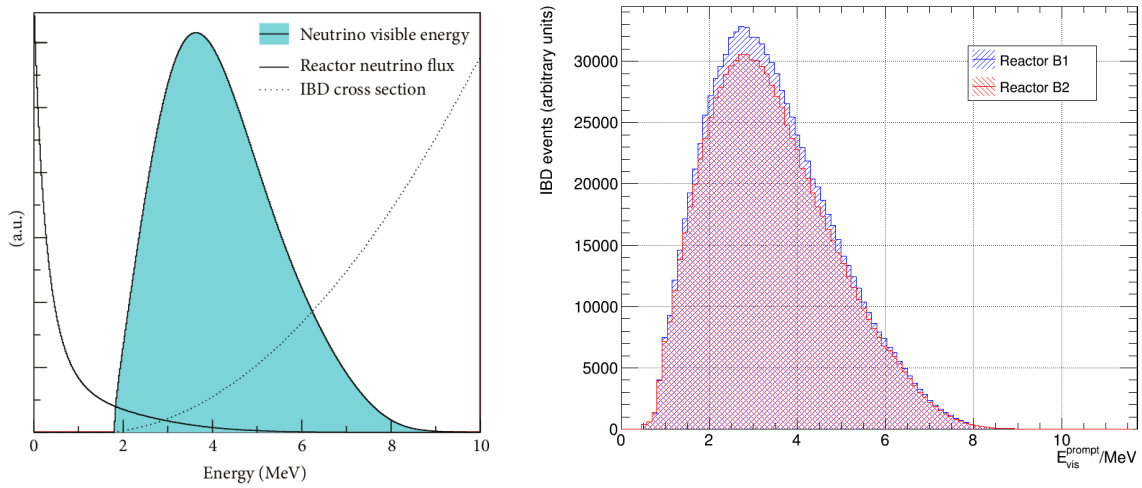

(a) (b)

Figure 3.6: Expected neutrino and prompt energy spectra. Figure (a) shows the neutrino energy spectrum resulting from the reactor neutrino flux and the IBD cross section [62, p. 2]. Figure (b) shows the simulated prompt energy spectrum taking into account detection effects.

neutron with respect to the proton (1.3 MeV [17]). Above the threshold, the cross section increases with energy [61, p. 2] as shown in figure 3.6a.

The neutrino energy is connected to the corresponding positron energy via the equation [12, p. 18]

$$E_{\bar{\nu}_e} = E_{e^+} + (m_n - m_p) + \mathcal{O}(E_{\bar{\nu}_e}/m_n). \tag{3.3}$$

Here, the total positron energy is denoted as E_{e^+}, the total neutrino energy is denoted as $E_{\bar{\nu}_e}$ and the masses of the proton and neutron are denoted as m_n and m_p, respectively.

The positron annihilates promptly with an electron of the scintillator and deposits $2 \cdot 511\,\text{keV}$ rest energy [17] and the kinetic energy from the initial neutrino in the scintillator [13, p. 10]

$$E_{vis}^{prompt} = E_{e^+} + m_{e^-}. \tag{3.4}$$

The deposited energy is called the visible prompt energy E_{vis}^{prompt}. Due to the large mass difference between positron and neutron, only a negligible amount of kinetic energy is transferred to the neutron. Hence, the expected prompt energy spectrum seen in figure 3.6b is by equation 3.3 similar to the predicted neutrino energy spectrum in figure 3.6a. As seen in figure 3.7a, the measured prompt energy spectra in all detectors follow the expected shape.

The neutron in reaction 3.2 produces a second signal, called the delayed signal, when it is captured by a nucleus. In the target volume, the dominant capture process is involving gadolinium which has a high neutron capture cross section. In addition, neutrons get captured by hydrogen in the γ-catcher volume and also subdominantly in the target volume. Hydrogen is present in both volumes as part of the liquid scintillator, but has a low cross section for the capture of neutrons compared to gadolinium. Captures by other isotopes are negligible. The gadolinium and hydrogen nuclei get excited by the neutron capture and emit during their deexcitation one or more photons. For gadolinium, several isotopes can contribute with

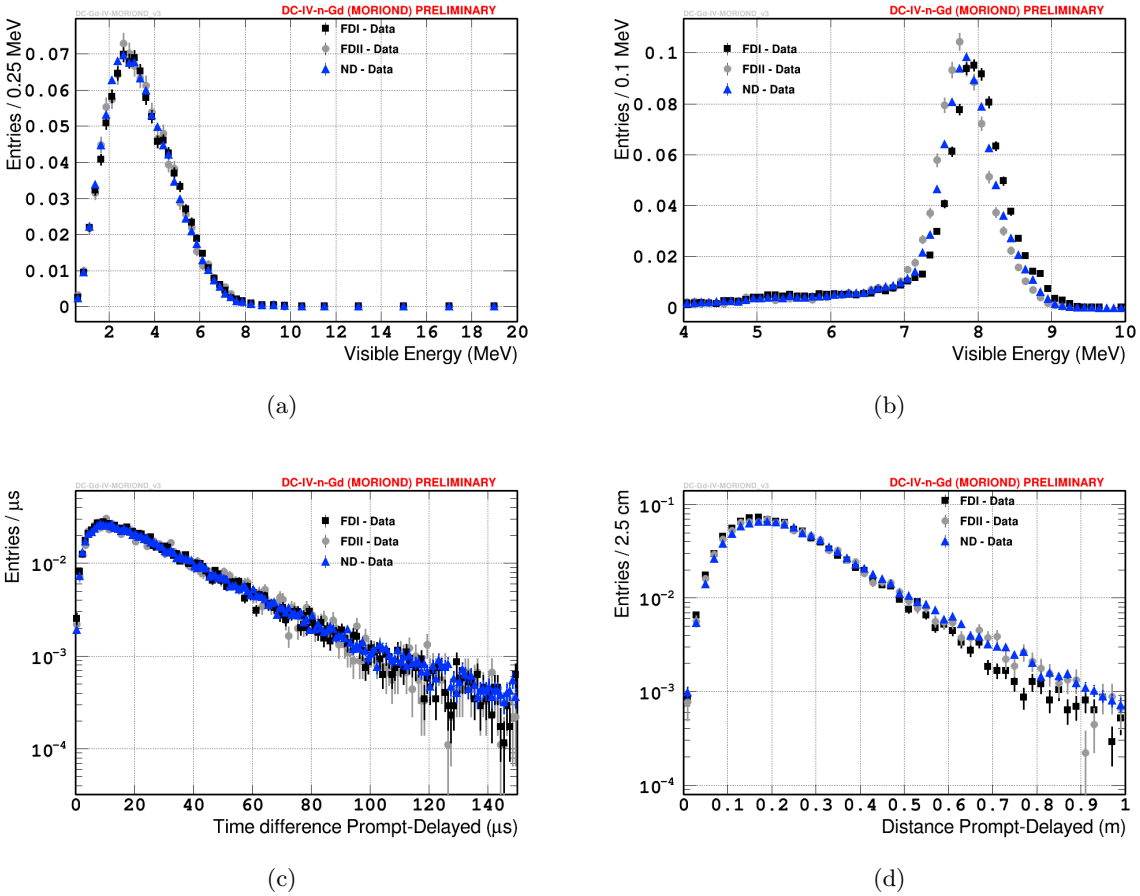

Figure 3.7: Measured inverse β-decay candidate spectra. Figure (a) shows the prompt energy spectrum, figure (b) the delayed energy spectrum and figure (c) the delay time between prompt and delayed events. The increase at small time differences is caused by the neutron thermalisation process while the exponential decrease at large time differences is caused by the capture process. Figure (d) shows the reconstructed vertex distance between prompt and delayed events. [42]

an approximate deexcitation energy of 8 MeV [63; 64]. The measured energy of the neutron captures can be seen in figure 3.7b. For hydrogen, 2.23 MeV energy is released [65].

The neutron needs to thermalise, i.e. to decelerate to thermal energies, before the cross section for a neutron capture becomes so high that the capture actually takes place. This causes a delay between the prompt and the delayed signal of a few microseconds (cf. rising edge for small time differences in figure 3.7c). Following the thermalisation, the capture happens with a time constant of 30 μs for gadolinium and 200 μs for hydrogen [66, p. 68] causing an additional delay.

The delay between a wide spread prompt and a narrow delayed energy deposition is the characteristic signal of an inverse β-decay (cf. figure 3.7c). Thus, for the selection of neutrino events in the detector, a cut on the prompt signal and delayed signal energy as well as the signal delay is used.

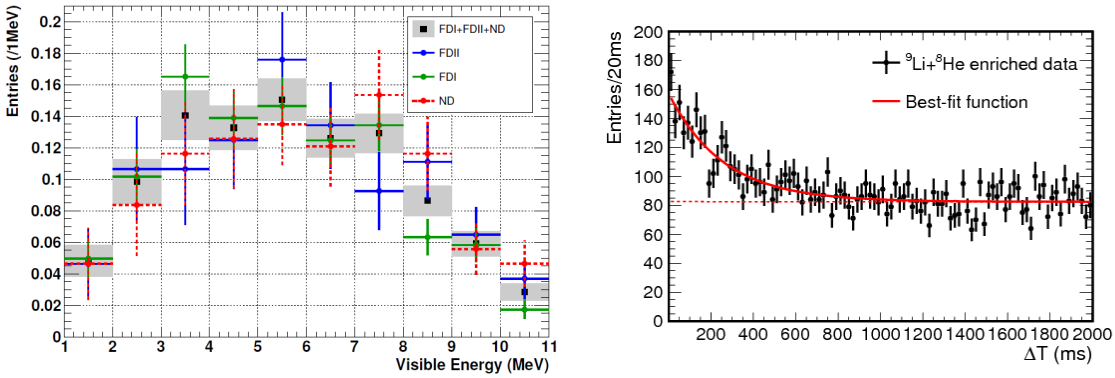

(a) (b)

Figure 3.8: β-n decay background spectra. Figure (a) shows the measured prompt energy spectra of all three datasets [46, p. 11]. Figure (b) shows the delay time spectrum between the prompt event and the inducing muon event in a lithium enriched data sample. The solid red line denotes the best fit to the lithium component including a flat background component of accidental coincidences (dashed line) [10, p. 23].

3.6 Background Processes

Many processes can mimic the signal of an IBD. These are either correlated processes, with a similar signature as the IBD signal or random coincidences of backgrounds coming from different sources. Relevant intrinsic sources are unavoidable radioactive contaminations of the detector materials as well as artificial light produced by hardware components in the detectors. As external source, atmospheric muons dominate. They are part of particle showers which are produced when a high energy particle from outer space collides with Earth's atmosphere.

In the following, all relevant background types will be discussed briefly highlighting only their most relevant properties. Moreover, the principle idea of discriminating them will be explained. A more thorough discussion of the background rejection criteria will be given in chapter 5. Only the backgrounds as they appear in the data sample derived from delayed neutron captures by gadolinium will be discussed. Backgrounds of the hydrogen sample, which is not used in this thesis, are discussed in reference [67].

3.6.1 β-n Decay Background

Atmospheric muons are able to enter the detector and fissure carbon atoms, which are a major component of the scintillator. Thus spallation products get generated in the detectors. Among them are lithium-9 and helium-8 nuclei which can perform a β^--n decay after a relatively long lifetime of 257 ms and 172 ms, respectively [67, p. 9] (cf. figure 3.9). Their energy spectrum looks very similar to the IBD spectrum (cf. figures 3.7a and 3.8a). Although the decays are likely to happen shortly after the inducing muon has crossed the detector (cf. figure 3.8b), it is not possible to reject this background fully by introducing a veto time after muons. This is caused by the high muon rate and thus by the impossibility to apply a sufficiently large veto time without vetoing at almost all times. The β-n isotope background is thus the hardest background to discriminate.

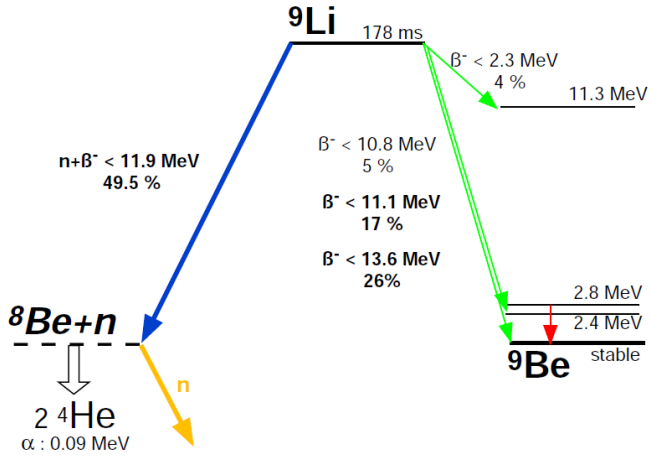

(a)

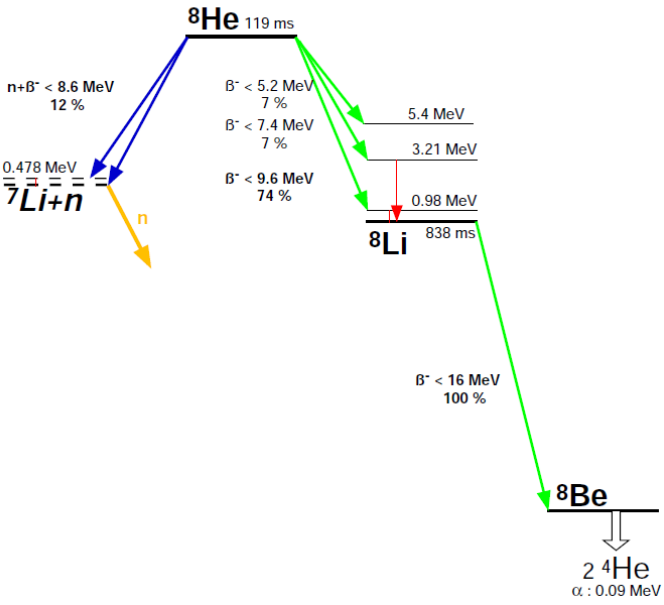

(b)

Figure 3.9: Decays of (a) lithium and (b) helium isotopes which are able to undergo β-n decays (blue) [12, p. 60 & seq.].

3.6.2 Fast Neutron Background

Apart from long living $\beta^- n$-decay isotopes, the spallation of carbon atoms outside the detector can produce neutrons with high energies. These fast neutrons can mimic an IBD when they enter the detector and perform proton recoils in the liquid scintillator before they get captured or when many neutrons enter the detector in a burst. By vetoing muons regardless if they pass or cross the inner detector, a large fraction of fast neutron events can be rejected. However, since the inducing muon can pass the detector without hitting a veto system, fast neutrons can enter the detector without a large energy deposition. For delayed captures by gadolinium,

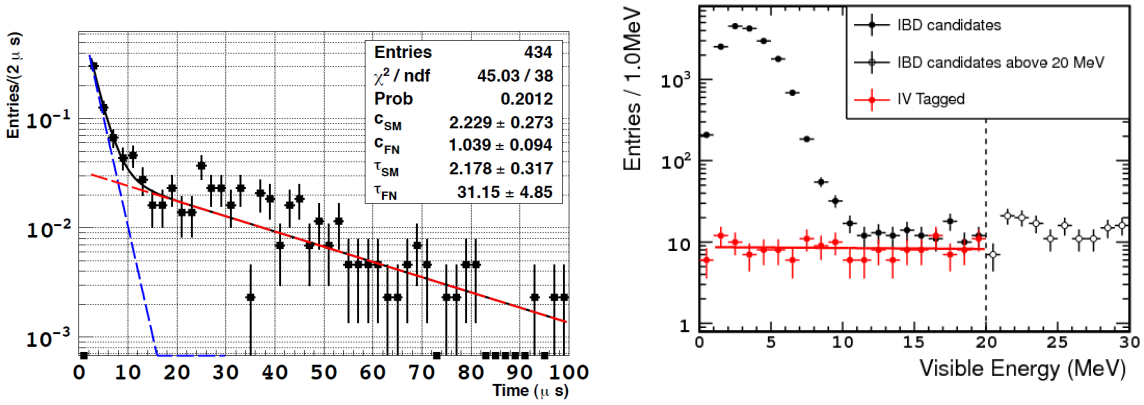

(a) (b)

Figure 3.10: Stopping muon and fast neutron background spectra. Figure (a) shows the delay time spectrum between prompt and delayed events [68, p. 113]. The fast component (dashed blue) shows a time constant of 2.18 μs. It is consistent with decaying muons. The slow component shows a time constant of 31.15 μs. It is consistent with neutron captures by gadolinium. Figure (b) shows the prompt energy spectrum [10, p. 25]. By looking at events that pass the full IBD selection, but deposit energy in the IV, the flat background contribution by stopping muons and fast neutrons (solid red line) can be identified.

the remaining prompt signal of fast neutron events shows a flat energy spectrum over the relevant energy range for IBDs (cf. figure 3.10b).

3.6.3 Stopping Muon Background

In addition to the background due to the spallation of atoms by muons, the muons themselves can mimic IBD signals when they enter the detector at very low velocities. In this scenario, the last ionisations along the muon track before the muon stops can mimic the prompt IBD signal, while the decay Michel-electron or Michel-positron can mimic the delayed IBD signal. This background can be rejected by its short delay time, which reassembles the small lifetime of muons (cf. figure 3.10a). The remaining prompt energy spectrum shows a flat shape (cf. figure 3.10b). Thus, the stopping muon background is treated in the following often together with the fast neutron background.

3.6.4 Accidental Background

Apart from correlated background signals induced by muons, background signals caused by radioactive decays are a non-negligible contribution. This accidental background can be produced by different types of random delayed coincidences, e.g. between a radioactive decay and a spallation neutron or between two radioactive decays. Radioactive decays are caused by isotopes naturally present in the steel of the vessels like uranium, thorium or cobalt and their decay products. Moreover, potassium is present as natural contamination in many materials due to its very long decay time of $\tau_K = (12.7 \pm 0.5) \cdot 10^8$ a [69]. This background appears dominantly at low prompt energies (cf. figure 3.11). However, since it is not a correlated process,

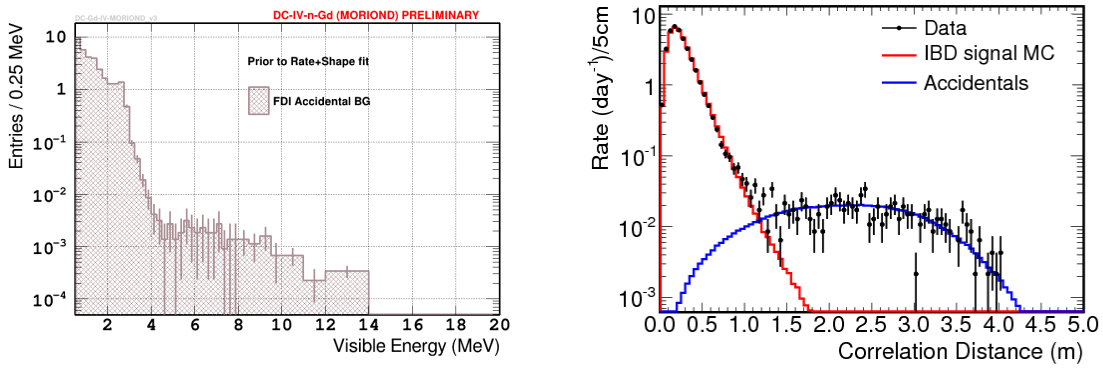

(a) (b)

Figure 3.11: Accidental background spectra. Figure (a) shows the prompt energy spectrum in the FD-I dataset [42]. Energy spectra of the other datasets can be found in appendix C. Figure (b) shows the spatial distance spectrum between prompt and delayed events [10, p. 15]. IBD events show a small distance between prompt and delayed vertex because positron and neutron are produced at the same vertex. In contrast, prompt and delayed vertex of accidental background events show on average a larger distance since they are produced in two different processes with randomly distributed locations.

its spatial distance between prompt and delayed events is randomly distributed (cf. figure 3.11b). By introducing a spatial distance cut, this background can mostly be discriminated.

3.6.5 Light Noise Background

In addition to the particle physics backgrounds, an electronic background is present in the detectors. This background is caused by spontaneous light emissions due to discharges in gas bubbles trapped in the epoxy of the PMT bases [70]. As the bases of the PMTs are transparent for the emitted light, this light can be recorded by the PMTs themselves. The light emission can be relatively bright such that it can trigger the data acquisition of the detector. This background can be rejected by evaluating the isotropy of the detector illumination for each event. Most light noise events are likely to deposit a significant fraction of their light in only a few neighbouring PMTs. The light noise background is strongly suppressed in the near detector, because light noise reducing black caps were installed around the PMT bases during the installation of the near detector after the discovery of this background in the far detector [70].

Chapter 4

The Data Handling System

As for all experiments, the handling of data is one of the crucial elements towards a successful measurement. In this context, the term "data" does not only include the "physics data" taken to measure the targeted observable, i.e. in case of the Double Chooz experiment the observable $\sin^2(2\theta_{13})$. It also includes such things as detector monitoring data, data about the processing of the physics data, data of external parameters, like weather data, and even organisational data like data taking shift schedules. This data has to be collected, distributed and provided in a simple, but still reliable and robust way.

As an example, we can look at the processing of the physics data. A normal physics run consists of two types of files. One file type is produced by the inner veto and inner detector, a second file type is produced by the outer veto. Each type of file is present multiple times depending on the run length. These files contain raw data and have to be processed into a user friendly format in order to be suitable for analysis. This processing is not done in Chooz, but at the central computing facility of the in2p3 institute, which is mainly located in Lyon, France. The raw data files are guided through several servers before they can be converted into the required file format. The existence of new data files, their tracking as well as their processing status and storage location has to be monitored during the entire time and at any time.

As a further example, we can look at the monitoring of the detector systems. To guarantee a high duty cycle of the detector as well as a high quality of the physics data, it is essential to operate the entire detector well within stable conditions. An unstable voltage of the HV supply would directly influence the gain of the PMTs and bias the energy calibration. Overheating of hardware can damage it severely and can require a significant downtime of the detector for repairs. To prevent such scenarios, the voltages, temperatures, ventilation fan speeds, electrical currents, pressures and many other parameters of various systems are monitored in real time. By this, it is possible to detect failures even before they influence the physics data or the hardware itself. For example one can detect the failure of a ventilation fan well before the increase in temperature causes damage to the hardware. To enable the data taking shift crew to do this, several graphical user interfaces have been implemented like Java based interfaces or websites.

The Double Chooz collaboration relies on the database software MySQL [71] for the collection, handling and distribution of the afore-mentioned data in real time. Several instances of MySQL servers have been implemented in different locations to provide a fast and fail-safe system. In the following sections, the databases setup used in the single detector phase

(section 4.1) will be reviewed, the implementation of the current setup for the two detector phase will be described (section 4.2) and its performance since the start of nominal detector operations in February 2015 will be analysed (section 4.6). In addition, the monitoring system (section 4.3) and the commissioning (section 4.5) of the current setup will be reviewed as well as the graphical user interfaces (section 4.4).

4.1 The Previous Database System in the Single Detector Phase

In the single detector phase (far detector only), four servers were used to provide the databases system [72; 73; 74]. Two servers located inside the far detector laboratory built the primary databases instance, called the master instance. A third server located at the central computing facility in Lyon (centre de calcul) built the secondary databases instance, called the slave instance. It also accommodated some stand-alone databases which were not copied from the far detector laboratory. The fourth server was also located at the centre de calcul and hosted additional stand-alone databases.

4.1.1 Implementation of the System

The master instance consisted of the server dcfovmon.in2p3.fr and dcfovserv.in2p3.fr which were used in a high availability setup. A high availability setup is a compound of two or more separate servers that share their resources to provide high availability and also high scalability. The idea is that one of the servers (also called nodes in this context) is taking the active role while the other node(s) are having a passive role. Data is always written to all nodes simultaneously with the active node handling the communication with the users (also called clients in this context). In case of problems on the active note such as connectivity, CPU load, hardware failure &c, a passive node takes over the active role while the active node becomes a passive node. This is done automatically and thus a high availability of the system is guaranteed. If the issue on the former active node can be handled automatically, e.g. if it was a temporarily high CPU load due to other processes on the node, the former active node continues running unharmed. If the issue cannot be solved automatically, e.g. in case of hardware failure, the former active node is detached from the high availability setup and human intervention is required.

The high availability setup appeared to the outside as a separate server instance called dcfmysql.in2p3.fr which was a virtual IP (cf. figure 4.1). The slave instance at centre de calcul was a separate server known as ccdchoozdb.in2p3.fr and was open for connections from the entire world. The master instance in Chooz was only reachable from inside Chooz, i.e. only systems in Chooz could connect to it. The slave server was used for two purposes. It was connected to the master server in Chooz and received all data written, updated or deleted on the master server. This happened in real time making it an exact copy of the master server. This connection was realised by the MySQL-internal replication resource. Its configuration allowed a maximal delay between master and slave of 10 days before the delay could not be recovered by the system automatically. Moreover, the slave would tolerate the absence of commands by the master for 30 minutes before it requests a confirmation of the connection from the master and consequently before it would attempt to reconnect to the master or consider the connection between master and slave as broken. In addition

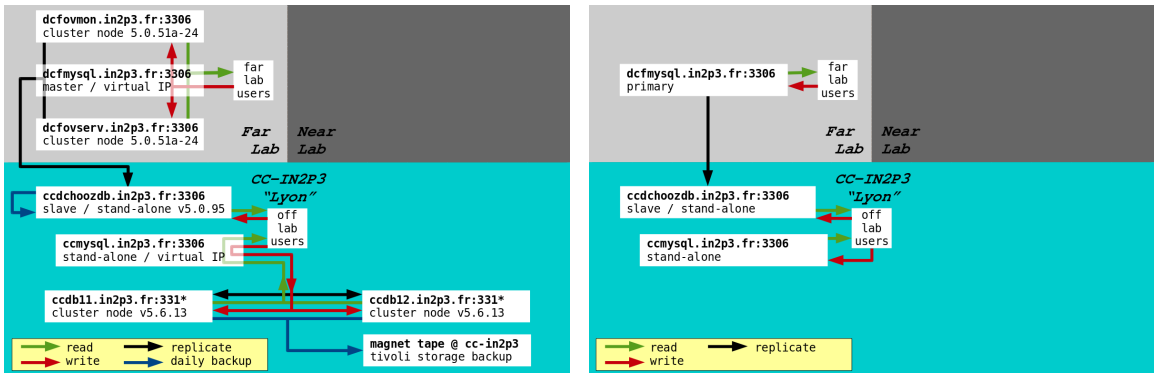

(a) (b)

Figure 4.1: Sketch of the databases servers infrastructure in the single detector phase. (a) Sketch of the full system. (b) A simplified version of the system as it appears to users.

to the data replicated from the master server, the slave server accommodated stand-alone databases. These databases were written at centre de calcul directly and contained data generated outside of Chooz. Such data is for example the location of physics data files on the mass storage device at centre de calcul. Additional stand-alone databases were located on the server ccmysql.in2p3.fr. This server was in fact another virtual IP giving access to a second high availability and scalability setup located at centre de calcul. The nodes in this setup were the servers ccdb11.in2p3.fr and ccdb12.in2p3.fr (cf. figure 4.1).

A daily backup was run on ccdchoozdb.in2p3.fr to recover the system in case of data loss or corruption due to hardware failure, human error or other incidents. The daily backup files were kept for one week. Additionally, weekly backup files were kept for four weeks and monthly backup files were kept for six months. The same backup strategy was performed on ccmysql.in2p3.fr. However, the backup files for this server were stored on magnet tapes (cf. figure 4.1).

4.1.2 Identification of Design Flaws and Improvements

Although the databases setup described in subsection 4.1.1 offers a particularly high duty cycle, it shows some flaws in terms of failure safety. Furthermore, its structure is not easily expendable to the two detector phase.

One possible point of failure is the write configuration of the slave ccdchoozdb.in2p3.fr at centre de calcul. It is possible to write, i.e. insert, update or delete, any data on the slave server. Although this is necessary for the stand-alone databases that are unique on this server, it is a possible cause of inconsistency in the databases replicated between the master and the slave server. A change on the slave server is not transferred to the master server as the replication is one-way only. By this, it is possible that different versions of the same tables and databases exist on the two server instances. In fact, it was the case that the environment database contained some tables on the slave server that the original version of the database on the master server did not contain.

Moreover, the stand-alone databases were split across two different servers. This was mainly owed to the historical growth of the databases. While the early databases were located on ccmysql.in2p3.fr, databases created after the commissioning of ccdchoozdb.in2p3.fr

were located on the ccdchoozdb.in2p3.fr server. A migration of the earlier databases to the ccdchoozdb.in2p3.fr was never performed. This makes it a priori difficult to browse for data and complicates the database structure unnecessarily.

Another point of failure is given by the backup strategy of ccdchoozdb.in2p3.fr. The only backup of laboratory data was performed on the slave server. On the one hand, all databases were backed, but on the other hand, only data transferred to the slave server was backed. The internet connection between Chooz and centre de calcul however, appeared to be broken on multiple occasions, e.g. by rat browsing damages. In these cases, the data collected in Chooz by the automated systems was without proper backup. The high availability setup consisting of two nodes is able to prevent data loss due to hardware failure on its own system, but is unable to do so in case of human error or failures on the user systems. In this case, a daily backup would be the only way to recover data. As no daily backups were performed on the master servers, the collected data of several days in case of a network outage between Chooz and centre de calcul remains unsecured.

Furthermore, considering the amount and rate of data written to the databases at the far detector laboratory and considering the location were data is read, the high availability setup appears to be oversized. Data is written to the master server only by the minute and the amount of data is in the order of 100 kB/h. Moreover, the data is read in Chooz only by a few systems, like the physics data migration system and the graphical user interface used by the data taking shift crew, while the majority of systems uses the slave server at centre de calcul for reading. Thus, a high availability and scalability setup, if any, would be required rather at centre de calcul than in Chooz.

Another design flaw that became an issue in early 2014 is the data replication configuration and monitoring. The maximum number of days that the system can cope with a stopped data replication before the connection is eventually disrupted is 10 days. Such a stopped data replication can be caused by a broken network or, as in early 2014, by an invalid master server statement that caused an error on the slave server. The data of the slave server was incoherent with the master server data due to the write permissions on the slave server. As there was no monitoring system for the databases, such stopped data replications could only be detected by human investigation. This can take more than 10 days as many systems at centre de calcul stop gracefully without an error when the transfer of recent data to centre de calcul stops assuming that there is in fact no recent data.

4.2 The Database System in the Two Detector Phase

For the two detector phase, a system built from seven servers is used to provide the databases infrastructure. In each laboratory, two servers are installed. These are the master servers of the laboratories and their first backup servers. The remaining three servers are located at the centre de calcul in Lyon. Two servers are used as second backup servers for the laboratories while the third one is used as a stand-alone server for data produced at the centre de calcul.

The following subsections explain the fundamental idea of the servers layout as well as its advantages. For a full and detailed discussion of the technical implementation of the servers the reader may refer to the databases manual [75].

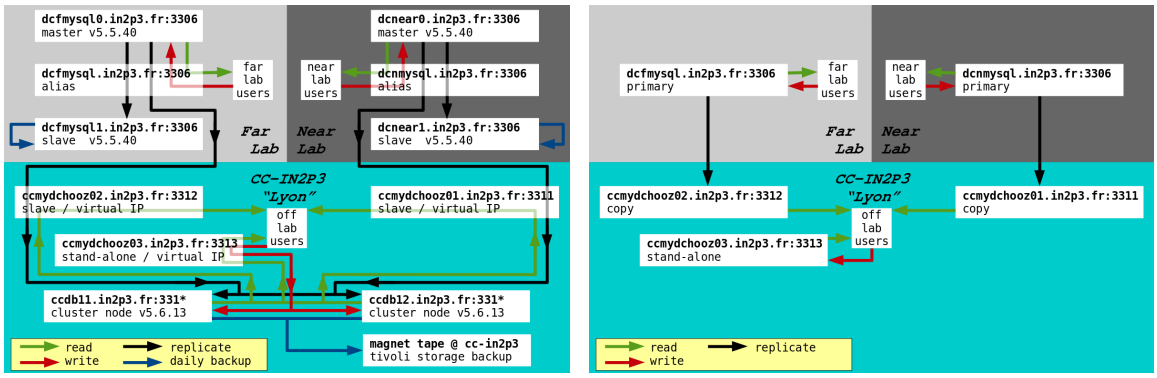

(a) (b)

Figure 4.2: Sketch of the databases servers infrastructure in the two detector phase. (a) Sketch of the full system. (b) A simplified version of the system as it appears to users.

4.2.1 Implementation of the System

The seven servers of the databases system can be grouped into three so called "server chains". Each of the two laboratories possesses its own separate server chain consisting of three servers while the third server chain is not connected to a laboratory and consists of only one single server. Please refer to figure 4.2 for a sketch of the server layout. The server chains of the far and the near laboratory are designed almost identically such that only the near laboratory server chain will be described in the following. Differences to the far laboratory server chain will be discussed separately.

The laboratory server chain consists of three servers. The primary master server dcnear0.in2p3.fr is located inside the laboratory. Additionally, a slave server dcnear1.in2p3.fr is located inside the laboratory. The third server in the chain is called ccmydchooz01.in2p3.fr and is located at the centre de calcul in Lyon. This server is also a slave server. The master server appears to the user not by its proper hostname, but by the alias dcnmysql.in2p3.fr. The slave server at centre de calcul is only one instance of several database server instances on the high availability and scalability database framework installed at the centre de calcul and built from the two servers ccdb11.in2p3.fr and ccdb12.in2p3.fr. Both slave servers are configured read-only while the master server is configured read+write. The two slave servers are connected directly to the master server, i.e. they form rather two parallel short chains than a single long chain. The servers inside the laboratory can only be accessed by servers inside of Chooz as they are located behind the firewall in Chooz. The server at the centre de calcul can be accessed from any location.

All data written, updated or deleted on the master server is transferred in real time from the master server to the two slave servers. Thus, each server contains the exact same data. The data is organised in several databases as detailed in table 4.2. All data can be read by a read-only account. Writing privileges are granted in two levels and only database-wise to dedicated user and administrator accounts, respectively. Furthermore, global administrator accounts are available for top level administration. An overview of the user accounts is given in tables 4.3 and 4.4.

The two connections between the master and the two slave servers are configured such that the slave servers will only allow a maximum time of 10 minutes without data transfer

hostname	port	MySQL ID	purpose
alias	IP	MySQL version	location
dcfmysql0.in2p3.fr	3306	8	far master
dcfmysql.in2p3.fr	134.158.249.74	5.5.40-0+wheezy1-log	far lab
dcfmysql1.in2p3.fr	3306	7	far slave
–	134.158.249.75	5.5.40-0+wheezy1-log	far lab
ccmydchooz02.in2p3.fr	3312	3	far slave
ccdb11.in2p3.fr/ccdb12.in2p3.fr	134.158.107.192	5.6.13-log	CC-IN2P3
dcnear0.in2p3.fr	3306	5	near master
dcnmysql.in2p3.fr	134.158.249.248	5.5.40-0+wheezy1-log	near lab
dcnear1.in2p3.fr	3306	4	near slave
–	134.158.249.235	5.5.40-0+wheezy1-log	near lab
ccmydchooz01.in2p3.fr	3311	3	near slave
ccdb11.in2p3.fr/ccdb12.in2p3.fr	134.158.107.191	5.6.13-log	CC-IN2P3
ccmydchooz03.in2p3.fr	3313	3	stand-alone
ccdb11.in2p3.fr/ccdb12.in2p3.fr	134.158.107.195	5.6.13-log	CC-IN2P3

Table 4.1: Overview of all database servers.

Database	Purpose
dc_env_nd	environmental and monitoring data, respectively
dc_hv_idiv_nd	HV related and monitoring data of the ID and IV PMTs
dc_hv_ov_nd	HV related and monitoring data of the OV
dc_lmpc_nd	liquids monitoring data (ND only/different system used in FD)
dc_mapping_nd	mapping of the entire electronics
dc_ov_nd	OV physics data related data
dc_runinfo_nd	physics/calibration/test run processing related data
dc_shiftstats_nd	data connected to the DTS website
doublechooz_ov_nd	OV physics data related data (FD suffix “far” instead of “fd”)

Table 4.2: The near laboratory server chain databases. Far laboratory tables have the suffix “fd” instead of “nd”, if not noted otherwise.

from the master before they check the connection for failure and attempt a reconnect. An interrupted connection between a slave server and its master server can be recovered automatically upon reconnect if the connection was not interrupted for more than 30 days. Backups of all databases are performed daily on each slave server. Daily backups are stored for seven days. Moreover, weekly backups are stored for four weeks and monthly backups are stored for six months.

The near laboratory server chain differs from the far laboratory server chain by the

Username	Hostname	Near lab chain	Far lab chain	Stand-alone server
ENVadmin	%.in2p3.fr	✓	✓	
ENVuser	%.in2p3.fr	✓	✓	
SSadmin	%.in2p3.fr	✓	✓	
SSuser	%.in2p3.fr	✓	✓	
SMadmin	%.in2p3.fr			✓
SMuser	%.in2p3.fr			✓
DMadmin	%.in2p3.fr	✓	✓	
DMuser	%.in2p3.fr	✓	✓	
HVadmin	%.in2p3.fr	✓	✓	
HVuser	%.in2p3.fr	✓	✓	
OVadmin	%.in2p3.fr	✓	✓	
OVuser	%.in2p3.fr	✓	✓	
OVRCuser	%.in2p3.fr	✓	✓	
MAPadmin	%.in2p3.fr	✓	✓	
MAPuser	%.in2p3.fr	✓	✓	
HVOVadmin	%.in2p3.fr	✓	✓	
HVOVuser	%.in2p3.fr	✓	✓	
RCadmin	%.in2p3.fr	✓	✓	
RCuser	%.in2p3.fr	✓	✓	
LIadmin	%.in2p3.fr	✓	✓	
LIuser	%.in2p3.fr	✓	✓	
LMadmin	%.in2p3.fr	✓		
LMuser	%.in2p3.fr	✓		
ValidityAdmin	%.in2p3.fr			✓
ValidityUser	%.in2p3.fr			✓
dcMunich	%.natpool.mwn.de			✓
dccalib	%.in2p3.fr			✓
dcprod	%.in2p3.fr	✓	✓	✓
dcquality	%.in2p3.fr			✓
dcreactor_adm	%			✓
RGmember	%			✓
DCmember	%			✓
dc_dev	%			✓
dc_radiopurity	%			✓
dc_reader	%			✓
dc_writer	%			✓
dchooz_mat_admin	%			✓
dcweb_admin	%			✓
doublechooz_wp	%			✓
dcreader	%	✓	✓	✓
OnlineReader	%	✓	✓	

Table 4.3: User accounts. See table 4.4 for explanation.

Username	Hostname	Near lab chain	Far lab chain	Stand-alone server
root	%.in2p3.fr	(✓)	(✓)	
dcadmin	%.in2p3.fr	✓	✓	✓
sentinel	%.in2p3.fr	✓	✓	
replicant-near	dcnear1.in2p3.fr	✓		
replicant-nearCC	ccdb___.in2p3.fr	✓		
backupmaker-near	localhost	✓		
replicant-far	dcfmysql1.in2p3.fr		✓	
replicant-farCC	ccdb___.in2p3.fr		✓	
backupmaker-far	localhost		✓	
debian-sys-maint	localhost	(✓)	(✓)	
ccdba	%.in2p3.fr	[✓]	[✓]	✓

Table 4.4: Administrative accounts. The column hostname specifies the hostnames from which connections by the respective user account are accepted. In this column, a "_" indicates a one-character wildcard and a "%" indicates a wildcard of arbitrary length. A checkmark indicates the presence of an account on the corresponding server. If the checkmark is enclosed in round brackets, the account is present only on the servers located in Chooz. If it is enclosed in square brackets, the account is present only on the server at centre de calcul. In table 4.3, the first section contains accounts having extended privileges. These accounts are restricted to different databases. The second section contains accounts with global access. However, these accounts have read-only privileges. In table 4.4, the first section contains administrative accounts with maximal or highly specialised privileges. The second and third sections contain accounts used for automated subsystems of the databases system. The fourth section contains system accounts used by the servers itself.

names of the servers, by the user accounts and by the databases. The server names are dcfmysql0.in2p3.fr for the master and dcfmysql1.in2p3.fr and ccmydchooz01.in2p3.fr for the slaves, respectively. The master server is aliased by dcfmysql.in2p3.fr. The names of the databases in the near laboratory server chain arise from the far laboratory server chains by interchanging the suffix "fd" by "nd". Moreover, the naming pattern for the database of the outer veto system was changed (cf. table 4.2). Furthermore, an additional database for the new version of the liquids monitoring system in the near laboratory and additional user accounts for this database are present only in the near laboratory server chain (cf. tables 4.2 and 4.3).

The third server chain is built from the single server ccmydchooz03.in2p3.fr and hosted by the same high availability and scalability framework at the centre de calcul as the laboratory server chain slave servers at centre de calcul. This server and its chain, respectively, is also known as stand-alone server. The server is configured read+write and can be accessed from every location in the world. The data on this server is organised in several databases as detailed in table 4.5. Like in the laboratory chains, data can be written database-wise by two different accounts having two different levels of writing privileges. In contrast to the

Database	Purpose
dcreactordb	reactor related user friendly data
dcreactor_adm	reactor related expert data
dcweb_db	deprecated/empty
dc_channel	electronic channel quality related data
dc_constants	calibration constants
dc_radiopurity	material data
dc_file	Monte Carlo data and Common Trunk related data
dc_runinfo_munich	data for the physics/calibration/test run backup in Munich
dc_runinfo_fd	aperiodically rendered copy of laboratory database
dc_runinfo_nd	aperiodically rendered copy of laboratory database
dc_shift_management	data connected to the shift management website
dc_validity_fd	data mainly connected to run validation of the far detector
dc_validity_nd	data mainly connected to run validation of the near detector
dc_ov_fd	aperiodically rendered copy of laboratory database
doublechooz_ov_nd	aperiodically rendered copy of laboratory database
doublechooz	oscillation analysis as detailed in chapter 6
doublechooz_temp	empty/temporary data
doublechooz_wp	collaboration website data
doublechooz_material_db	older version of dc_radiopurity
FinalFitH	additional oscillation analysis
FinalFitSterile	additional oscillation analysis
phpbb_phpBB3	DOGS forum data

Table 4.5: The stand-alone server databases.

laboratory server chains, reading is possible by two separate read-only accounts where one account can read all databases with exception of the databases of the reactor working group and the other account can read the reactor databases only. The backup strategy is the same as for the laboratory chains: backups of all databases are performed daily, daily backups are stored for 7 days, weekly backups are stored for 4 weeks and monthly backups are stored for 6 months.

4.2.2 Advantages of the System

The new setup shows various advantages over the previous setup. Firstly, in Chooz, the installation of two separated systems inside each laboratory provides certain fail-safe mechanisms. If only one shared system located outside the laboratories would be present in Chooz, network interruptions between a laboratory and the outside server room would immediately interrupt the writing of any data from the laboratories. With the current setup and in the case of a network interruption between a laboratory and the outside server room, data from the laboratory can still be written to the databases servers inside the laboratory. Moreover,

with the backup performed not only on the server at centre de calcul, but also on the servers inside the laboratory, the written data is also properly secured during network interruptions.

The use of two separate systems inside each laboratory is also preferable as a hardware failure would only affect one laboratory, while the second detector is unaffected in its duty cycle. Moreover, in the case of hardware failure on a server inside the laboratory, the presence of two servers inside each laboratory provides a fast way to reestablish a working system: In case of a hardware failure on the slave server, the daily backup can be enabled on the master server by a simple software switch. This action does not cause any loss in duty cycle. In this case, the already rendered daily backups are not lost, as they have been rendered a second time on the second slave server at centre de calcul. In the case of a hardware failure on the master server, the slave server can be promoted to master server. For this, the slave server has to be rendered read+write and the hostname alias (dcfmysql.in2p3.fr or dcnmysql.in2p3.fr) has to be modified to point to the new master server. This can also be done via software. In any case, no action inside the laboratory is required as all software changes can be used via remote control.

Secondly, at centre de calcul, the use of a high availability and scalability framework is advantageous compared to the former single server setup. As especially in times of data (re)processing campaigns the load on the servers at centre de calcul is high, the presence of this framework ensures a high performance of the databases. Moreover, the use of slave servers locally at centre de calcul rather than accessing the servers in Chooz accelerates the processing of queries issued at centre de calcul. Furthermore, the presence of a slave server per laboratory at centre de calcul ensures the continuation of computing jobs during a network interruption between Chooz and the centre de calcul. In this scenario, only new data is not present at centre de calcul, while all data up to the moment of network interruption is still available. The use of two read-only slave servers and a separate read+write server at centre de calcul ensures that no inconsistency between the servers in Chooz and their copies at centre de calcul can happen.

4.3 Monitoring of the System

In order to monitor all databases servers and their replications, a custom monitoring programme was implemented on a separate server in Chooz. This programme connects to each databases server and collects status information of each system which are then processed to an overall system status. The status is then displayed on a website functioning as human interface device and hosted on `http://dcmonitor.in2p3.fr/DatabaseMonitor/`. An example view of the interface can be found in figure 4.3.

The status of each system component is diagnosed every minute. Possible states are “FINE”, “WARNING”, “CRITICAL”, “UNKNOWN” or “ERROR”. A server is considered as “FINE”, if it is running stably for a long time, has no server errors, processes queries fast and if it is not fully occupied. A replication is considered as “FINE”, if the connection between master and slave server is established, the reading and writing processes on the slave are running and the slave does not lag behind the master. If a server or replication deviates from the set margins, it is depending on the magnitude of deviation considered as “WARNING” or “CRITICAL”. Moreover, a system has the status “UNKNOWN”, if the monitor was not able to determine its proper state due to an error on server side or a connection timeout. Finally, a system has an “ERROR” status, if the monitor was not able to determine its proper state

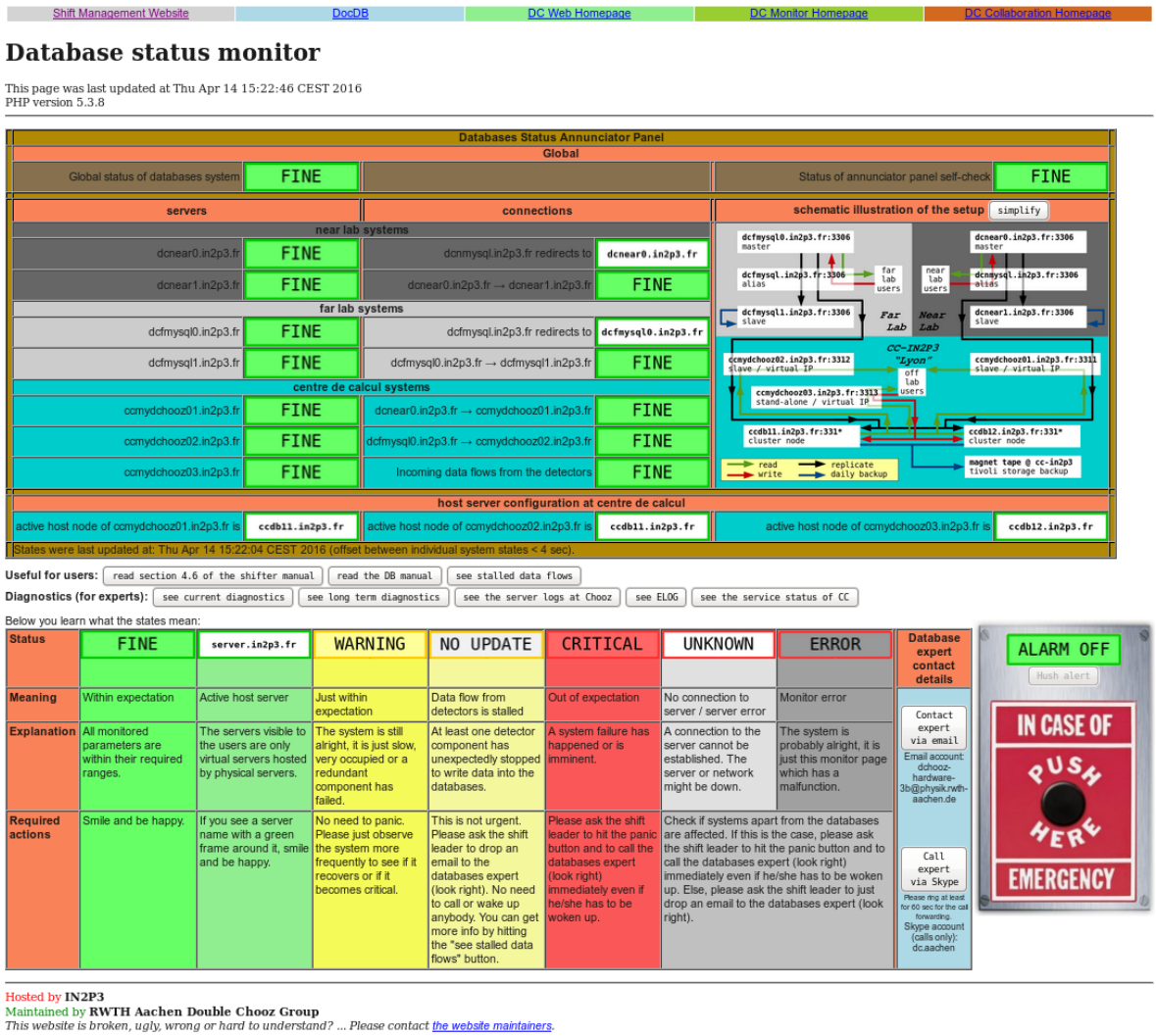

Figure 4.3: `http://dcmonitor.in2p3.fr/DatabaseMonitor/` – The status monitor of the databases system

due to an internal error.

If a system component is in a state other than “FINE” or “WARNING” for more than 10 minutes, the system is considered as exceptional. In this case, an error message is dispatched to the data taking shift crew via their graphical user interface (cf. figure 4.4). The shift crew can then investigate if the current situation needs expert intervention or not. If all databases systems recover to a “FINE” state, an all-clear message is sent to the data taking shift crew. Additionally, messages are sent to the system experts via email and text message. Moreover, the monitoring website also enables the data taking shift crew or any other person to issue a separate alert propagated to all system experts using a panic button at any time (cf. figure 4.3 lower right).

An overview of the monitored system variables and the definition of the system states can be seen in tables 4.6 and 4.7 for the server and replication systems, respectively. The mapping between states and values in those tables will be discussed in the following.

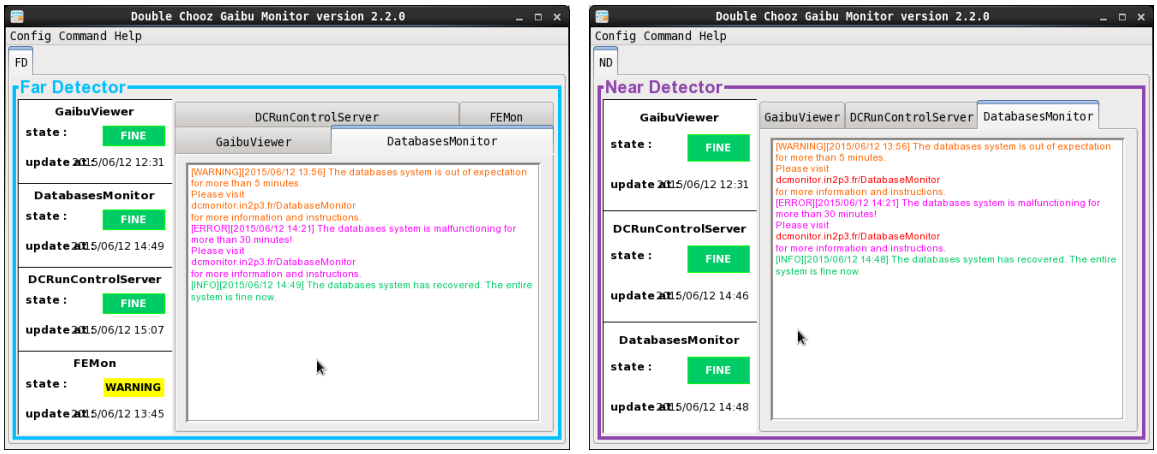

(a) (b)

Figure 4.4: Databases part of the data taking crew notification system for (a) the far detector and (b) the near detector. A warning, an error and an all-clear message is exemplary shown for both detectors.

For the servers, the uptime was chosen as one of the monitored variables because a frequent restart of the servers due to malfunctioning hardware or due to a change in the physical host server at centre de calcul will break active connections of that server. This will lead most probably to failures in dependent systems and has thus to be detected. This is especially important when considering data loss in the laboratories due to loss of meta data. Since a server restart should never happen during normal operation, the warning threshold was set to 3600 seconds in order to trigger at least one automated alert. The connected system state was chosen as only “WARNING”, since only the restart of the server is considered harmful, but not the time after the restart. The number of slow queries was chosen as monitored variable in order to detect performance loss. However, a small number of slow queries is tolerated on the servers as users may seldom send very extensive queries to the servers. The number of connected threads and the number of connections were chosen as monitored variables to recognise if a user swamps the database server with requests. If the capacity of connections or threads of a server is fully reached, other users will be blocked when connecting to the database and this will effectively stall data taking or data processing. Finally, the response time of each server to the query of the monitor is recorded. The response time is considered as fine if it is faster than twice the average time for a cross-network query. If the response time for queries becomes to large, many websites and other systems, especially when issuing a series of queries, will take too much time to function properly. When all monitored system variables are within their required margins, the state of the system is recognised as “FINE”. If at least one of the monitored system variables is in the warning region, the system is recognised as “WARNING”. However, if at least one of the monitored system variables is in the critical region, the system is recognised as “CRITICAL” instead. Likewise, all states can be superseded by the “UNKNOWN” state in case of an arbitrary server error. This includes also network connection errors or timeouts. Finally, in case the monitor system was unable to determine the system state due to an internal error, the system state is recognised as “ERROR”.

Status	FINE	WARNING	CRITICAL	UNKNOWN	ERROR
Uptime in sec (since last flush status)	$a > 3600$	$0 < a \leq 3600$	$a = 0$	n.c.	unknown
Number of slow queries since start of server	$b < 2$	$2 \leq b \leq 5$	$b > 5$	n.c.	unknown
Fraction of open connections	$c < 80\%$	$80\% \leq c < 95\%$	$c \geq 95\%$	n.c.	unknown
Number of connected threads	$d < 500$	$500 \leq d < 600$	$d \geq 600$	n.c.	unknown
Response time of monitor query in msec	$r < 500$	$500 \leq r \leq 4000$	$r > 4000$	n.c.	unknown
Number of server errors	n.c.	n.c.	n.c.	$e > 0$	n.c.
Multiplicity condition	all of above fulfilled	one of above fulfilled	one of above fulfilled	n.c.	one of above fulfilled
Gets superseded by	UNKNOWN ERROR	CRITICAL UNKNOWN ERROR	UNKNOWN ERROR	–	UNKNOWN

Table 4.6: Definitions of the states of the servers in the monitoring system. If a variable is **n**ot **c**onsidered for a status, it is marked as "n.c.".

For each replication connection (cf. table 4.7), the input-output thread and the writing thread as well as the overall replication state is monitored. If one of the items appears to be not running, the replication is directly considered to be in a critical state. The "WARNING" state is not used in this context as the fact that a replication thread is not running automatically implies an error. Additionally to the threads themselves, the delay between the input-output thread and the writing thread is monitored to detect loss of performance on the slave servers. Since it is also possible that the input-output thread of the slave server lacks behind the master server, the positions of the logbooks of master and slave are compared against each other. Since the average overall writing velocity of the Double Chooz master servers is approximately 110000 logbook entries per minute, the thresholds of 900 seconds and $1.7 \cdot 10^6$ logbook entries are chosen to roughly match. For the replication connections, the same pattern with respect to superseding of states is applied as described above for the servers.

Additionally to the system variables, the monitor keeps also track of the host servers used at centre de calcul and in Chooz. By this, problems that arise from a malfunctioning physical host server at centre de calcul can easily be detected if all virtual servers hosted by this single physical host server show the same exceptions.

Status	FINE	WARNING	CRITICAL	UNKNOWN	ERROR
Slave running enabled	ON	n.c.	OFF	n.c.	unknown
Slave I/O thread running	Yes	n.c.	No	n.c.	unknown
Slave SQL thread running	Yes	n.c.	No	n.c.	unknown
Seconds the SQL thread is behind the I/O thread	$i < 60$	$60 < i \leq 900$	$i > 900$	n.c.	unknown
The master's and slave's bin log file and position mismatch	file and position match	file mismatch of ≤ 1 and position mismatch of $< 1.7 \cdot 10^6$	file mismatch of > 1 or position mismatch of $\geq 1.7 \cdot 10^6$	n.c.	unknown
Number of server errors	n.c.	n.c.	n.c.	$e > 0$	n.c.
Multiplicity condition	all of above fulfilled	one of above fulfilled	one of above fulfilled	n.c.	one of above fulfilled
Gets superseded by	UNKNOWN ERROR	CRITICAL UNKNOWN ERROR	UNKNOWN ERROR	–	UNKNOWN

Table 4.7: Definitions of the states of the replications in the monitoring system. If a variable is **n**ot **c**onsidered for a status, it is marked as "n.c.".

In addition to the server surveillance, the rendering of the daily backups on the servers inside the laboratories are monitored. Messages are sent either if the backup process failed completely or if it had any type of problem regardless if it was solved automatically or not. The messages are dispatched via the graphical user interface of the data taking shift crew similar to the messages shown in figure 4.4.

Apart from the databases itself, the databases monitoring system is also capable of monitoring the input data flow of all connected user systems. For this purpose, the user systems are divided into regularly updating systems and sporadically updating systems. Regularly updating systems are all primary monitoring systems as well as data taking and data processing systems. Sporadically updating systems are logbooks and organisational webpages. The data flow of sporadically updating systems is not monitored. If a regularly updating system stopped data taking for more than 10 days, a warning message is dispatched to the data taking shift crew and the experts as described above. The delay time of 10 days is owed to the systems with the longest updating cycle. These are the weekly used calibration systems. Because the use of the calibration systems can vary by a few days due to special detector conditions, an extra buffer of 3 days was added to the weekly update cycle. Since all critical systems are monitored live by dedicated tools there is no need for a shorter delay time.

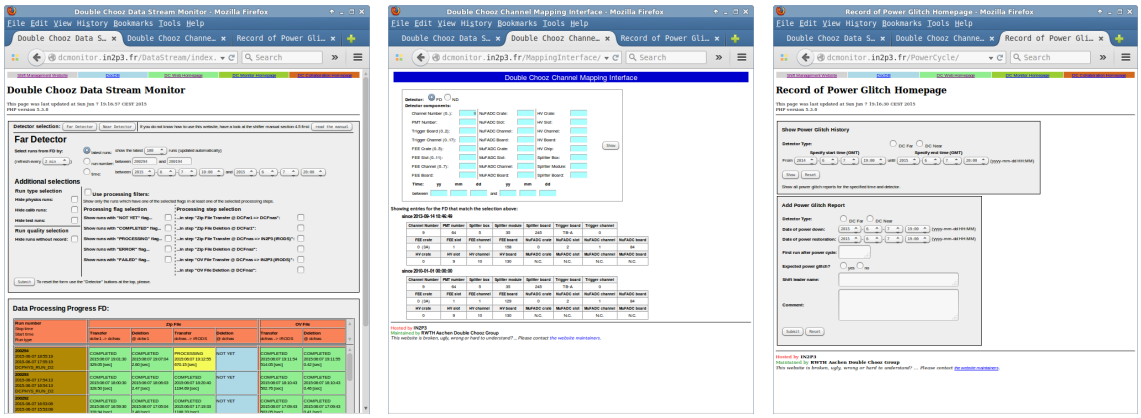

(a) (b) (c)

Figure 4.5: Example of GUIs: (a) Data migration monitor used to display and select meta data about the processing of recorded physics data. (b) Electronic channel mapping catalogue used to look up connections of electronic components and electronic signal routes. (c) Power glitch record system used to record and display power glitch events in the detectors.

4.4 Graphical User Interfaces to the Databases

The data stored in the databases system is of importance not only for automated systems, but also for human tasks like data taking or data analysis. Thus, data access must be provided in an intuitive and database language independent way. To meet this requirement, a variety of **g**raphical **u**ser **i**nterfaces (GUI) has been developed. Most of these GUIs were implemented as php-based websites and are hosted on password protected webservers `dcmonitor.in2p3.fr` or `dcweb.in2p3.fr`. For the majority of the GUIs, it was possible to extend their functionality from the single detector setup to the new two detector setup without large modifications. These GUIs were using the stand-alone part of the former server ccdchoozdb.in2p3.fr at centre de calcul. This data was migrated to the new stand-alone server ccmydchooz03.in2p3.fr. However, due to the new databases server structure at the centre de calcul, some GUIs had to be revised. These GUIs were using detector data previously stored in the slave part of the former ccdchoozdb.in2p3.fr server. With the commissioning of the near detector, this data was divided between the two slave servers ccmydchooz01.in2p3.fr and ccmydchooz02.in2p3.fr. Examples of such GUIs are the data migration monitor, the electronic channel mapping catalogue and the power glitch record system as pictured in figure 4.5. While preserving the optical appearance of the GUIs to a large extend, these GUIs were modified to read and write data from and to both new databases servers.

4.5 Commissioning of the System

For the commissioning of the new databases system, several aspects had to be considered. Since the old system was not simply extended but fully renewed, it was important to perform changes to the old system with a minimal downtime. This was necessary to maintain a high duty cycle of data taking. Furthermore, the software interfaces to the databases had to be adapted for each change. These interfaces are rather branched and were not designed for

the new databases system structure. Thus, too large modifications in the database structure would have complicated the adaptation process and would have caused too large downtimes. Moreover, the storage disk capacity in the laboratories had to be taken into account. Since the servers of the far detector laboratory were, due to their age, rather small sized, new dedicated servers had to be installed in the far detector laboratory. The near laboratory servers offered enough space such that no additional servers were installed.

In order to achieve a particularly small downtime of all systems, a gradual commissioning plan with six phases was realised. In the first phase transition (subsection 4.5.1), the stand-alone databases were merged and a consistent far detector database system was established. In the following phase transition (subsection 4.5.2), the new system of the near detector was commissioned. In the third phase transition (subsection 4.5.3), the old far detector laboratory system was replaced by the newly designed system. In the final phase transition (subsection 4.5.4), the stand-alone databases were migrated to the final servers. In the following, a detailed account is given of modifications made in each phase transition.

4.5.1 Commissioning Phase 1

In the first phase transition, all modifications to the present system not imposing a downtime on the data taking cycle, were performed. It is therefore a preparatory phase of commissioning phase 3. Furthermore, techniques to perform and verify uncorrupted data migration between servers were tested to ensure a quicker data migration in the time critical third phase.

Starting from the original setup in figure 4.6.0, the stand-alone databases located on ccdchoozdb.in2p3.fr were migrated to ccmysql.in2p3.fr. In the consequence, ccdchoozdb.in2p3.fr became a pure slave server of dcfmysql.in2p3.fr. It was then rendered read-only in order to prevent data inconsistencies between dcfmysql.in2p3.fr and ccdchoozdb.in2p3.fr (cf. figure 4.6.1). To ensure that data migrated from ccdchoozdb.in2p3.fr to ccmysql.in2p3.fr remained unaltered after the migration, data snapshots of ccdchoozdb.in2p3.fr and ccmysql.in2p3.fr were taken before and after the migration, respectively. The comparison showed no data corruption or modification. Additionally, data snapshots of dcfmysql.in2p3.fr and ccdchoozdb.in2p3.fr were taken after the modifications. Data inconsistency was found with respect to the environmental data. The inconsistency was owed to a table of weather data that was written to the slave server directly without involving the master server. The weather data was migrated to the master server and the recording system was adapted to write future weather data to the master server. No further inconsistencies were detected.

Finally, the software interfaces and automated systems running at centre de calcul were modified to the new setup. It was found that all systems, as expected, were flexible enough to be adapted to the new setup.

4.5.2 Commissioning Phase 2

After the installation of computers and network connections in the near detector laboratory, the new near detector databases system was implemented. The master server instance was implemented on dcnear0.in2p3.fr and the slave server instance was implemented on dcnear1.in2p3.fr. In order to provide a simple appearance to users, the alias dcnmysql.in2p3.fr was established for the dcnear0.in2p3.fr server (cf. figure 4.6.2). The virtual IP ccmydchooz01.in2p3.fr was established as a second slave server at the centre de calcul spread among the cluster nodes ccdb11.in2p3.fr and ccdb12.in2p3.fr. The connections between slaves and

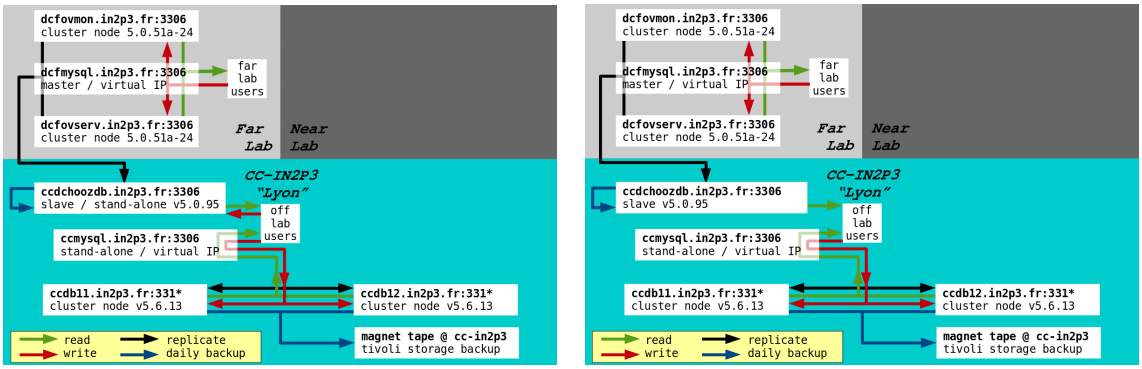

(0)

(1)

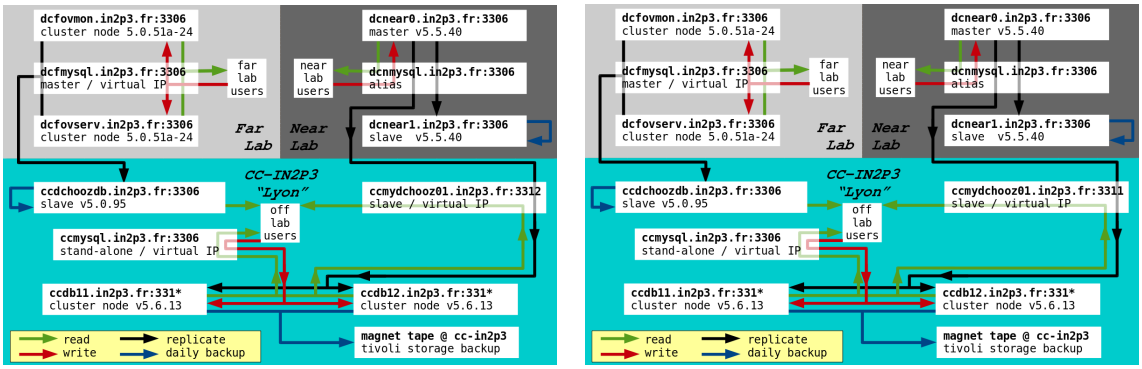

(2)

(2a)

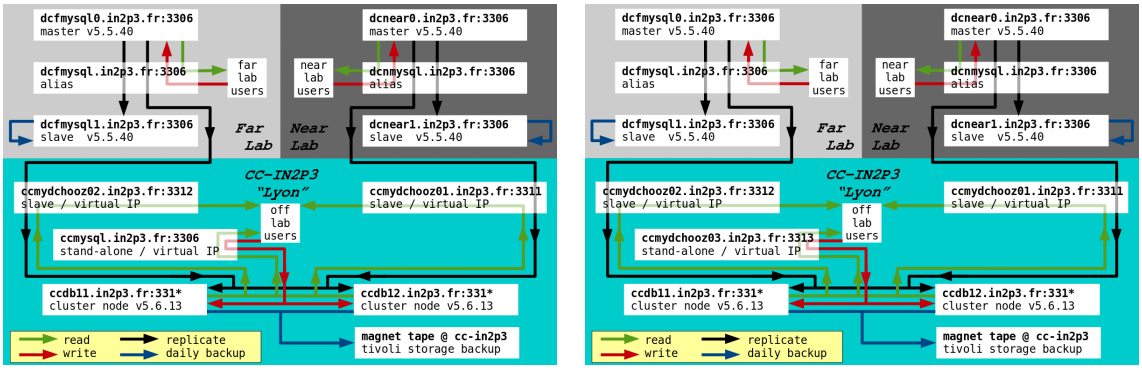

(3)

(4)

Figure 4.6: Commissioning phases of the database system: (0) Original single detector setup. (1) All stand-alone databases are migrated to ccmysql.in2p3.fr. (2) Installation of the near laboratory system. (2a) Correction of the port number of ccmydchooz01.in2p3.fr. (3) Installation of the new far laboratory system. (4) Migration of the Double Chooz databases from the mutualised stand-alone server ccmysql.in2p3.fr to a dedicated server ccmydchooz03.in2p3.fr.

master servers were established successfully and the backup process was initiated on both slave servers.

First test data was written to dcnmysql.in2p3.fr and its propagation to the slave servers as well as its propagation to their backups was verified. The failure of master or slave servers

and of network connections was simulated and the behaviour of the remaining servers was observed. In all scenarios, subsystems behaved within their expectations. However, it was found that the port number for the slave instance at centre de calcul was set to 3312 instead of 3311. The port number was changed in an intermediate phase (cf. figure 4.6.2a) to meet the more intuitive pattern of using port 331X on server ccmydchooz0X.in2p3.fr.

Finally, the database and user account structure of the far detector system was copied to the near detector system. Since some of the systems in the near detector laboratory differ from their counterparts in the far detector laboratory, slight changes were made to the structure of the near detector laboratory databases. These are summarised in table 4.2. Due to the user account policy of MySQL, user connections from foreign servers are handled differently than user connections from the local server. Since the MySQL master instance is running on the dcnear0.in2p3.fr server, dcnmysql.in2p3.fr and dcnear0.in2p3.fr are the same server. Thus, connections established to dcnmysql.in2p3.fr from users on dcnear0.in2p3.fr are local connections. This is different from the far detector laboratory system that is hosted on dedicated servers. As a result, for each user account in the near detector system, two sub-accounts exist. This effectively doubles the number of user accounts in the near detector system with respect to the far detector system.

4.5.3 Commissioning Phase 3

After the successful commissioning of the near detector databases system, an identical system was installed in the far detector laboratory. Since the new system in the far detector laboratory would be directly used as a full replacement of the running old system, the new near detector laboratory system was used as a test case for the new design. As the system in the near detector laboratory showed no design flaws, failures or performance losses during the gradual commissioning of the near detector, the new design was adapted unchanged for the far detector system.

In order to ensure a minimal downtime of the data taking cycle in the far detector, the full system was prepared and tested as described for the near detector system while the existing far detector system remained unchanged. The new system was implemented on the newly installed dedicated servers dcfmysql0.in2p3.fr (master) and dcfmysql1.in2p3.fr (slave) as well as ccmydchooz02.in2p3.fr (slave). Refer to figure 4.6.3 for a sketch. During this operation, the hostname dcfmysql.in2p3.fr was still pointing to the old system.

In order to commission the new system, a data snapshot of the running system had to be migrated from the running system to the new system. From this point on, newly recorded data of the far detector would have been lost since it would not be imported to the new system. Thus, the generation of the data snapshot started the data taking downtime.

A successful data migration was performed and verified by the method described in subsection 4.5.1. Finally, the IP address of the hostname dcfmysql.in2p3.fr was altered such that dcfmysql.in2p3.fr points towards dcfmysql0.in2p3.fr. This implies no changes in the configuration of the far detector systems that use the databases system. The old system remained in standby as fast switch-back option in case the new system would have experienced massive failures. It was renamed as dcfmysql2.in2p3.fr. However, the new system showed excellent performance and no switch-back was required.

It was possible to narrow the overall interruption in the data taking cycle to 9 hours. Approximately 5 h were required for the actual migration of the databases and the following verification of data consistency. The additional 4 h were owed to the reconfiguration

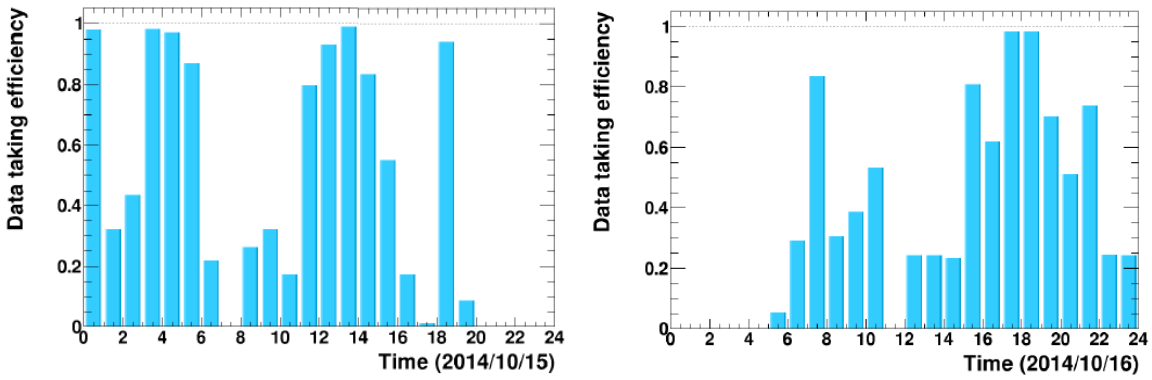

(a) (b)

Figure 4.7: Data taking duty cycle during the commissioning of the far detector databases system [76, p. 5]. Blue bars indicate test data while yellow bars (not present) would indicate physics data. The transition to the new databases system was performed between 20h00 CEST in figure (a) and 05h00 CEST in figure (b).

of the DNS server in Chooz that needed to accept and propagate the new IP address of dcfmysql.in2p3.fr. This was estimated to be performed earlier by the responsible automated system. However, in the week of the phase transition, the far detector was most of the time in a test data taking regime with low duty cycle (cf. figure 4.7) such that the duty cycle on physics data was not affected.

As for the phase 1 transition, software interfaces and automated systems running at centre de calcul were modified to the new setup. Some of the systems had to be rebuilt to incorporate the new two detector setup as detailed in section 4.4.

4.5.4 Commissioning Phase 4

The setup as described up to the current point and as depicted in figure 4.6.3 was originally foreseen as final configuration. Nevertheless, an additional fourth phase transition was required due to the extensive traffic the Double Chooz collaboration caused on the server ccmysql.in2p3.fr. This server is a mutualised server shared between several user parties of the centre de calcul. As this server is used extensively during data processing and reprocessing campaigns, the overall performance of the server became too poor. The Double Chooz data processing campaigns had negative effects for all user groups at centre de calcul. This effect was underestimated in the design phase of the system.

It was decided to implement a third dedicated server instance for the Double Chooz collaboration at centre de calcul. The server instance was called ccmydchooz03.in2p3.fr. All databases and user accounts on ccmysql.in2p3.fr belonging to the Double Chooz collaboration were migrated from the mutualised server to the new server (cf. figure 4.6.4). Data consistency was checked as explained before and no inconsistencies were found. As for the earlier transitions, software interfaces and automated systems running at centre de calcul were modified to the new setup. This was done without problems as the systems were already adapted to the new server structure and only the hostname and port number of one server had to be altered in the configuration of the systems.

State	dcfmysql0	dcfmysql1	ccmydchooz02	dcnear0	dcnear1	ccmydchooz01
FINE	98.9 %	97.8 %	98.4 %	99.0 %	98.3 %	98.4 %
WARNING	0.4 %	0.2 %	1.2 %	0.2 %	0.2 %	1.2 %
CRITICAL	0.1 %	0.5 %	<0.1 %	0.0 %	0.0 %	<0.1 %
UNKNOWN	0.6 %	1.4 %	0.3 %	0.8 %	1.4 %	0.3 %
ERROR	<0.1 %	<0.1 %	<0.1 %	<0.1 %	<0.1 %	<0.1 %

(a)

State	ccmydchooz03
FINE	96.5 %
WARNING	2.7 %
CRITICAL	0.3 %
UNKNOWN	0.5 %
ERROR	<0.1 %

(b)

State	far→far	far→cc	near→near	near→cc
FINE	96.3 %	98.7 %	98.1 %	98.5 %
WARNING	0.7 %	<0.1 %	<0.1 %	<0.1 %
CRITICAL	1.3 %	0.9 %	0.5 %	1.1 %
UNKNOWN	1.4 %	0.3 %	1.4 %	0.3 %
ERROR	0.3 %	<0.1 %	<0.1 %	<0.1 %

(c)

Table 4.8: Overview of the overall databases server and replication performance. Table (a) shows the three servers from the far and near laboratory chain and table (b) the stand-alone system. Table (c) shows the two replications per chain. See figure 4.2 for the full layout.

4.6 Analysis of the Long Term Performance

In order to evaluate and improve the current databases system, monitoring data of one year starting in February 2015 was analysed. The recorded data includes the states of each subsystem as diagnosed by the monitoring programme introduced in section 4.3 as well as its input variables from each detector subsystem.

The data shows an overall high duty cycle of all system components. Table 4.8 shows that each system was functioning without critical problems for at least 98.0 % of the time and each replication line for at least 97.0 %. The crucial primary systems in the laboratories reach even more than 99.2 %. This corresponds to an average downtime of the detector data acquisitions of 10.8 min per day. Most of this time is caused by laboratory-wide power cuts for maintenance works. Correcting for this, the detector data acquisition downtime that is caused only by the data handling system alone is negligible with 1.5 sec per day. In comparison with the total downtime caused primarily by any detector component, the data handling system contributes a fraction of <0.1 %. By this, the design goal of the system has been fully accomplished.

The dominant fraction of fatal performance problems is caused by scheduled maintenance operations. As visible in table 4.8, the stand-alone server shows a slightly worse performance with a higher fraction of "WARNING" states. This is caused by the high usage during data processing and MC file production. In peak times, the system shows a high load leading to a "WARNING" state. However, a critically high load with impact on the computing speed of the user processes is reached for only less than 5 min per day.

For each system, the amount of server-side errors or connection errors, both leading to an "UNKNOWN" state, is small with less than 1.4 %. They are mostly caused by scheduled power-cuts in the laboratories due to maintenance work. For the backup-servers in the laboratories, dcfmysql1 and dcnear1, and their replications, a high value of 1.4 % is reached.

System	Total number of incidents
electronics voltage monitor	2
electronics temperature sensors	5
humidity sensors	6
detector temperature sensors	3
data file migration system	5
front end electronics power supply	3
high voltage power supply	2
missed weekly calibration	3
OV data acquisition	2
primary detector monitoring	1
data file backup	1

Table 4.9: Detected system issues in 2015 grouped by subsystem.

This is connected to a period in December 2015 in which a general server upgrade on all computers of the laboratories was performed over a few days. This lead to an interruption between the databases primary servers and the backup servers and was resolved after the end of the general upgrade. The primary servers and the backup servers at centre de calcul were operational during the entire time.

The larger fraction of critical problems in the far laboratory replication can be tracked down to the daily backup-process. During this process, new data is buffered, but not written to disk causing a delay and subsequently a critical state. This delay is larger for the far laboratory system due to the larger amount of data (cf. figure 4.8). This special state is now detected and displayed as non-critical "BACKUP" state in the monitoring tool.

An additional modification made to all laboratory chain servers was the introduction of a maximal number of connections one user account can establish to a server. This was necessary after one user system was filling the entire list of allowed connections without using them. A restriction to maximal 100 connections is now in place for each user account. This is approximately 20-fold the average occupancy.

As shown in figure 4.8, the amount of recorded data has moderately increased over time in the detector related replication chains. The larger absolute value in the far detector system is caused by the five years (factor 3.5) longer operation time of the far detector. For the stand-alone system, an overall flat data size evolution can be observed for the first months. During the last months, a heavily varying data amount and two general increases of data storage can be observed. This is connected to the oscillation analysis presented in chapter 6 and to two additional oscillation analyses. All three analyses use the tool developed in this thesis. It buffers intermediate data on the stand-alone system in order to accelerate the computing process. The current data amount represents 6 % of the total capability in the far detector and 3 % of the total capability of the near detector system. The stand-alone system currently shows an occupancy of 10 % with an intermediate maximal occupancy of 45 %. Thus, the systems are in their current layout well suited for the full runtime of the Double Chooz experiment.

When looking at table 4.9 of detected subsystem failures, one can see that the databases-

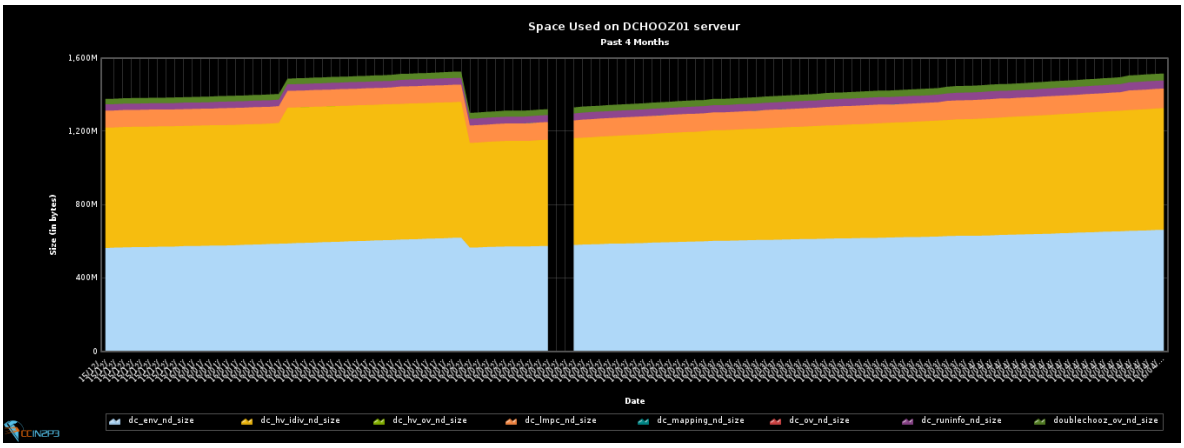

(a)

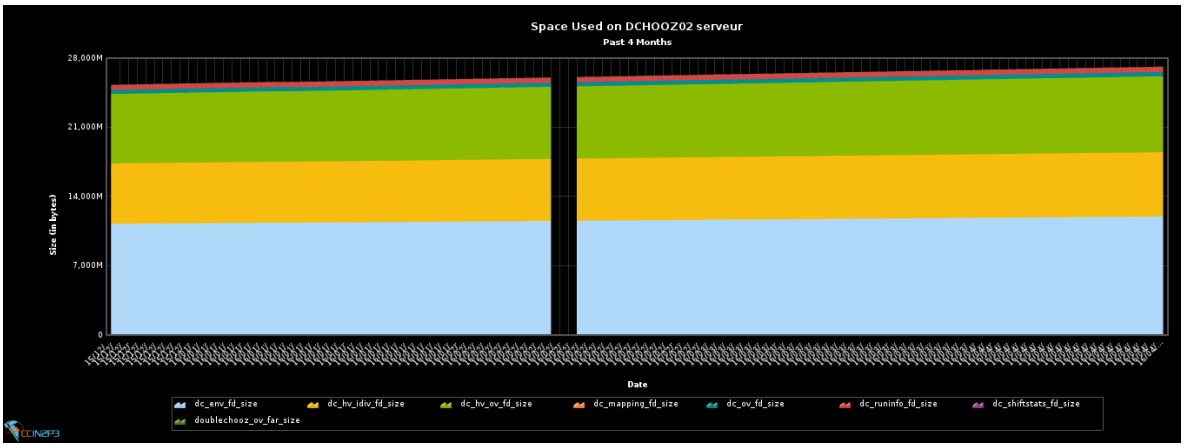

(b)

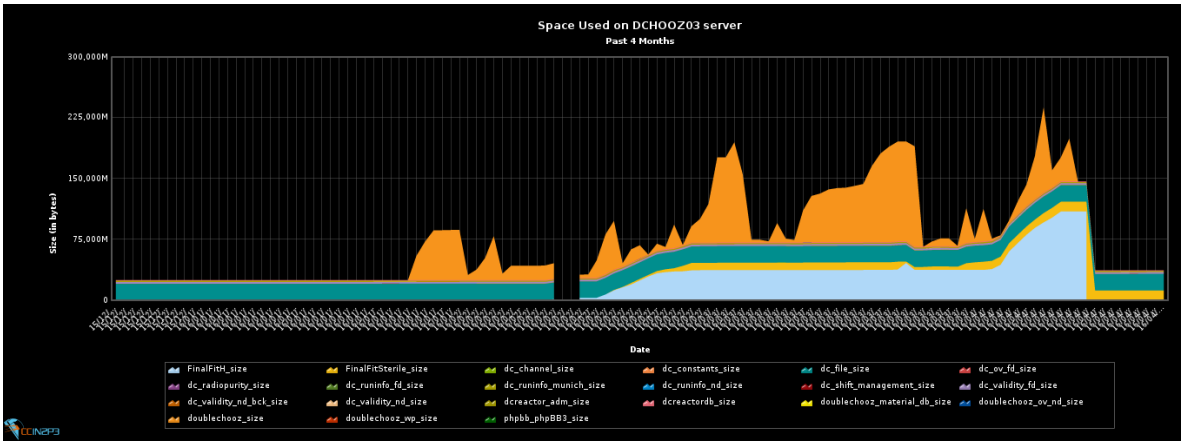

(c)

Figure 4.8: Development of recorded data amount per day between December 22nd 2015 and April 22nd 2016. The (a) near detector, (b) far detector and (c) stand-alone system is shown. The different databases as detailed in tables 4.2 and 4.5 are colour-coded. [77]

based monitor system was able to identify a series of malfunctions. One of the most frequent problems was a lost connection to the front end electronics voltage or temperature monitoring data acquisition units. This could be solved by a manual reset of the acquisition systems inside the laboratory. Most severe problems were the actual loss of front end electronic modules or high voltage modules due to power supply failures. Those could be uniquely detected by this monitoring tool and the data taking crews were alarmed. Additionally, an automated shutdown of the malfunctioning power supply was implemented for those cases. The shutdown functionality worked in every case. In addition, no such incident was missed by the monitoring tool or wrongly detected. Additionally detected problems were a hardware failure on the environment data acquisition system and drained batteries in environment sensors. Data of those systems is analysed only every few months such that a lost sensor would normally not be recognised for weeks. Moreover, occasional software problems in the data file migration system could be identified before a significant pileup of data files blocked the main data acquisition system. Furthermore, three missed weekly routine calibration sequences could be identified and could then be caught up by the following data taking shift crew. Finally, rare problems like the failure of the data file backup system, two failures of the outer veto data acquisition without alarm in the primary monitor and a failure in the primary monitoring system itself could be identified.

In conclusion, the databases system shows an overall good performance, reaching its design goal of negligible impact on user system performances, especially the physics data taking. Its initial specifications in speed and size match the user demands. It is moreover suitable for monitoring the entire experiment and has successfully detected a variety of issues.

Chapter 5

Determination of the Oscillation Analysis Inputs

The goal of the oscillation analysis is the determination of the oscillation parameter θ_{13} by finding a model for the oscillated reactor neutrino flux and the residual background fluxes that describes best the recorded number of neutrino candidates. As a first step, a dedicated discrimination of background events and a selection of signal events out of the total recorded dataset (cf. figure 3.2) is required. This endeavour is detailed in this chapter. The energy spectra of signal and background events derived in this chapter are used as inputs for the oscillation analysis described in chapter 6. In addition to the input spectra, several parameters relevant for the matching of the MC neutrino prediction and the measured background spectra are determined. Those parameters are the energy scale correction as well as normalisation parameters. They are additional inputs to the oscillation analysis.

As detailed in section 3.5, it is possible to define two disjoint datasets of neutrino candidates by distinguishing the energy of the delayed event and thereby distinguishing between the capture of the neutron by hydrogen or gadolinium. Both samples can be used for the oscillation analysis. However, only the gadolinium sample has yet been analysed in the new two detector regime. Thus, this chapter presents the gadolinium analysis only. The two detector hydrogen sample is currently under preparation. Results for the single detector hydrogen sample are given for comparison only. A full account on this analysis can be found in reference [67].

In this chapter, the analysis as presented in the Rencontres de Moriond conference 2016 is described [46]. It is the first two detector analysis of the Double Chooz collaboration. It extends the previous gadolinium analysis as presented in [10]. The far detector data recorded during this single detector phase is denoted as "FD-I" in the following. Similarly, "FD-II" denotes the far detector data recorded during the two detector phase. The final determination of the oscillation parameter $\sin^2(2\theta_{13})$ is described in the dedicated chapter 6.

5.1 Energy Calibration

Before a high-level analysis can be performed, the taken raw data has to be processed. This process includes low-level electronic readout processing (described in [78]) and intermediate-level energy calibration [10, p. 6 & seqq.].

The energy calibration aims for the conversion of the raw charge data of the PMTs to

energy. The result of this process is called the visible energy. Moreover, Monte Carlo samples are calibrated in energy, as well, in order to match them with taken physics data (cf. section 3.4). The energy calibration process for data and Monte Carlo is composed of several steps of which some are common among data and MC. The single steps are:

- Linearised PE calibration
- Uniformity calibration
- Energy scale calibration
- Stability calibration
- Charge non-linearity calibration
- Light non-linearity calibration

Details on the individual step are given in the following subsections.

5.1.1 Linearised PE Calibration

The first calibration step is the conversion from recorded PMT charge to **p**hoto **e**lectrons (PE). The total number of PE of an event in the entire detector is given as [10, p. 7]

$$N^m_{p.e.} = \sum_{i=1}^{390} (n^m_{p.e.})_i = \sum_{i=1}^{390} Q_i / G^m_i(Q_i, t) \tag{5.1}$$

where Q_i represents the charge of the ith PMT, t represents time, m distinguishes between MC and data and G^m_i is the non-linearity corrected gain of each individual PMT given by [79, p. 4]

$$G^m_i(Q_i, t) = \begin{cases} g_i(t) + l_i(t) \cdot (Q_i - c_i(t)) & Q_i < c_i(t) \\ g_i(t) & Q_i \geq c_i(t) \end{cases} \tag{5.2}$$

where g_i, l_i and c_i are determined empirically by a fit to the latest weekly recorded IDLI calibration data preceding time t (cf. section 3.3). The correction of gain non-linearity is necessary due to digitisation effects in the case of small PMT charges. The gain is determined time-dependently, because it was found that a power cycle of the PMT waveform digitisers has significant impact on the gain [10, p. 8].

5.1.2 Uniformity Calibration

Due to a position dependence of the conversion from charge to PE, a uniformity correction has to be applied in the following. The correction is performed by using neutron capture events by hydrogen. Those captures have a narrow energy peak of 2.23 MeV [65] and are present in the detectors with high statistics due to the presence of protons in the liquid scintillator molecules. The vertex of the capture is determined by a maximum likelihood reconstruction algorithm using charge and timing information of all ID-PMTs [79, p. 6]. The correction is applied relative to the centre of the detector and depicted in figure 5.1.

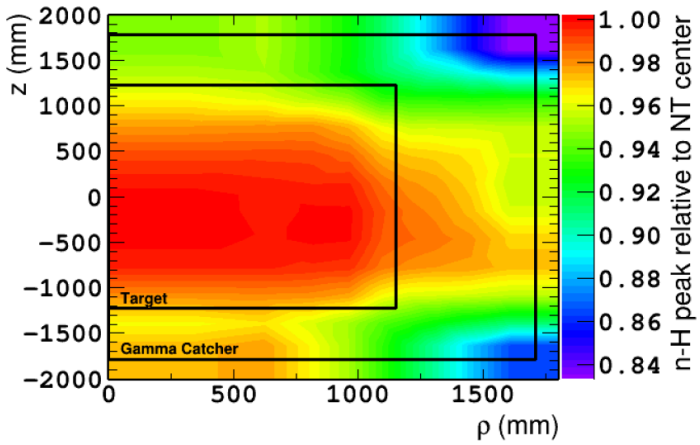

Figure 5.1: Uniformity correction map relative to the centre of the FD [10, p. 9].

5.1.3 Energy Scale Calibration

The following step is the conversion of PE to energy, the so-called visible energy. This is performed by evaluating neutron captures by hydrogen at the centre of the detector. The data is recorded during the deployment of a 252-californium source by the z-axis calibration system (cf. section 3.3) [79, p. 6].

5.1.4 Stability Calibration

After the conversion steps, the stability of this conversion over time has to be accounted for. This is done by evaluating neutron captures by hydrogen and gadolinium, as well as decays of 212-polonium deployed during calibration campaigns, over time. Effects for a time dependence of the energy conversion are mainly given by the scintillator light yield. The measurements therefore use captures in the entire scintillator-filled volume [79, p. 8].

5.1.5 Non-Linearity Calibrations

After these common conversion and correction steps for MC and data, a special correction has to be applied. This energy non-linearity correction is applied to the visible energy in the MC only. By this, a possible mismatch in the simulation of read-out electronics or scintillator properties (cf. section 3.4) is compensated and consequently a better agreement with data is achieved. The non-linearities are composed of charge non-linearities and light non-linearities [79, p. 11]. Since the light non-linearities are particle type dependent, they are not included in the common energy calibration, but enter the final oscillation analysis step (chapter 6) as optimisation parameters. The charge non-linearity correction, however, could enter the common energy calibration. Nevertheless, this correction is also included as optimisation parameters in the final oscillation analysis step. This is done for two reasons: Firstly, the evaluation of inter detector correlations for all energy scale parameters was not ready for the current oscillation analysis. Thus, a fully uncorrelated treatment is utilised as very conservative approach. Secondly, the uncorrelated treatment allows for an effective proof that the detectors are identical as they are supposed to be by design. It is expected that the oscillation analysis finds the same parameters for each detector and thereby proves

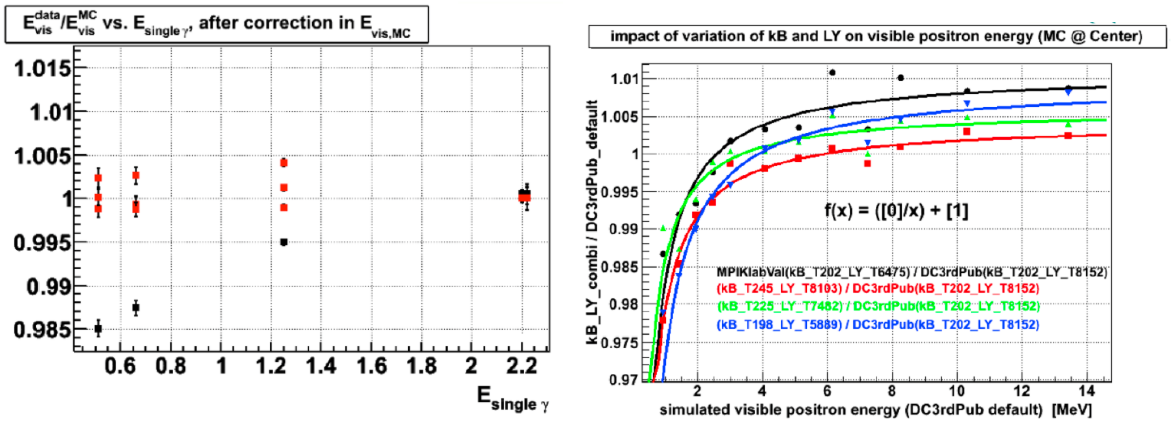

(a) (b)

Figure 5.2: Light non-linearity corrections [79, p. 13]. (a) Ratio between visible prompt energy of data and MC events of various calibration sources as function of single photon energies[1]. Black points indicate default light non-linearity parameters while red points indicate three different parameter combinations with good agreement as explained in the text. (b) Ratio between light non-linearity corrected and uncorrected positron energy. Each colour denotes a light non-linearity correction corresponding to one of the four different light non-linearity parameter combinations shown in figure 5.2a.

their alikeness. This strategy will only be used for the intermediate results presented in this thesis. For the publication result in winter 2016/2017, it is planned to account fully for inter detector correlations.

The charge non-linearity correction is determined by evaluating the difference between data and MC of neutron captures by gadolinium and hydrogen. The used captures are recorded at the centre of the detector during the deployment of a 252-californium calibration source. The differences between data and MC are originating from imperfections in the electronics read-out simulation of the PMTs, the front-end electronic and the waveform digitisers. Moreover, imperfections in the charge reconstruction algorithm contribute to it.

The effect of light non-linearity is caused by imperfections in the scintillator modelling. The two relevant factors in this context are the light yield and the quenching of the scintillator. The light yield is dependent on the fraction between Cherenkov and scintillator light. The quenching is dependent on the material-dependent Birk's constant. To determine the correct values for these light non-linearity parameters, various MC simulations of photon and neutron calibration sources were generated with different light non-linearity parameters applied [79, p. 12]. These were then compared to corresponding datasets. Four combinations of light non-linearity parameters were found to give good agreement with data (cf. figure 5.2a). Applying the extracted four parameter combinations as corrections to the visible energy of positrons yields four different correction functions (cf. figure 5.2b). Each function is a best-fit model describing heuristically the corresponding points. Including correction factors for the uniformity and charge non-linearity corrections, it can be shown that the final energy

[1] Note that the single photons from neutron captures by gadolinium are around 2.2 MeV although the total event energy is around 8 MeV.

	FD-I	FD-II	ND
e_0	(0.0 ± 0.06667) MeV	(0.0 ± 0.06645) MeV	(0.0 ± 0.06636) MeV
e_1	1.0 ± 0.02247	1.0 ± 0.02151	1.0 ± 0.02179
e_2	(0.0 ± 0.0006002) MeV^{-1}	(0.0 ± 0.0004197) MeV^{-1}	(0.0 ± 0.0009408) MeV^{-1}

(a)

FD-I	e_0	e_1	e_2
e_0	1.0	-0.001951	$-4.538 \cdot 10^{-5}$
e_1	-0.001951	1.0	-0.1000
e_2	$-4.538 \cdot 10^{-5}$	-0.1000	1.0

(b)

FD-II	e_0	e_1	e_2
e_0	1.0	0.0003268	-0.0006204
e_1	0.0003268	1.0	-0.01976
e_2	-0.0006204	-0.01976	1.0

(c)

ND	e_0	e_1	e_2
e_0	1.0	$6.427 \cdot 10^{-5}$	0.002865
e_1	$6.427 \cdot 10^{-5}$	1.0	-0.04384
e_2	0.002865	-0.04384	1.0

(d)

Table 5.1: Input model energy parameters. Figure (a) shows the central values and uncertainties while figure (b-d) show the intra detector parameter correlations. All inter detector correlations are assumed to be equal to zero.

correction reads as [10, p. 31]:

$$E^{init}_{visible} = e_0 + e_1 \cdot E^{final}_{visible} + e_2 \cdot (E^{final}_{visible})^2 \tag{5.3}$$

with $E^{final}_{visible}$ denoting non-linearity corrected visible prompt energy in the MC, $E^{init}_{visible}$ denoting uncorrected visible prompt energy in the MC and e_j with $j \in \{0, 1, 2\}$ denoting three polynomial coefficients. Their values and correlations are summarised in table 5.1.

In the oscillation analysis presented in chapter 6, the corrected neutrino MC energy scale $E^{final}_{visible} = E^{final}_{visible}(E^{init}_{visible}; e_0, e_1, e_2)$ is optimised according to the uncertainties of the three polynomial coefficients e_0, e_1 and e_2. By this, best matching between the neutrino MC energy scale and the background data energy scale is achieved.

5.2 Neutrino Candidate Selection

The next step, following the energy calibration, is the selection of neutrino candidate events. The applied selection cuts are explained in the following and summarised in table 5.2 [10; 46].

The main selection focuses on the characteristic signal of an electron antineutrino. This signal is the inverse beta decay as detailed in section 3.5. Additionally, dedicated cuts to reduce specific backgrounds are employed.

At first, a cleaning of the dataset is performed to remove invalid events, i.e. unphysical monitoring/random triggers, low energy noise and high energy events, as well as muons, most muon-induced background and light noise events. Unphysical triggers are directly identified by the trigger-based event category. Low energy noise and high energy events are rejected by requiring a prompt event energy of $0.3\,\text{MeV} < E_{vis} < 100.0\,\text{MeV}$.

	FD-I (n-Gd)	FD-II (n-Gd)	ND (n-Gd)
Cleaning	must be a valid trigger (see table 5.2b)		
IBD selection	$0.5\,\text{MeV} < E_{vis}^{prompt} < 20\,\text{MeV}$ $4.0\,\text{MeV} < E_{vis}^{delayed} < 10.0\,\text{MeV}$ $0.5\,\mu\text{s} < \Delta T_{delay} < 150.0\,\mu\text{s}$ $\Delta R_{delay} < 100\,\text{cm}$		
Multiplicity	$\Delta T_{valid}^{before} > 200\,\mu\text{s}$ $\Delta T_{valid}^{after} > 600\,\mu\text{s}$		
FV veto	$E_{vis}^{delayed} > 0.068 \cdot \exp(\frac{FV}{1.23})$	$E_{vis}^{delayed} > 0.120 \cdot \exp(\frac{FV}{1.60})$	
IV veto	prompt event is not an IV veto event (see table 5.2b)		
OV veto	$\Delta T_{OV-prompt} > 224\,\text{ns}$		
^{9}Li veto	$\mathcal{L}_{Li}^{prompt} < 0.4$		
Charge ratio veto	—	$\frac{Q_{max}}{Q_{tot}} < 0.106 \cdot E_{vis}^{-0.42}$	
CPS veto	—	$\frac{\mathcal{L}_{prompt}^{chimney}}{\mathcal{L}_{prompt}^{vertex}} + \frac{\mathcal{L}_{delayed}^{chimney}}{\mathcal{L}_{delayed}^{vertex}} < 2$	

(a)

	FD-I (n-Gd)	FD-II (n-Gd)	ND (n-Gd)
ID muon	$E_{vis} > 100\,\text{MeV}$		
IV muon	$Q_{IV} > 30\,000\,\text{DUQ}$	$Q_{IV} > 50\,000\,\text{DUQ}$	$Q_{IV} > 30\,000\,\text{DUQ}$
IV trigger	—	PMT group multiplicity > 10	
level muon	—	trigger energy > 100 MeV	
Light noise	$\frac{Q_{max}}{Q_{tot}} > 0.12$ or $Q_{diff} > 30\,000\,\text{DUQ}$ or $[\text{RMS}(t_{start}) > 36\,\text{ns}$ and $\text{RMS}(Q) > 464 - 8 \cdot \text{RMS}(t_{start})]$	$\frac{Q_{max}}{Q_{tot}} > 0.20$ or $Q_{diff} > 100\,000\,\text{DUQ}$ or $[\text{RMS}(t_{start}) > 36\,\text{ns}$ and $\text{RMS}(Q) > 1680 - 28 \cdot \text{RMS}(t_{start})]$	
Valid trigger	not a random trigger not a muon $0.3\,\text{MeV} < E_{vis} < 100.0\,\text{MeV}$ not a light noise trigger $\Delta T_{\mu} > 1.0\,\text{ms}$		
IV veto event	IV PMT multiplicity ≥ 2 $Q_{IV} > 400\,\text{DUQ}$ $\Delta d_{ID-IV} < 3.7\,\text{m}$ $-110\,\text{ns} < \Delta T_{ID-IV} < -10\,\text{ns}$	IV PMT multiplicity ≥ 2 $Q_{IV} > 300\,\text{DUQ}$ $\Delta d_{ID-IV} < 3.7\,\text{m}$ $-10\,\text{ns} < \Delta T_{ID-IV} < 60\,\text{ns}$	

(b)

Table 5.2: Neutrino selection cuts as explained in the text. The main cuts are listed in table (a). An event that fulfils all conditions is accepted as an IBD candidate. Table (b) summarises additional cuts used in the main cuts. In both tables, the unit DUQ denotes an uncalibrated **d**igital **u**nit of **charge**. See the text for further explanations.

Muon-induced backgrounds are especially fast neutrons and long living β-n-decay isotopes as explained in sections 3.6.1 and 3.6.2. They are rejected by imposing a veto time of $\Delta T_\mu > 1.0\,\text{ms}$ after muon events (cf. orange window in figure 5.3). As seen in figure 3.8b, after 1.0 ms no excess of β-n-decay events can be seen with respect to the flat component caused by accidental coincidence background. Muon events themselves are tagged either by an energy deposition of $E_{vis} > 100\,\text{MeV}$ in the inner detector or by a charge deposition of $Q_{IV} > 30\,000\,\text{DUQ}$ in the FD-I, $Q_{IV} > 50\,000\,\text{DUQ}$ in the FD-II and $Q_{IV} > 30\,000\,\text{DUQ}$ in the ND, respectively. Here, the unit DUQ denotes an uncalibrated **d**igital **u**nit of **charge**. Moreover, an energy deposition of $> 100\,\text{MeV}$ as seen by the trigger system and activity in more than 10 PMT trigger groups is used to tag muon events in the FD-II and ND datasets. This type of tagging was not used in the single detector phase.

Light noise events are caused by discharges inside the PMT bases as detailed in section 3.6.5. They are rejected by several cuts which evaluate homogeneity and isotropy properties of the detector illumination for each event. Firstly, the requirement of a small ratio of $\frac{Q_{max}}{Q_{tot}} \leq 0.12$ in the FD-I and $\frac{Q_{max}}{Q_{tot}} \leq 0.20$ in the FD-II or ND datasets, respectively, between the maximal charge among all single PMTs Q_{max} and total charge in all PMTs of an event Q_{tot} ensures that the event has not happened in the immediate vicinity of a PMT, i.e. it ensures that the charge is distributed equally among several PMTs. Likewise, the requirement of a small non-uniformity of the PMT charge distribution around the PMT with highest charge of $Q_{diff} < 30\,000\,\text{DUQ}$ in the FD-I and $Q_{diff} < 100\,000\,\text{DUQ}$ in the FD-II or ND datasets, respectively, is employed to reject events in the vicinity of a single PMT. The quantity Q_{diff} used in this cut is defined as

$$Q_{diff} := \frac{1}{|B_{1\text{m}}(\vec{X}_{max})|} \sum_{i \in B_{1\text{m}}(\vec{X}_{max})} \frac{(Q_{max} - Q_i)^2}{Q_i} \tag{5.4}$$

where $B_{1\text{m}}(\vec{X}_{max})$ denotes the set of all PMTs inside a ball of radius 1 m around the position $\vec{X}_{max}$ of the PMT with the maximal charge and Q_i denotes the charge of the ith PMT inside $B_{1\text{m}}(\vec{X}_{max})$ while Q_{max} denotes the charge of the PMT with maximal charge. As third cut, the spread in PMT pulse start times $RMS(t_{start})$ and charges $RMS(Q)$ is utilised to further reduce events located close to a single PMT. For those events, most of the light arrives early at the PMTs in the vicinity of the noisy PMT, while PMTs on the opposite site of the noisy PMT see only little light at later times. This effect is exploited by requiring that the spread of the start times $\text{RMS}(t_{start})$ of all PMT pulses fulfils the condition $\text{RMS}(t_{start}) \leq 36\,\text{ns}$ or alternatively the spread of PMT charges $\text{RMS}(Q)$ has to satisfy the condition $\text{RMS}(Q) \leq 464 - 8 \cdot \text{RMS}(t_{start})$ in the FD-I and $\text{RMS}(Q) \leq 1680 - 28 \cdot \text{RMS}(t_{start})$ in the FD-II or ND datasets, respectively. All light noise cuts were optimised for a small inefficiency with respect to IBD events.

Following the cleaning cuts, the proper IBD selection cuts are applied as listed in table 5.2a. The inverse β-decay is characterised by a prompt energy deposition between 1.02 MeV and approximately 11 MeV followed by a delayed energy deposition of $(2.230 \pm 0.007)\,\text{MeV}$ for a neutron capture by hydrogen [65] and on average of $(8.36 \pm 0.46)\,\text{MeV}$ for all possible neutron captures by gadolinium [63; 64], respectively. Thus, a cut on prompt energy of $0.5\,\text{MeV} < E_{vis}^{prompt} < 20\,\text{MeV}$ and on delayed energy of $4.0\,\text{MeV} < E_{vis}^{delayed} < 10.0\,\text{MeV}$ is utilised. The large cut window on the prompt energy E_{vis}^{prompt} is chosen in order to provide a sufficient amount of background dominated analysis bins. This is found to yield a smaller uncertainty as background rates can be constraint better in the final analysis step presented in chapter

6: The energy region around 9 MeV is dominated by β-n isotope background (cf. section 3.6.1) allowing to constrain this background while the high energy bins are dominated by fast neutrons/stopping muons (cf. section 3.6.2) allowing to constrain the fast neutrons/stopping muon background. The lower energy bound of 0.5 MeV was determined to be large enough for showing negligible trigger inefficiency [80]. The delayed energy signal cut $E_{vis}^{delayed}$ was optimised to allow minimal contamination by fast neutron background in the high energy part and high signal efficiency in the low energy part.

The neutron capture happens after a thermalisation period of around 10 μs, with a time constant of 200 μs for neutron captures by hydrogen and with a time constant of 30 μs for neutron captures by gadolinium [66, p. 68]. Therefore, a delay time cut of $0.5\,\mu s < \Delta T_{delay} < 150.0\,\mu s$ is imposed (cf. blue window in figure 5.3). The time delay cut ΔT_{delay} was optimised in the short time regime to suppress stopping muon events on the one hand (cf. figure 3.10a), while respecting the increased capture probability of neutrons due to the end of their thermalisation process on the other hand (cf. figure 3.7c). Moreover, it was optimised in the long time regime to minimise signal inefficiencies while reducing at the same time systematic uncertainties in the modelling of the so called spilling effect[2]. An additional spatial distance cut between prompt and delayed event of $\Delta R_{delay} < 100$ cm is introduced to reject accidental background coincidences that are likely to happen at much larger distances between prompt and delayed vertex than proper IBD events (cf. figure 3.11b).

To achieve a reduction of background events originating from a large number of muon-induced neutrons, i.e. multiple neutron capture background, a multiplicity condition of precisely one event is imposed in a time interval $[-\Delta T_{valid}^{before}; \Delta T_{valid}^{after}] = [-200\,\mu s; 600\,\mu s]$ around an IBD prompt event (cf. red window in figure 5.3). In this time interval, only the IBD de-

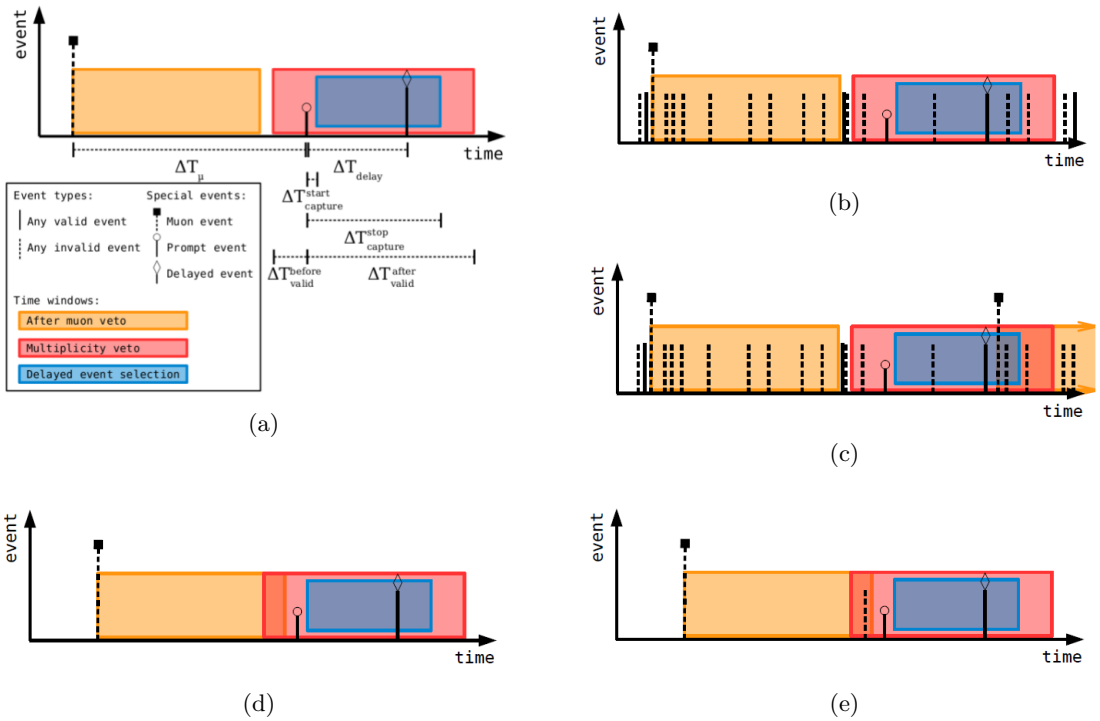

[2] The spilling effect is discussed in greater detail in section 5.7

layed event candidate is allowed within the time interval defined by ΔT_{delay} (blue window in figure 5.3). Any additional valid event within the multiplicity veto time interval will reject the neutrino-candidate event (cf. figures 5.3h to 5.3k). However, additional invalid events within the multiplicity veto time interval will not reject the neutrino-candidate event (cf. figures 5.3b, 5.3c and 5.3e). The multiplicity time interval boundaries have been optimised such that no excess of multiple neutron captures over the flat background of accidental events could be seen outside the region of isolation.

To reduce the background of stopping muons, the **f**unctional **v**alue (FV) veto cut FV is used. It evaluates the negative log-likelihood of the best-fit hypothesis of the used vertex reconstruction algorithm. This algorithm takes recorded PMT charges and their timing into account. A high FV is achieved for not point-like events or events with wrongly reconstructed location. The required cut condition is defined relative to the energy of the delayed event as

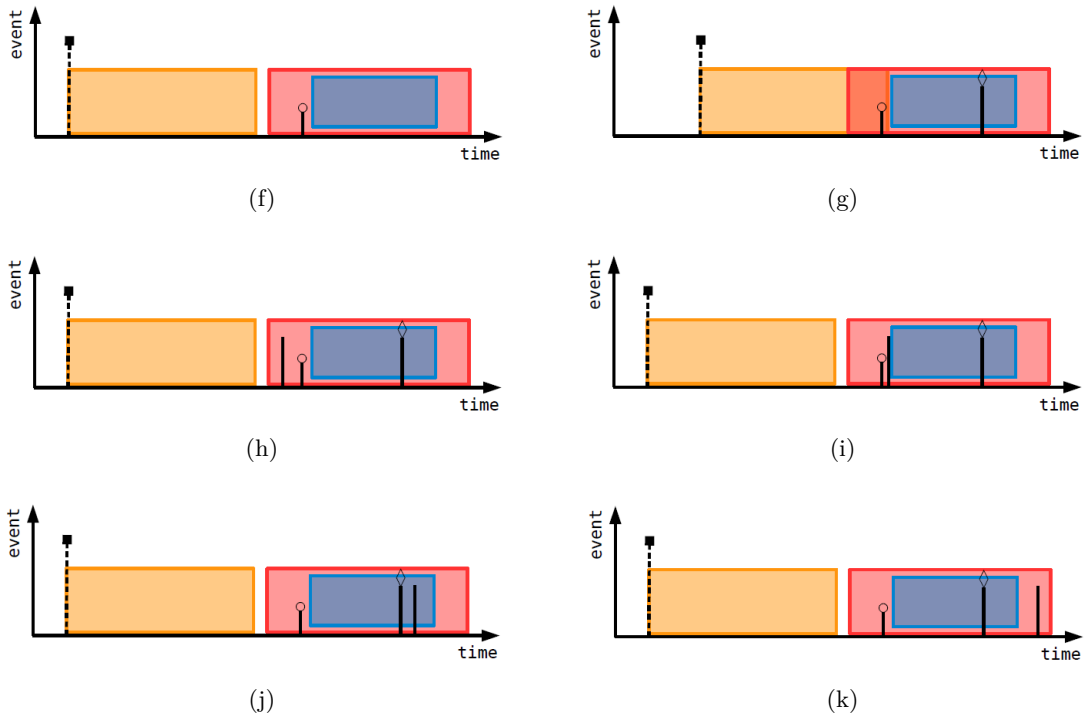

Figure 5.3: Examples of accepted (a-e) and rejected (f-k) neutrino-candidate events. (a) accepted and fully isolated candidate. (b) accepted candidate accompanied by invalid events. (c) accepted candidate accompanied by invalid events and subsequent close in time muon. (d) accepted candidate with overlapping muon veto window and multiplicity veto window. (e) same as before, but with additional invalid event. (f) rejected candidate due to missing delayed event. (g) rejected candidate due to a prior close in time muon (opposite of (c)). (h-k) rejected candidates due to additional valid events in the multiplicity veto window. Event (h) could become an accepted candidate if a prior close in time muon exists (case (e)). Events (j,k) could become accepted candidates if a subsequent close in time muon exists (case (c)). Thus, close in time muons can in some cases partially neutralise the multiplicity veto. See text for further explanation.

$E_{vis}^{delayed} > 0.068 \cdot \exp(\frac{FV}{1.23})$ in the FD-I and $E_{vis}^{delayed} > 0.120 \cdot \exp(\frac{FV}{1.60})$ in the FD-II or ND datasets, respectively. The cut is optimised to separate IBD candidates from stopping muon candidates in the energy-FV plane. Figure 5.4 shows the blue separation cut line between the cluster of IBD events with low FV and the cluster of stopping muon events with medium FV. The FV is also capable of rejecting light noise events. Those show a high FV in figure 5.4.

In order to discriminate the fast neutron background, energy depositions in the inner detector are rejected if they are correlated in space Δd_{ID-IV} and time ΔT_{ID-IV} to an inner veto energy deposition. Such correlated events are likely caused by one or more fast neutrons being produced outside of the detector and then entering the detector through the inner veto. The inner veto energy deposition is considered to be correlated with the inner detector energy deposition if the distance between ID and IV energy deposition fulfils the condition $\Delta d_{ID-IV} < 3.7\,\text{m}$. Additionally, the correlation in time has to be such that the IV event has to happen before the ID event meeting the requirement of $-110\,\text{ns} < \Delta T_{ID-IV} < -10\,\text{ns}$ in the FD-I and $-10\,\text{ns} < \Delta T_{ID-IV} < 60\,\text{ns}$ in the FD-II or ND datasets, respectively. Furthermore, the IV event charge has to satisfy the condition $Q_{IV} > 400\,\text{DUQ}$ in the FD-I and $Q_{IV} > 300\,\text{DUQ}$ in the FD-II or ND datasets, respectively, and the inner veto energy deposition has to be seen by at least two IV PMT groups, i.e. the IV events must not be a local low energy noise event. This cut is applied for prompt events only in the gadolinium sample, while it is exploited for prompt and delayed events in the hydrogen sample.

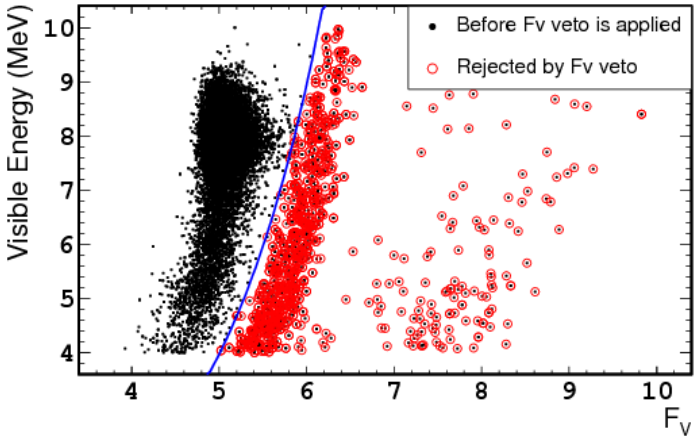

Figure 5.4: Functional value cut plane of the FD-I. The separation line of the cut is given in blue [10, p. 16].

To reject muon events that are not detected by the inner parts of the detector, an outer veto veto is applied. Those muons are mainly passing muons that travel through the rock surrounding the inner detector parts. Nevertheless, those muons can induce several backgrounds that are able to enter the detector as explained above. It is also possible that muons can enter the detector unseen by the inner veto, if they enter through the chimney, i.e. the hatch for calibration source deployment in the top of the detector, and stop afterwards inside the detector. If the time between a prompt event and an OV event is so small that $\Delta T_{OV-prompt} \leq 224\,\text{ns}$, the event is rejected.

A dedicated cut to reject β-n-decay isotopes, e.g. lithium-9, is performed by evaluating the likelihood $\mathcal{L}_{Li}^{prompt}$ that an IBD candidate prompt event can be a lithium-9 prompt event. The likelihood is based on the time and distance between the current event and all possible previous muon events within 700 ms that might have caused a spallation that resulted in the production of a β-n-decay isotope. Additionally, the number of neutron events following the previous muon is taken into account for evaluating the number of potential spallations the muon might have induced. A value of $\mathcal{L}_{Li}^{prompt} \geq 0.4$ causes a rejection of the prompt event.

	FD-I	FD-I reactor off	FD-II	ND
pred. IBD signal/d^{-1}	38.04 ± 0.67	0.217 ± 0.065	40.39 ± 0.69	280.5 ± 4.7
accidental bkgrd/d^{-1}	0.070 ± 0.003		0.106 ± 0.002	0.344 ± 0.002
fast-n+stop-μ bkgrd/d^{-1}	0.586 ± 0.061			3.42 ± 0.23
β-n bkgrd/d^{-1}	$0.97^{+0.41}_{-0.16}$			5.01 ± 1.43
total prediction/d^{-1}	39.63 ± 0.73	1.85 ± 0.30	42.06 ± 0.75	289.3 ± 4.9
meas. IBD cand./d^{-1}	37.64	0.97	40.29	293.4
meas. IBD cand.	17351	7	8551	44233
lifetime/d	460.93	7.24	212.21	150.76

Table 5.3: IBD candidate sample and prediction for signal and backgrounds as derived in the text [46, p. 20]. The evolution of IBD candidate rate over time can be seen in figure 3.2.

In order to reduce the number of stopping muon events, the charge ratio between the maximal charge among all single PMTs Q_{max} and total charge in all PMTs of an event Q_{tot} is compared against a function of the visible energy of the event. A value of $\frac{Q_{max}}{Q_{tot}} \geq 0.106 \cdot E_{vis}^{-0.42}$ in the FD-II or ND datasets leads to a rejection of the corresponding event. This cut rejects foremost stopping muon events in the vicinity of PMTs. Those stopping muons can yield a non-negligible amount of light due to a small liquid scintillator contamination in the top part of the ND buffer vessel. The charge ratio cut has been newly introduced for the two detector setup.

To reduce the number of stopping muons further, the **c**himney **p**ulse **s**hape (CPS) likelihood ratio is considered. The likelihood takes the pulse shape of the prompt and delayed events into account. If it is more likely that prompt and delayed events happened in the chimney instead of at the best-fit vertices of the central region, the event is rejected. This condition corresponds to a value of $\frac{\mathcal{L}_{prompt}^{chimney}}{\mathcal{L}_{prompt}^{vertex}} + \frac{\mathcal{L}_{delayed}^{chimney}}{\mathcal{L}_{delayed}^{vertex}} \geq 2$ in the FD-II or ND datasets. The CPS cut has also been newly introduced for the two detector setup.

With the described selection strategy, an IBD candidate sample as listed in table 5.3 is achieved. By comparing the expected total rate predictions with the measured candidates, it is already obvious that a deficit in IBD candidates is observed in the far detector datasets. The following sections will detail the rendering of the background and signal predictions shown in table 5.3. A quantitative result for the observed deficit and its consistency with neutrino oscillations is derived in chapter 6.

5.3 Neutrino Prediction

The expected rate of anti-neutrinos $R_{i,d}^{\bar{\nu}_e}$ is calculated from reactor and detector specific inputs. For the ith energy bin and detector $d \in \{FD, ND\}$ it is given as [81]

$$R_{i,d}^{\bar{\nu}_e} = \frac{1}{4\pi}\epsilon_d N_d^p \cdot \sum_{r\in\{B1,B2\}} \left[\frac{1}{L_{r,d}^2} \frac{P_{th,r}}{\sum_{k\in I} \alpha_{r,k}^{DC} \langle E_f \rangle_k} \left(\langle \sigma_f \rangle^{Bu} + \sum_{k\in I} \left[\alpha_{r,k}^{DC} - \alpha_{r,k}^{Bu} \right] \langle \sigma_f \rangle_k \right) \right] \quad (5.5)$$

with ϵ_d denoting the detection efficiency in each detector (cf. sections 5.7 and 5.8) and N_d^p

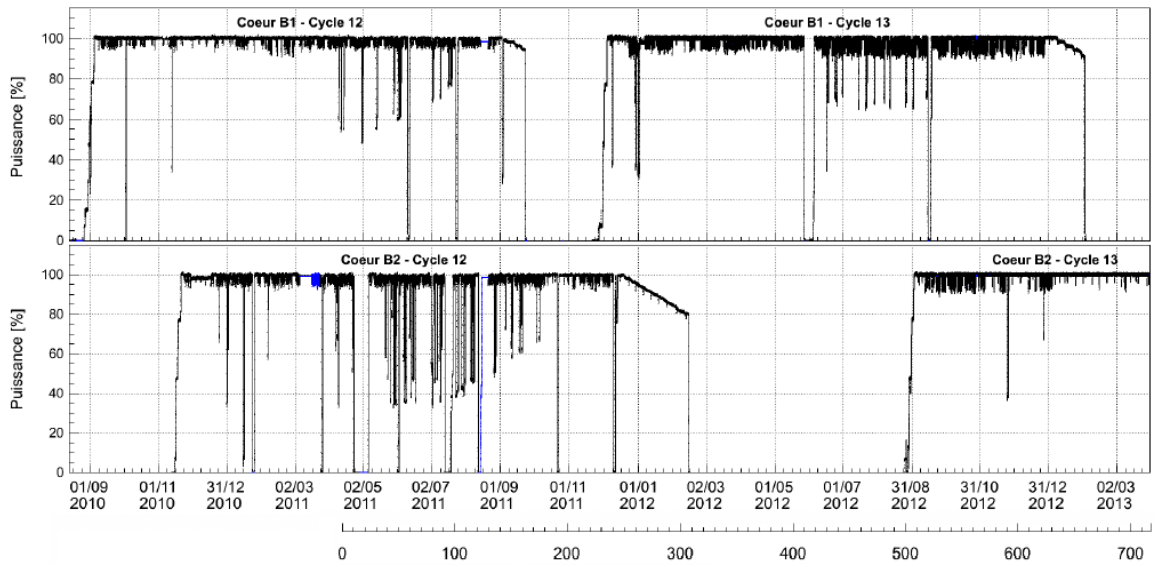

Figure 5.5: Evolution of reactor thermal power over time for fuel cycles 12 and 13 of the CHOOZ-B1 and CHOOZ-B2 reactor cores [82, p. 198][3]. The exposure time of the far detector is indicated by an additional time axis. Long downtimes are due to reactor core assembly changes which mark the beginning of a new cycle.

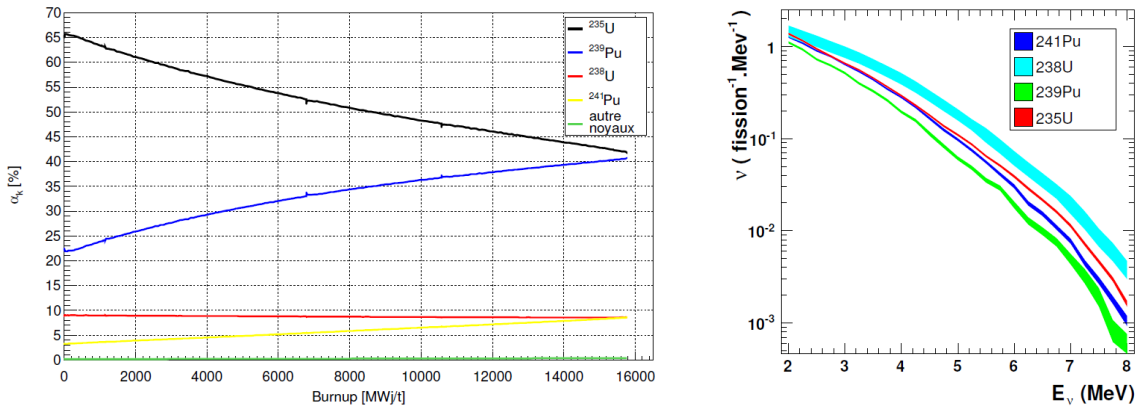

(a) (b)

Figure 5.6: Reactor inventory evolution and antineutrino spectra. Figure (a) shows the reactor inventory evolution, i.e. the evolution of the relative number of fissions per fuel isotope, for the fuel cycle 13 of the CHOOZ-B1 reactor [82, p. 205][4]. The fission of ^{235}U enriches ^{239}Pu through neutron capture by ^{238}U as shown in figure 3.3. Figure (b) depicts the spectra of emitted antineutrinos per fission for the four dominant isotopes [82, p. 54].

denoting the number of protons in the fiducial volume of each detector. Moreover, $L_{r,d}$

[3] puissance (fr.) = power
cœur (fr.) = *here:* reactor core

[4] autre noyaux (fr.) = other isotopes

denotes the distance between each reactor and detector and $P_{th,r}$ represents the thermal power in each reactor r. Its measured evolution over time can be seen in figure 5.5. The thermal power is measured every minute in the primary loop of each reactor. The quantity $\langle E_f \rangle_k$ denotes the mean energy release per fission. The relative fuel inventory composition in each CHOOZ-B reactor is denoted by $\alpha_{r,k}^{DC}$, where $k \in I := \{^{235}\mathrm{U}, ^{238}\mathrm{U}, ^{239}\mathrm{Pu}, ^{241}\mathrm{Pu}\}$. The relative fuel inventory composition is defined as the relative number of fissions happening by those isotopes. For the Bugey reactor, $\alpha_{r,k}^{Bu}$ denotes the same quantity. A typical evolution of the fuel inventory composition over time can be seen in figure 5.6a.

The Bugey-4 reactor neutrino experiment [83] with its 15 m baseline is used to normalise the CHOOZ-B reactor flux prediction and to reduce its uncertainty. This is done by comparing the CHOOZ-B mean cross-section per fission and per isotope $\langle \sigma_f \rangle_k$ to the Bugey-4 measurement of mean cross-section per fission and per isotope $\langle \sigma_f \rangle^{Bu}$. The mean cross-section is evaluated by different strategies. On the one hand, it can be calculated from first principles for some of the possible decay chains of the fuel components. On the other hand, it is calculated by effective measurements of electron spectra that accompany the production of antineutrinos in the decays as shown in figure 3.3. This can be done by captures of neutrons on thin foils made from the different reactor fuel components. Also a mixed strategy is employed for certain decay chains. As recently discovered [84; 85] during a reevaluation of the original β-decay spectra measurements [86], the original measurement appears to have underestimated the total flux by 6.5 %. Using an experimentally achieved normalisation for the antineutrino flux, i.e. the Bugey-4 antineutrino flux measurements, avoids normalisation problems caused by this discovery. Among all available measurements the Bugey-4 measurement was chosen due to its small uncertainty, the similar reactor fuel inventory composition between the Bugey and CHOOZ-B reactors, the short baseline of the Bugey-4 detector and due to an overlap between the former Bugey-4 collaboration and the Double Chooz collaboration introducing valuable expertise.

The latest prediction for the number of neutrinos per fission is pictured in figure 5.6b. This falling neutrino flux yields, together with the increasing cross-section for the IBD-reaction, the spectrum depicted in figure 3.6a. The increasing IBD cross section is caused by the higher mean energy transfer and consequently by the higher chance to convert the target proton into a neutron [61, p. 2]. The IBD-reaction can only happen above 1.8 MeV (cf. figure 3.6a) were the kinetic energy of the neutrino is sufficiently large to generate the additional masses of the new particles in reaction equation 3.2. The final error on the neutrino flux shows the uncertainty contributions as listed in table 5.4.

	FD-I	FD-II	ND
Bugey-4 measurement	1.40 %		
energy per fission $\langle E_f \rangle_k$	0.16 %		
cross section per fission $\langle \sigma_f \rangle_k$	0.20 %		
baseline $L_{r,d}$	< 0.01 %	< 0.01 %	0.01 %
fuel inventory $\alpha_{r,k}^{DC}$	0.82 %	0.74 %	0.73 %
thermal power $P_{th,r}$	0.44 %	0.44 %	0.44 %
total	1.70 %	1.66 %	1.66 %
far-far correlation	0.72		—
far-near correlation	—	> 0.99	

Table 5.4: Reactor flux uncertainties for each detector. Due to simultaneous running of both detectors and the similar flux ratio between the two reactors for the two detectors, i.e. isofluxness, a high correlation exists in the multi-detector phase. [46, p. 15]

5.4 β-n Decay Background Prediction

The background contamination by β-n-decay isotopes like lithium-9 or helium-8 has been evaluated in several ways. An exploited method is the extrapolation of β-n-decay event rate of events directly after muons. For this, only events located close in time and space to a muon track are considered and the muon energy dependent production rate of β-n-decay events is taken into account. This method yields a rate of $2.20^{+0.35}_{-0.27}$ d^{-1}. When using only β-n-decay event candidates following high energy muon events and accompanied by spallation neutron events, a very pure β-n-decay event candidate sample can be achieved. The thereby yielded rate of (2.05 ± 0.13) d^{-1} is used as a lower limit. Combining both measurements gives a rate of $2.10^{+0.41}_{-0.15}$ d^{-1} [79, p. 34].

During the estimation of this rate, the dedicated lithium likelihood cut to reduce β-n-decay isotope background, e.g. lithium-9 background (cf. section 5.2 and table 5.2a), was not applied in order to get a higher sample statistic. Applying this cut reduces the rate down to its final value of $0.97^{+0.41}_{-0.16}$ d^{-1} for the FD [46, p. 20]. For the ND, a value of 5.01 ± 1.43 d^{-1} is obtained [87, p. 12] due to the smaller detector overburden. Here, no asymmetric value for the uncertainty is given as the dedicated analysis to determine the lower limit was not performed. Such determination of the lower limit was not necessary, as the uncertainties of the rate are not entering the oscillation analysis any more in the two detector phase. This has been the case for the original FD-only analysis. The decision to treat the β-n-decay event rate unconstrained in the oscillation analysis was made in order to avoid a possible bias caused by a wrongly estimated β-n-decay event rate. Such a wrongly estimated β-n-decay event rate is likely, since previous oscillation analyses showed a tension between the best-fit and input values for the β-n-decay event rate [10, p. 32] and since there are unresolved problems in precisely determining the contamination by other background types in the β-n-decay isotope background samples [88].

The energy shape spectrum of the β-n-decay isotope background is rendered by taking all events passing each selection cut described in section 5.2, but not the lithium-9 likelihood cut. From this sample, the IBD event contamination is subtracted by using a high likelihood IBD sample, i.e. a sample of IBD candidates being far in time from any muon event [79, p. 36]. The remaining data spectrum as shown in figure 3.8a is used as input to the final oscillation analysis. This is done to reduce shape uncertainties in the MC simulation.

5.5 Fast Neutron and Stopping Muon Background Prediction

The background contamination of the final IBD candidate sample by fast neutron and stopping muon events is evaluated by selecting all events that pass each selection cut described in section 5.2, but not the IV veto cut. This yields a background enriched sample as fast neutrons and stopping muons are likely to produce light in the IV the same way as they do in the ID. The spectral shape of those events is found to be flat with no evidence for a non-flat shape [79, p. 38]. Thus, a flat distribution without shape uncertainties is used as input to the final oscillation analysis.

The remaining background rate is estimated by selecting all events that pass each selection cut described in section 5.2, but with the prompt energy between $20\,\text{MeV} < E_{vis}^{prompt} < 30\,\text{MeV}$ instead of $0.5\,\text{MeV} < E_{vis}^{prompt} < 20\,\text{MeV}$. By this, a rate of (0.586 ± 0.061) d^{-1} is estimated for the FD [46, p. 20]. Additionally, a rate of (3.42 ± 0.23) d^{-1} is estimated for the ND [89; 90].

5.6 Accidental Background Prediction

The background contamination by accidental event coincidences is determined by selecting all events that pass each selection cut described in section 5.2, but with the time delay window ΔT_{delay} being shifted multiple times from zero offset, i.e. $0.5\,\mu\text{s} < \Delta T_{delay} < 150\,\mu\text{s}$, to more than 1 ms offset. The prompt event energy shape and rate of accidental background events are both estimated by this method [79, p. 28]. Since prompt and delayed events are strongly separated in time, the thereby achieved value has to be corrected for four systematic effects [91]:

- Muon events happening after the prompt and before the delayed events can veto the delayed event in addition to muon events happening before the prompt event (cf. orange-marked veto time in figure 5.3). Thus, more events are vetoed and the accidental background is underestimated.

- A multiplicity veto is introduced around the delayed event in addition to the prompt event (cf. red-marked time in figure 5.3). This causes an increased rejection probability and underestimates the accidental background.

- The lithium-likelihood cut $\mathcal{L}_{Li}^{prompt}$ (cf. section 5.2 and table 5.2a) rejects less accidental background events. The omitted events are those where the β-decay of muon-induced boron-12 mimics a delayed IBD-event. In the original neutrino selection without shifted time window, the prompt event would in this case be so close in time to the inducing muon that it has a high lithium-likelihood and is rejected. However, in the shifted time window scenario, the prompt event happens before the muon. Thus only the delayed event shows a high lithium-likelihood. However, the lithium-likelihood cut is only applied to prompt events, therefore the entire event is not rejected. In consequence the accidental background is overestimated. This overestimation is dominant in comparison to all previous corrections.

- Moreover, for prompt event candidates at the end of each data taking run, it is not possible to analyse the full amount of shifted time windows due to the finite run length. Thus the accidental background rate at the end of each run is underestimated.

The four correction factors modify the estimated rate to $(0.0701 \pm 0.0026)\ \text{d}^{-1}$ for the FD-I dataset [91, p. 11]. Similar analyses are performed for the ND and the FD-II. The value for the FD-II is given as $(0.1059 \pm 0.0023)\ \text{d}^{-1}$, while the ND has an accidental background rate of $(0.3441 \pm 0.0022)\ \text{d}^{-1}$ [91, p. 11]. The listed rate uncertainties are caused almost exclusively by the uncertainties on the four systematic corrections presented above. Statistical uncertainties are negligible due to the high number of shifted delay time windows.

5.7 Neutron Detection Efficiency

As the neutrino or IBD spectrum is derived from MC simulations and the background spectra are derived from data, it is required to apply an efficiency correction, i.e. an overall normalisation, to the MC spectrum. This is done to achieve a better matching between data and MC samples. The detection efficiency correction is composed from three individual independent contributions:

- The relative fraction of neutron captures by gadolinium and by hydrogen: If the concentration of gadolinium in the liquid scintillator is higher than the targeted concentration, i.e. the value in the MC, more IBD candidates are detected in the gadolinium analysis than expected and a smaller neutrino oscillation effect might be measured in the gadolinium analysis. At the same time, less neutrons than expected are captured by hydrogen and in consequence a larger neutrino oscillation effect might be measured in the hydrogen analysis. The value of the neutron capture fraction is corrected by comparing the measured fraction from calibration data recorded in the centre of the detector (cf. section 3.3) versus the expected fraction from the corresponding calibration MC [92, p. 127 & seqq.].

- The selection efficiency of IBD events: This efficiency is evaluated by two complementary methods. One evaluates the vertex dependent selection efficiency by utilising calibration data of calibration sources deployed at different positions. The other one exploits the IBD candidate sample directly evaluating the inclusive and exclusive cut efficiencies of the time delay ΔT_{delay} cut, the vertex distance ΔT_{delay} cut and the delayed energy $E_{vis}^{delayed}$ cut [79, p. 43].

- The neutron spilling effect: The spilling effect describes the misidentification of the detector subvolume in which an IBD event took place. The misidentification is due to the movement of the IBD neutron, i.e. the spill of events from one subvolume into another. When an IBD event takes place, the produced positron annihilates after a few millimetres path length close to the vertex of the IBD event, while the neutron travels several centimetres before it has thermalised and gets captured [93, p. 792 & seqq.]. If the IBD event is located close to a border between two detector subvolumes, the neutron can get captured in a different volume than the volume of the IBD vertex. This is called a spilling event. Due to the few millimetres path length of the positron, the prompt event vertex is in principle a good approximation for the IBD event vertex. However, it is not possible to use this prompt event vertex for the determination of the IBD event vertex due to the insufficient vertex resolution in liquid scintillator detectors. Instead, the capture energy of the IBD neutron is used to determine in which volume the IBD event took place. A capture energy around 8 MeV indicates a capture by gadolinium which can only happen in the gadolinium-loaded scintillator of the target volume. A capture energy around 2.23 MeV indicates a neutron capture by hydrogen which mainly happens in the γ-catcher volume and additionally happens subdominantly in the target volume (cf. sections 3.2 and 3.5). In case of a spilling event, the method of using the delayed event energy for IBD vertex determination likely yields a false result, as the dominant neutron capture energy differs between the target and γ-catcher volumes. The spilling currents in both directions do not cancel, because the contributing volumes of the target and γ-catcher at the connection surface have different size. This is due to the cylinder geometry. Moreover, the travel length for neutrons are shorter in the target scintillator than in the γ-catcher scintillator[5]. The main uncertainty in the spilling correction is the correct modelling of the neutron thermalisation process, i.e. the neutron movement, prior to the neutron capture. The free neutron gas model and the molecular bond model

[5] The scintillators are rather matched in their respective densities to ensure the structural integrity of the acrylic vessels. Moreover, they are matched with respect to the light yield instead of matching them to cancel the spilling effect (cf. section 3.2).

	FD-I		FD-II		ND	
	value	uncert.	value	uncert.	value	uncert.
Gd-fraction	0.9744	0.0025	0.9744	0.0026	0.9744	0.0028
IBD-selection	0.9985	0.0021	0.9985	0.0016	0.9985	0.0017
spilling	1.0000	0.0027	1.0000	0.0027	1.0000	0.0027
selection cut ineff.	0.9389	0.0011	0.9299	0.0009	0.7697	0.0002
Proton number	1.0000	0.0030	1.0000	0.0030	1.0000	0.0030
DAQ ineff.	1.0000	<0.0001	1.0000	<0.0001	1.0000	<0.0001
total	0.9135	0.0049	0.9047	0.0047	0.7489	0.0038

Table 5.5: Neutrino MC correction factors as explained in sections 5.7 and 5.8. [46, p. 19][95, p. 4][96, p. 12]

derived from the Tripoli4 simulation package [94] and a custom NeutronTH simulation package are evaluated to determine the net spill current. Discrepancies in the two simulations are considered as systematic uncertainties [79, p. 48].

Only the capture process fraction yields a correction factor different from unity. The combined detection efficiency correction factors for each detector are given in table 5.5.

5.8 Other Efficiencies

Apart from the neutron detection efficiency, several other correction factors of minor impact contribute to the normalisation of neutrino and IBD MC, respectively. Those additional contributions are also listed in table 5.5. The contributions are in detail:

- Several cut inefficiencies: Due to the veto cuts presented in section 5.2, the effective lifetime of the data sample is reduced. This has to be corrected in the reactor neutrino MC lifetime. The correction is larger for the ND due to the smaller laboratory overburden and the consequently increased background rate. Inefficiencies are determined by analysing data samples recorded by external random triggers and by determining signal and background contributions of rejected events by specific properties of the event categories [97].

- Proton number in target: The number of protons inside the target volume of the detector that can be hit by antineutrinos in an IBD process. It is determined from weight measurements obtained during the filling of the detector which are then corrected for several effects including e.g. volume expansion due to temperature [98].

- Data acquisition, electronic and trigger inefficiencies: Dead times of those hardware components can cause a further reduction in the lifetime of the data sample. Additionally, a high energy readout threshold of the trigger system could cause the loss of low energy events. Trigger readout inefficiency and hardware deadtimes have been shown to be non-existent [80].

Many of those quantities are correlated due to the identical detector geometry and the identical scintillator liquids. For the correlation between FD-I and FD-II a value of 0.75 is found. The ND and FD-I datasets show a correlation of 0.77 while the ND and FD-II datasets show a correlation of 0.78. Those correlations are included into the input model of the oscillation analysis as detailed in chapter 6.

Chapter 6

Oscillation Analysis

The goal of the oscillation analysis is the determination of the oscillation parameter θ_{13} by finding a model for the oscillated reactor neutrino flux and the residual background fluxes that describes best the recorded events of neutrino candidates. This analysis uses data recorded until 2014 during the far detector only time period and data recorded simultaneously with far and near detector since early 2015.

For the oscillation analysis, energy spectral shape and rate information is used. During the single detector phase, first oscillation analysis results were derived by two identical but independent implementations of χ^2 based optimisation methods [99; 100; 101]. This analysis strategy is continued in the two detector phase and is addressed as "(first and second) χ^2 based analysis" in the following. In this chapter, a new oscillation analysis approach based on a maximum likelihood method is developed. As for the χ^2 based oscillation analysis, neutrino energy spectral shape and rate information is used. The central idea to increase accuracy in the new approach is the utilisation of a Poissonian likelihood for modelling statistical uncertainties rather than using a Gaussian approximation as done in the χ^2 based analysis. Additionally, the approximative two flavour vacuum oscillation model is replaced by a three flavour oscillation scenario including matter effects. Moreover, the MC energy scale correction (cf. section 5.1) is not applied by means of a precalculated response map, but recalculated at every oscillation parameter space point.

After illustrating the general idea of the likelihood-based oscillation analysis and the mathematical methods used within this analysis in section 6.1, the input model of the analysis is described in section 6.2. The technical description of the algorithm and its validation is given in sections 6.3 and 6.4, respectively. Results of the oscillation analysis and several cross-checks are presented in sections 6.5 and 6.6, respectively. Finally, details on the future precision of the Double Chooz experiment are given in section 6.7.

6.1 General Idea and Statistical Methods

This section illustrates the general idea of the likelihood-based oscillation analysis. Furthermore, it introduces to the statistical methods utilised to define confidence intervals and to quantify the goodness of fit between the data and the best-fit model describing the data.

The oscillation analysis follows a maximum likelihood approach. For this approach, the number of measured neutrino candidate events n_i in each energy bin $1 \leq i \leq N$ is assumed to be independently distributed and to follow in each bin a known class of **p**robability **d**ensity

functions (pdf) $f_i(n_i;\vec{\theta})$ that are dependent on an unknown parameter $\vec{\theta} \in \Theta$ out of a set Θ of possible parameter values. The joint pdf over all N energy bins is then given as

$$f(n_1, ..., n_N; \vec{\theta}) = \prod_{i=1}^{N} f_i(n_i; \vec{\theta}). \tag{6.1}$$

For a fixed set of data points n_i, $1 \leq i \leq N$, the function $f(n_1, ..., n_N; \vec{\theta})$ can also be understood as dependent on the variable $\vec{\theta}$:

$$\mathcal{L}(\vec{\theta}; n_1, ..., n_N) = f(n_1, ..., n_N; \vec{\theta}). \tag{6.2}$$

The maximum likelihood approach then aims for maximising this so called likelihood function $\mathcal{L}(\vec{\theta}; n_1, ..., n_N)$ with respect to the variable $\vec{\theta}$. By this, the likeliest value for $\vec{\theta}$ is found, i.e. the particular value for $\vec{\theta}$ that describes the measured data $n_1, ..., n_N$ best [102, p. 24].

In this thesis, $\vec{\theta}$ includes several variables like oscillation parameters, background event rates and energy scale model parameters. All parameters are listed in table 6.2. Only the oscillation parameter θ_{13} is of interest in the analysis. All other parameters ν_j, $1 \leq j \leq M$, are already constrained by prior knowledge and can be understood as nuisance parameters. The prior knowledge on a set of M nuisance parameters ν_j, $1 \leq j \leq M$ is included in the likelihood function by multiplying it with the pdfs of the individual nuisance parameters that express the prior knowledge

$$\mathcal{L}(\vec{\theta}; n_1, ..., n_N, \vec{\eta}_1, ..., \vec{\eta}_M) = \prod_{i=1}^{N} f_i(n_i; \vec{\theta}) \cdot \prod_{j=1}^{M} g_j(\nu_j; \vec{\eta}_j) \tag{6.3}$$

with $\vec{\eta}_j$ being fixed and known parameters of the pdfs g_j. In this thesis, the $\vec{\eta}_j$ include e.g. the central values and variances of the distributions g_j. By this method, the parameters contained in $\vec{\theta}$ are optimised such that they describe best the measured data points and the prior knowledge.

Apart from finding the likeliest value for the oscillation parameter θ_{13}, it is also of interest to define a confidence interval for this parameter. In this thesis, this is achieved by exploiting Wilks' theorem [103]: Under certain regularity conditions and in the limit of increasing sample size, it holds that the statistic

$$\Lambda(n_1, ..., n_N, \vec{\eta}_1, ..., \vec{\eta}_M) := -2 \cdot \ln \frac{\sup_{\vec{\theta} \in \Theta_0} \{\mathcal{L}(\vec{\theta}; n_1, ..., n_N, \vec{\eta}_1, ..., \vec{\eta}_M)\}}{\sup_{\vec{\theta} \in \Theta} \{\mathcal{L}(\vec{\theta}; n_1, ..., n_N, \vec{\eta}_1, ..., \vec{\eta}_M)\}} \tag{6.4}$$

follows a χ^2 distribution with the degrees of freedom given as the dimensionality difference between Θ_0 and Θ. Thus, by choosing Θ_0 and Θ as nested models, e.g. Θ_0 is Θ but with one parameter $\tilde{\theta}$ fixed, Λ is χ^2-distributed with one degree of freedom. For finding a confidence interval of confidence level $\alpha \in [0, 1]$ for $\tilde{\theta}$ one has to find the values of $\tilde{\theta}$ that correspond to the $1-\alpha$ quantile of the χ^2-distribution with one degree of freedom. A table of such quantiles can be found e.g. in [104, p. 47].

Wilks' theorem can also be used for evaluating the goodness of fit achieved with the maximum likelihood ansatz. For this, the likelihood ratio

$$\Lambda_S(n_1, ..., n_N, \vec{\eta}_1, ..., \vec{\eta}_M) := -2 \cdot \ln \frac{\sup_{\vec{\theta} \in \Theta} \{\mathcal{L}(\vec{\theta}; n_1, ..., n_N, \vec{\eta}_1, ..., \vec{\eta}_M)\}}{\sup_{\vec{\theta} \in \Theta_S} \{\mathcal{L}(\vec{\theta}; n_1, ..., n_N, \vec{\eta}_1, ..., \vec{\eta}_M)\}} \tag{6.5}$$

is used as deviance, where Θ_S denotes the saturated model, i.e. a model with an additional parameter for each observation. In case of the oscillation analysis, this model contains one additional normalisation parameter per energy bin. The saturated model is thus describing the data perfectly and without any discrepancy [102, p. 24]. Again, the likelihood ratio Λ_S follows a χ^2-distribution with the degrees of freedom given as dimensionality difference between the saturated model Θ_S and the nested model Θ, i.e. the number of observations in our case. This can be transformed into a goodness of fit p-value by looking at the quantiles of the χ^2-distribution as detailed above.

6.2 Description of the Input Model

The oscillation analysis described in this work is performed with four separate datasets. The datasets are:

- FD1: far detector in single detector phase (FD-I) with at least one reactor on
- FD2: far detector in two detector phase (FD-II)
- ND: near detector in two detector phase
- FD1off: far detector in the single detector phase (FD-I) with both reactors off.

Details about the datasets are listed in table 5.3 and in the top of table 6.2. For each dataset, the expected rate of neutrino events in comparison to the measured rate of IBD candidates is shown in figure 3.2.

The measured IBD candidates in each energy bin of the four datasets are modelled by the sum of four contributions. Those contributions are the IBD-signal prediction from the reactors and the three background types as discussed in chapter 5. Their input model spectra are shown in figures 6.1, 6.2 and 6.3 for each detector. The three background spectra are measured in-situ as described in chapter 5 and enter the oscillation analysis model without energy correction. Each of the three background contributions is optimised during the oscillation analysis within its rate and shape uncertainties to match the measured IBD candidates best. In contrast to the background spectra, the IBD-signal prediction is derived by a reactor and detector MC simulation. The IBD-signal contribution is thus optimised during the oscillation analysis with respect to the energy scale uncertainties between MC and data, the flux uncertainty from the reactor simulation, several normalisation corrections between MC and data as listed in table 5.5 and the neutrino oscillation parameters $\sin^2(2\theta_{13})$ and Δm^2_{ee} as introduced in chapter 2.

region	range	bin width	bins
IBD dominated	[0.5, 8.0) MeV	0.25 MeV	30
Li/He dominated	[8.0, 10.0) MeV	0.50 MeV	4
intermediate region	[10.0, 12.0) MeV	1.00 MeV	2
FNSM dominated	[12.0, 20.0) MeV	2.00 MeV	4
total	[0.5, 20.0) MeV	–	40

Table 6.1: Energy spectrum binning used in the oscillation analysis. The far detector reactor off sample is treated in a single bin.

All background and signal parameters, their uncertainties and their correlations are listed in table 6.2 or shown in figures 6.5 and 6.6. In the optimisation process, the background

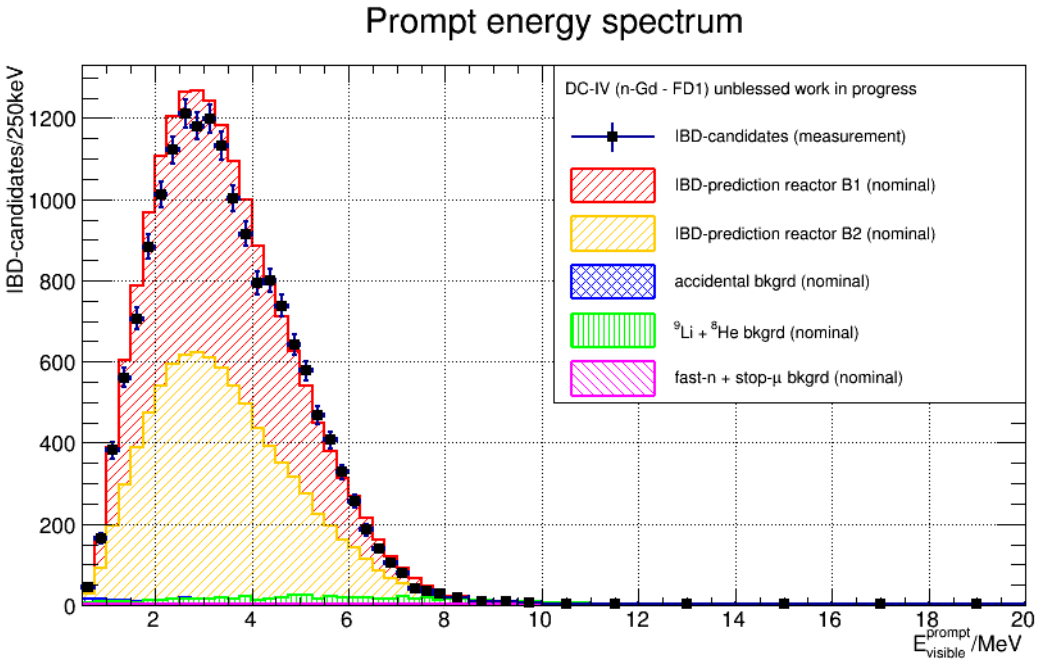

(a)

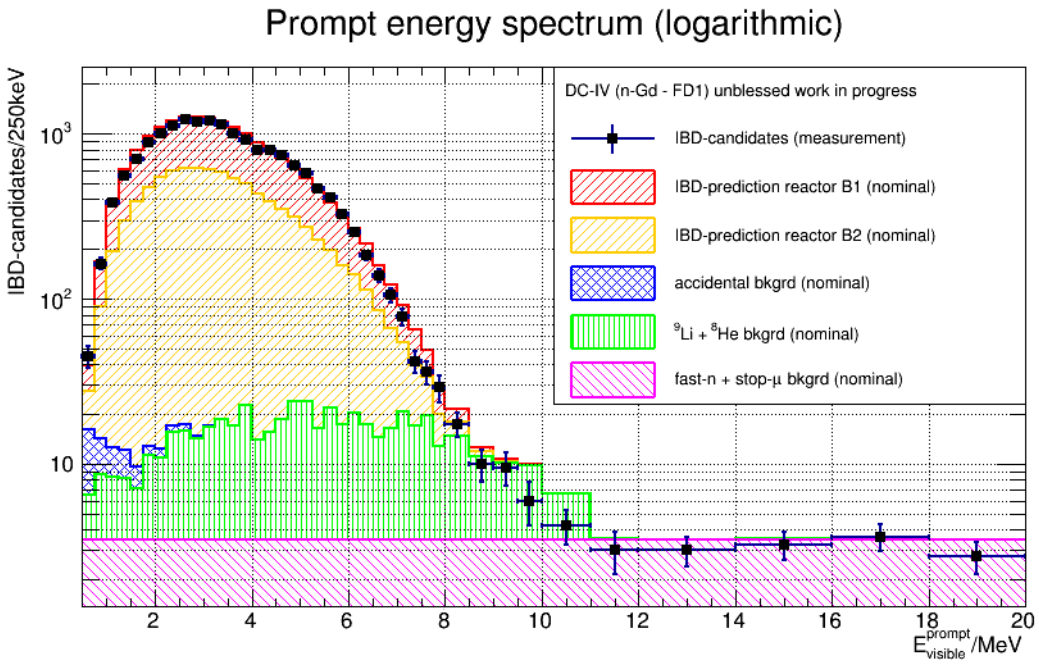

(b)

Figure 6.1: Input model of the oscillation analysis (no oscillation) as derived in chapter 5 for the FD1 dataset.

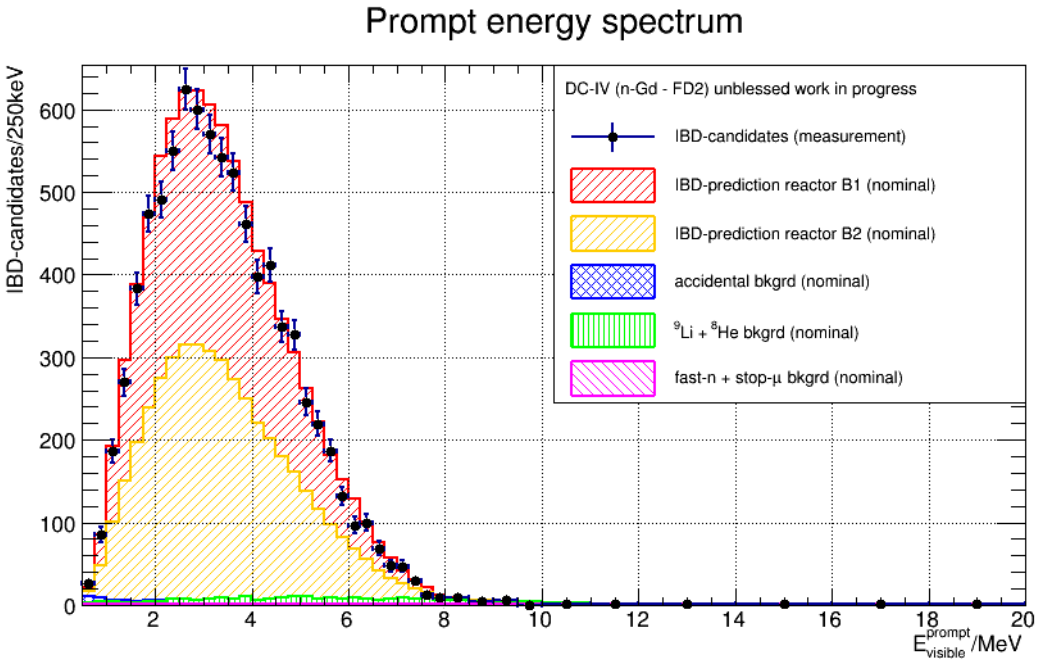

(a)

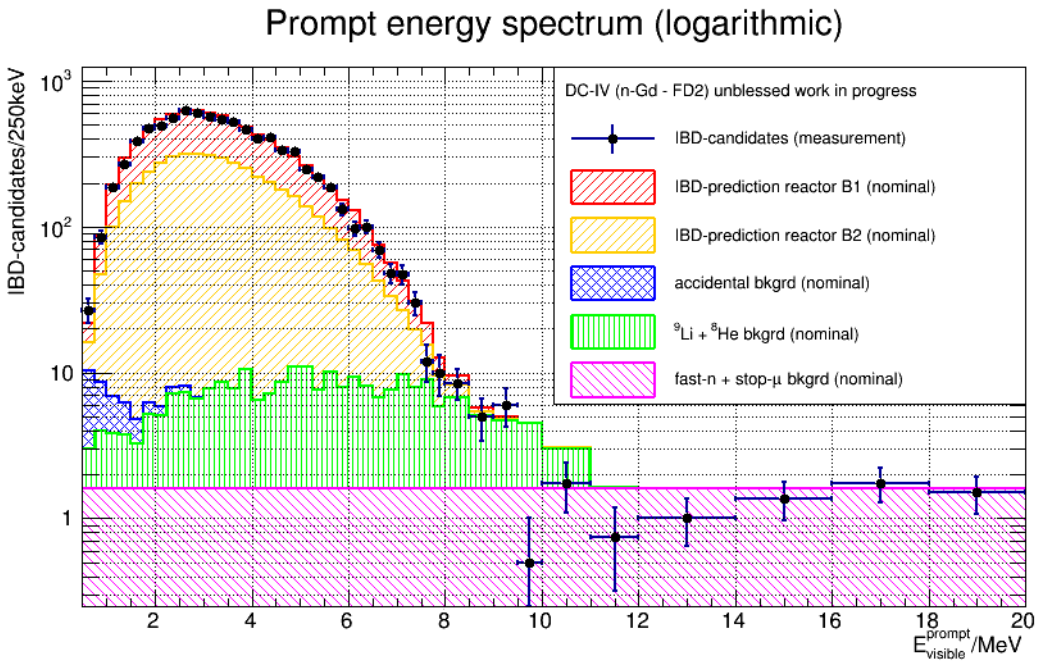

(b)

Figure 6.2: Input model of the oscillation analysis (no oscillation) as derived in chapter 5 for the FD2 dataset.

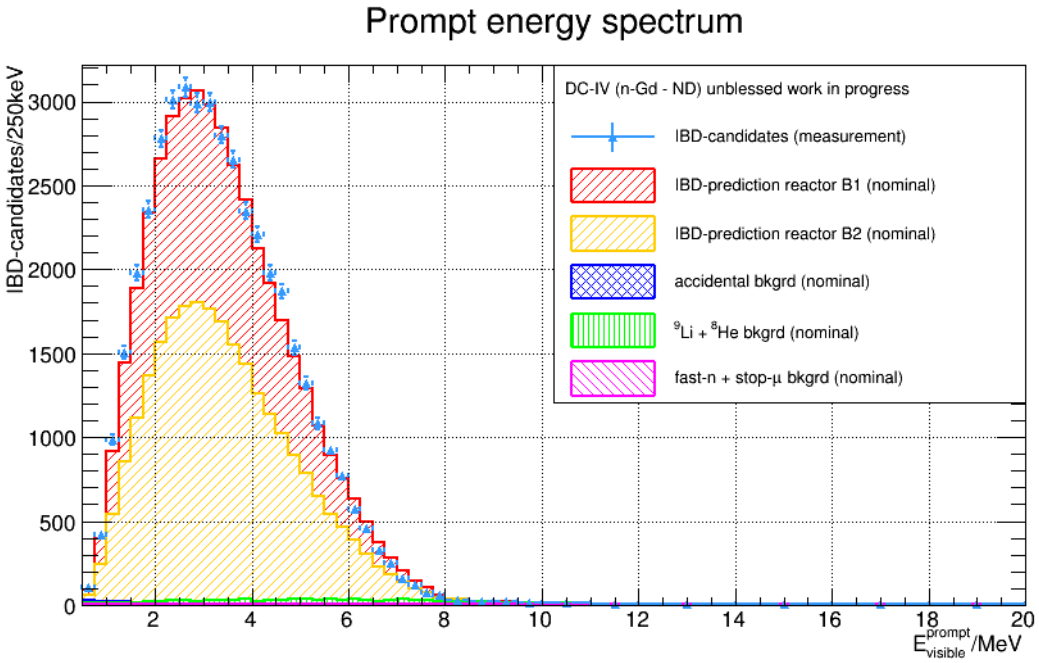

(a)

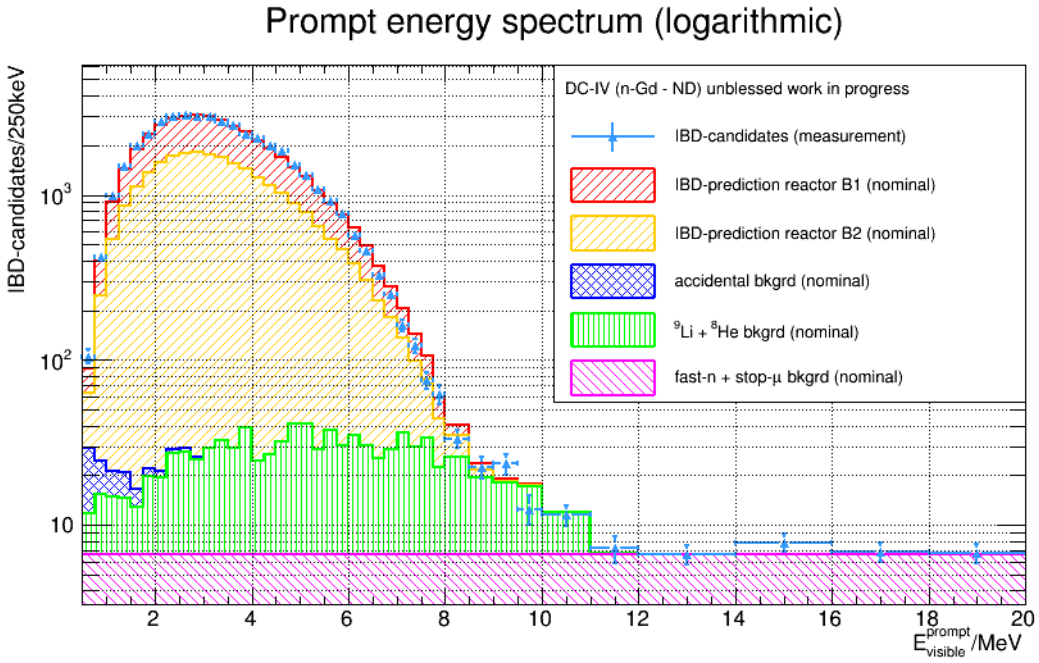

(b)

Figure 6.3: Input model of the oscillation analysis (no oscillation) as derived in chapter 5 for the ND dataset.

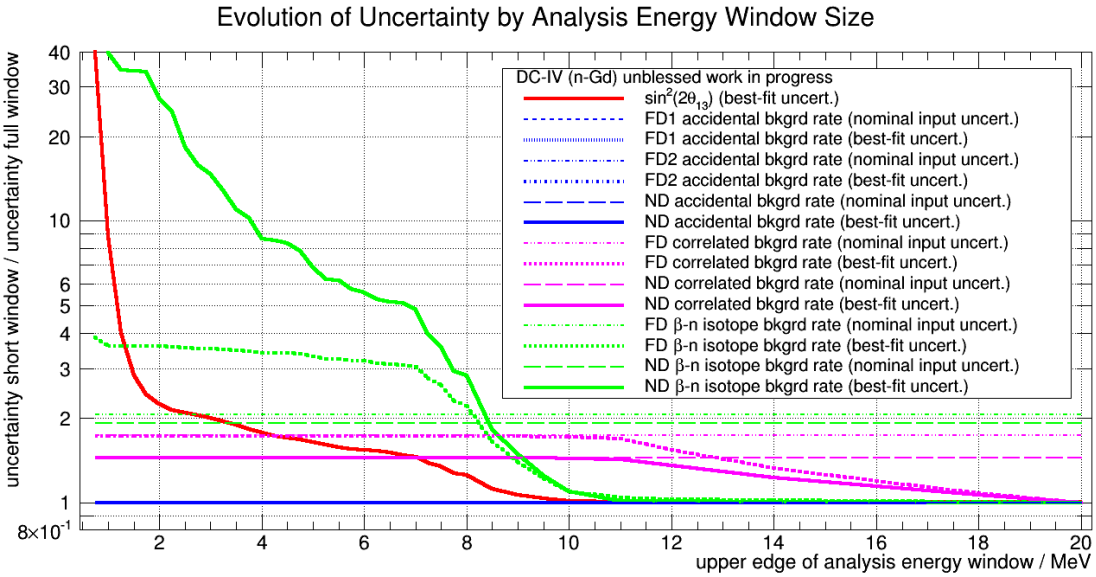

Figure 6.4: Effect of the energy window size. The uncertainties of several parameters are shown as function of the analysis energy window upper edge. The lower edge is kept fix at 0.5 MeV. The uncertainties are plotted relative to the respective uncertainties achieved when using the full energy window. The lines for all accidental backgrounds are located at a value of 1.

rate parameters b_ζ^{rate}, $\zeta \in \{LiHe, corr, acc\}$, and the signal normalisation corrections ν^{norm} are scaling the single input spectra over the entire energy range. The background shape parameters b_ζ^{shape}, $\zeta \in \{LiHe, corr, acc\}$, and reactor flux parameters ν^{r+s} are able to distort the single spectra in a bin-to-bin correlated way. The bin-to-bin correlations are depicted in figures 6.5 and 6.6. In addition to the rate and shape parameters, the energy scale correction parameters e_ξ, $\xi \in \{0, 1, 2\}$, are optimised during the oscillation analysis to match the IBD-signal MC spectra with the background data spectra. Details on the implementation and the role of the individual parameters will be given in section 6.3.

With exception of the rate only FD1off dataset, each dataset is analysed in 40 energy bins allowing for spectral information to be included into the analysis. The applied energy binning is shown in table 6.1. As listed, each energy region is dominated by a different event type. This allows to constrain certain background types in the oscillation analysis. Figure 6.4 shows this effect by depicting the best-fit uncertainties of the three background rates and the oscillation amplitude as function of the upper edge of the analysis energy window. One can see that the uncertainty on the Li/He, i.e. β-n isotope, background rates is especially suppressed when their dedicated energy range is included in the analysis window (cf. table 6.1 and e.g. figure 6.1b). Likewise, the uncertainty on the fast neutron and stopping muon, i.e. correlated, background rates is strongly suppressed when their dedicated high energy range is included. With this strategy, it is possible to constrain the background rates even beyond their input model uncertainties as indicated in figure 6.4. While the correlated background rates are constrained by their input model uncertainties, the suppression beyond the input uncertainties is also possible for the β-n isotope background rates, which are treated fully

dataset	FD1	FD2	ND	FD1off
detector phase	single detector	two detector	two detector	single detector
reactor status	at least one active	at least one active	at least one active	all inactive
calender year(s)	2011 – 2013	2015	2015	2011 – 2013
lifetime	460.93 d	212.21 d	150.76 d	7.24 d
IBD-prediction				
energy parameter e_0	(0.0 ± 0.06667) MeV	(0.0 ± 0.06645) MeV	(0.0 ± 0.06636) MeV	unused
energy parameter e_1	(1.0 ± 0.02247)	(1.0 ± 0.02151)	(1.0 ± 0.02179)	unused
energy parameter e_2	(0.0 ± 0.0006002) MeV^{-1}	(0.0 ± 0.0004197) MeV^{-1}	(0.0 ± 0.0009408) MeV^{-1}	unused
MC normalis. ν^{norm}	(0.9151 ± 0.0049)	(0.9036 ± 0.0047)	(0.7511 ± 0.0038)	(0.9151 ± 0.0049)
flux uncertainty ν^{r+s}	figure 6.5	figure B.1a	figure B.1b	unused
residual rate $R^{\bar{\nu}_e}_{Off}$	unused	unused	unused	(0.217 ± 0.065) d^{-1}
IBD-prediction (global parameters)				
amplitude $\sin^2(2\theta_{13})$	free			
frequency Δm^2_{ee}	$(2.44 \pm 0.09) \cdot 10^{-3}$ eV^2			
β-n decay isotope background/lithium-9+helium-8 background				
rate b^{rate}_{LiHe}	$(0.97^{+0.41}_{-0.16})$ d^{-1} (free)	$(0.97^{+0.41}_{-0.16})$ d^{-1} (free)	(5.01 ± 1.43) d^{-1} (free)	$(0.97^{+0.41}_{-0.16})$ d^{-1} (free)
shape b^{shape}_{LiHe}	figure 6.6a	figure 6.6a	figure 6.6a	figure 6.6a
correlated background/fast neutron+stopping muon background				
rate b^{rate}_{corr}	(0.586 ± 0.061) d^{-1}	(0.586 ± 0.061) d^{-1}	(3.42 ± 0.23) d^{-1}	(0.586 ± 0.061) d^{-1}
shape b^{shape}_{corr}	unused	unused	unused	unused
accidental background				
rate b^{rate}_{acc}	(0.0701 ± 0.0026) d^{-1}	(0.1059 ± 0.0023) d^{-1}	(0.3441 ± 0.0022) d^{-1}	(0.0701 ± 0.0026) d^{-1}
shape b^{shape}_{acc}	figure 6.6b	figure 6.6b	figure 6.6b	figure 6.6b

Table 6.2: Overview of the input model parameters of the oscillation analysis as derived in chapter 5. Parameters denoted as "free" are not constrained in the oscillation analysis.

energy scale		FD1			FD2			ND		
		e_0	e_1	e_2	e_0	e_1	e_2	e_0	e_1	e_2
FD1	e_0	$+1.0$	-0.00195	$-4.538 \cdot 10^{-5}$	0.0	0.0	0.0	0.0	0.0	0.0
	e_1	-0.00195	$+1.0$	-0.10000	0.0	0.0	0.0	0.0	0.0	0.0
	e_2	$-4.538 \cdot 10^{-5}$	-0.10000	$+1.0$	0.0	0.0	0.0	0.0	0.0	0.0
FD2	e_0	0.0	0.0	0.0	$+1.0$	$+0.00033$	-0.00062	0.0	0.0	0.0
	e_1	0.0	0.0	0.0	$+0.00033$	$+1.0$	-0.01976	0.0	0.0	0.0
	e_2	0.0	0.0	0.0	-0.00062	-0.01976	$+1.0$	0.0	0.0	0.0
ND	e_0	0.0	0.0	0.0	0.0	0.0	0.0	$+1.0$	$+6.427 \cdot 10^{-5}$	$+0.00287$
	e_1	0.0	0.0	0.0	0.0	0.0	0.0	$+6.427 \cdot 10^{-5}$	$+1.0$	-0.04384
	e_2	0.0	0.0	0.0	0.0	0.0	0.0	$+0.00287$	-0.04384	$+1.0$

accidental background		FD1		FD2		ND	
		b_{acc}^{rate}	b_{acc}^{shape}	b_{acc}^{rate}	b_{acc}^{shape}	b_{acc}^{rate}	b_{acc}^{shape}
FD1	b_{acc}^{rate}	$+1.0$	0.0	0.0	0.0	0.0	0.0
	b_{acc}^{shape}	0.0	$+1.0$	0.0	0.0	0.0	0.0
FD2	b_{acc}^{rate}	0.0	0.0	$+1.0$	0.0	0.0	0.0
	b_{acc}^{shape}	0.0	0.0	0.0	$+1.0$	0.0	0.0
ND	b_{acc}^{rate}	0.0	0.0	0.0	0.0	$+1.0$	0.0
	b_{acc}^{shape}	0.0	0.0	0.0	0.0	0.0	$+1.0$

correlated background		FD1	FD2	ND
		b_{corr}^{rate}	b_{corr}^{rate}	b_{corr}^{rate}
FD1	b_{corr}^{rate}	$+1.0$	$+1.0$	0.0
FD2	b_{corr}^{rate}	$+1.0$	$+1.0$	0.0
ND	b_{corr}^{rate}	0.0	0.0	$+1.0$

β-n isotope background		FD1		FD2		ND	
		b_{LiHe}^{rate}	b_{LiHe}^{shape}	b_{LiHe}^{rate}	b_{LiHe}^{shape}	b_{LiHe}^{rate}	b_{LiHe}^{shape}
FD1	b_{LiHe}^{rate}	$+1.0$	0.0	$+1.0$	0.0	0.0	0.0
	b_{LiHe}^{shape}	0.0	$+1.0$	0.0	$+1.0$	0.0	$+1.0$
FD2	b_{LiHe}^{rate}	$+1.0$	0.0	$+1.0$	0.0	0.0	0.0
	b_{LiHe}^{shape}	0.0	$+1.0$	0.0	$+1.0$	0.0	$+1.0$
ND	b_{LiHe}^{rate}	0.0	0.0	0.0	0.0	$+1.0$	0.0
	b_{LiHe}^{shape}	0.0	$+1.0$	0.0	$+1.0$	0.0	$+1.0$

IBD prediction		FD1		FD2		ND	
		ν^{norm}	ν^{r+s}	ν^{norm}	ν^{r+s}	ν^{norm}	ν^{r+s}
FD1	ν^{norm}	$+1.0$	0.0	$+0.75$	0.0	$+0.77$	0.0
	ν^{r+s}	0.0	$+1.0$	0.0	$+0.715$	0.0	0.0
FD2	ν^{norm}	$+0.75$	0.0	$+1.0$	0.0	$+0.78$	0.0
	ν^{r+s}	0.0	$+0.715$	0.0	$+1.0$	0.0	$+0.998$
ND	ν^{norm}	$+0.77$	0.0	$+0.78$	0.0	$+1.0$	0.0
	ν^{r+s}	0.0	0.0	0.0	$+0.998$	0.0	$+1.0$

Table 6.3: Overview of the input model parameter correlations (Pearson product moment correlation) as derived in chapter 5 and detailed in section 6.2. All correlations between the parameters of table 6.2 which are not listed, are equal to zero.

unconstrained in the analysis. As one can see in figure 6.4, the precision on the oscillation amplitude $\sin^2(2\theta_{13})$ always profits from extending the analysis energy window further into the background dominated high energy range: It is monotonously falling as function of the upper energy window edge. In fact, a particular strong suppression of the uncertainty on $\sin^2(2\theta_{13})$ is achieved above 8 MeV when the uncertainty on the β-n isotope background rates is suppressed. This already shows a strong correlation between the oscillation amplitude and the two β-n isotope background rates in the ND and the FDs. This correlation will explicitly be shown later.

Some of the input model parameters for signal and background contributions are considered correlated across the four datasets. All non-zero correlations are listed in table 6.3. In addition, the single far detector (FD-I) datasets during the reactor-on (FD1) and the reactor-off (FD1off) phases are considered fully correlated and identical with respect to their background rates b^{rate}_{LiHe}, b^{rate}_{corr}, b^{rate}_{acc} and shapes b^{shape}_{LiHe}, b^{shape}_{corr}, b^{shape}_{acc} as well as their detection efficiency and MC normalisation ν^{norm}, respectively. Several other parameters are fully correlated and have identical values, as well. Those parameters are:

- the shape parameters b^{shape}_{LiHe} of the β-n isotopes across all datasets
- the rate parameters b^{rate}_{LiHe} of the β-n isotopes across all far detector datasets
- the rate parameters b^{rate}_{corr} of the correlated background across all far detector datasets
- all parameters common across the FD1 and FD1off datasets as listed above.

The identity of the FD1 and FD1off parameters is justified by the fact that the reactor-off data was recorded during two time periods of 1 and 7 days in-between the FD1 reactor-on periods (cf. figure 3.2a at day 193 and around day 415). During those time periods, the far detector has not undergone any changes. The identity of the FD1 and FD2 background rates b^{rate}_{LiHe} for β-n isotopes and correlated backgrounds b^{rate}_{corr} is assumed because the relevant parameters as laboratory overburden, the rock geology and detector geometry are identical between the two data taking phases. Since the near laboratory has much less overburden and the topology of the overburden is different, the rates for β-n isotopes b^{rate}_{LiHe} and correlated backgrounds b^{rate}_{corr} are assumed fully uncorrelated between detectors. The shape parameters for β-n isotopes b^{shape}_{LiHe} are in turn considered fully correlated across all datasets as those shape uncertainties have been determined by a common sample from all datasets (cf. section 5.4). The accidental background rate b^{rate}_{acc} and shape b^{shape}_{acc} is considered fully uncorrelated across all datasets as those backgrounds are mainly caused by radioactive contaminations inside each detector at low energies. Since the readout at low energies has been altered between FD1 and FD2, even those samples have been conservatively considered fully uncorrelated with respect to the accidental background parameters.

Since also the electronics have been significantly altered between FD1 and FD2, no correlations have been assumed between the energy scale parameters e_ξ, $\xi \in \{0, 1, 2\}$, which are including electronic responses. This assumption is also applied to the ND. Assuming no correlation for this is a conservative approach, as some properties like the scintillator are identical across FD1, FD2 and ND. However, this could not be evaluated sufficiently at the current stage of the analysis. More precise results are expected for the upcoming journal publication in winter 2016/2017.

Nevertheless, correlations in the detection efficiency and veto inefficiencies mainly due to identical detector design across all detectors could be evaluated between detectors and are

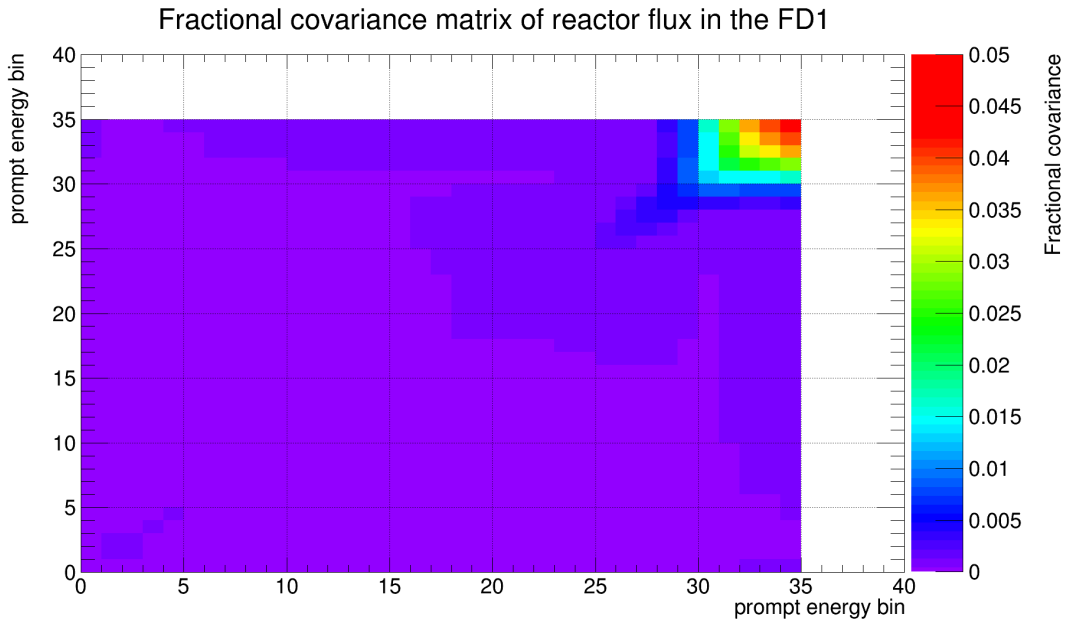

Figure 6.5: Fractionalised covariance matrix of the neutrino signal. Each bin shows the relative flux uncertainties in 40 energy bins (cf. table 6.1) as defined in equation 6.9. The FD1 dataset is shown exemplarily. Other datasets can be found in appendix B. The spectrum shows an overall positive correlation with non-zero values over the full support of the spectrum (bins 0 to 34). For bins with no reactor flux (above bin 34), entries are set to white colour.

accounted for accordingly. Those correlations of the parameters ν^{norm} as given in section 5.8 are summarised in table 6.3.

Since several aspects of the reactor flux prediction are correlated for all detectors (cf. table 5.4), all reactor flux parameters ν^{r+s} are considered correlated between all datasets. The very strong correlation between FD2 and ND is caused by the strong suppression of uncorrelated errors due to almost simultaneous running times (cf. figures 3.2b and 3.2c) and the approximate isoflux-condition between the two detectors. This isoflux-condition is illustrated in the inset of figure 3.1 (dashed blue line): the two detectors observe almost the same ratio between the neutrino flux from the two reactors. Due to these conditions, relative uncertainties in the thermal power and the reactor fuel burnup are strongly suppressed across the FD2 and ND datasets (cf. table 5.4).

In principle, this suppression is accounted for intrinsically by the oscillation analysis tool when treating the reactors as two distinct neutrino sources. However, the evaluation of the necessary inter-reactor correlations was not fully finished for this analysis such that the two reactors were combined into one effective reactor. As a consequence, the suppression factor had to be inserted a-priori as an additional fixed input number. The suppression factor used in this effective one reactor method was chosen such that it matches the worst suppression factor possible when using two distinct reactors [105]. By this, the reactors are effectively assumed to have an inter-reactor correlation in such a way that they give the worst possible precision on the oscillation amplitude $\sin^2(2\theta_{13})$. This extremely conservative treatment will be improved for the upcoming journal publication in winter 2016/2017.

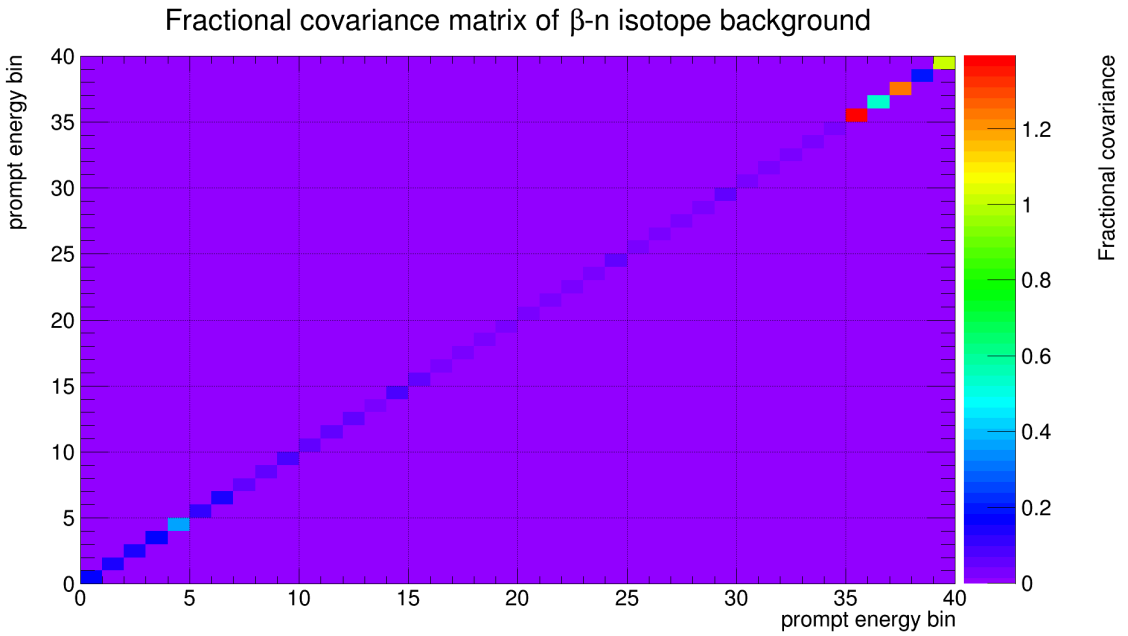

(a)

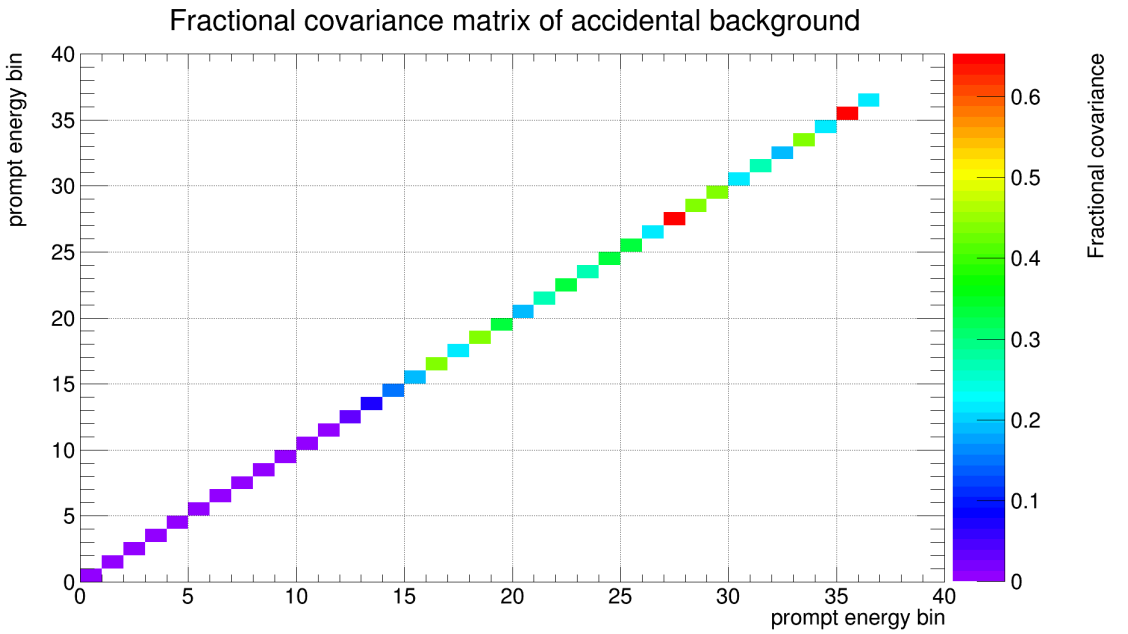

(b)

Figure 6.6: Fractionalised covariance matrices of backgrounds. Relative uncertainties in 40 energy bins (cf. table 6.1) are displayed as defined in equation 6.9: (a) β-n decay isotopes background, (b) accidental background. The β-n decay isotope background matrix shows an overall positive small correlation across all energy bins, while the accidental background matrix is diagonal. Bins equal to zero are depicted in white. In figure (b), bins with no background flux (above bin 36), are set to white colour, as well.

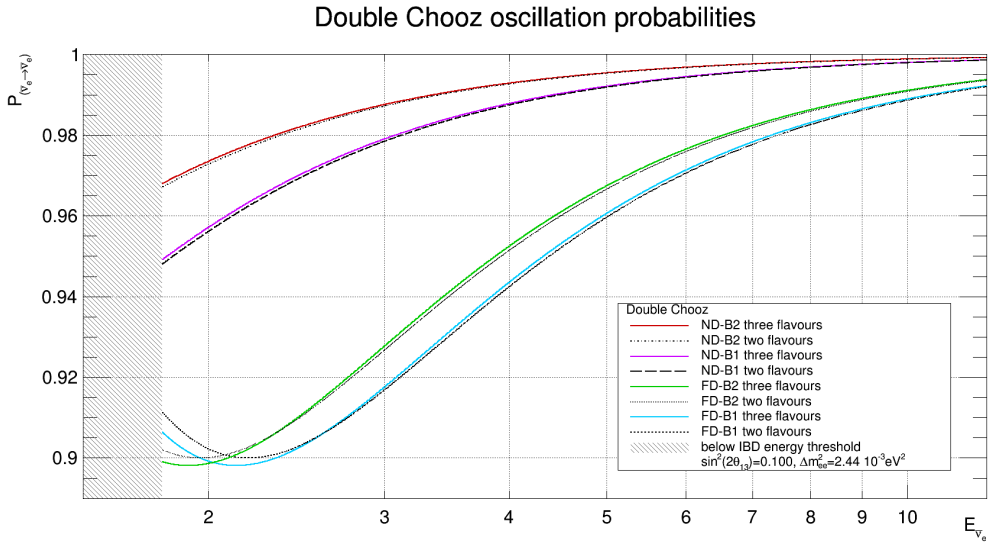

Figure 6.7: Oscillation model derived by the GLoBES programme [107; 108] as used in the oscillation analysis. The two flavour model used by the χ^2 based analysis is shown for comparison. Oscillation parameters not listed are those in table 2.1 as well as $\rho = 2.81 \frac{g}{cm^3}$ [45].

In addition to the per-dataset parameters, two global parameters enter the oscillation analysis model. Those are the oscillation parameters $\sin^2(2\theta_{13})$ and Δm^2_{ee} as introduced in chapter 2. The value for $\Delta m^2_{ee} = (2.44 \pm 0.09) \cdot 10^{-3}\text{eV}^2$ is taken from [36] using the conversion method proposed in [106]. The effect of neutrino oscillations on the IBD-signal prediction is modelled by exploiting a full three flavour neutrino oscillation scenario including interactions of neutrinos with matter. The differential equations for the three flavour model are solved by the GLoBES programme [107; 108]. Matter density and oscillation baselines have been determined by dedicated geological and geodesic surveys [41; 45]. Figure 6.7 shows the three flavour model for the Double Chooz setup in comparison to the two flavour model used in the χ^2 based analysis. As visible, the difference between the two models is non-negligible for the far detector baseline (long baseline) at small energies. This corresponds to the high $\frac{L}{E}$ range in figure 2.1 where the solar neutrino oscillations begin to emerge for the first time. Solar oscillations are not included into the approximative two flavour model. In terms of neutrino mass hierarchy, the input model assumes the normal neutrino mass hierarchy (cf. figure 2.4), i.e. a small absolute value of Δm^2_{32} (cf. table 2.1) resulting in a slightly faster oscillation (cf. equation 2.12) with the first oscillation minimum at shorter distance than for the inverted mass hierarchy (cf. figure 2.2).

All parameters, with exception of the oscillation parameter $\sin^2(2\theta_{13})$ and the β-n isotope rates b^{rate}_{LiHe}, are treated as constrained nuisance parameters in the oscillation analysis. The applied pull terms are given by the uncertainties as listed in table 6.2. The unconstrained treatment of the β-n isotope rates is caused by a $1.3\,\sigma$ disagreement between the input rates and the best-fit rates during previous oscillation analyses with the χ^2 based approach [10] on the one hand and the ability of the oscillation analysis to constrain the rates itself (cf. figure 6.4) on the other hand. Moreover, some difficulties to purify the β-n isotope background spectrum used in the input model makes an unconstrained rate treatment preferable [88]. By

using the β-n isotope rates as unconstrained parameters, a possible bias in the fit result due to a bias in the a-priori rate determination is omitted.

For the treatment of the statistical uncertainties, a Poissonian distribution of events is assumed in each single bin of the analysis. Although this treatment does not impose the need for combining the low statistic bins at high prompt energies (cf. e.g. figure 6.2b), the energy binning as detailed in table 6.1 is kept from the χ^2 based analysis, because all input spectra and bin-to-bin correlations are provided according to this binning scheme.

6.3 Implementation of the Algorithm

The model described in section 6.2 can be summarised in the following likelihood function:

$$
\begin{aligned}
-2\ln(\mathcal{L}) = & \sum_{d\in\{FD1,FD2,ND\}} \Bigg[-2\cdot\sum_{i=1}^{40} \Big\{ (n_i^{meas})_d \cdot \ln\Big[\Big((R_i^{\bar{\nu}_e})_d + (R_i^{bkgrd})_d\Big)\cdot(t_{On}^{live})_d\Big] \\
& - \Big[\Big((R_i^{\bar{\nu}_e})_d + (R_i^{bkgrd})_d\Big)\cdot(t_{On}^{live})_d\Big]\Big\} \\
& + \left(\frac{(b_{acc}^{rate})_d - (b_{acc}^{rate})_d^{CV}}{\sigma_{(b_{acc}^{rate})_d}}\right)^2 + \sum_{k=1}^{40}\left(\frac{(b_{acc}^{shape})_{d,k} - 0}{1}\right)^2 \\
& + \begin{pmatrix} (e_0)_d - (e_0)_d^{CV} \\ (e_1)_d - (e_1)_d^{CV} \\ (e_2)_d - (e_2)_d^{CV} \end{pmatrix}^{\mathrm{T}} \times \left(COV\left[\begin{pmatrix} (e_0)_d \\ (e_1)_d \\ (e_2)_d \end{pmatrix}\right]\right)^{-1} \times \begin{pmatrix} (e_0)_d - (e_0)_d^{CV} \\ (e_1)_d - (e_1)_d^{CV} \\ (e_2)_d - (e_2)_d^{CV} \end{pmatrix} \\
& + \sum_{m\in\{FD,ND\}} \left[\left(\frac{(b_{corr}^{rate})_m - (b_{corr}^{rate})_m^{CV}}{\sigma_{(b_{corr}^{rate})_m}}\right)^2\right] + \sum_{l=1}^{40}\left(\frac{(b_{LiHe}^{shape})_l - 0}{1}\right)^2 \\
& + \left(\frac{\Delta m^2_{ee} - (\Delta m^2_{ee})^{CV}}{\sigma_{\Delta m^2_{ee}}}\right)^2 + \left(\frac{(\nu_{Off}^{rate})_{FD1} - (\nu_{Off}^{rate})_{FD1}^{CV}}{\sigma_{(\nu_{Off}^{rate})_{FD1}}}\right)^2 \\
& + \left(\frac{\nu^{norm} - 0}{1}\right)^2 + \sum_{j=1}^{80}\left(\frac{(\nu^{r+s})_j - 0}{1}\right)^2 \\
& + \sum_{c\in\{FarFar,NearFar\}} \left[\left(\frac{(\nu_{split}^{norm})_c - 0}{1}\right)^2 + \left(\frac{(\nu_{split}^{r+s})_c - 0}{1}\right)^2\right] \\
& - 2\cdot\Big\{(n_{Off}^{meas})_{FD1}\cdot\ln\Big[\Big((R_{Off}^{\bar{\nu}_e})_{FD1} + (R^{bkgrd})_{FD1}\Big)\cdot(t_{Off}^{live})_{FD1}\Big] \\
& - \Big[((R_{Off}^{\bar{\nu}_e})_{FD1} + (R^{bkgrd})_{FD1})\cdot(t_{Off}^{live})_{FD1}\Big]\Big\}
\end{aligned}
\tag{6.6}
$$

In this equation, i, k, l denote the 40 energy bins as listed in table 6.1 and j denotes the 80 energy bins obtained when dividing the energy range between 0.0 MeV and 20.0 MeV in equidistant bins. The index d denotes the three datasets in the case where all three datasets are handled uncorrelated. The index m denotes the datasets in the case of identical parameters across the far detectors. The index c represents the two considered correlations between the two detector phase datasets ND and FD2 on the one hand and the far laboratory datasets FD1 and FD2 on the other hand.

Using this index scheme in equation 6.6, the measured number of IBD candidates in each detector and energy bin is given by $(n_i^{meas})_d$. It is compared with the expected number of IBD candidates using a Poissonian distribution function in each bin. The expected number of events in each bin is given by the product of the lifetime of the dataset $(t_{On}^{live})_d$ and the sum of the IBD-signal event rate $(R_i^{\bar{\nu}_e})_d$ and the background event rate $(R_i^{bkgrd})_d$. This is done likewise for the reactor off dataset FD1off as visible in the last lines of equation 6.6.

The signal rates

$$\begin{aligned}(R_i^{\bar{\nu}_e})_d := (R_i^{\bar{\nu}_e})_d \left(\nu^{norm}, (\nu_{split}^{norm})_c, (\nu^{r+s})_j, (\nu_{split}^{r+s})_c, (e_0)_d, (e_1)_d, (e_2)_d, \sin^2(2\theta_{13}), \Delta m_{ee}^2\right), \\ (d,c) \in \{(FD1, FarFar), (FD2, FarFar), (FD2, NearFar), (ND, NearFar)\}, \\ 1 \leq i \leq 40, \quad 1 \leq j \leq 80 \end{aligned} \tag{6.7}$$

and background rates

$$\begin{aligned}(R_i^{bkgrd})_d := (R_i^{bkgrd})_d \left((b_{acc}^{rate})_d, (b_{acc}^{shape})_{d,i}, (b_{corr}^{rate})_m, (b_{LiHe}^{rate})_m, (b_{LiHe}^{shape})_i\right), \\ (d,m) \in \{(FD1, FD), (FD2, FD), (ND, ND)\}, \quad 1 \leq i \leq 40 \end{aligned} \tag{6.8}$$

in each bin and dataset are dependent on many additional model parameters. Those parameters, as given in equations 6.7 and 6.8, are also included as nuisance parameters in the likelihood function shown in equation 6.6 with exception of the unconstrained β-n isotope rates $(b_{LiHe}^{rate})_m$. A normal distributed prior is assumed for each nuisance parameter. For the energy scale parameters e_0, e_1 and e_2 a multidimensional normal distribution is assumed using their covariance matrix explicitly in the likelihood function as shown in equation 6.6. There, one can also see that a one-dimensional normal distribution is assumed for the squared neutrino mass difference Δm_{ee}^2. A one-dimensional normal distribution is also used for all rate parameters $(b_{acc}^{rate})_d$ and $(b_{corr}^{rate})_m$, respectively, in equation 6.6, but with exception of the unconstrained β-n isotope rates $(b_{LiHe}^{rate})_m$. As central values and variances, the best estimates from the dedicated analyses presented in chapter 5 are inserted.

The remaining nuisance parameters like the shape parameters $(b_{acc}^{shape})_{d,i}$ and $(b_{LiHe}^{shape})_i$ as well as the detection efficiency correction ν^{norm} are treated as standard normal distributed variables. The central values and uncertainties of the systematic effects connected to those parameters are included implicitly in the oscillation analysis. For the case of the shape parameters, this is done by transforming the initially uncorrelated univariate standard normal distributed shape parameters into bin-to-bin correlated multivariate normal distributed parameters. For this purpose, an energy spectrum covariance matrix is generated for each input spectrum. The matrix takes into account the statistical uncertainties of the measured spectrum as well as systematic uncertainties in the spectra determination. Details on the procedure can be found in reference [109]. All those uncertainties are then considered as systematic uncertainties in the oscillation analysis regardless of their nature in the dedicated input analyses. The covariance matrices $M_{s,t}^{input}$ are thus fractionalised by the bin contents S_s^{input} in each of the corresponding bins $1 \leq s,t \leq 40$ of the original spectrum:

$$M_{s,t}^{frac} = \frac{M_{s,t}^{input}}{S_s^{input} \cdot S_t^{input}} \tag{6.9}$$

This means that the relative errors, i.e. the fractionalised systematic errors per bin, are calculated instead of dividing the covariance matrix by the variance in each bin, which yields the

correlation matrix, i.e. the fractionalised statistical errors. The fractionalised background covariance matrices are depicted in figure 6.6. During the oscillation analysis, the fractionalised covariance matrix is not used directly, but a modified covariance matrix $M_{s,t} = M_{s,t}(b_{rate})$ is used for each background type. The modified matrix is dependent on the rate of the corresponding background b_{rate}. The modified matrix is calculated as

$$M_{s,t} = M_{s,t}^{frac} \cdot S_s \cdot S_t \tag{6.10}$$

in each energy bin $1 \leq s, t \leq 40$. This step corresponds to defractionalising the fractionalised matrix $M_{s,t}^{frac}$ using the rate-scaled background spectrum

$$S_s := S_s^{input} \cdot \frac{b_{rate} \cdot t^{live}}{\sum_{u=1}^{40} S_u^{input}}, \quad 1 \leq s \leq 40. \tag{6.11}$$

Using this method, the relative errors including correlated errors are effectively scaled to the new background rate. The now defractionalised covariance matrix is then used to generate a 40-dimensional multivariate normal distribution $\vec{b}_{shape}^{corr}$ out of the 40 univariate standard normal distributions $\vec{b}_{shape}$. This will be detailed in the next paragraph. The so generated multivariate distribution then models correctly the shape correction with respect to the shape uncertainties of the respective background spectrum. The shape-corrected background spectrum S_s^{final} can thus be derived as

$$S_s^{final} = S_s + (\vec{b}_{shape}^{corr})_s, \quad 1 \leq s \leq 40. \tag{6.12}$$

To generate the multivariate distribution

$$\begin{aligned} \vec{b}_{shape}^{corr} :=& [(b_{shape}^{corr})_1, ..., (b_{shape}^{corr})_{40}]^{\mathrm{T}} \\ =& [(b_{shape}^{corr})_1 \left(\vec{b}_{shape}, b_{rate}\right), ..., (b_{shape}^{corr})_{40} \left(\vec{b}_{shape}, b_{rate}\right)]^{\mathrm{T}} \end{aligned} \tag{6.13}$$

the defractionalised covariance matrix $M = M(b_{rate})$ is decomposed into Choleski's triangle matrix $L = L(M(b_{rate}))$ such that

$$M = L \cdot L^{\mathrm{T}}. \tag{6.14}$$

Such decomposition is almost always[1] possible as proven in [110, p. 85]. The triangle matrix is then vector-matrix-multiplied with the vector $\vec{b}_{shape} := [(b_{shape})_1, ..., (b_{shape})_{40}]^{\mathrm{T}}$ built from the 40 univariate standard normal distributed variables:

$$\vec{b}_{shape}^{corr} = L \cdot \vec{b}_{shape}. \tag{6.15}$$

It can be proven that the vector $\vec{b}_{shape}^{corr}$ is indeed normal distributed with covariance matrix M, i.e. it can be proven that $\mathbb{E}[(\vec{b}_{shape}^{corr} - \mathbb{E}[\vec{b}_{shape}^{corr}]) \cdot (\vec{b}_{shape}^{corr} - \mathbb{E}[\vec{b}_{shape}^{corr}])^{\mathrm{T}}] = M$ holds:

$$\begin{aligned} & \mathbb{E}\left[(\vec{b}_{shape}^{corr} - \mathbb{E}[\vec{b}_{shape}^{corr}]) \cdot (\vec{b}_{shape}^{corr} - \mathbb{E}[\vec{b}_{shape}^{corr}])^{\mathrm{T}}\right] \\ =& \mathbb{E}\left[(L \cdot \vec{b}_{shape} - \mathbb{E}[L \cdot \vec{b}_{shape}]) \cdot (L \cdot \vec{b}_{shape} - \mathbb{E}[L \cdot \vec{b}_{shape}])^{\mathrm{T}}\right] \\ =& \mathbb{E}\left[(L \cdot \vec{b}_{shape} - L \cdot \mathbb{E}[\vec{b}_{shape}]) \cdot (L \cdot \vec{b}_{shape} - L \cdot \mathbb{E}[\vec{b}_{shape}])^{\mathrm{T}}\right] \end{aligned} \tag{6.16}$$

[1] The set of covariance matrices where the claim does not hold has Lebesgue-measure equal to zero.

$$
\begin{aligned}
&= \mathbb{E}\left[(L \cdot (\vec{b}_{shape} - \mathbb{E}[\vec{b}_{shape}])) \cdot (L \cdot (\vec{b}_{shape} - \mathbb{E}[\vec{b}_{shape}]))^{\mathrm{T}}\right] \\
&= \mathbb{E}\left[L \cdot (\vec{b}_{shape} - \mathbb{E}[\vec{b}_{shape}]) \cdot (\vec{b}_{shape} - \mathbb{E}[\vec{b}_{shape}])^{\mathrm{T}} \cdot L^{\mathrm{T}}\right] \\
&= L \cdot \mathbb{E}\left[(\vec{b}_{shape} - \mathbb{E}[\vec{b}_{shape}]) \cdot (\vec{b}_{shape} - \mathbb{E}[\vec{b}_{shape}])^{\mathrm{T}}\right] \cdot L^{\mathrm{T}} \\
&= L \cdot \mathbb{1}_{40} \cdot L^{\mathrm{T}} = L \cdot L^{\mathrm{T}} = M
\end{aligned}
$$

The vector $\vec{b}_{shape}^{corr}$, which now accommodates the correlated shape correction is then added energy bin-wise to the rate-scaled background spectrum S_s as shown in equation 6.12 such that the rate-scaled and shape-corrected background spectrum S_s^{final} is derived.

Prior to the described method, numerical artefacts in the defractionalised covariance matrix have to be patched in order to have a proper covariance matrix, i.e. a symmetric positive-definite matrix. First, the matrix is symmetrised by replacing entries that are not identical, although they should be, by their arithmetic mean. Secondly, the now symmetric matrix is spectral decomposed, negative or proper complex eigenvalues are exchanged by slightly positive real eigenvalues and the matrix is then reassembled from the new patched spectral decomposition. The negative eigenvalues are typically in the order of $\mathcal{O}(-10^{-12})$ while the patched eigenvalues are typically in the order of $\mathcal{O}(+10^{-12})$. About 5 % of the eigenvalues have to be patched in this way. The corrections are tiny compared to the other eigenvalues which are in the order of $\mathcal{O}(10^{-5})$ and larger. Likewise, the resulting modifications in the covariance matrix bins are negligible as they are below 10^{-7} %. Thus, a quick and simply replacement of eigenvalues is employed instead of a more sophisticated but time consuming algorithm that yields the closest covariance matrix with respect to the Frobenius norm as proposed in [111].

The entire procedure is performed likewise for the β-n isotope background and the accidental background to model their spectral uncertainties, but not for the correlated background, which is considered flat over the entire energy range with no shape uncertainty (cf. section 5.5). The three final background spectra are then summed bin-wise to give the total background contribution $R_i^{bkgrd} \cdot t^{live}$ used in equation 6.6.

For the flux uncertainty on the IBD-signal prediction, a similar method is applied to include the uncertainties and their correlations given in the reactor flux covariance matrices (cf. figure 6.5) into the oscillation analysis. The corresponding parameters in this case are the uncorrelated and univariate standard normal distributed parameters $(\nu^{r+s})_j$, $1 \leq j \leq 80$. The number of shape parameters differs for the case of the neutrino signal because a different binning scheme is used. A number of 80 equidistant bins of 0.25 MeV width are used over the full energy range from 0.00 MeV up to 20.00 MeV. This is possible, because the reactor MC spectrum, in contrast to the background spectra, is provided unbinned. The bin width of 0.25 MeV is chosen, because it is the greatest common divisor of all oscillation analysis bin widths as given in table 6.1. The lower edge of the energy range of 0.00 MeV has been chosen to be below the lower edge of the analysis energy window of 0.50 MeV (cf. table 6.1) since the inclusion of the low energy bins ensures a better behaviour of the energy scale correction, as described later.

Prior to the flux correction via the above explained mechanism, the unoscillated IBD-signal prediction is transformed into an oscillated IBD-prediction. To ensure high accuracy, this transformation is applied MC event-wise. Firstly, for each MC event k, its true neutrino energy $E_k^{\bar{\nu}_e}$ and its true baseline L_k is extracted. The baseline is accounting for the exact vertex within the reactor assembly where the neutrino was created in the reactor simulation

and for the exact vertex within the detector where the IBD process took place in the detector simulation. From the true energy and true baseline, an individual survival probability $P_{\bar{\nu}_e \to \bar{\nu}_e}$ is derived for each MC neutrino according to the oscillation model described in section 6.2. Secondly, the true visible prompt energy $(E^p_{vis})_k$ of each MC neutrino is extracted from the simulation. Each MC neutrino is then added to the equidistantly binned oscillated spectrum taking into account its true visible prompt energy and weighting it with its individual weighting factor. Those weighting factors are the individual survival probabilities $P_{\bar{\nu}_e \to \bar{\nu}_e}$ and the MC statistics reduction factor w_{MC}. For the far detector datasets, the reduction factor is 0.01 and for the near detector dataset the reduction factor is 0.1. The reduction factors account for the fact that the MC spectra have been generated with 100 times and 10 times statistic, respectively. This has been done to achieve a sufficiently smooth spectrum with respect to the underlying binning of 0.25 MeV. The bin content n_i^{ini} in each prompt energy bin i can then be represented as

$$n_i^{ini} := \sum_{k=1}^{N^{MC}_{\bar{\nu}_e}} \left[\mathbb{1}_{[E_{i-1}^{ini}; E_i^{ini})} \left((E^p_{vis})_k \right) \cdot w_{MC} \cdot P_{\bar{\nu}_e \to \bar{\nu}_e} \left(E_k^{\bar{\nu}_e}; L_k; \sin^2(2\theta_{13}); \Delta m^2_{ee} \right) \right], \quad 1 \leq i \leq 80 \tag{6.17}$$

using the notation introduced above and with E_i^{ini} denoting the lower edge of the ith energy bin.

The reason why a time-intensive event-wise transformation is unavoidable in order to achieve an oscillated spectrum with high accuracy is given in figure 6.8. As shown in figure 6.8a, the neutrino simulation used to extract $(E^p_{vis})_k$ in equation 6.17 shows a non-negligible amount of MC neutrino events outside the main cluster. For those events, more than the expected energy for the generation of neutron and positron masses (cf. section 3.5) is lost. This is caused by quenching effects and other imperfections in the light conversion of the detector. A large amount of those imperfect conversions is caused by annihilations in the acrylics. This causes the loss of light from the kinetic energy and some annihilation light. In figure 6.8a, the cluster of events just below 1 MeV prompt energy consists of those events. As a general consequence, the low end of the prompt energy spectrum shown in figure 3.7a contains on average high energy neutrino events as depicted in figure 6.8b.

After the IBD-signal prediction spectrum has been transformed into an oscillated spectrum and has been flux corrected, the energy correction is applied to the MC spectrum to match it with the measured spectrum and the background spectra in visible prompt energy. The energy correction function is given as

$$E_i^{ini} = e_2 \cdot (E_i^{fin})^2 + e_1 \cdot E_i^{fin} + e_0, \quad 1 \leq i \leq 80 \tag{6.18}$$

where E_i^{ini} stands for the initial prompt energy prior to the energy correction, E_i^{fin} represents the prompt energy after the energy correction and the e_γ with $0 \leq \gamma \leq 2$ are the nuisance parameters from equation 6.6. It has been found that the likelihood function given in equation 6.6 does not suffice the required regularity conditions for the minimisation with respect to the energy scale parameters if the energy correction is applied direct to each individual MC neutrino event. This is caused by the situation that the number of MC neutrino events, despite their already high statistic, is yet not high enough. As a consequence, it is the case that, with respect to the machine precision, infinitesimal changes in the energy parameters do not necessarily cause any MC prompt event to be shifted into a new energy bin. As a result, the likelihood function is a discontinuous step-function of the energy scale parameters.

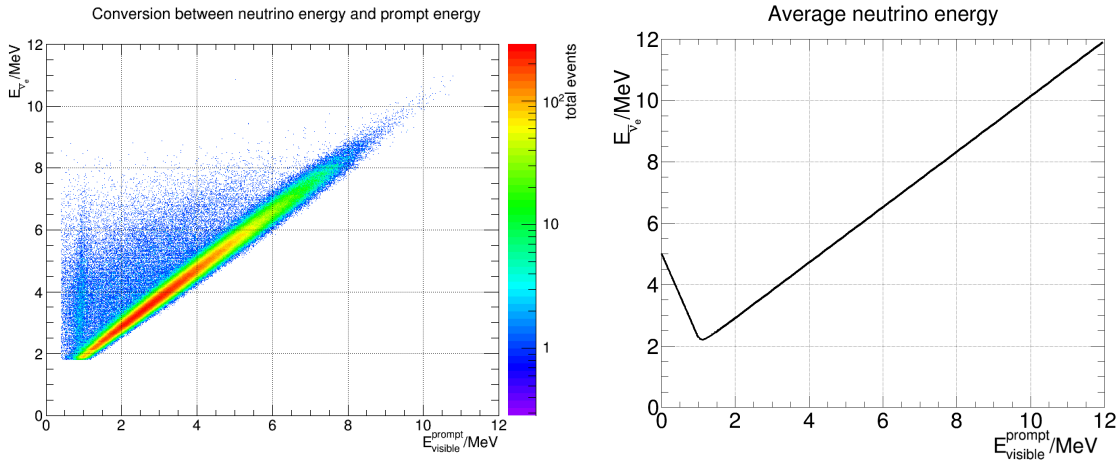

(a) (b)

Figure 6.8: Neutrino energy conversion derived from the detector simulation. The (a) event-wise conversion between neutrino true energy and visible prompt energy and the (b) average conversion between those energies is shown. For low visible prompt energies, the events off the main cluster in figure (a) are dominant leading to the turning point in figure (b).

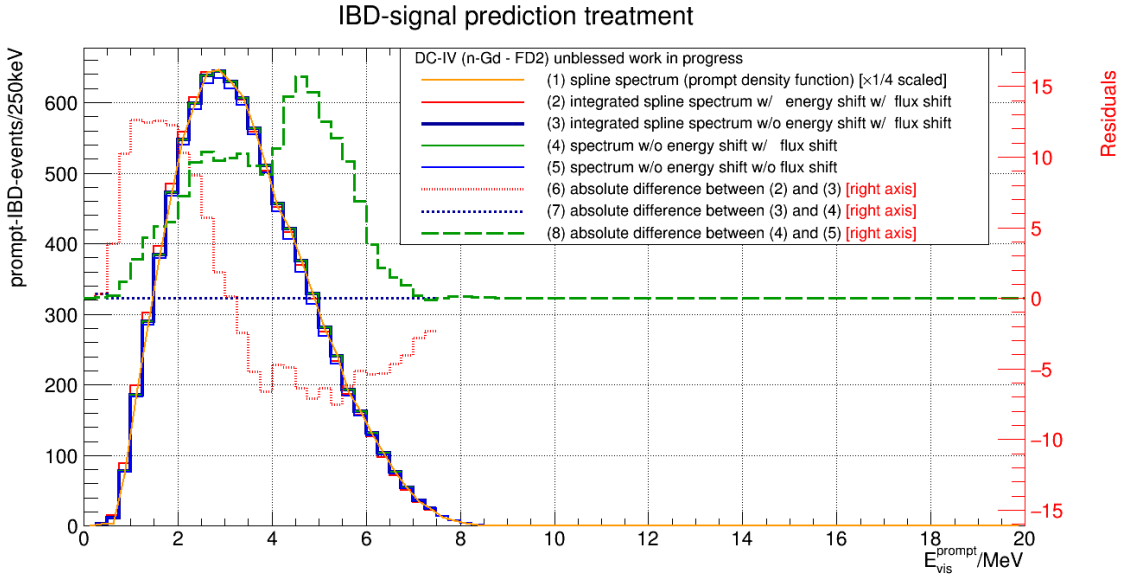

Figure 6.9: Treatment of IBD-signal prediction spectrum. Details can be found in the text.

The binned oscillated and flux-corrected IBD-signal spectrum has thus to be converted into a smooth density function before the energy correction can be applied. It was found that a kernel density estimation is too computational hard to be utilised in the minimisation given the high MC statistic. As a much faster alternative, a spline interpolation has been chosen. A linear spline interpolation has been found to give good results without any oscillatory behaviour of the spline. As a cross-check, a cubic spline interpolation has been tested, as

well. It was found to give consistent results as shown later in section 6.5. For the spline function $\zeta(E) = \zeta(E|\{n_i^{int}; 1 \leq i \leq 80\})$ a number of 80 knots has been chosen. The spline knots are located at the centres of the equidistant uncorrected prompt energy bins. The spline function is fitted to the oscillated and flux-corrected spectrum using a least-squares method such that the condition

$$\int_{E_{i-1}^{ini}}^{E_i^{ini}} \zeta(E)\,\mathrm{d}E = n_i^{int} \tag{6.19}$$

holds for each bin $1 \leq i \leq 80$ within the sub-permille level. Figure 6.9 shows the result of this interpolation. The spline density function is in the following integrated inside the energy scale corrected new bin edges E_i^{fin}. The result of this integration

$$n_i^{fin} := \int_{E_{i-1}^{fin}}^{E_i^{fin}} \zeta(E)\,\mathrm{d}E \tag{6.20}$$

yields the bin contents n_i^{fin}, $1 \leq i \leq 80$, of the 80 bins of the oscillated, flux-corrected and energy scale corrected IBD-signal prompt energy spectrum (cf. figure 6.9). The n_i^{fin} are then summed to the official binning (cf. table 6.1) if required. The summation is always possible as the equidistant bin width of 0.25 MeV has been chosen as the greatest common divisor of all bin width of the official binning. As a final step, the derived spectrum has to be corrected for differences in the detection efficiency and the veto times. Those corrections are energy independent and denoted by the parameter ν^{norm} in equation 6.6.

Since some corrections are partly uncorrelated across datasets, the parameters $(\nu_{split}^{norm})_c$ and $(\nu_{split}^{r+s})_c$ are introduced. They allow for a splitting of the parameters ν^{norm} and $(\nu^{r+s})_j$, $1 \leq j \leq 80$, within their uncorrelated uncertainties. Those splittings via

$$\nu_{ND}^{norm} = \nu^{norm} - (\nu_{split}^{norm})_{NearFar} \tag{6.21}$$

$$\nu_{FD2}^{norm} = \nu^{norm} + (\nu_{split}^{norm})_{NearFar} \tag{6.22}$$

are allowed for the correlations c between FD2 and ND on the one hand and FD2 and FD1 on the other hand. The parameters $(\nu_{split}^{norm})_c$ and $(\nu_{split}^{r+s})_c$ are included as nuisance parameters in the likelihood function given in equation 6.6 and constrained by the respective uncorrelated errors.

The last remaining parameter in equation 6.6 is the residual neutrino rate $(R_{Off}^{\bar{\nu}_e})_{FD1}$. This parameter describes the expected rate of neutrinos from the inactive reactor cores during a full shutdown of both reactors. A dedicated study to determine this rate and the energy spectrum of residual neutrinos has been performed in [112]. From this study, an average residual neutrino energy of 2.74 MeV is expected. Due to the small contribution of the residual neutrinos in this background-only measurement, all residual neutrinos are considered to have this average energy and no computational hard treatment of a dedicated reactor off MC neutrino spectrum is used. The neutrinos are assumed to originate with equal fraction from both reactors. Their survival probability is calculated assuming the average baseline between each reactor core and the far detector. A reactor flux correction is omitted because the neutrinos are not created in a controlled chain reaction, but in spontaneous decays. Likewise, the energy correction is not applied since the FD1off dataset is a rate-only dataset. The loss of neutrino events due to an energy shift out of the analysis energy window is with less than 10^{-3} % negligible. However, the correction due to detection efficiency and veto times is applied as for the FD1 dataset.

The optimisation of all parameters to find the best fitting model for the recorded data is performed by minimising the function given in equation 6.6. As numerical routine, the Minuit2 programme [113] is used within the ROOT framework [56]. As convergence criterion, an estimated distance to the functional minimum of 10^{-4} is required. The final uncertainties for each parameter are calculated by two approaches. As reference the MINOS routine, which performs a precise scan, is used. As cross-check, a symmetric uncertainty estimate is derived from evaluation of the Hesse-matrix used in the Taylor-expansion of the likelihood function inside the numerical routine.

6.4 Validation of the Algorithm

Prior to the oscillation analysis as presented in section 6.5, a rigorous validation process was performed. Upon passing the validation process, data unblinding for the FD1 and FD1off datasets was granted, which were previously evaluated by the χ^2 based oscillation analysis and published in [10]. Upon passing this real data test, full data unblinding was granted. The validation process was assembled from a series of internal tests followed by a mock data challenge performed with externally provided MC data. After passing the internal tests, the mock data challenge was performed. The absolute performance of the oscillation analyses as well as the relative comparison between this work, the χ^2 based analysis tool and the identically, but independently implemented second χ^2 based analysis tool was monitored and evaluated during all stages.

The first step was the internal validation. For this, the expected accuracy, expected precision and expected no-oscillation hypothesis exclusion limits were evaluated. Additionally, the behaviour of all nuisance parameters was tested. Figure 6.10 shows the outcome of 1000 MC data fits generated at the benchmark point of $\sin^2(2\theta_{13}) = 0.100$ and assuming the input model as presented in section 6.2. Two MC data ensembles were generated for this test. The first ensemble is generated from the input model by allowing only for statistical fluctuations. The second ensemble is generated allowing for statistical and systematic fluctuations. All statistic fluctuations are modelled as Poissonian distributed. All systematics are modelled normal distributed following the input model. For the case of the energy parameters, an explicitly correlated three-dimensional normal distribution is utilised. For the β-n isotope rates, an asymmetric normal distribution is used in the far detector datasets. The central values, uncertainties and parameter correlations are those given in tables 6.2 and 6.3, respectively. From figure 6.10 one can see that the accuracy bias of the oscillation analysis is negligible compared to the expected precision. A mean central value of $\sin^2(2\theta_{13}) = 0.1006 \pm 0.0004$ with a mean uncertainty on $\sin^2(2\theta_{13})$ of $^{+0.0199}_{-0.0198}$ is reached for the statistics-only ensemble. For the systematic and statistical shifts, a mean central value of $\sin^2(2\theta_{13}) = 0.1083 \pm 0.0023$ with a mean uncertainty of $^{+0.0202}_{-0.0201}$ is achieved. Moreover, all nuisance parameters are found to be in agreement with their input model values.

The behaviour of all nuisance parameters is additionally evaluated by performing a profile likelihood scan in $\sin^2(2\theta_{13})$, i.e. the value of $\sin^2(2\theta_{13})$ is fixed to values between 0.0 and 0.2 and a maximum likelihood fit is performed at each point. The value of the likelihood function is then compared against the value of the likelihood function when allowing $\sin^2(2\theta_{13})$ to move freely. For the profile likelihood scan, the input model is assumed as presented in section 6.2, $\sin^2(2\theta_{13}^{true}) = 0.1$ is assumed in the generation of the MC data and no statistical or systematic fluctuations are simulated in the MC data. As visible from figures 6.11 and 6.12, all nuisance

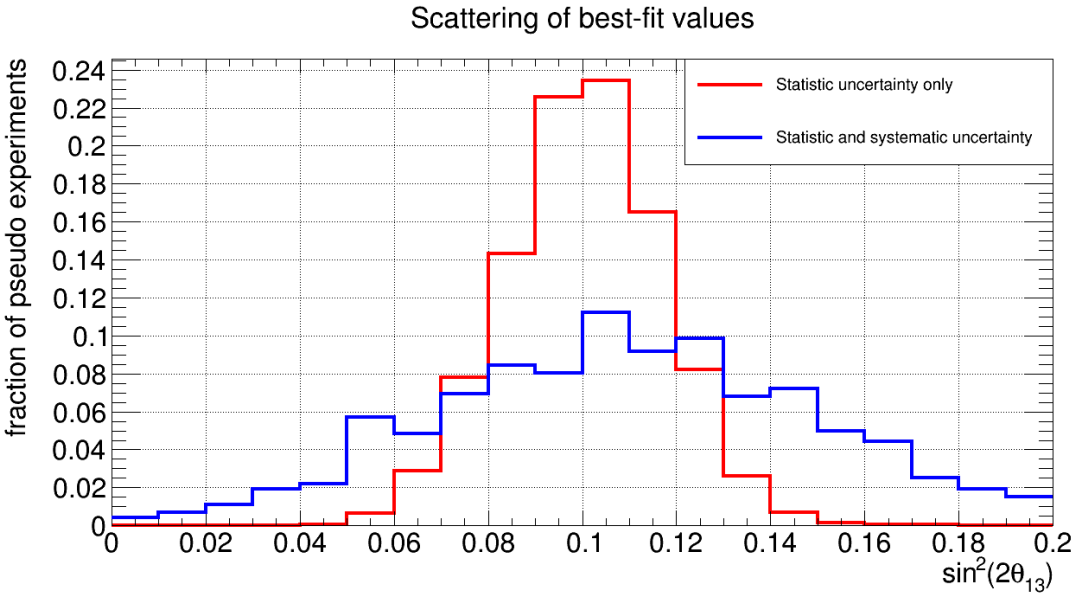

Figure 6.10: Results of the internal accuracy validation. The pdfs of the best-fit values for the oscillation amplitude $\sin^2(2\theta_{13})$ are shown.

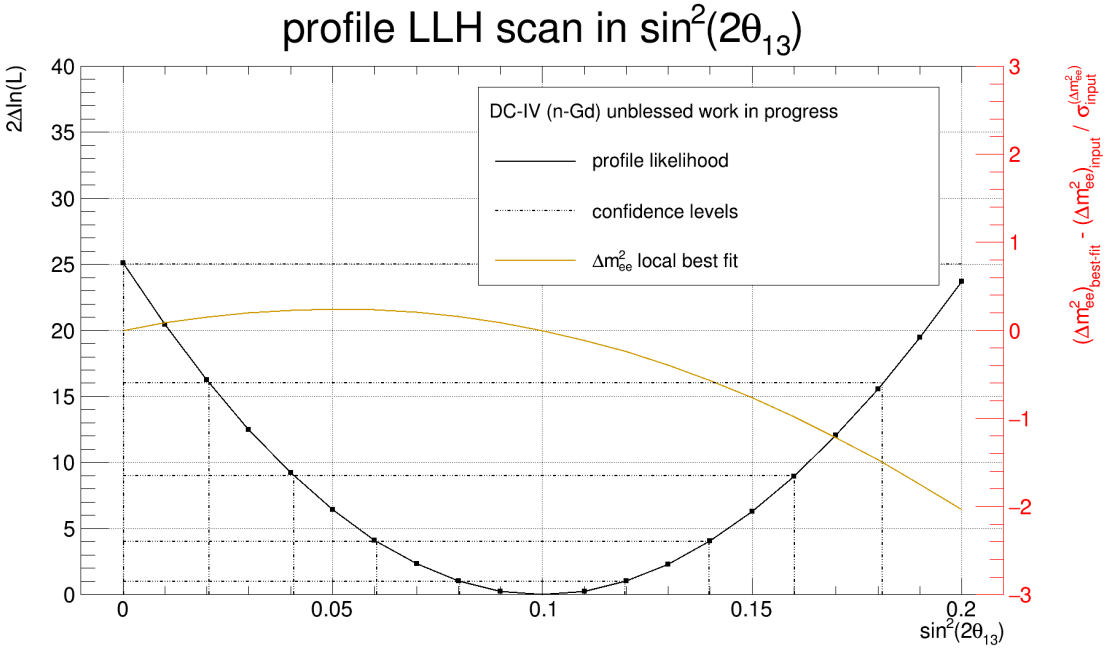

Figure 6.11: Results of a MC data likelihood profile scan assuming $\sin^2(2\theta_{13}^{true}) = 0.1$ as explained in the text. See also figure 6.12.

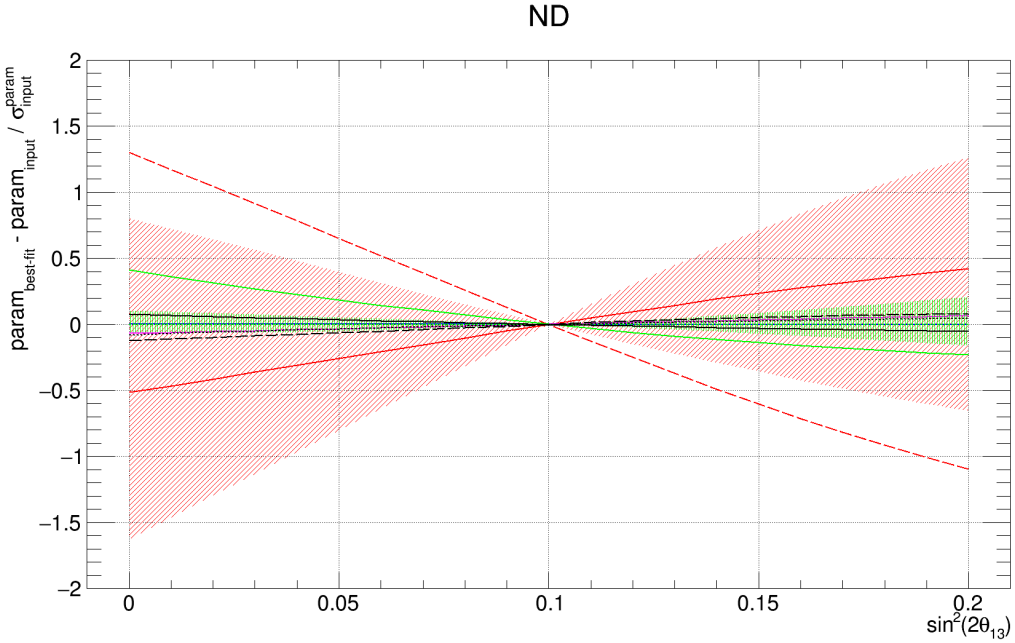
ND
param_best-fit - param_input / σ^param_input
sin²(2θ13)

(a)

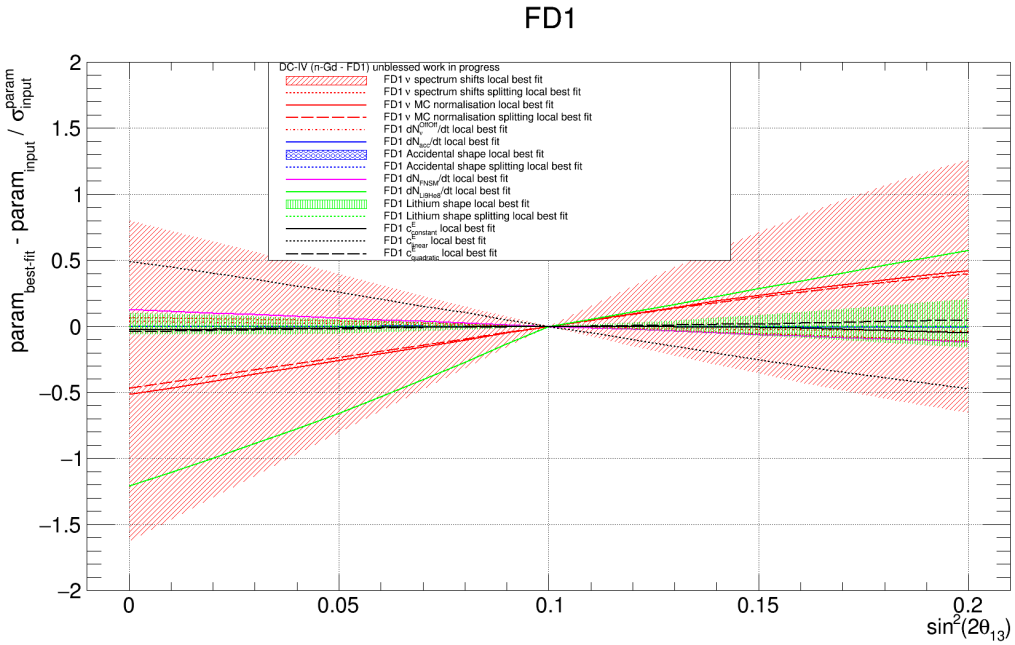
FD1
DC-IV (n-Gd - FD1) unblessed work in progress
FD1 ν spectrum shifts local best fit
FD1 ν spectrum shifts splitting local best fit
FD1 ν MC normalisation local best fit
FD1 ν MC normalisation splitting local best fit
FD1 Accidental shape local best fit
FD1 Accidental shape splitting local best fit
FD1 Lithium shape local best fit
FD1 Lithium shape splitting local best fit
param_best-fit - param_input / σ^param_input
sin²(2θ13)

(b)

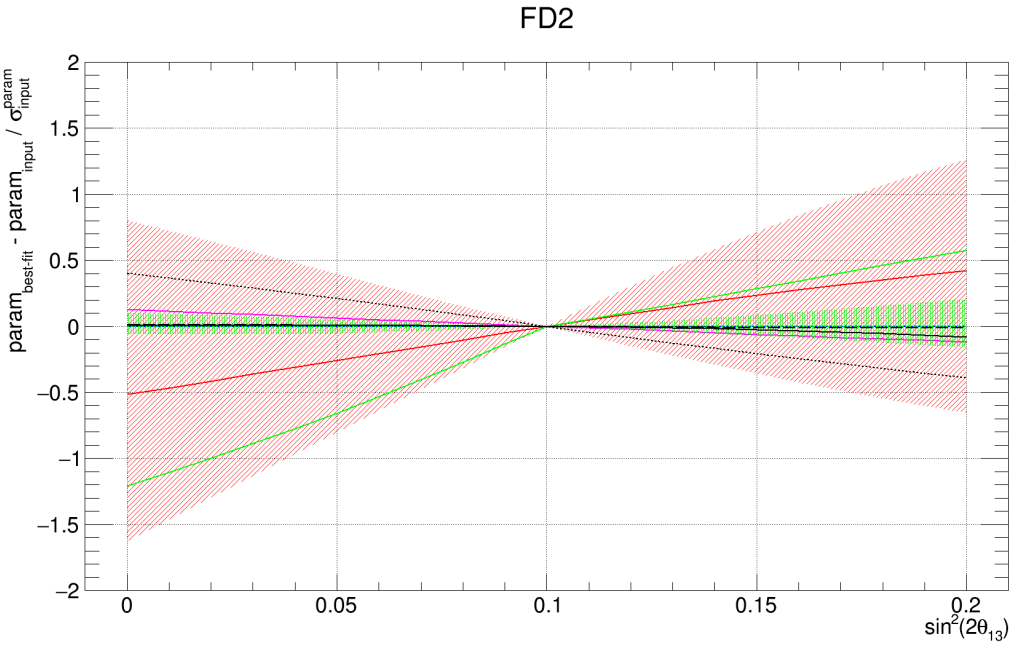

(c)

Figure 6.12: Behaviour of nuisance parameters during a MC data likelihood profile scan presented in figure 6.11. (a) ND, (b) FD1/FD1off, (c) FD2 datasets. Shape parameters have been summarised in shaded bands. The legend in figure (b) applies to all datasets.

$\sin^2(2\theta_{13}) = 0.090$	1st χ^2 based analysis		2nd χ^2 based analysis		this work	
mock dataset	C.V.	uncert.	C.V.	uncert.	C.V.	uncert.
dataset 1	0.110	± 0.018	0.109	± 0.018	0.109	± 0.019
dataset 2	0.115	± 0.018	0.110	± 0.018	0.116	± 0.019
dataset 3	0.093	± 0.019	0.092	± 0.018	0.089	± 0.019
dataset 4	0.080	± 0.018	0.079	± 0.018	0.092	± 0.019
dataset 5	0.076	± 0.018	0.075	± 0.018	0.072	± 0.019
dataset 6	0.112	± 0.018	0.110	± 0.018	0.115	± 0.020
dataset 7	0.083	± 0.019	0.083	± 0.018	0.077	± 0.020
dataset 8	0.071	± 0.018	0.070	± 0.018	0.076	± 0.019
dataset 9	0.092	± 0.018	0.092	± 0.018	0.094	± 0.019
dataset 10	0.054	± 0.019	0.054	± 0.018	0.062	± 0.020
average	0.088	± 0.018	0.087	± 0.018	0.090	± 0.019

Table 6.4: Results of the mock data challenge with nominal statistics for the oscillation amplitude. The results for the **c**entral **v**alue (C.V.) and uncertainty of the two χ^2 based oscillation analysis approaches and of this work are compared [114]. See also figure 6.13 and table 6.5.

parameters show no tension to their input model values, i.e. the oscillation analysis extracts them faithfully with respect to their true input values. Following the explanations given in section 6.1 one can also extract from figure 6.11 that for $\sin^2(2\theta_{13}^{true}) = 0.1$ the no-oscillation hypothesis exclusion is expected to be at 5.0 standard deviations C.L. corresponding to a value of $2\Delta\ln(\mathcal{L}) = 25$. This is in good agreement with the expectations of the χ^2 based oscillation analysis tools [115, p. 5].

Following these internal tests, the validation process using external MC mock data was performed. A total of 10 MC datasets with nominal statistics was provided. Additionally, 10 MC datasets with heavy energy scale bias were processed. Finally, 5 MC datasets with 10-fold nominal statistics were evaluated. Figure 6.13 as well as tables 6.4 and 6.5 show the

FD b_{LiHe}^{rate} =0.97 d^{-1}	1st χ^2 based analysis		2nd χ^2 based analysis		this work	
mock dataset	C.V.	uncert.	C.V.	uncert.	C.V.	uncert.
dataset 1	0.94 d^{-1}	± 0.16 d^{-1}	0.91 d^{-1}	± 0.15 d^{-1}	0.89 d^{-1}	± 0.15 d^{-1}
dataset 2	1.01 d^{-1}	± 0.16 d^{-1}	0.96 d^{-1}	± 0.15 d^{-1}	0.90 d^{-1}	± 0.15 d^{-1}
dataset 3	1.02 d^{-1}	± 0.17 d^{-1}	0.97 d^{-1}	± 0.16 d^{-1}	0.94 d^{-1}	± 0.16 d^{-1}
dataset 4	0.78 d^{-1}	± 0.15 d^{-1}	0.75 d^{-1}	± 0.14 d^{-1}	0.72 d^{-1}	± 0.14 d^{-1}
dataset 5	0.92 d^{-1}	± 0.15 d^{-1}	0.90 d^{-1}	± 0.15 d^{-1}	0.86 d^{-1}	± 0.14 d^{-1}
dataset 6	1.12 d^{-1}	± 0.18 d^{-1}	1.05 d^{-1}	± 0.17 d^{-1}	0.95 d^{-1}	± 0.16 d^{-1}
dataset 7	0.99 d^{-1}	± 0.16 d^{-1}	0.94 d^{-1}	± 0.15 d^{-1}	0.85 d^{-1}	± 0.15 d^{-1}
dataset 8	0.89 d^{-1}	± 0.15 d^{-1}	0.86 d^{-1}	± 0.15 d^{-1}	0.82 d^{-1}	± 0.15 d^{-1}
dataset 9	0.81 d^{-1}	± 0.16 d^{-1}	0.80 d^{-1}	± 0.15 d^{-1}	0.75 d^{-1}	± 0.15 d^{-1}
dataset 10	0.87 d^{-1}	± 0.16 d^{-1}	0.83 d^{-1}	± 0.15 d^{-1}	0.81 d^{-1}	± 0.15 d^{-1}
average	1.01 d^{-1}	± 0.16 d^{-1}	0.90 d^{-1}	± 0.15 d^{-1}	0.85 d^{-1}	± 0.15 d^{-1}

(a)

ND b_{LiHe}^{rate} =5.82 d^{-1}	1st χ^2 based analysis		2nd χ^2 based analysis		this work	
mock dataset	C.V.	uncert.	C.V.	uncert.	C.V.	uncert.
dataset 1	6.72 d^{-1}	± 0.97 d^{-1}	6.57 d^{-1}	± 0.92 d^{-1}	6.37 d^{-1}	± 0.73 d^{-1}
dataset 2	5.21 d^{-1}	± 0.94 d^{-1}	5.04 d^{-1}	± 0.88 d^{-1}	4.76 d^{-1}	± 0.82 d^{-1}
dataset 3	7.65 d^{-1}	± 1.00 d^{-1}	7.35 d^{-1}	± 0.93 d^{-1}	7.28 d^{-1}	± 0.88 d^{-1}
dataset 4	6.31 d^{-1}	± 0.97 d^{-1}	6.21 d^{-1}	± 0.92 d^{-1}	6.12 d^{-1}	± 0.84 d^{-1}
dataset 5	5.52 d^{-1}	± 0.90 d^{-1}	5.43 d^{-1}	± 0.87 d^{-1}	5.27 d^{-1}	± 0.78 d^{-1}
dataset 6	6.05 d^{-1}	± 0.96 d^{-1}	5.75 d^{-1}	± 0.87 d^{-1}	5.31 d^{-1}	± 0.81 d^{-1}
dataset 7	8.03 d^{-1}	± 1.10 d^{-1}	5.55 d^{-1}	± 0.95 d^{-1}	7.40 d^{-1}	± 0.94 d^{-1}
dataset 8	5.18 d^{-1}	± 0.85 d^{-1}	5.17 d^{-1}	± 0.85 d^{-1}	5.03 d^{-1}	± 0.76 d^{-1}
dataset 9	6.84 d^{-1}	± 0.98 d^{-1}	6.68 d^{-1}	± 0.92 d^{-1}	6.87 d^{-1}	± 0.88 d^{-1}
dataset 10	5.94 d^{-1}	± 0.98 d^{-1}	5.68 d^{-1}	± 0.89 d^{-1}	5.56 d^{-1}	± 0.86 d^{-1}
average	6.35 d^{-1}	± 0.97 d^{-1}	6.14 d^{-1}	± 0.90 d^{-1}	6.00 d^{-1}	± 0.83 d^{-1}

(b)

Table 6.5: Results of the mock data challenge with nominal statistics for the β-n isotope rates. The results for the **c**entral **v**alue (C.V.) and uncertainty of the two χ^2 based oscillation analysis approaches and of this work are compared [114]. See also figure 6.13 and table 6.4.

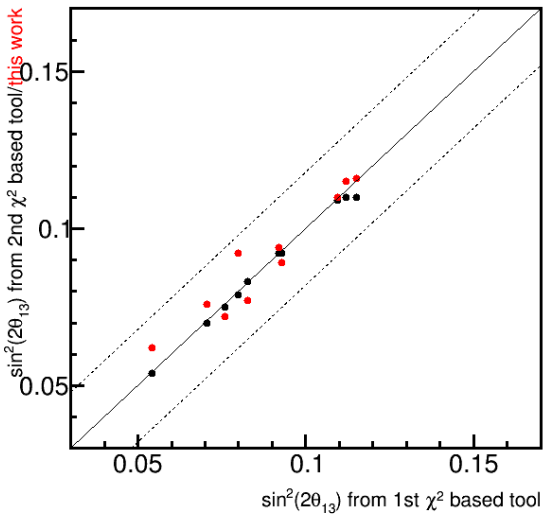

(a)

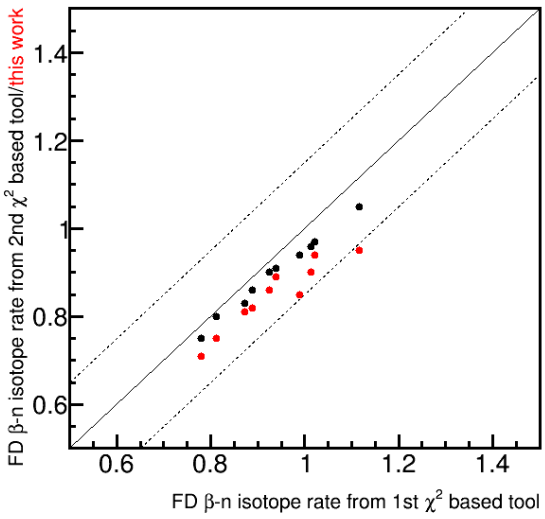

(b)

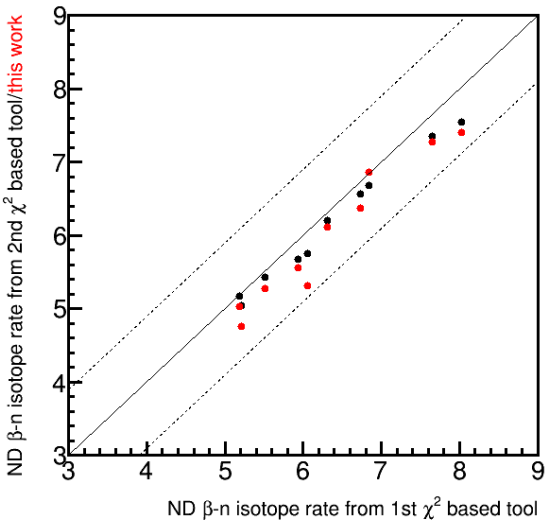

(c)

Figure 6.13: Results of the mock data challenge with nominal statistic. The results of the secondary χ^2 based oscillation analysis approach and of this work are compared to the primary χ^2 based oscillation analysis approach. The dashed lines show the average uncertainty of the primary χ^2 based analysis. (a) $\sin^2(2\theta_{13})$ with true value 0.09 (cf. table 6.4), (b) far detector β-n isotope rate with true value $0.97\,\mathrm{d}^{-1}$ (cf. table 6.5a), (c) near detector β-n isotope rate with true value $5.82\,\mathrm{d}^{-1}$ (cf. table 6.5b). [114]

comparison between the three oscillation analyses, i.e. the two χ^2 based analyses [99; 100; 101] and this work, for the 10 nominal statistics datasets. An overall good agreement between the oscillation analysis approaches can be seen. No systematic bias between the analyses and almost perfect agreement between the two identical χ^2 based approaches is visible for the oscillation amplitude (cf. figure 6.13a). For the β-n isotope rates, a mild systematic discrepancy

1-fold stats, $\sin^2(2\theta_{13}) = 0.090$	1st χ^2 based analysis		this work	
modelled effects	C.V.	uncert.	C.V.	uncert.
only statistics	0.088	± 0.009	0.090	± 0.009
only stat+energy	0.085	± 0.010	0.089	± 0.011
only stat+β-n	0.098	± 0.010	0.090	± 0.010
only stat+IBD norm.	0.102	± 0.012	0.105	± 0.012
only stat+reactor	0.114	± 0.014	0.116	± 0.014
FD b^{rate}_{LiHe} =0.97 d^{-1}	0.99 d^{-1}	± 0.11 d^{-1}	0.96 d^{-1}	± 0.11 d^{-1}
ND b^{rate}_{LiHe} =5.82 d^{-1}	6.62 d^{-1}	± 0.54 d^{-1}	6.77 d^{-1}	± 0.61 d^{-1}

(a)

10-fold stats, $\sin^2(2\theta_{13}) = 0.090$	1st χ^2 based analysis		this work	
modelled effects	C.V.	uncert.	C.V.	uncert.
only statistics	0.090	± 0.003	0.090	± 0.003
only stat+energy	0.089	± 0.003	0.089	± 0.003
only stat+β-n	0.090	± 0.003	0.090	± 0.003
only stat+IBD norm.	0.089	± 0.005	0.090	± 0.005
only stat+reactor	0.086	± 0.001	0.090	± 0.005
FD b^{rate}_{LiHe} =0.97 d^{-1}	0.99 d^{-1}	± 0.05 d^{-1}	0.98 d^{-1}	± 0.04 d^{-1}
ND b^{rate}_{LiHe} =5.82 d^{-1}	5.82 d^{-1}	± 0.23 d^{-1}	5.82 d^{-1}	± 0.23 d^{-1}

(b)

Table 6.6: Comparison of differences in systematics treatment between oscillation analyses. Table (a) shows nominal statistics and table (b) shows 10-fold nominal statistics. In each table, the top part shows results for $\sin^2(2\theta_{13})$ while the bottom part shows results for ND and FD b^{rate}_{LiHe} when modelling β-n systematics. See text for further explanations.

is visible between all analyses (cf. figures 6.13b and 6.13c). A different statistical treatment between this work and the two χ^2 based analyses can explain this difference. This work uses a Poissonian distribution to model statistical uncertainties while the χ^2 based approach uses a normal distribution. To verify this in a more detailed way, a dataset with nominal statistics and a dataset with 10-fold nominal statistics was evaluated multiple times while only one systematic effect at a time was modelled during each evaluation. All other systematic effects were assumed to be perfectly known and their corresponding parameters were fixed, i.e. infinitesimal small uncertainties were assumed. Table 6.6a indeed shows that the estimate for $\sin^2(2\theta_{13})$ differs most among all effects when including β-n isotope systematics. Likewise, the yielded β-n isotope rate differs mildly. However, for 10-fold nominal statistics, almost all discrepancies vanish as shown in table 6.6b. In this case, the Poissonian and normal distribution have become effectively identical. The only remaining effect showing a difference between the χ^2 based approach and this work is the reactor flux systematic. This systematic is indeed treated very differently between the two analyses. As detailed in section 6.3, this analysis is correcting the IBD-spectrum by adding correlated shifts to the spectrum in order to model possible distortions within the flux uncertainties. The χ^2 based approach does not model any flux uncertainties and does not correct the spectrum accordingly. Instead, it introduces a relaxed penalty in the optimisation based on the size of the flux uncertainty when comparing the

measured data with the prediction. From table 6.6a, one can also see that recalculating the energy correction function yields a smaller bias than using a precalculated energy correction as done in the χ^2 based analysis. However, with increasing statistics, the difference vanishes as seen in table 6.6b. In summary, all analyses show an overall sufficient performance, while the accuracy of this work with respect to $\sin^2(2\theta_{13})$ is on average marginally better than those of the χ^2 based approaches (cf. table 6.4).

An additional test performed during the mock data challenge was the evaluation of the oscillation analysis performance under the condition of a heavy energy scale input bias. This test was performed since the energy scale inputs were expected to be not ready in full detail when data unblinding should happen [116, p. 6]. Instead, a conservative approach of fully uncorrelated energy scales across detectors is employed. Moreover, the energy scale inputs will not include any a-priori knowledge on the energy scale correction, but will assume no initial correction. The oscillation analyses are then expected to extract the precise non-linearity energy scale correction from each detector. By this, it shall be demonstrated that the design goal of effectively identical detectors was achieved. This mechanism was tested under rather extreme energy bias conditions: Figure 6.14 shows the results for the energy correction functions extracted from the best-fit models of 10 MC datasets with nominal statistics. On average, the energy scale bias is recovered correctly in all detectors. A better recovery is achieved for the high statistics ND dataset and for the medium statistics FD1 dataset (cf. table 5.3). The results are in general found to be sufficient.

Following the MC data tests, a partial data unblinding for the previously published single detector FD1 and FD1off datasets was performed. The results were compared to the published results [10] derived from the χ^2 based analyses. For this, the previous input model for that analysis, also known as Gd-III, was used. It is a slightly modified input model with smaller background statistics compared to section 6.2. It can be seen in table 6.7 along with the results. As shown, the agreement with the published results is good: The relative tension for each parameter is well below $1\,\sigma$ and tensions to the input model are similar for both

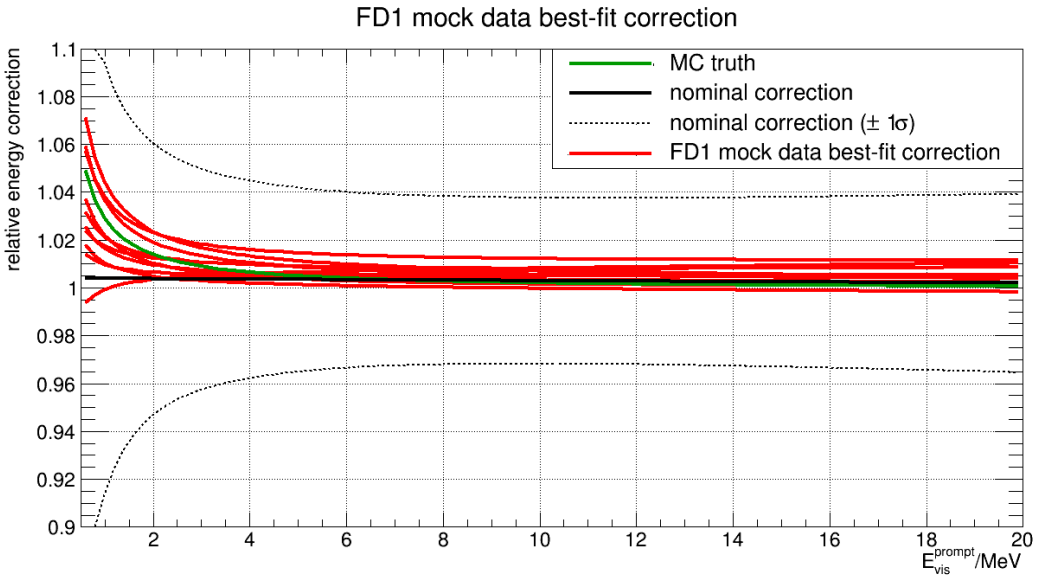

(a)

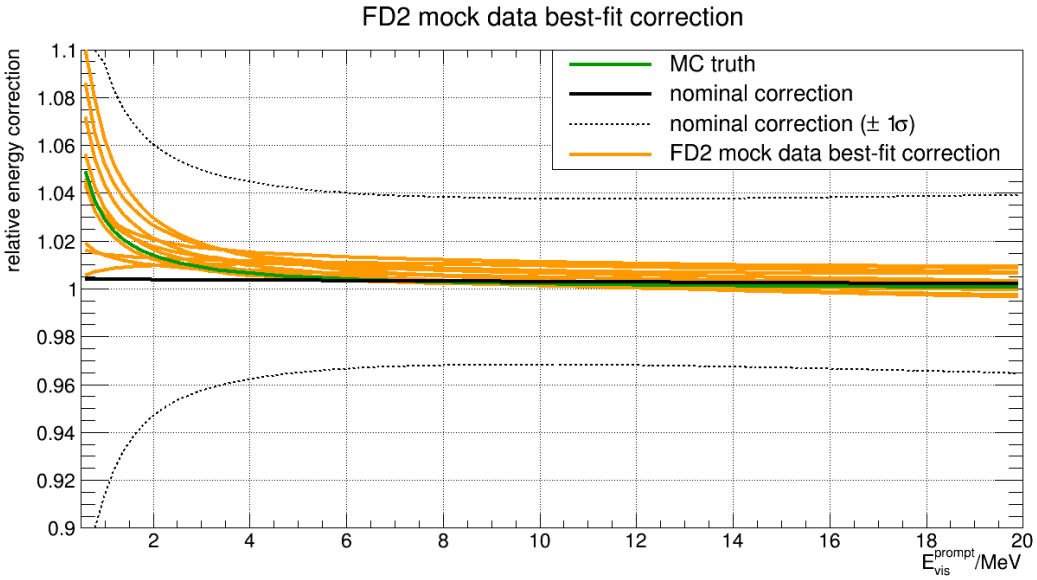

(b)

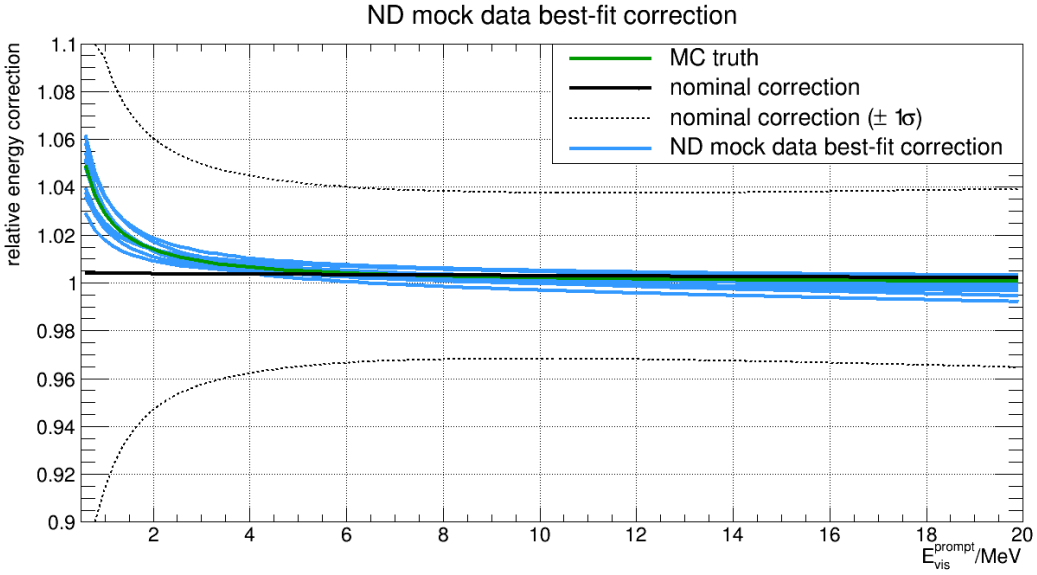

(c)

Figure 6.14: Results of the mock data energy scale test. The outcome of 10 MC datasets with nominal statistics is compared with the true MC energy scale and the input energy scale in the (a) FD1, (b) FD2 and (c) ND.

oscillation analyses.

Since all validation tests were passed successfully, full data unblinding for the Gd-IV (Moriond) datasets (cf. table 5.3) was granted by the Double Chooz collaboration. The results are presented in section 6.5.

Gd-III	published	this work	input model
$\sin^2(2\theta_{13})$	$0.090^{+0.032}_{-0.029}$	0.112 ± 0.030	—
Δm^2_{ee}	$2.44^{+0.09}_{-0.10} \cdot 10^{-3}\text{eV}^2$	$(2.44 \pm 0.09) \cdot 10^{-3}\text{eV}^2$	$(2.44 \pm 0.09) \cdot 10^{-3}\text{eV}^2$
$R^{\bar{\nu}_e}_{Off}$	(0.204 ± 0.065) d^{-1}	(0.207 ± 0.065) d^{-1}	(0.217 ± 0.065) d^{-1}
ν^{norm}	not used	(91.64 ± 0.49) %	(91.49 ± 0.58) %
e_0	$-0.0270^{+0.006}_{-0.005}$ MeV	(-0.0269 ± 0.0054) MeV	(-0.0271 ± 0.0062) MeV
e_1	$1.0119^{+0.004}_{-0.006}$	1.0053 ± 0.0054	1.0120 ± 0.0077
e_2	$-0.0006^{+0.0007}_{-0.0005}$ MeV^{-1}	(-0.0006 ± 0.0005) MeV^{-1}	(-0.0001 ± 0.0006) MeV^{-1}
b^{rate}_{LiHe}	(0.74 ± 0.13) d^{-1}	(0.77 ± 0.11) d^{-1}	$0.98^{+0.41}_{-0.16}$ d^{-1}
b^{rate}_{corr}	$0.568^{+0.038}_{-0.037}$ d^{-1}	(0.559 ± 0.036) d^{-1}	(0.604 ± 0.051) d^{-1}
b^{rate}_{acc}	(0.0703 ± 0.0026) d^{-1}	(0.0702 ± 0.0026) d^{-1}	(0.0701 ± 0.0026) d^{-1}

Table 6.7: Results for the Gd-III dataset. Published values are extracted from [10].

6.5 Determination of the Oscillation Angle

The oscillation analysis performed with the fully unblinded Gd-IV (Moriond) datasets and input model as described in section 6.2 yields an oscillation amplitude of $\sin^2(2\theta_{13}) = 0.117 \pm 0.019$. The new measurement has an improved relative uncertainty of 16 % compared to 27 % achieved with the previous Gd-III single detector measurement shown in table 6.7. The value for the oscillation amplitude has slightly increased by $+0.26\,\sigma$ with respect to the Gd-IV uncertainty. It is in agreement with the result of $\sin^2(2\theta_{13}) = 0.111 \pm 0.018$ derived by the χ^2 based analysis [46, p. 25]. The detailed results can be seen in table 6.8 and figures 6.15, 6.16 and 6.17.

In table 6.8 one sees that the outcome shows no tension for all nuisance parameters with exception of a $-2.2\,\sigma$ tension for the β-n isotope rate in the far detector. This has also been observed in earlier oscillation analyses [10] and is the reason why the β-n isotope rate parameters are treated unconstrained. By this, a bias in the oscillation amplitude due to a bias in the input model is avoided. Indeed, there is some difficulty to calculate the remaining β-n isotope contamination after background discrimination in the input model [88] and therefore the risk of an input model bias exists, as reported earlier. The tension in the β-n isotope rate is only present in the far detector (-37 %), but not in the near detector (-5 %). Further investigations by the β-n isotope working group will happen and an alternative way to estimate the β-n rate is currently investigated.

From table 6.8, one finds that the energy scale parameter are showing similar outcomes across all detectors. This result was expected as detailed in section 6.4 because the detectors are built identically with respect to many items like the scintillator, electronics or geometry. The similar outcome of the energy parameters despite the uncorrelated treatment of the parameter across detectors can be considered as an effective proof of that claim. Figure 6.18 and 6.19 show the energy scale correction and compare it to the correction previously utilised in the Gd-III analysis. For the far detectors, excellent agreement is achieved as seen in figure 6.18b. The near detector shows a slightly larger correction from 2.0 MeV upwards. Compared to the Gd-III results in figure 6.18a, the FD1 shows a correction in opposite direction. This can be understood from the fact that for the Gd-III analysis, the constrain on the energy correction function (black lines, cf. also figure 5.2b) was much stronger than in the Gd-IV analysis. However, the deviation between the Gd-III and Gd-IV results is within the $1\,\sigma$ range

Gd-IV (Moriond)	this work		input model	
	C.V.	uncert.	C.V.	uncert.
global				
$\sin^2(2\theta_{13})$	0.117	$\pm$ 0.019	—	—
Δm^2_{ee}	$2.44 \cdot 10^{-3}\text{eV}^2$	$\pm$ $0.09 \cdot 10^{-3}\text{eV}^2$	$2.44 \cdot 10^{-3}\text{eV}^2$	$\pm$ $0.09 \cdot 10^{-3}\text{eV}^2$
FD1/FD1off				
$R^{\bar{\nu}_e}_{Off}$	$0.209\,\text{d}^{-1}$	$\pm$ $0.065\,\text{d}^{-1}$	$0.217\,\text{d}^{-1}$	$\pm$ $0.065\,\text{d}^{-1}$
ν^{norm}	91.72 %	$\pm$ 0.49 %	91.51 %	$\pm$ 0.49 %
e_0	-0.022 MeV	$\pm$ 0.016 MeV	0.000 MeV	$\pm$ 0.0067 MeV
e_1	0.9993	$\pm$ 0.0081	1.0000	$\pm$ 0.0225
e_2	$-0.0002\,\text{MeV}^{-1}$	$\pm$ $0.0006\,\text{MeV}^{-1}$	$0.0000\,\text{MeV}^{-1}$	$\pm$ $0.0006\,\text{MeV}^{-1}$
b^{rate}_{acc}	$0.0701\,\text{d}^{-1}$	$\pm$ $0.0026\,\text{d}^{-1}$	$0.0701\,\text{d}^{-1}$	$\pm$ $0.0026\,\text{d}^{-1}$
FD2				
ν^{norm}	90.58 %	$\pm$ 0.47 %	90.36 %	$\pm$ 0.47 %
e_0	-0.022 MeV	$\pm$ 0.021 MeV	0.000 MeV	$\pm$ 0.066 MeV
e_1	0.9953	$\pm$ 0.0084	1.0000	$\pm$ 0.0215
e_2	$0.0000\,\text{MeV}^{-1}$	$\pm$ $0.0004\,\text{MeV}^{-1}$	$0.0000\,\text{MeV}^{-1}$	$\pm$ $0.0004\,\text{MeV}^{-1}$
b^{rate}_{acc}	$0.1059\,\text{d}^{-1}$	$\pm$ $0.0023\,\text{d}^{-1}$	$0.1059\,\text{d}^{-1}$	$\pm$ $0.0023\,\text{d}^{-1}$
joined FDs				
b^{rate}_{LiHe}	$0.61\,\text{d}^{-1}$	$^{+0.13}_{-0.12}\,\text{d}^{-1}$	$0.97\,\text{d}^{-1}$	not used
b^{rate}_{corr}	$0.529\,\text{d}^{-1}$	$\pm$ $0.034\,\text{d}^{-1}$	$0.586\,\text{d}^{-1}$	$\pm$ $0.061\,\text{d}^{-1}$
ND				
ν^{norm}	75.33 %	$\pm$ 0.38 %	75.11 %	$\pm$ 0.38 %
e_0	-0.014 MeV	$\pm$ 0.012 MeV	0.000 MeV	$\pm$ 0.066 MeV
e_1	0.9917	$\pm$ 0.0070	1.0000	$\pm$ 0.0218
e_2	$-0.0008\,\text{MeV}^{-1}$	$\pm$ $0.0008\,\text{MeV}^{-1}$	$0.0000\,\text{MeV}^{-1}$	$\pm$ $0.0009\,\text{MeV}^{-1}$
b^{rate}_{acc}	$0.3441\,\text{d}^{-1}$	$\pm$ $0.0022\,\text{d}^{-1}$	$0.3441\,\text{d}^{-1}$	$\pm$ $0.0022\,\text{d}^{-1}$
b^{rate}_{LiHe}	$4.73\,\text{d}^{-1}$	$^{+0.75}_{-0.71}\,\text{d}^{-1}$	$5.01\,\text{d}^{-1}$	not used
b^{rate}_{corr}	$3.52\,\text{d}^{-1}$	$\pm$ $0.16\,\text{d}^{-1}$	$3.42\,\text{d}^{-1}$	$\pm$ $0.23\,\text{d}^{-1}$

Table 6.8: Results for the Gd-IV (Moriond) dataset.

and thus acceptable.

One can see from table 6.8 that some of the parameters get significantly constrained with respect to the input model. Those parameters are especially the rates of the β-n isotope backgrounds and the rates of the correlated backgrounds. For the β-n isotope rates, these constraints are even better than the constraints derived from dedicated analyses which yield $\pm$ $1.43\,\text{d}^{-1}$ for the ND and $^{+0.41}_{-0.16}$ d^{-1} for the FD. This is the case even though the input constraints do not enter the input model. This effect has already been shown in figure 6.4 and was discussed there. Additionally, the background-only sample FD1off can constrain the total background rate.

The smaller oscillation effect in the ND due to its shorter baseline (cf. figure 6.7) can be seen immediately when comparing e.g. figures 6.15c and 6.16c. When comparing figures 6.15b and 6.16b, one can clearly see that the muon-induced backgrounds have become more

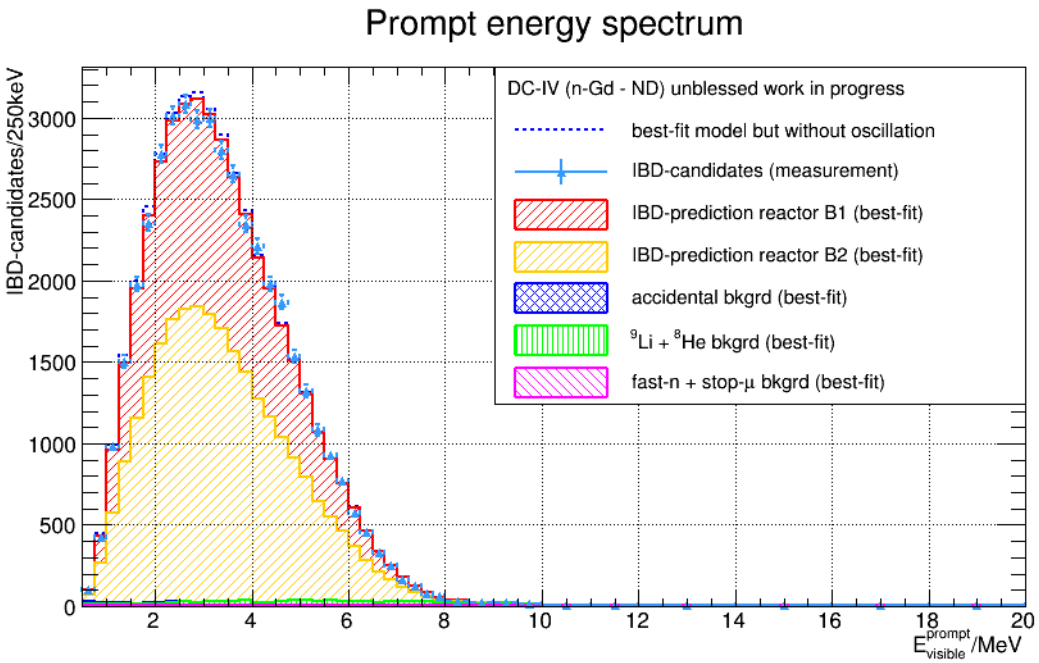
Prompt energy spectrum
DC-IV (n-Gd - ND) unblessed work in progress
best-fit model but without oscillation
IBD-candidates (measurement)
IBD-prediction reactor B1 (best-fit)
IBD-prediction reactor B2 (best-fit)
accidental bkgrd (best-fit)
9Li + 8He bkgrd (best-fit)
fast-n + stop-μ bkgrd (best-fit)
IBD-candidates/250keV
E prompt visible /MeV

(a)

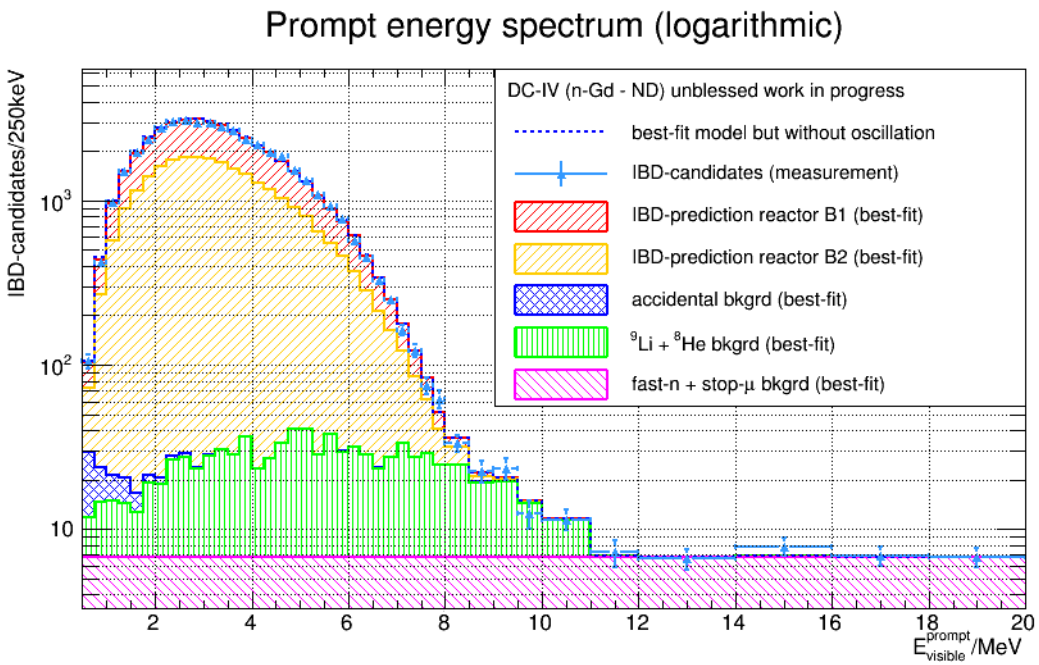
Prompt energy spectrum (logarithmic)
DC-IV (n-Gd - ND) unblessed work in progress
best-fit model but without oscillation
IBD-candidates (measurement)
IBD-prediction reactor B1 (best-fit)
IBD-prediction reactor B2 (best-fit)
accidental bkgrd (best-fit)
9Li + 8He bkgrd (best-fit)
fast-n + stop-μ bkgrd (best-fit)
IBD-candidates/250keV
E prompt visible /MeV

(b)

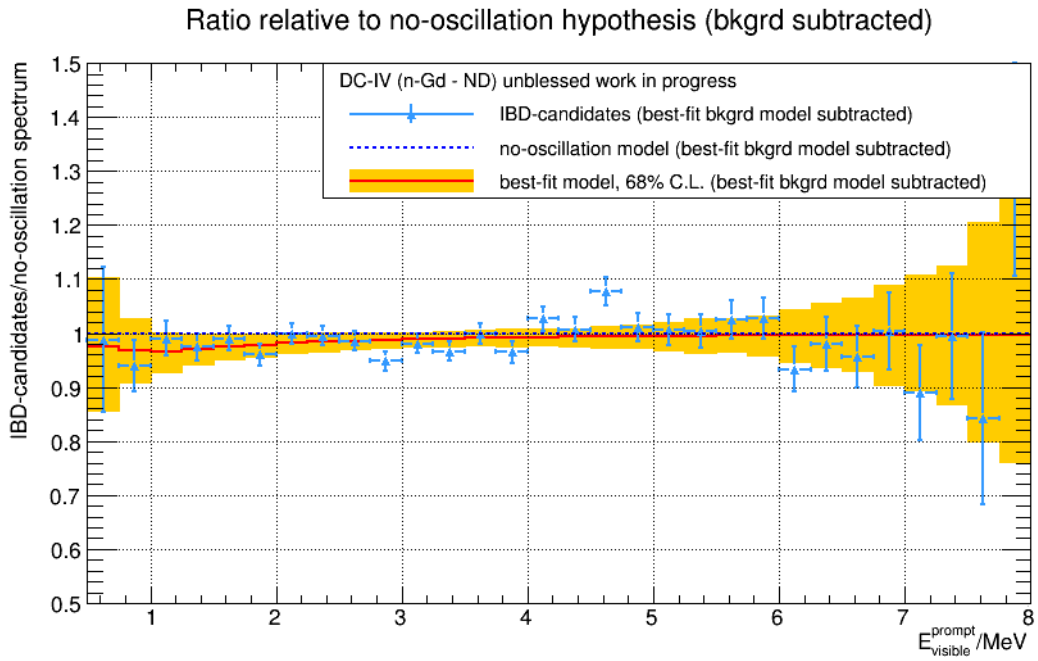

(c)

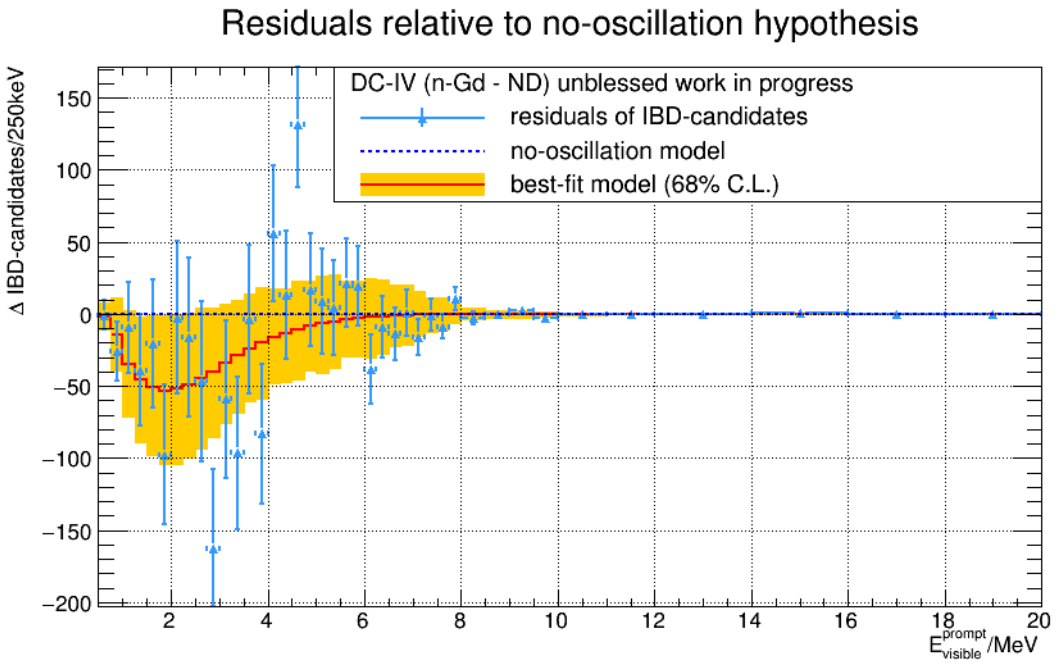

(d)

Figure 6.15: Best-fit spectra for the Gd-IV ND dataset. See also figures 6.16 and 6.17.

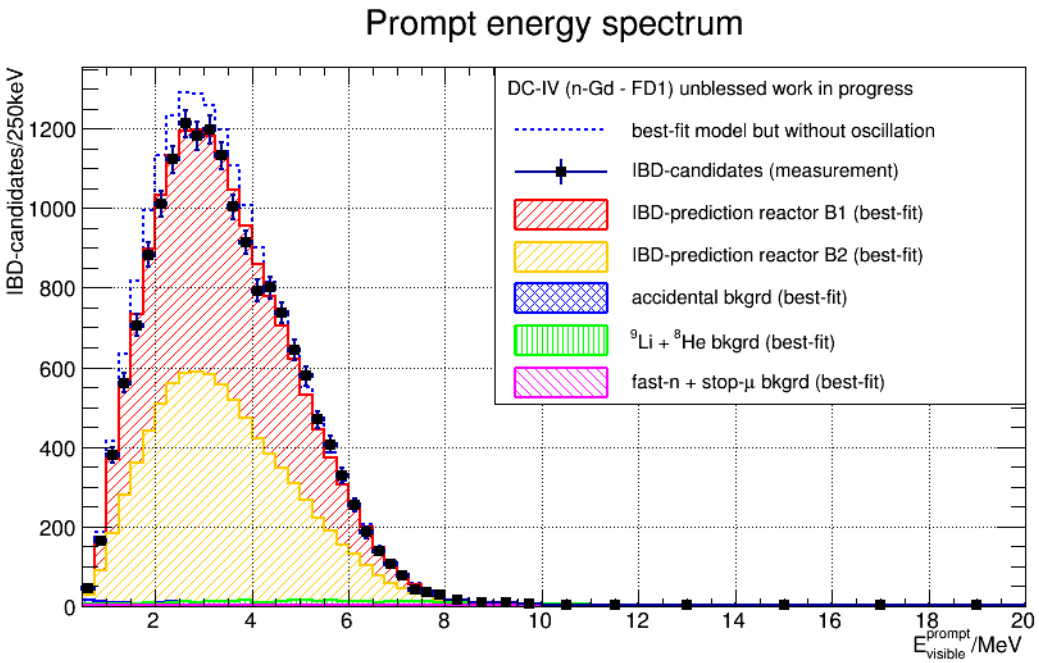
Prompt energy spectrum
DC-IV (n-Gd - FD1) unblessed work in progress
best-fit model but without oscillation
IBD-candidates (measurement)
IBD-prediction reactor B1 (best-fit)
IBD-prediction reactor B2 (best-fit)
accidental bkgrd (best-fit)
^{9}Li + ^{8}He bkgrd (best-fit)
fast-n + stop-μ bkgrd (best-fit)
IBD-candidates/250keV
$E^{prompt}_{visible}$/MeV

(a)

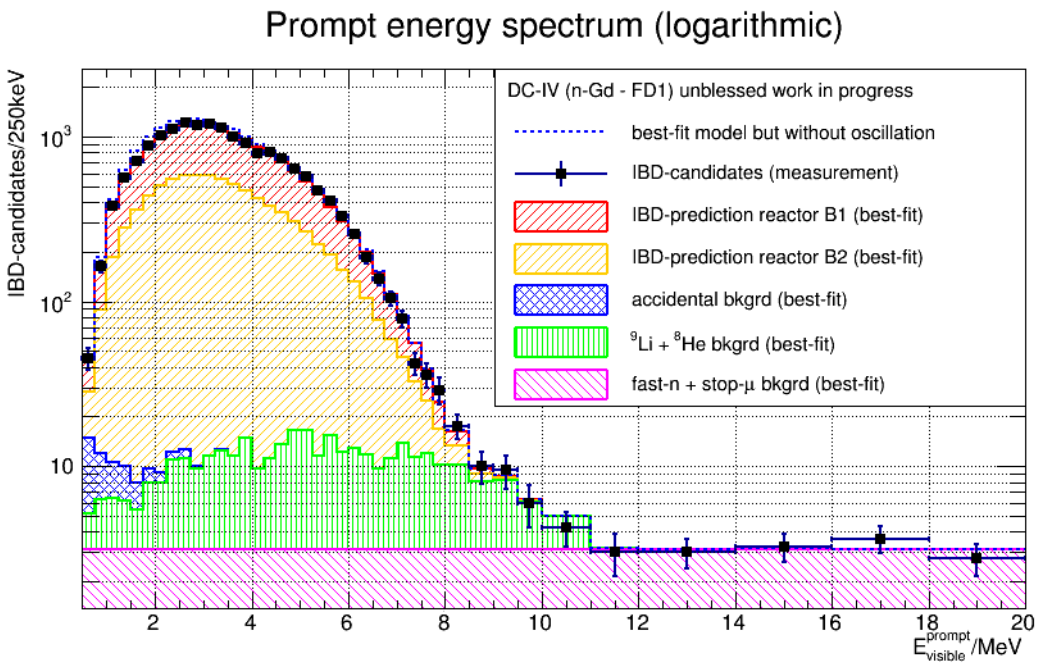
Prompt energy spectrum (logarithmic)
DC-IV (n-Gd - FD1) unblessed work in progress
best-fit model but without oscillation
IBD-candidates (measurement)
IBD-prediction reactor B1 (best-fit)
IBD-prediction reactor B2 (best-fit)
accidental bkgrd (best-fit)
^{9}Li + ^{8}He bkgrd (best-fit)
fast-n + stop-μ bkgrd (best-fit)
IBD-candidates/250keV
$E^{prompt}_{visible}$/MeV

(b)

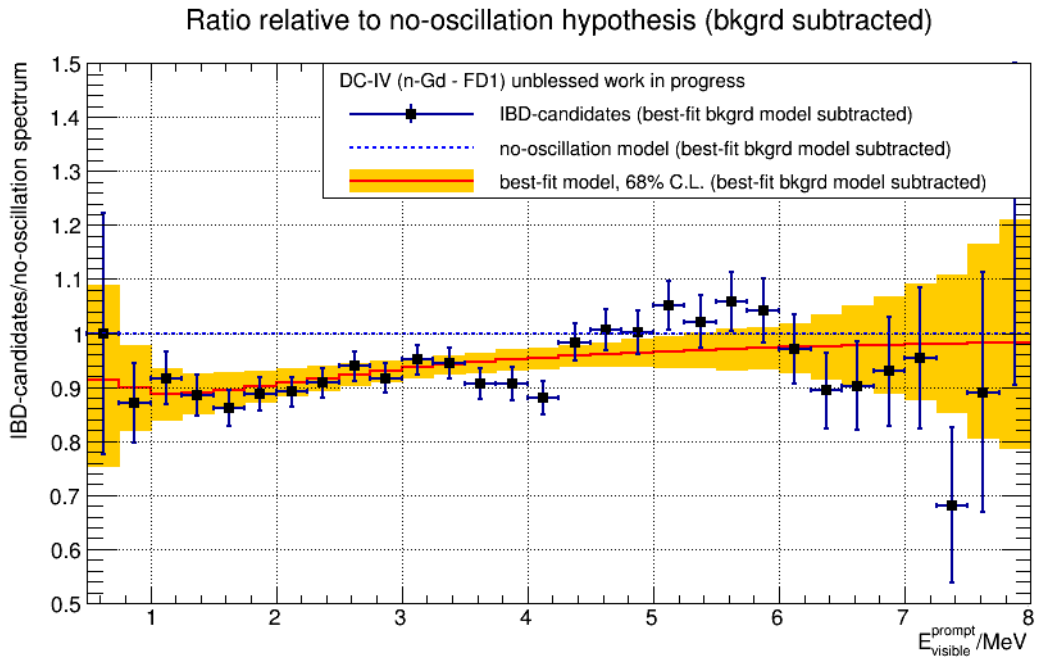

(c)

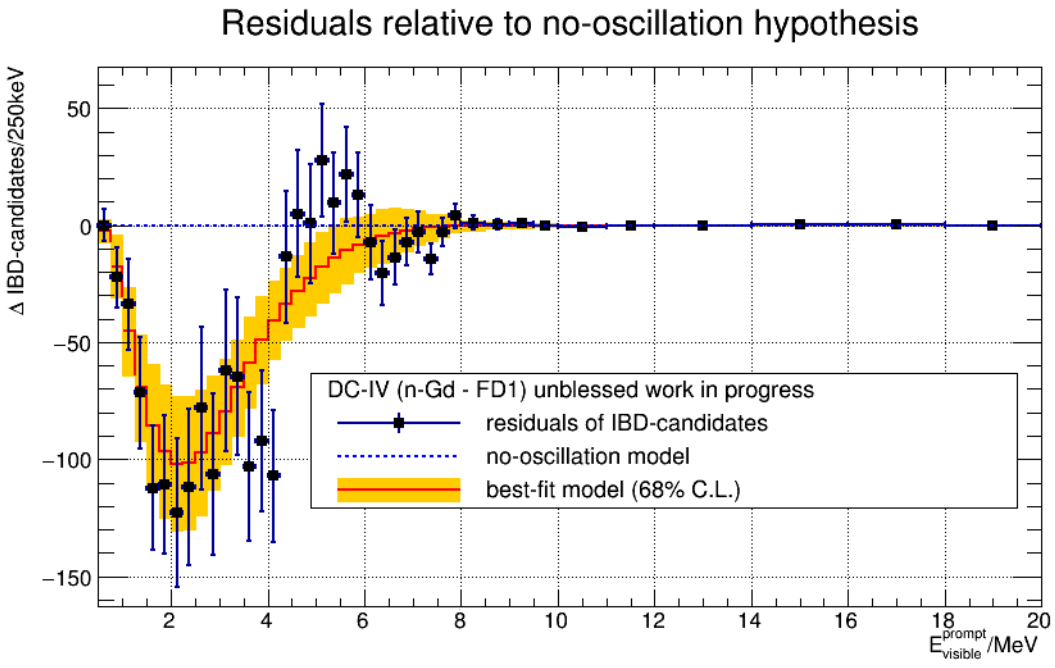

(d)

Figure 6.16: Best-fit spectra for the Gd-IV FD1 dataset. See also figures 6.15 and 6.17.

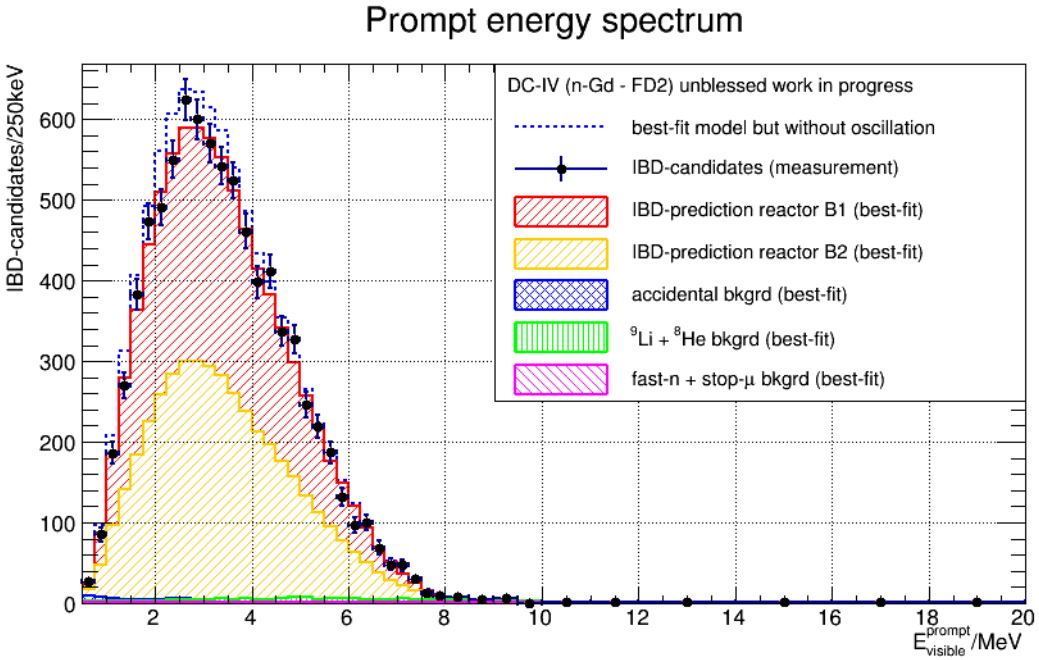
Prompt energy spectrum
DC-IV (n-Gd - FD2) unblessed work in progress
best-fit model but without oscillation
IBD-candidates (measurement)
IBD-prediction reactor B1 (best-fit)
IBD-prediction reactor B2 (best-fit)
accidental bkgrd (best-fit)
^{9}Li + ^{8}He bkgrd (best-fit)
fast-n + stop-μ bkgrd (best-fit)
IBD-candidates/250keV
$E^{prompt}_{visible}$/MeV

(a)

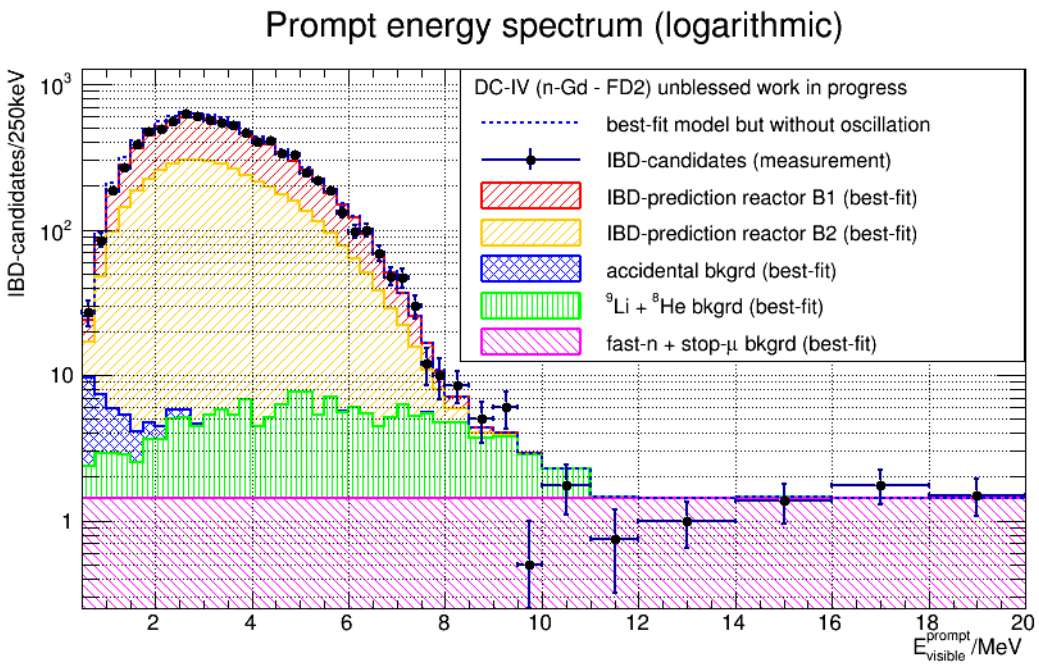
Prompt energy spectrum (logarithmic)
DC-IV (n-Gd - FD2) unblessed work in progress
best-fit model but without oscillation
IBD-candidates (measurement)
IBD-prediction reactor B1 (best-fit)
IBD-prediction reactor B2 (best-fit)
accidental bkgrd (best-fit)
^{9}Li + ^{8}He bkgrd (best-fit)
fast-n + stop-μ bkgrd (best-fit)
IBD-candidates/250keV
$E^{prompt}_{visible}$/MeV

(b)

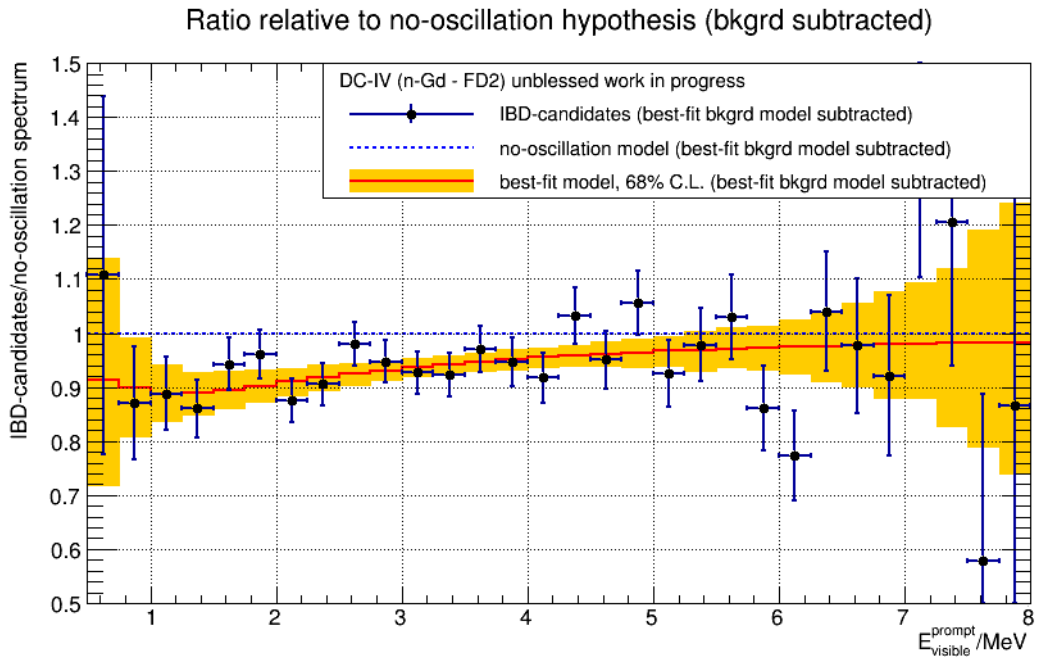

(c)

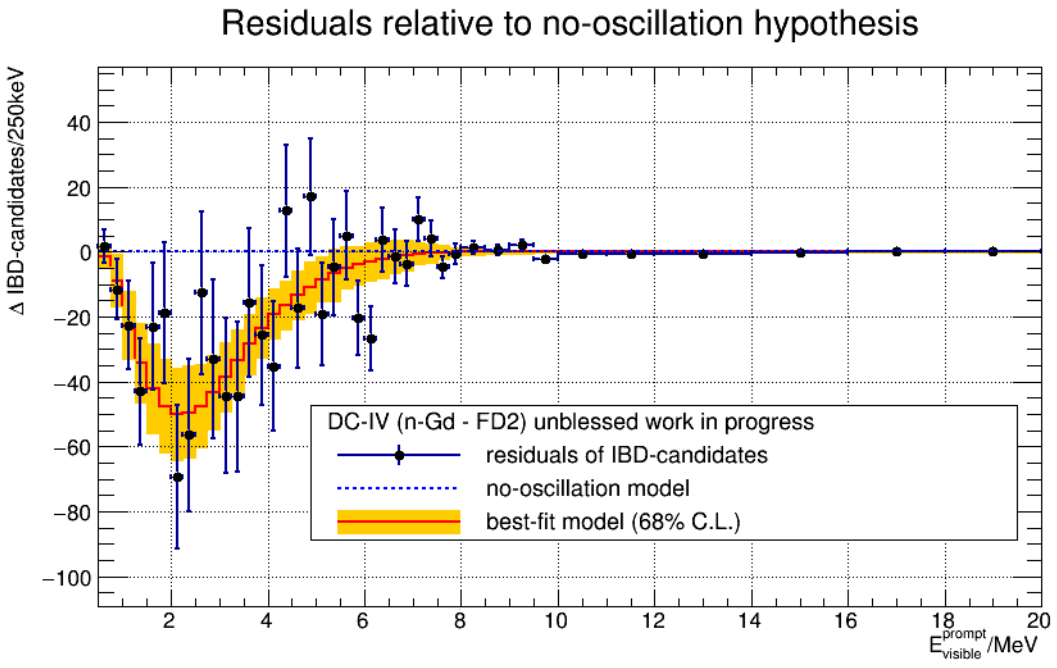

(d)

Figure 6.17: Best-fit spectra for the Gd-IV FD2 dataset. See also figures 6.15 and 6.16.

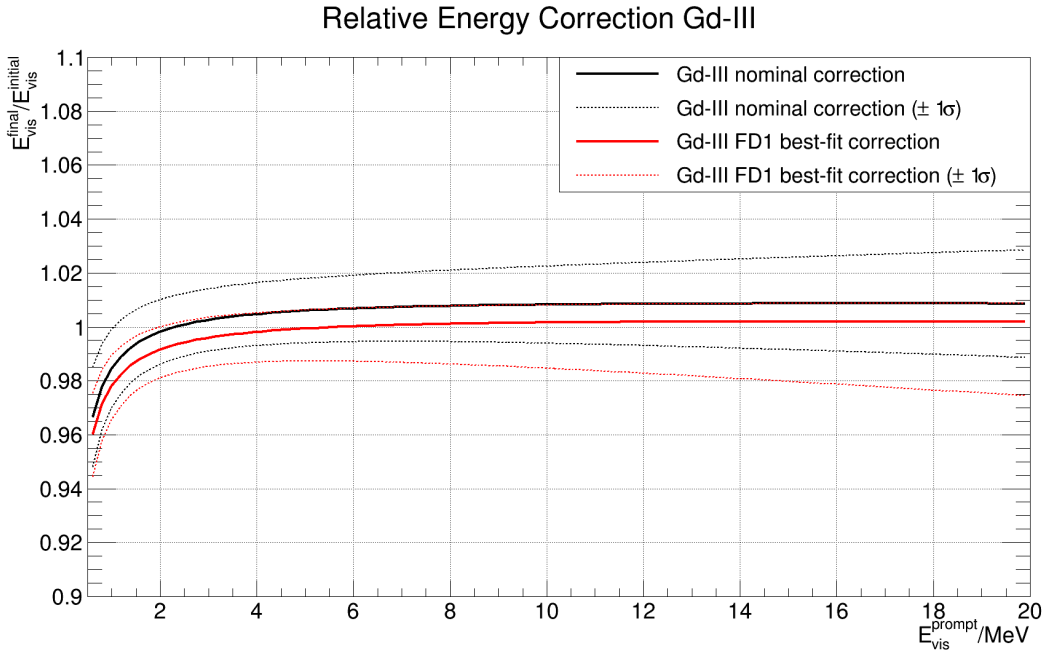

(a)

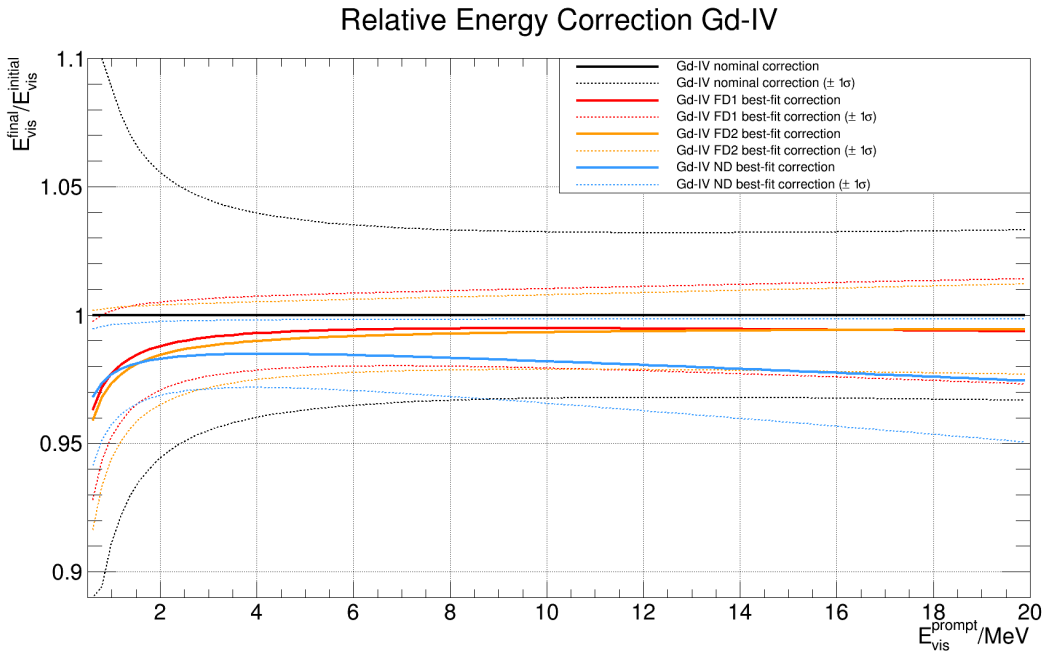

(b)

Figure 6.18: Results of the (b) Gd-IV energy correction (relative scale) as given in equation 6.18 compared to the (a) Gd-III correction. See figure 6.19 for absolute scaling.

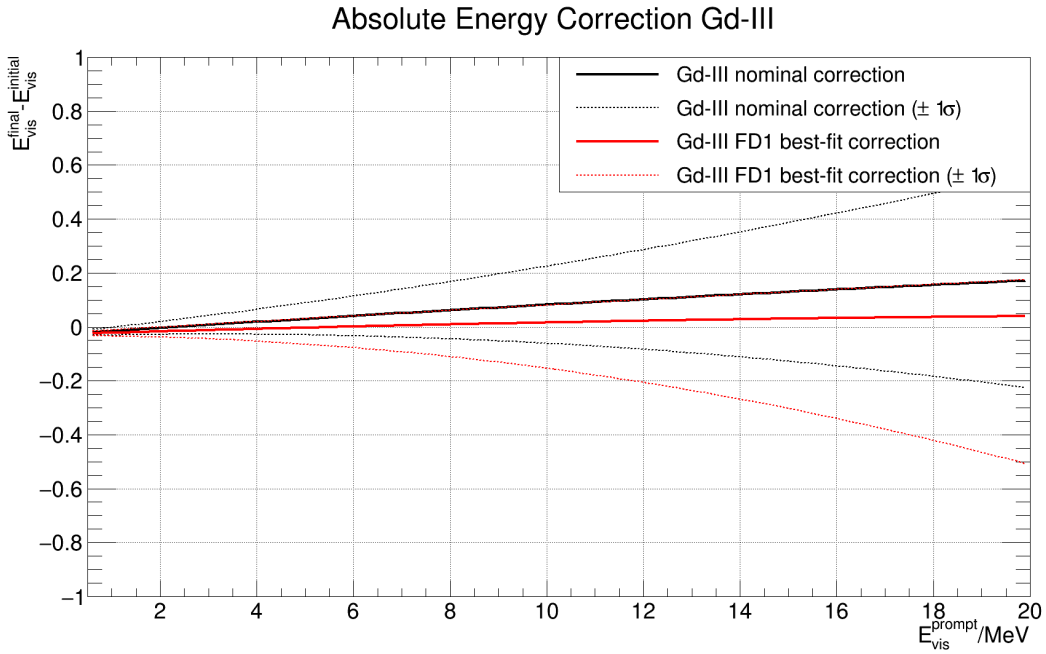

(a)

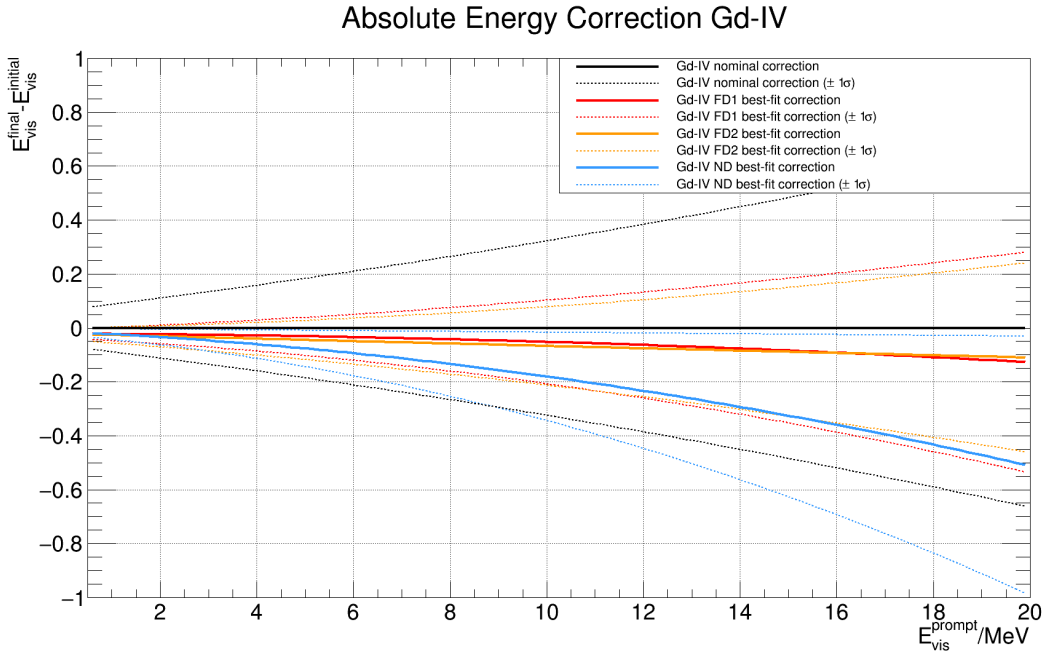

(b)

Figure 6.19: Results of the (b) Gd-IV energy correction (absolute scale) as given in equation 6.18 compared to the (a) Gd-III correction. See figure 6.18 for relative scaling.

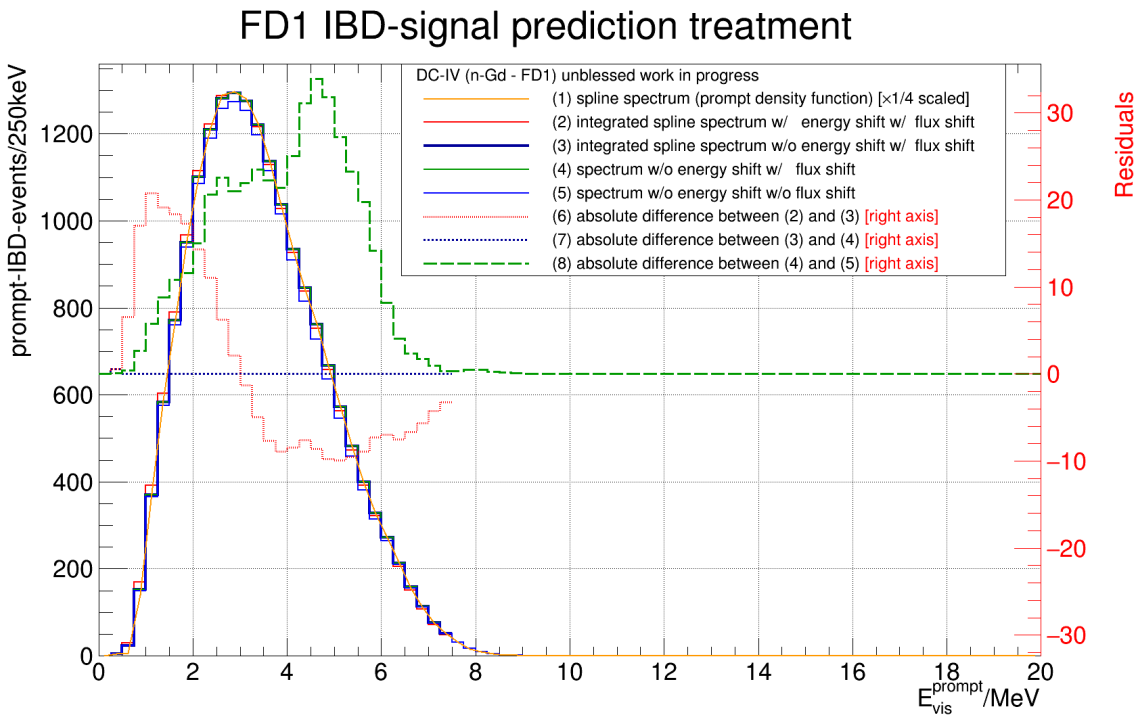
FD1 IBD-signal prediction treatment
DC-IV (n-Gd - FD1) unblessed work in progress
(1) spline spectrum (prompt density function) [×1/4 scaled]
(2) integrated spline spectrum w/ energy shift w/ flux shift
(3) integrated spline spectrum w/o energy shift w/ flux shift
(4) spectrum w/o energy shift w/ flux shift
(5) spectrum w/o energy shift w/o flux shift
(6) absolute difference between (2) and (3) [right axis]
(7) absolute difference between (3) and (4) [right axis]
(8) absolute difference between (4) and (5) [right axis]
prompt-IBD-events/250keV
Residuals
E_{vis}^{prompt}/MeV

(a)

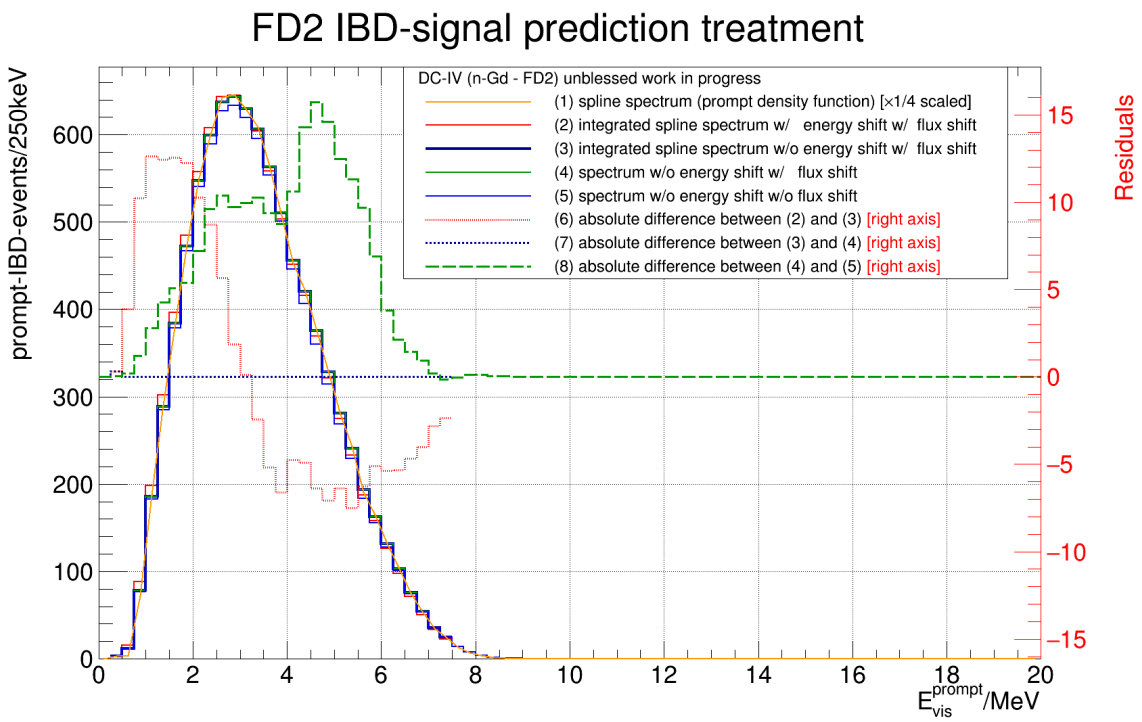
FD2 IBD-signal prediction treatment
DC-IV (n-Gd - FD2) unblessed work in progress
(1) spline spectrum (prompt density function) [×1/4 scaled]
(2) integrated spline spectrum w/ energy shift w/ flux shift
(3) integrated spline spectrum w/o energy shift w/ flux shift
(4) spectrum w/o energy shift w/ flux shift
(5) spectrum w/o energy shift w/o flux shift
(6) absolute difference between (2) and (3) [right axis]
(7) absolute difference between (3) and (4) [right axis]
(8) absolute difference between (4) and (5) [right axis]
prompt-IBD-events/250keV
Residuals
E_{vis}^{prompt}/MeV

(b)

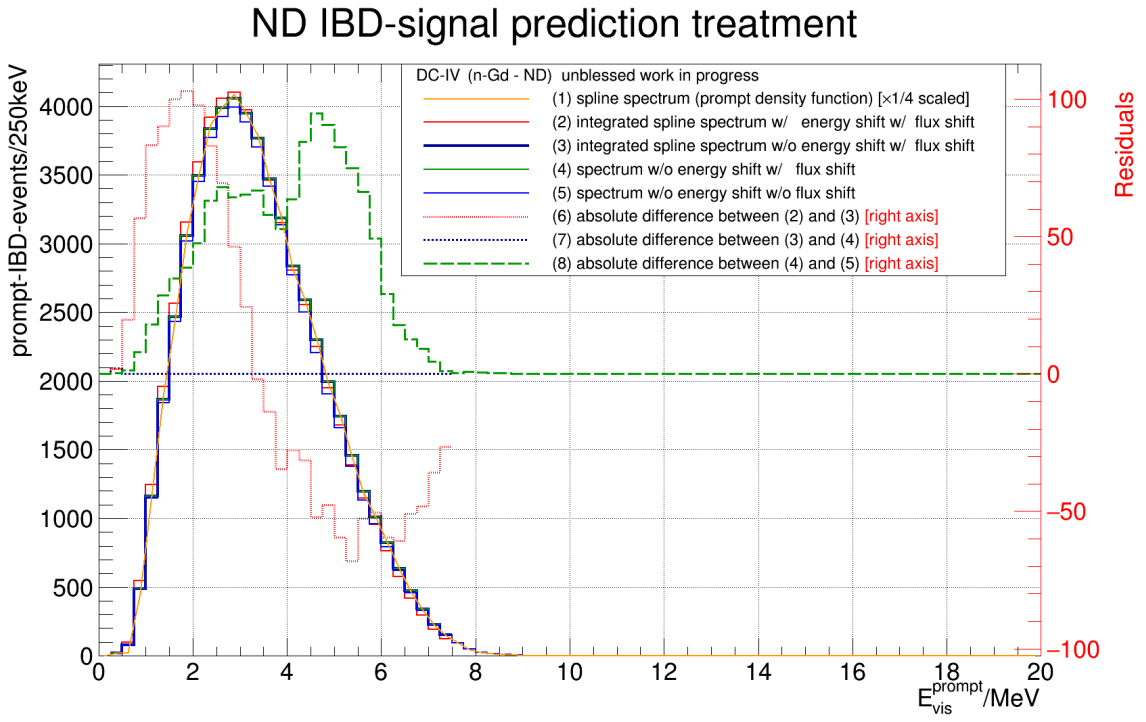

(c)

Figure 6.20: IBD-signal treatment in the Gd-IV oscillation analysis. The treatment is shown for the (a) FD1, (b) FD2, (c) ND.

prominent in the ND with respect to the radioactivity-driven accidental background. However, the neutrino flux in the ND has increased even larger such that the signal purity in the ND is increased with respect to the FDs despite the absolute increase in backgrounds.

Looking at the best-fit spectra in figures 6.15, 6.16 and 6.17, one finds an overall good description of the data with exception of the energy region around 5 MeV. In the FD1 dataset, a clear excess at 5 MeV surrounded by two deficits is visible when comparing the data points to the best-fit model in figure 6.16c. The spectral distortion has previously been reported to be caused by a flaw in the prediction of the reactor spectrum. It has been verified by independent experiments [62]. Its cause is under current investigation, e.g. by comparing the shape and magnitude of the distortion between reactors of different fuel compositions [117]. The overall goodness of fit as shown in table 6.9 nevertheless testifies a good agreement between model and data. With increasing statistics in the ND and FD2, the distortion should become more prominent in those datasets and the goodness of fit is expected to decrease. Nevertheless, the spectral distortion might bias the estimate for the oscillation amplitude $\sin^2(2\theta_{13})$. To determine the impact of this effect, a MC dataset is generated including a spectral distortion. As model for the spectral distortion, the recent measurements of the shape of the distortion by the Daya Bay and RENO collaborations as given in [62] are used. The bias in $\sin^2(2\theta_{13})$ is by this method determined to be $-2.5\,\%$ or $-0.13\,\sigma$, i.e. a slightly smaller value for $\sin^2(2\theta_{13})$ with respect to the true input value is extracted. The small bias can be understood by recognising that the region around 5 MeV has a much smaller signal purity than the region around 3 MeV (cf. figure 6.1a). The oscillation amplitude is thus foremost determined by the

region around 3 MeV and the region around 5 MeV has only minor impact. In the simulation, the IBD-signal spectrum and the β-n isotope spectrum are adapted to the spectral distortion in the MC data spectrum. The parameters show a maximal tension to their input values around the peak of the simulated spectral distortion of $1.2\,\sigma$ for the IBD-signal spectrum and $0.4\,\sigma$ for the β-n isotope spectrum. The same effect can also be seen in the best-fit model for the IBD-signal flux in the analysis of the real Gd-IV data. Figure 6.20 shows the best-fit corrections applied to the IBD-signal spectrum as explained in section 6.3. The residual plots between the flux-uncorrected and the flux-corrected histograms show clearly the structure of a spectral distortion around 5 MeV. The analysis is thus capable of modelling the spectral distortion within its input model uncertainties to some extent. It is however not able to fully describe the distortion within the input model uncertainties, which becomes evident when looking at figure 6.16c. In this figure, the spectral distortion is still visible, i.e. the model has not fully adapted to the distortion. In consequence, one can infer that the input model is underestimating the reactor flux uncertainties. Due to the strong correlation of the reactor flux across detectors (cf. table 6.3), the effect of the spectral distortion is visible with the same magnitude in all detectors depicted in figure 6.20.

With the presented data, it is possible to falsify the no-oscillation hypothesis with 6.0 standard deviations significance as visible from figure 6.21a. With this, the Double Chooz experiment has now confirmed the previous discovery of reactor antineutrino oscillations by the Daya Bay [7] and RENO [8] experiments. The higher exclusion significance compared to figure 6.11 is foremost caused by the higher central value of the oscillation amplitude with respect to the MC data assumption. The value is in good agreement with the value of $5.8\,\sigma$ derived with the χ^2 based analysis [46, p. 25].

method	$\frac{\chi^2}{n.d.f.}$	p-value
likelihood ratio	$\frac{110.40}{121}$	0.75
Pearson's χ^2	$\frac{109.16}{120}$	0.75
KS test	—	0.78

Table 6.9: Goodness of fit for the Gd-IV dataset. The likelihood ratio (main result) uses the saturated model to calculate the deviance as detailed in section 6.1. Pearson's χ^2 and a Kolomogorov-Smirnov test yield consistent results. The number of degrees of freedom is determined from 40 energy bins in three datasets plus one energy bin in the FD1off dataset. In Pearson's χ^2 test, one degree of freedom is subtracted for the oscillation amplitude parameter $\sin^2(2\theta_{13})$.

Figure 6.21 shows that the nuisance parameters are indeed showing no tension with exception of the β-n isotope rate in the FDs as reported earlier in table 6.8. The fact that the discrepancy in the β-n isotope rate is larger in the FDs than in the ND is artificially amplified in figure 6.21 because the definition of the reference uncertainty for the β-n isotope rate differs between the detectors. Since the decision to not constrain the β-n isotope rate in the oscillation analysis was made in an early analysis stage, the ND rate does not have a reduced lower uncertainty. This is because the now unnecessary dedicated analysis for reducing this error was not performed for the ND (cf. section 5.4). For the FD, the earlier analysis with reduced lower uncertainty was nevertheless used.

Looking at the parameter correlations of the best-fit model in figure 6.22, one finds a rather prominent correlation of the energy parameters across detectors despite the uncorrelated treatment across detectors in the input model. This is especially evident between the two high statistic datasets of the ND and the FD1. It shows again that the energy scales are indeed similar despite the conservative input model assumption of uncorrelated energy scales.

Investigating further the parameter correlations in figure 6.22, one can see that the oscilla-

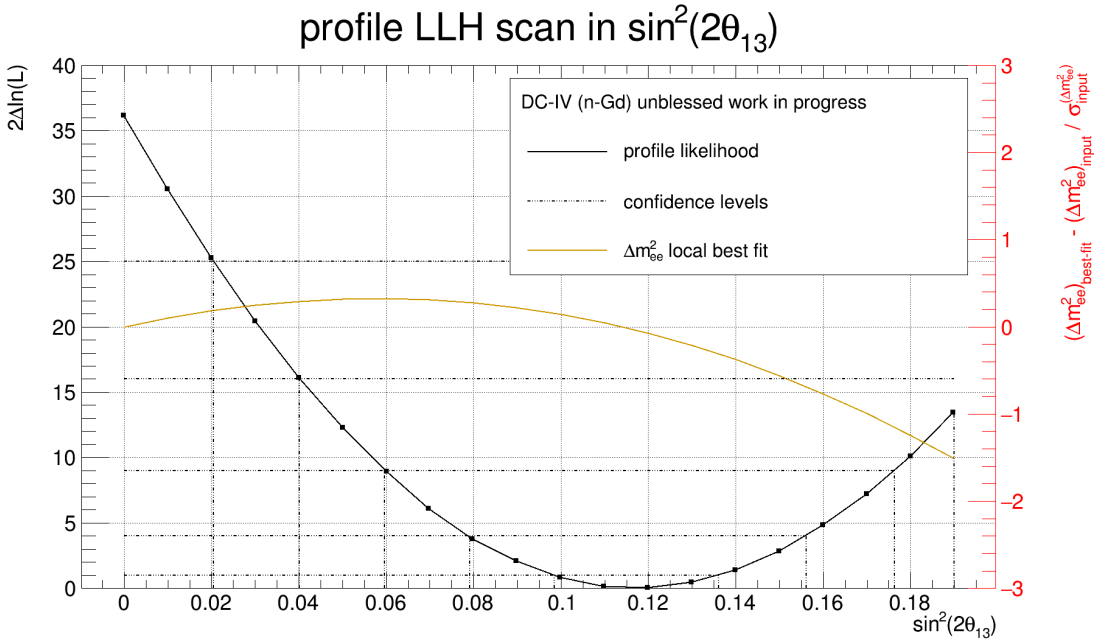
profile LLH scan in sin²(2θ13)
2Δln(L)
DC-IV (n-Gd) unblessed work in progress
profile likelihood
confidence levels
Δm²ee local best fit
(Δm²ee)best-fit - (Δm²ee)input / σ(Δm²ee)input
sin²(2θ13)

(a)

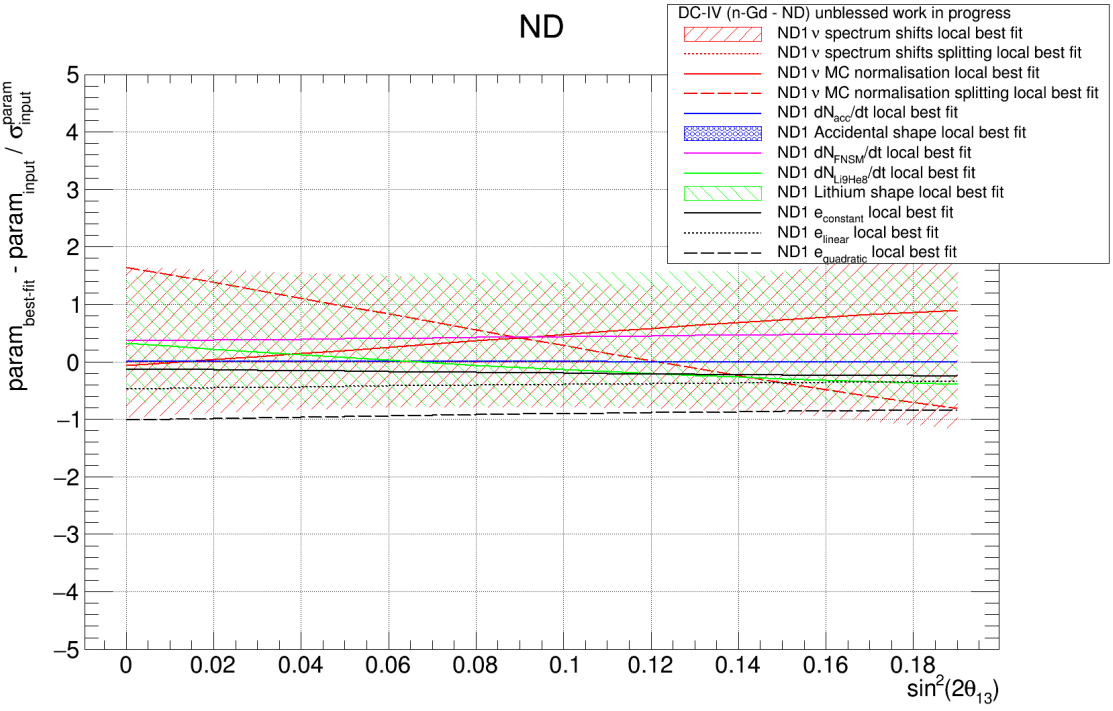
ND
DC-IV (n-Gd - ND) unblessed work in progress
ND1 ν spectrum shifts local best fit
ND1 ν spectrum shifts splitting local best fit
ND1 ν MC normalisation local best fit
ND1 ν MC normalisation splitting local best fit
ND1 dNacc/dt local best fit
ND1 Accidental shape local best fit
ND1 dNFNSM/dt local best fit
ND1 dNLi9He8/dt local best fit
ND1 Lithium shape local best fit
ND1 econstant local best fit
ND1 elinear local best fit
ND1 equadratic local best fit
paramparambest-fit - paraminput / σparaminput
sin²(2θ13)

(b)

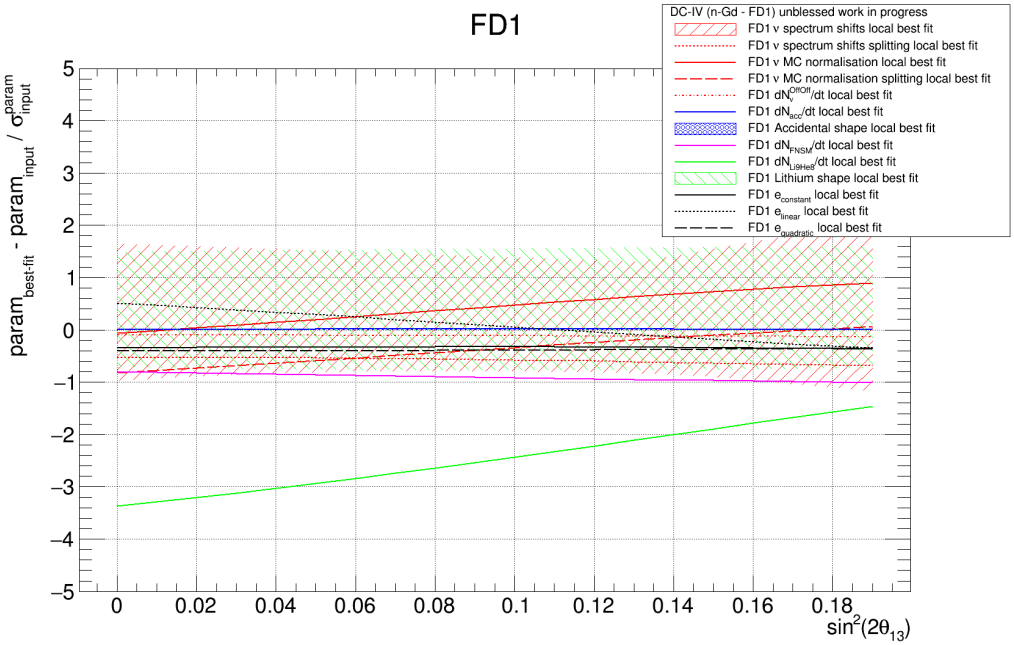

(c)

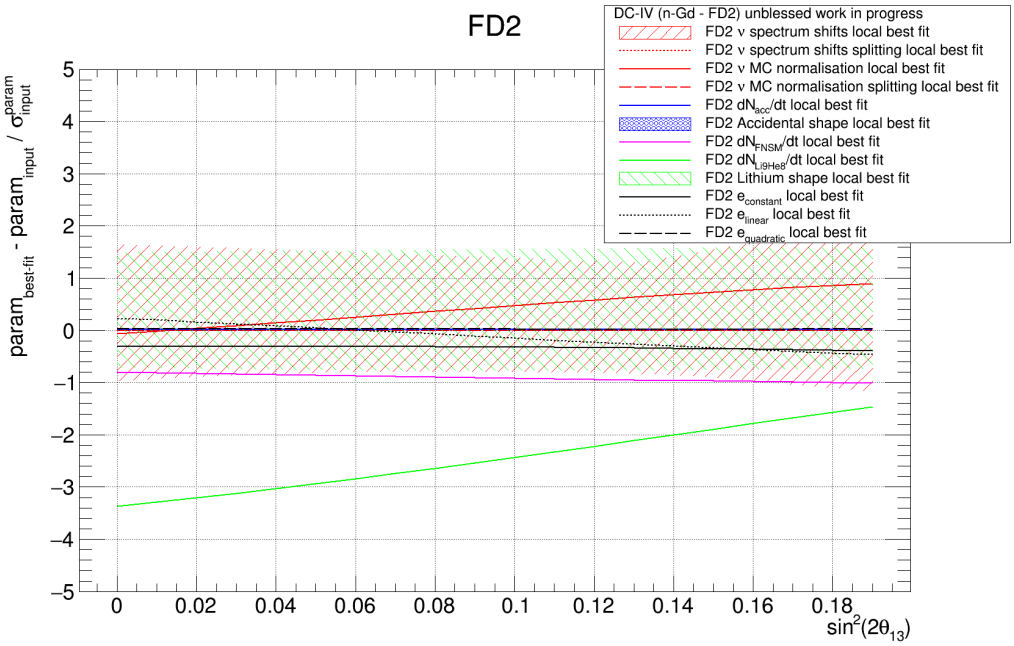

(d)

Figure 6.21: Results of the Gd-IV likelihood profile scan. The profile is shown in (a). The behaviour of all nuisance parameters is given additionally for the (a) global parameters as well as (b) ND, (c) FD1/FD1off and (d) FD2 datasets. Shape parameters have been summarised in shaded bands showing their maximal deviations.

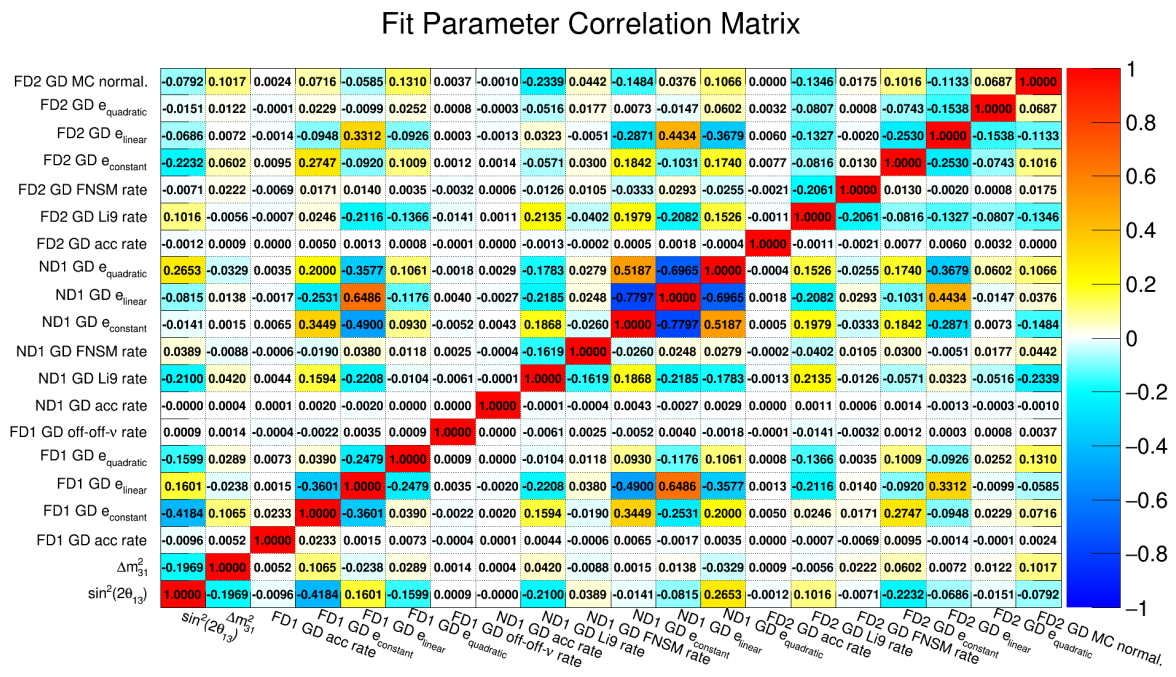

Figure 6.22: Parameter correlations of the Gd-IV (Moriond) best-fit model. Non-global parameters which are identical across detectors are accounted to the FD2 dataset. Shape parameters are not shown.

tion amplitude shows correlations with the oscillation frequency, the energy scale parameters and the detection efficiency. All those parameters are affecting the IBD-signal prediction spectrum directly in the input model as presented in section 6.2. In addition, a correlation with the β-n isotope rate is found. This correlation is in positive direction for the FDs, while it is an anti-correlation for the ND. In turn, the β-n isotope rates show as only background rates, correlations to the energy scale parameters and the overall MC normalisation. This can be understood by looking at e.g. figure 6.16b. The spectral shape of the β-n isotopes is very similar to the IBD-signal prediction spectra. The two contributions are influenced similarly by the data. This again shows that an unconstrained treatment of the β-n isotope rate is important to avoid any bias to the oscillation amplitude $\sin^2(2\theta_{13})$. The fact that the correlation is opposite-signed for the two detectors with respect to the oscillation amplitude can be understood by a strong reactor flux correlation between the two detectors and a different initial normalisation, as will be shown later.

One can also see from figure 6.22 that the correlated background rates are anti-correlated to the β-n isotope rates of the same detector. This can be understood when recognising that the flat correlated background spectrum (cf. e.g. figure 6.16b) is effectively normalising the β-n isotope background to some extent. The accidental background rates show no correlations as they are very localised at low energies (cf. e.g. figure 6.16b).

Observing the correlations of the residual neutrino rate in the FD1off dataset, one finds that despite the overall small correlations, the β-n isotope rate in the FD1 has by one order of magnitude the strongest correlation, an anti-correlation. This shows that the very background-pure reactor-off dataset FD1off is foremost affecting the β-n isotope rate.

	$\sin^2(2\theta_{13})$
ND-only	-0.013
FD1-only	0.105
FD2-only	0.067
ND+FD2	0.095
ND+FD1+FD2	0.117

(a)

	$\sin^2(2\theta_{13})$
default input model	0.117
w/o reactor flux correlation	0.090
w/o detection efficiency correlation	0.113
w/ energy scale correlation	0.132

(b)

Table 6.10: Single detector oscillation analyses are shown in (a) and impact of correlations is shown in (b). The combination of the ND with any number of FDs yields always a larger oscillation amplitude than the single detectors. The assumption of IBD-signal spectrum parameter correlations always increases the value of the oscillation amplitude in the multi-detector analysis. See text for explanation.

As announced above, the opposite-signed correlations of the β-n isotope rates with respect to the oscillation amplitude $\sin^2(2\theta_{13})$ can be explained by different initial normalisations between the ND and the FDs. As shown in figure 6.23, an excess of events with respect to the input model is visible in the ND while a deficit is visible in the FDs. This causes a tension between the three datasets. By performing three single-detector oscillation analyses, this tension becomes obvious. As shown in table 6.10a, the FD1 dataset yields a large oscillation amplitude, while the FD2 and ND datasets prefer a smaller value. The ND dataset even sees an excess of neutrinos, i.e. an unphysical negative oscillation amplitude[2]. The tension is handled by converging to a higher value for $\sin^2(2\theta_{13})$, i.e. the unphysical negative oscillation amplitude in the ND is recognised as overall underestimation of the reactor flux. In consequence, the overall flux is elevated and thus a larger deficit in the FDs and by this a larger oscillation amplitude is detected. The elevation of the overall normalisation can be seen when comparing figures 6.15c and 6.23c. The driving mechanism behind the elevation is the strong correlation in reactor flux between the detectors. A shown in table 6.10b, assuming a fully uncorrelated reactor flux across all detectors yields a value of $\sin^2(2\theta_{13})$ in between the single detector results. The assumption of uncorrelated detection efficiencies, i.e. an uncorrelated overall normalisation has only minor influence. In contrast, the assumption of a correlated energy scale, which is a more realistic scenario as argued before, increases the value of the oscillation amplitude further. This effect can also be illustrated by comparing figures 6.20 and 6.24. For both cases, one sees for the ND in figures 6.20c and 6.24c that the best-fit model includes an overall large upwards flux correction in addition to the correction of the spectral distortion around 5 MeV. This correction becomes necessary since the FDs, especially the high statistics FD1 dataset, is pulling the oscillation amplitude to a large value, while the ND sees initially an excess (cf. figure 6.23c). This tension in the ND is released by correcting the flux model upwards. While the situation looks similar for the ND in both cases, the FDs show a different behaviour. In the uncorrelated case, no overall flux correction, but only the correction around the spectral distortion at 5 MeV, can be seen for the FD1 in figure 6.24a. The FD2 shows a smaller overall correction and no spectral distortion at 5 MeV in

[2] For numerical reasons, $\sin^2(2\theta_{13})$ is treated as a real-valued variable in the oscillation analysis regardless of its proper definition as function with codomain [0,1], i.e. θ_{13} is not recognised as fundamental parameter.

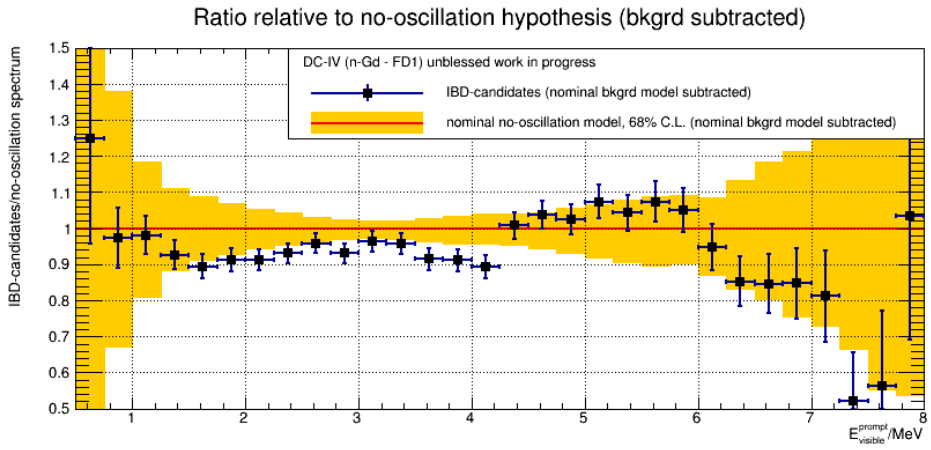

(a)

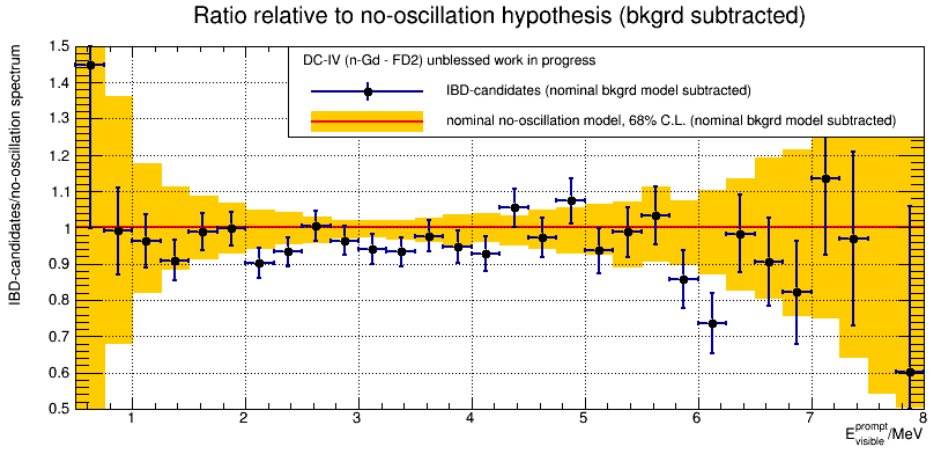

(b)

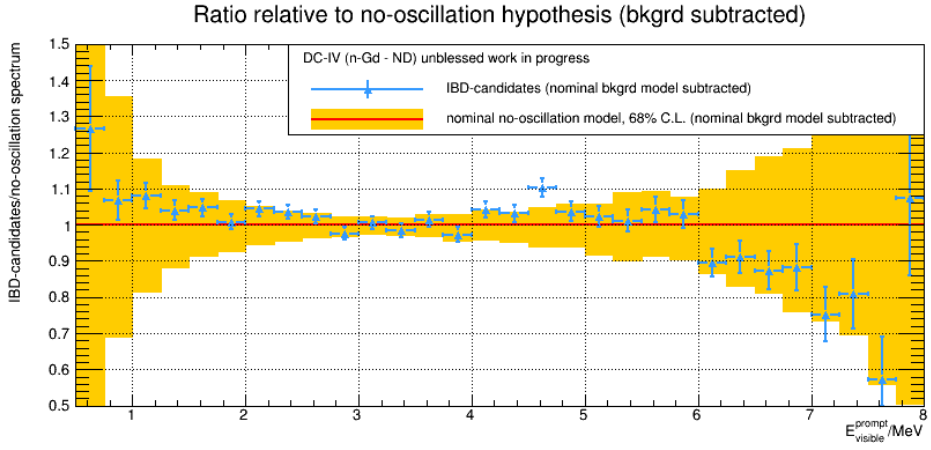

(c)

Figure 6.23: Oscillation analysis input model (ratio plots). The background subtracted ratio between the data and the no-oscillation prediction as derived in chapter 5 is shown for (a) the FD1, (b) the FD2 and (c) the ND. See figures 6.1, 6.2 and 6.3 for the absolute spectra used for these ratios.

figure 6.24b. The spectral distortion is hidden by the small statistics. In the correlated case, figures 6.20a and 6.20b show overall upwards flux corrections. Those corrections are induced from the ND flux correction due to the strong reactor flux correlation. In consequence, the oscillation amplitude has to be enlarged in the best-fit model to compensate the additional IBD-signal events in the FDs. This causes then a new upwards flux correction in the ND and so on. This feedback-loop finally settles at the value for the oscillation amplitude $\sin^2(2\theta_{13})$ as listed in table 6.10. The magnitude of the additional flux correction can be seen in the ND when comparing figures 6.20c and 6.24c. As listed in table 6.10b, a fully correlated energy scale across detectors increases the value of the oscillation amplitude. This can be understood

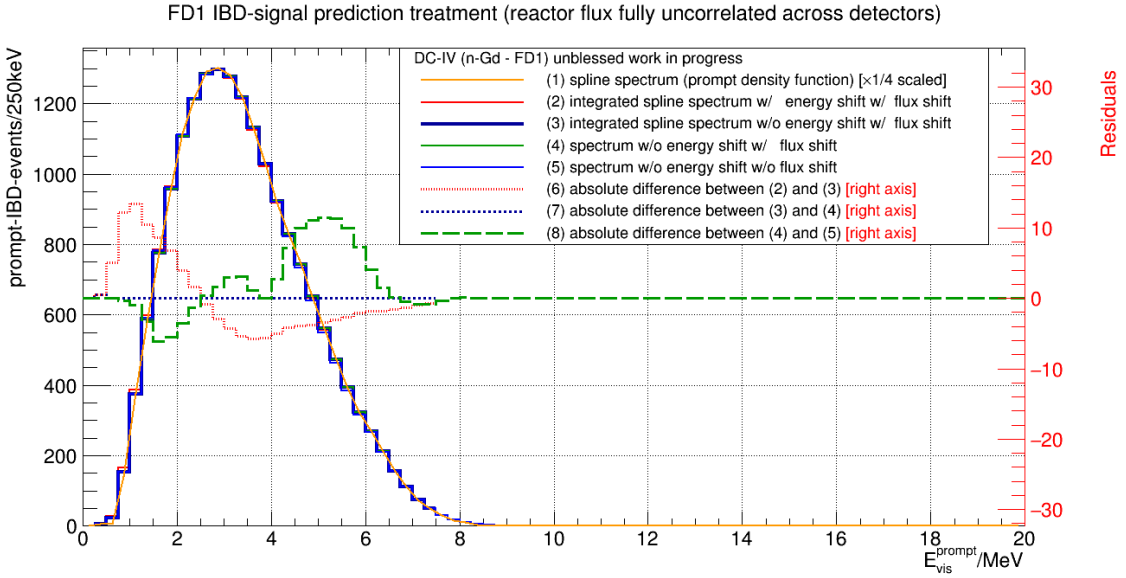

(a)

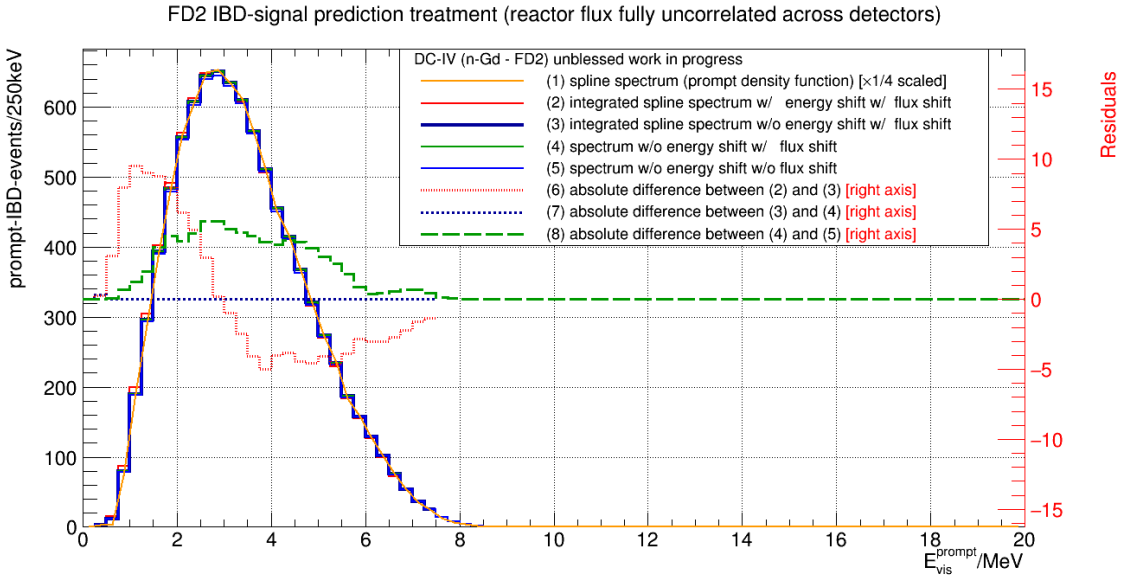

(b)

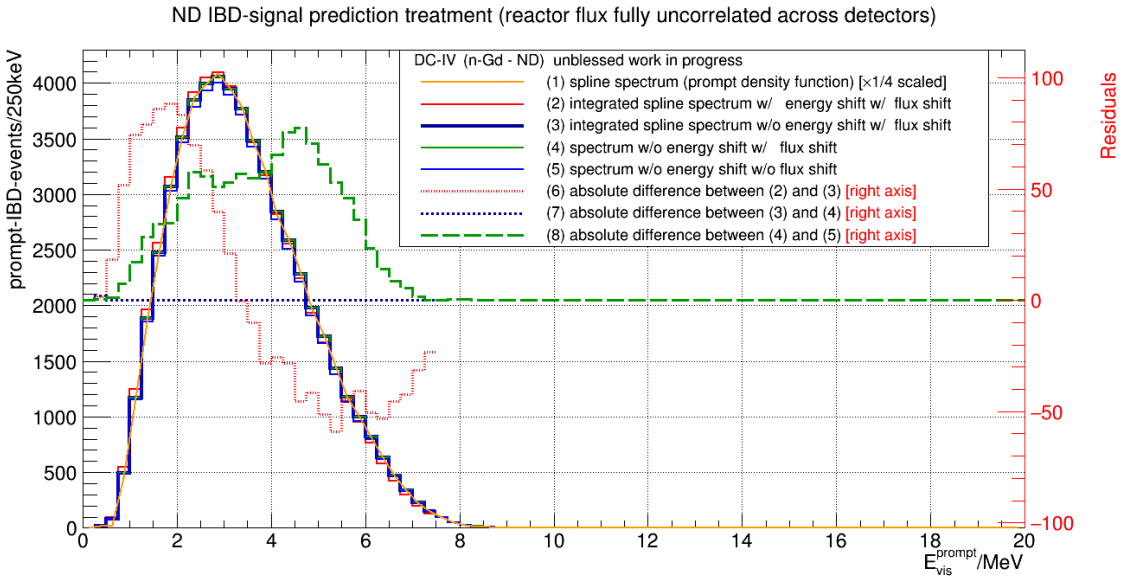

(c)

Figure 6.24: IBD-signal treatment in the Gd-IV oscillation analysis assuming no reactor flux correlation. The treatment is shown for the (a) FD1, (b) FD2, (c) ND. See figure 6.20 for the default analysis including reactor flux correlation.

by recognising that the energy scale corrections are compensating the feedback loop detector-wise to some extent. By introducing a correlation across detectors, an additional feedback loop is established.

This effect shows that in addition to the increased precision in the reactor flux prediction also the accuracy of the flux prediction is improved when using the near detector to measure the unoscillated neutrino flux. This measurement complements the prediction from the nuclear reactors itself. The newly commissioned ND is therefore an essential item for both, precision and accuracy of the Double Chooz experiment.

6.6 Cross-Checks of the Oscillation Analysis

To validate the correctness of the results of the oscillation analysis and to estimate internal systematic uncertainties, a series of cross-checks is performed. The outcomes are listed in table 6.11.

Firstly, the numerical precision requirement for convergence is sufficient. This was tested by using different start parameters for the optimisation routine within $\pm$ 100 % with respect to the default parameters. The deviations are negligible as they are in the order of $10^{-3}\,\sigma$. Uncertainties due to the constant oscillation parameters used in the three flavour oscillation model are estimated to be below $6.8 \cdot 10^{-2}\sigma$. The maximal deviation is achieved from assuming a two flavour versus three flavour oscillation model. Furthermore, the simplified treatment of neutrino oscillations in the reactor off sample FD1off, as explained in the end of section 6.3, shows negligible deviation. The effect is estimated to be below $9.2 \cdot 10^{-3}\sigma$, where this maximal deviation was achieved when no neutrino oscillations in the reactor off sample were

	$\sin^2(2\theta_{13})$	max. deviation
default analysis	0.1174 ± 0.0193	—
different seed	0.1174 ± 0.0194	$1.6 \cdot 10^{-3}\sigma$
oscillation model	0.1187 ± 0.0197	$6.8 \cdot 10^{-2}\sigma$
oscillation in FD1off dataset	0.1172 ± 0.0193	$9.2 \cdot 10^{-3}\sigma$
interpolation method	0.1176 ± 0.0193	0.01σ
covariance matrix patching	0.1174 ± 0.0193	$< 10^{-5}\sigma$
machine accuracy	0.1174 ± 0.0193	$< 10^{-5}\sigma$

Table 6.11: Overview of oscillation analysis cross-checks performed on the Gd-IV (Moriond) dataset. For each series of cross checks, the maximal deviation with respect to central value and uncertainty is listed. See text for explanations.

assumed. The systematic uncertainty arising from the choice of the interpolation method for the IBD-signal prediction spectrum is evaluated by exchanging the linear interpolation with a cubic spline interpolation. The deviation resulting from this is again negligible as it is $0.01\,\sigma$. Moreover, the influence of the patching level for negative eigenvalues of the defractionalised covariance matrices is tested. Varying the replacement value for negative eigenvalues by up to five orders of magnitude yields a negligible impact on $\sin^2(2\theta_{13})$ of less than $10^{-5}\,\sigma$. As final cross check, a possible bias by the machine accuracy is evaluated. For this, the interface to the database system is disabled. The interface is used to accelerate the computation process. By disabling the interface, numerical rounding is avoided. However, the impact is found to be negligible with less than $10^{-5}\,\sigma$. In summary, all additional systematic uncertainties introduced by the oscillation analysis itself are found to be negligible compared to the current level of precision.

A further series of cross-checks has been performed to evaluate the impact of different aspects of the input model presented in section 6.2. For this, certain assumptions of the input model have been altered as listed in table 6.12. Some of those alternations have already been discussed in previous sections and are not detailed again in this section.

Firstly, it can be seen that allowing the correlated background spectrum to have a non-flat shape does not influence the best-fit model. The shape model used for this cross-check is motivated by the identical model used previously in the hydrogen analysis [67] and is given as

$$s \cdot \exp(\epsilon \cdot E_{vis}) + c \text{ with } s, c, \epsilon \in \mathbb{R} \tag{6.23}$$

and a flat shape, i.e. $(s, c, \epsilon) = (1, 0, 0)$, is chosen as start value. With this alternative input model, the best-fit model still prefers a flat shape. The value for $\sin^2(2\theta_{13})$ also remains unchanged. The flat correlated background shape thus appears to describe the data well.

By leaving the detection efficiency, i.e. the MC normalisation, unconstrained in the input model, it is possible to perform a shape-only oscillation analysis as an additional cross-check. This analysis shows a good agreement with the default analysis, i.e. the rate+shape analysis, and yields a value for the oscillation amplitude of $\sin^2(2\theta_{13}) = 0.129$. The overall MC normalisation, when moving freely, now compensates the initial excess in the ND (cf. figure 6.23c) by deviating $6.5\,\sigma$ upwards. This energy-independent global scaling replaces the neutrino flux correction discussed in the end of section 6.5.

	$\sin^2(2\theta_{13})$	ND b^{rate}_{LiHe}	FD1 b^{rate}_{LiHe}	FD2 b^{rate}_{LiHe}
default analysis	0.117	$4.73^{+0.75}_{-0.71}$ d^{-1}	$0.61^{+0.13}_{-0.12}$ d^{-1}	
uncorr. β-n isotope rate	0.118	$4.74^{+0.75}_{-0.71}$ d^{-1}	$0.57^{+0.14}_{-0.13}$ d^{-1}	$0.71^{+0.21}_{-0.19}$ d^{-1}
β-n isotope rate constr.	0.123	$4.95^{+0.68}_{-0.65}$ d^{-1}	$0.75^{+0.11}_{-0.10}$ d^{-1}	
without FD1off dataset	0.119	$4.78^{+0.76}_{-0.72}$ d^{-1}	$0.64^{+0.13}_{-0.12}$ d^{-1}	
non-flat corr. bkgrd	0.117			
shape-only	0.129			
energy scale fully corr.	0.132			
reactor flux fully uncorr.	0.090			
detec. eff. fully uncorr.	0.113			
fixed reactor flux model	0.089			
fixed β-n bkgrd model	0.133			
fixed corr. bkgrd model	0.116			
fixed acc. bkgrd model	0.117			
fixed energy scale model	0.117			
fixed detec. eff. model	0.117			
fixed residual ν rate	0.117			
fixed neutrino mass diff.	0.117			
inv. mass hierarchy	0.121			

Table 6.12: Overview of oscillation analyses with alternative input models performed on the Gd-IV (Moriond) dataset. Changes of the uncertainty on $\sin^2(2\theta_{13})$ are negligible and thus not listed.

The simulation of a spectral distortion in a MC dataset did not show any influence on the β-n isotope rates. Thus, the earlier discussed effect of a smaller β-n rate with respect to the input values may indicate an overestimated β-n isotope rate in the FDs rather than an issue due to the spectral distortion. Indeed, all developed methods to estimate the β-n isotope rate have certain limitations that imply such possible overestimations [88]. Therefore, by treating the β-n isotope rates unconstrained, the oscillation analysis is less prone for a bias caused by this overestimation, as discussed earlier. To estimate the possible bias on $\sin^2(2\theta_{13})$ caused by the overestimation, the constraints on the β-n isotope rates of (5.01 ± 1.43) d^{-1} in the ND and $(0.97^{+0.41}_{-0.16})$ d^{-1} in the FDs are included in the input model. They cause the β-n isotope rates to converge to a higher value. Consequently, the oscillation amplitude converges towards a higher value of $\sin^2(2\theta_{13}) = 0.123$ to compensate the additional IBD candidate events. The result shows that at the current precision level, the bias that could be introduced by the problematic β-n rate estimation would be minor.

When allowing for different β-n isotope rates in the FDs, the FD1 shows a slightly smaller rate of $0.57^{+0.14}_{-0.13}$ d^{-1} while the FD2 prefers a higher rate of $0.71^{+0.21}_{-0.19}$ d^{-1} compared to a rate of $0.61^{+0.13}_{-0.12}$ d^{-1} when combining the two FD datasets. The individual rates agree well with the combined rate showing that the assumption of identical β-n isotope rates in the FDs is justified.

As one can see from an oscillation analysis performed without the background-pure FD1off dataset, the FD1off dataset points towards a slightly smaller β-n isotope rate: Without the FD1off dataset, the β-n isotope rate in the ND is found to be $4.78^{+0.76}_{-0.72}$ d^{-1} compared to $4.73^{+0.75}_{-0.71}$ d^{-1}. In the FD, the β-n isotope rate without the FD1off dataset is $0.64^{+0.13}_{-0.12}$ d^{-1} compared to $0.61^{+0.13}_{-0.12}$ d^{-1}. These findings support the indications for overestimated β-n isotope background rates discussed above.

It is very important to allow the β-n isotope prediction to be optimised unconstrained in the oscillation analysis. This can be seen by changing the input model to allow for no correction in the β-n isotope prediction. The result is a 14 % larger oscillation amplitude, i.e. a $0.84\,\sigma$ effect. With exception of the reactor flux model, which is responsible of handling the spectral distortion and at the same time the initial excess in the ND as detailed earlier, fixing all other parts of the input model does not show any impact on the oscillation amplitude (cf. table 6.12). This is understandable by recognising that all parameters connected to those effects are almost unchanged between the input model and the best-fit model as presented in table 6.8. By this, one can also infer that the best-fit model shows only discrepancies to the input model in terms of the β-n isotope rate in the FDs and the reactor flux spectrum shape. All other aspects appear to describe the data well.

Finally, the input model is altered by assuming the inverted neutrino mass hierarchy (cf. figure 2.4 and table 2.1). The corresponding effective value for the mass splitting of $(\Delta m^2_{ee})_{IH} = (2.53 \pm 0.09) \cdot 10^{-3}\text{eV}^2$ is again taken from [36] using the conversion method proposed in [106]. As seen in figure 2.2, the mass hierarchy has a small influence on the oscillation probability curve. The oscillation analysis assuming inverted mass hierarchy yields indeed only a slightly different value of $\sin^2(2\theta_{13}) = 0.121 \pm 0.020$.

6.7 Study of Future Precision

The results presented in this chapter mark the begin of the two detector phase of the Double Chooz experiment. The experiment is currently collecting additional data and is improving further the analysis of systematics. In order to estimate future improvements and in order to identify crucial systematic effects, the precision on $\sin^2(2\theta_{13})$ is investigated for different scenarios.

Firstly, it is investigated how the precision improves when certain systematic effects are understood perfectly. For this study, a series of oscillation analyses is performed using the Gd-IV datasets. Each time, the input model is altered by setting and fixing the parameters belonging to a certain systematic effect to the values of the best-fit model derived in section 6.5. By this, the uncertainties caused by the systematic effect is eliminated, i.e. perfect knowledge on the systematic effect is assumed.

As shown in figure 6.25, the uncertainties of eight systematic effects have been eliminated in the input model one by one. Perfect knowledge on the accidental or correlated backgrounds has only negligible impact (<0.1 %) on the overall precision on $\sin^2(2\theta_{13})$. Those background spectra also show almost no correlation with the oscillation amplitude in figure 6.22. Likewise, elimination of the uncertainty in the residual neutrino rate of the reactor-off dataset causes an reduction of less than 0.1 %. As before, this parameter is strongly uncorrelated to the oscillation amplitude in figure 6.22. Moderate improvements are gained from eliminating the uncertainties in the neutrino mass splitting and the overall MC normalisation, i.e. the detection efficiency and the physics cuts inefficiencies (both 5 %). Having no uncertainty in the

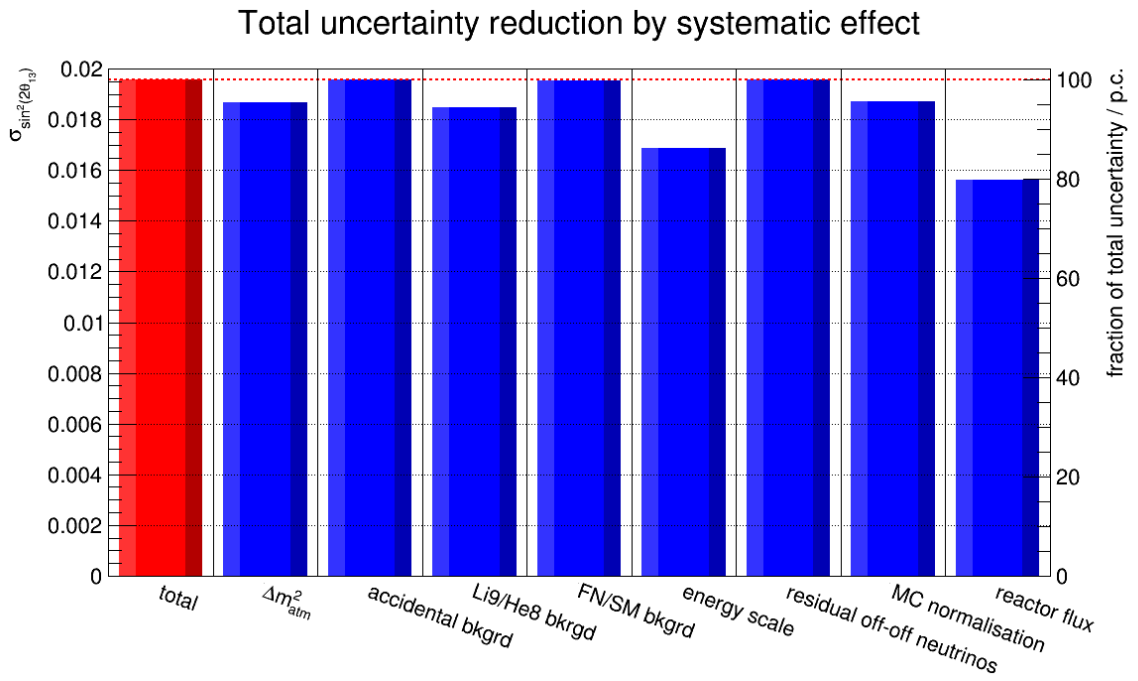

Figure 6.25: Reduction of total uncertainty by systematic effects. For each single effect, full reduction of uncertainties is assumed. The statistical uncertainty is kept unchanged.

β-n spectrum also moderately improves the total uncertainty by 6 %. This can be understood from recognising the high similarity between the β-n spectrum and the IBD-signal spectrum shape, as illustrated earlier. Perfect understanding of the energy scale causes in turn a sizeable improvement of 15 %. To exploit this, a dedicated calibration campaign with unprecedented statistics is currently carried out in both detectors. Moreover, employing an energy scale treatment similar to the Gd-III model, i.e. including knowledge on the charge non-linearities into the input model, will reduce the uncertainty as well. Another large improvement of 20 % is achieved if the reactor flux uncertainties are eliminated. By collecting more ND data it is possible to replace the reactor flux prediction by using the ND data as effective prediction. By this, reactor flux uncertainties can indeed be eliminated from the input model in the future.

Secondly, the improvement in precision due to the increase in statistics is investigated. For this study, MC datasets with various statistics are evaluated. The systematic uncertainties for all MC datasets are those of the input model described in section 6.2. Figure 6.26 shows that within the next 3 years of data taking, a precision of 0.013 can be achieved. The timespan of 3 additional years is indeed the currently targeted runtime for the Double Chooz experiment. By adding hydrogen data to the oscillation analysis further improvement is expected. The hydrogen analysis performed with the oscillation analysis tool developed in this work is currently under preparation [118]. Additionally, the FD1 dataset is currently extended by processing additional, already recorded, data that was not analysed yet in favour of the recent two detector phase data.

By looking at the asymptotic behaviour of the curve depicted in figure 6.26, the total uncertainty can be split into a statistical part of ± 0.019 and a systematic part of ± 0.004. This clearly shows that the Double Chooz experiment is, with the current Gd-IV (Moriond)

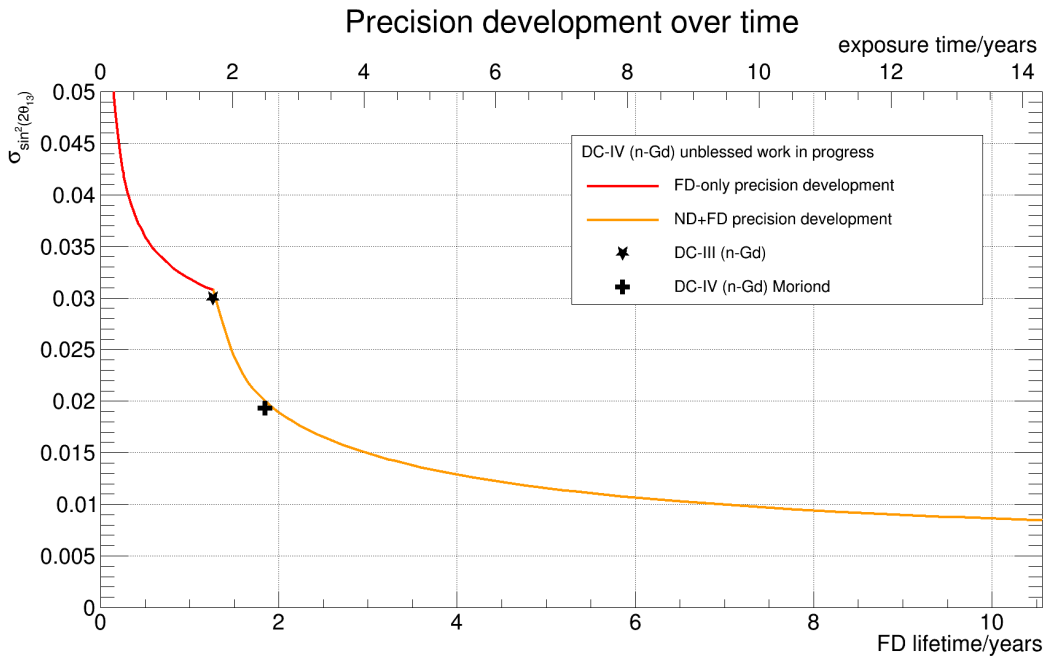

Figure 6.26: Estimate of the uncertainty on $\sin^2(2\theta_{13})$ over time. The input model described in section 6.2 is used while the statistics are varied as a function of time. The upper time axis shows the exposure time, i.e. real time, excluding the far detector upgrade phase between the end of FD-I phase and the start of FD-II plus ND phase. The lower axis shows the effective data taking time of the FD. ND statistics is scaled in the same way as the FD statistics assuming the current ratio between FD-II lifetime and ND lifetime. The red curve shows the development during the single detector phase, the orange curve shows the two detector phase. The uncertainties of the Gd-III and Gd-IV (Moriond) datasets are shown for comparison.

model and datasets, statistics dominated. Thus, the processing of additional single detector data and the recording of further two detector data, as well as a more detailed treatment of the energy scale systematics will improve the future precision substantially. Moreover, the collection of additional data will also increase the background sample statistics which in turn will reduce the model uncertainty for those backgrounds. This improves the precision on the oscillation amplitude in addition mildly as shown in figure 6.25. Finally, the currently collected high statistics calibration campaign data will reduce the model uncertainty of the MC normalisation which yields again an additional mild improvement. The results of the improved analysis are under preparation and expected to be published in winter 2016/2017.

Chapter 7

Conclusion and Outlook

The first part of this thesis discussed the design, installation and commissioning of a data handling system for the two detector phase of the Double Chooz experiment (cf. chapter 4). To match the new requirements of the two detector phase, the system was fully redesigned with respect to the previous system. For the first time, the data handling system now provides a redundantly backed setup with a variety of fail-safe mechanisms, diagnostics and coherent data on all instances. The new data handling system guarantees uninterrupted support of the data taking in the laboratories and the data processing in the central computing facility. The data handling system shows an overall good performance with the optimal performance reached for more than 97 % of the time. Its impact on data taking is negligible with less than 1.5 sec downtime per day. Moreover, the data capacity appears to be well suited for the lifespan of the Double Chooz experiment. The system is moreover used as a monitoring tool for the entire experiment. It is capable of detecting a variety of detector issues and supplements the primary monitoring tools.

The second part of this thesis described the development of a new oscillation analysis using neutrino rate and spectral shape information. As presented in chapter 6, the new analysis improves the χ^2 based oscillation analysis by modelling several aspects more detailed: Its novel adaptive modelling of shape uncertainties gives new insights into the mechanism of the oscillation analysis itself. The accuracy of the new oscillation analysis is improved by the Poissonian modelling of statistical uncertainties as well as the utilisation of the full three flavour oscillation model and the direct application of energy scale corrections.

The analysis was successfully validated in a Monte Carlo data challenge before data was unblinded. For the first time, two detector data of the Double Chooz experiment was analysed in this oscillation analysis. The new data yields a value of

$$\begin{aligned} \sin^2(2\theta_{13}) &= 0.117 \pm 0.019\ (\text{stat.}) \pm 0.004\ (\text{sys.}) \\ &= 0.117 \pm 0.019\ (\text{tot.}) \end{aligned} \tag{7.1}$$

assuming $\Delta m^2_{ee} = (2.44 \pm 0.09) \cdot 10^{-3}\text{eV}^2$ and normal mass hierarchy. The uncertainty in equation 7.1 is improved by 37 % compared to the previous single detector measurement. The new data allows the Double Chooz experiment to confirm the existence of reactor antineutrino oscillations by excluding the no-oscillation hypothesis with a confidence of 6.0 standard deviations.

By comparing the new two detector result of the Double Chooz experiment with the latest results of the RENO and Daya Bay experiments in figure 7.1 one can see that the statistics

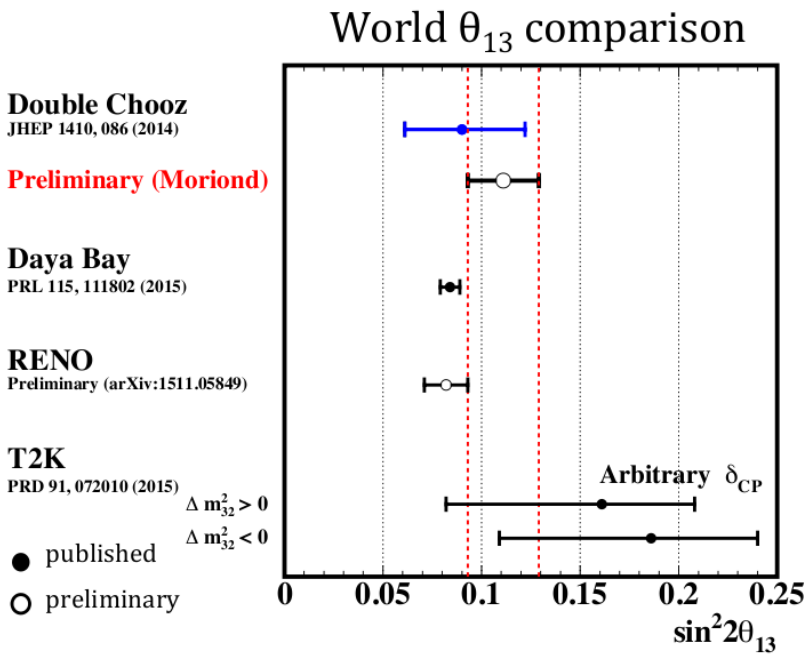

Figure 7.1: Global comparison of $\sin^2(2\theta_{13})$ measurements [46, p. 27]. The single detector result and preliminary double detector result (this work) of the Double Chooz experiment are compared to the results of the reactor experiments RENO and Daya Bay as well as the accelerator experiment T2K.

of the dataset analysed in this work are not sufficient to achieve similar significance as the RENO and Daya Bay experiments. As visible from figure 6.26, it is in principle possible to reach a similar significance by accumulating additional data over time. However the required time of more than 10 years is far beyond the currently foreseen runtime of the Double Chooz experiment. An extension of the fiducial volume to the γ-catcher volume (cf. section 3.2) by including hydrogen data will allow a faster accumulation of statistics. This analysis is currently under preparation.

The new central value for the oscillation amplitude is in better agreement with long baseline neutrino experiments while it shows a mild deviation from the current world average of reactor experiments as shown in figure 7.1. Additional data which is currently collected will show whether this upwards deviation becomes more significant. At the same time, it was found that the high rate of IBD candidates in the ND (cf. figure 6.23c) which is driving the high value of the oscillation amplitude (cf. end of section 6.5) is related to a possible underestimation of the Gd-fraction in the ND. Recent studies show that some previously undetected Gd-admixture in the γ-catcher volume of the ND might cause a higher neutron detection efficiency in the ND [119]. The result of a currently ongoing precise evaluation of the magnitude of this admixture can be an upwards correction of the MC signal normalisation in the ND. However, the size of the correction is unclear at the moment.

"Leute, ich hab's doch nicht."

Anselm Stüken

Appendix

A Structure of the Oscillation Analysis Programme

<table>
<tr><td colspan="5">main programme</td></tr>
<tr><td colspan="5">llhmotherfitter
combines all individual detectors and propagates common parameters/correlations to them</td></tr>
<tr><td colspan="5">3 llhfitter objects (one per detector/dataset)
combines individual signal and background predictions with data</td></tr>
<tr><td>reactorprediction
reactor B1</td><td>reactorprediction
reactor B2</td><td>bkgrdprediction
accidentals</td><td>bkgrdprediction
β-n isotopes</td><td>fnsmprediction
correlated bkgrd</td></tr>
<tr><td colspan="2">oscprobcalculator
interface to GLoBES</td><td colspan="3"></td></tr>
</table>

Table A.1: Overview of the oscillation analysis programme structure. Depicted are the main C++ class objects and their interplay. Helper classes are omitted.

B Fractional Reactor Flux Covariance Matrices

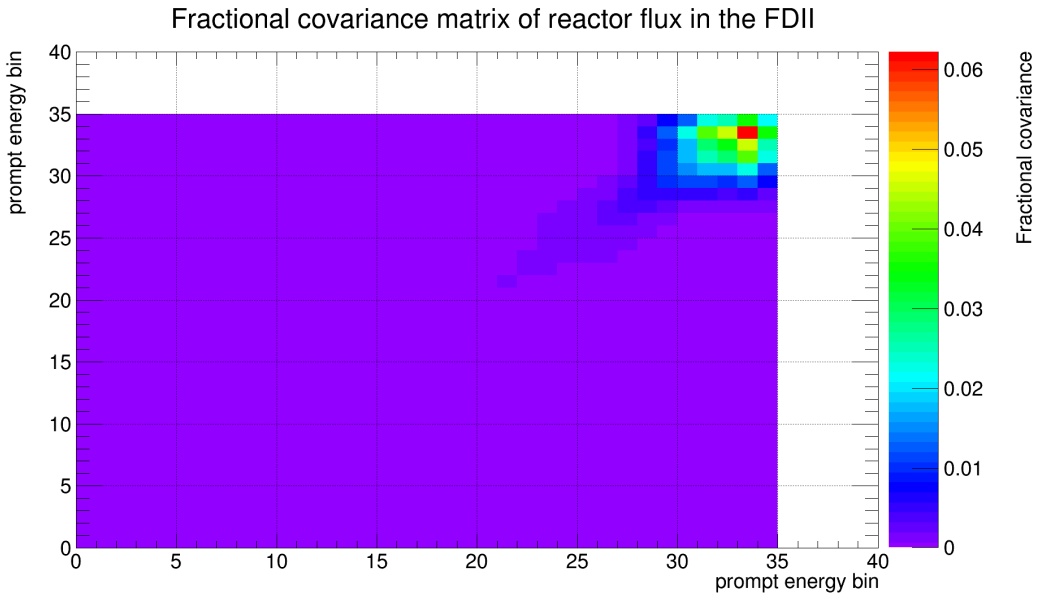

(a)

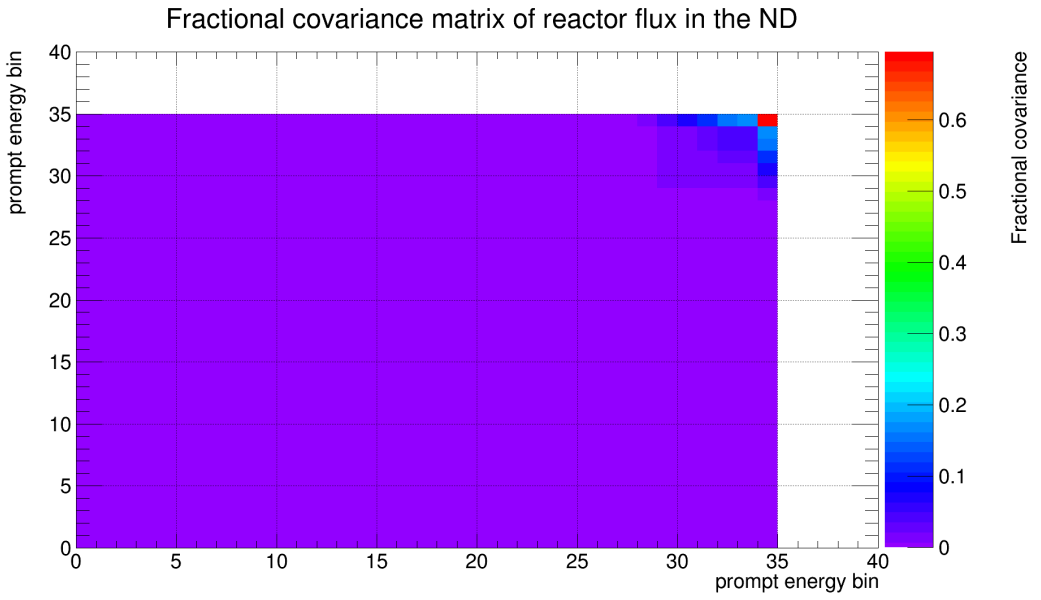

(b)

Figure B.1: Additional fractionalised covariance matrices of the neutrino signal. The (a) FD2 and (b) ND datasets are shown. The FD1 dataset and further explanations can be found in figure 6.5.

C Accidental Background Spectra

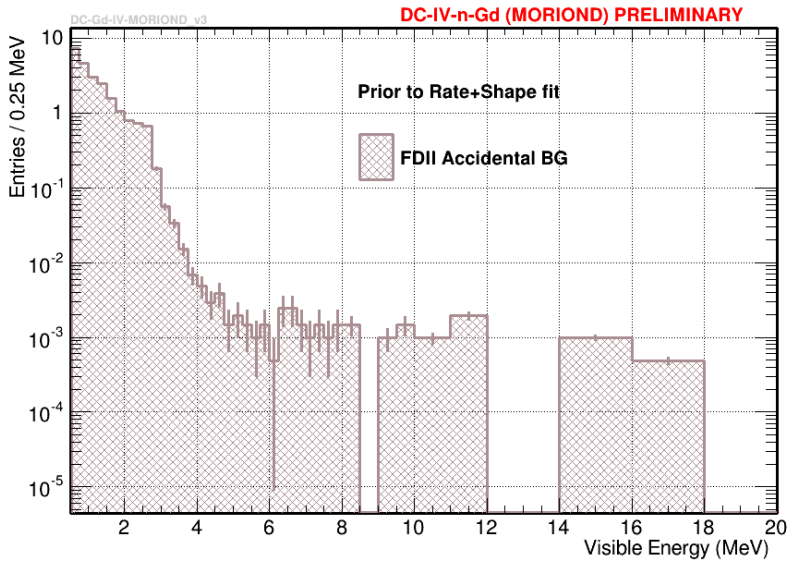

(a)

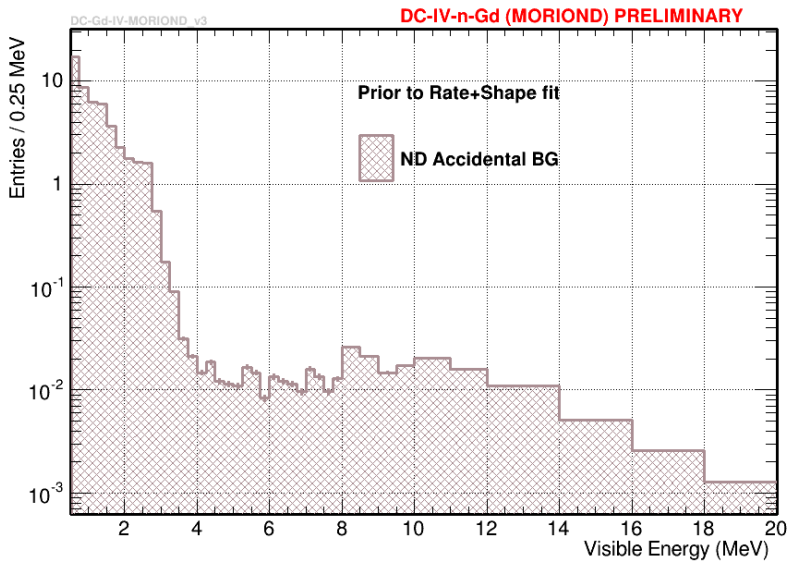

(b)

Figure C.1: Additional accidental background energy spectra of the (a) FD-II and (b) ND datasets [42]. The FD-I dataset can be found in figure 3.11a.

References

[1] R. Davis Jr., D.S. Harmer and K.C. Hoffman, Search for Neutrinos from the Sun, *Physical Review Letters* **20**: 1205–1209 (1968), https://doi.org/10.1103/PhysRevLett.20.1205.

[2] Y. Ashie *et al.* (Super-Kamiokande Collaboration), Measurement of atmospheric neutrino oscillation parameters by Super-Kamiokande I, *Physical Review D* **71**(11): 112005 (2005), https://doi.org/10.1103/PhysRevD.71.112005.

[3] Q.R. Ahmad *et al.* (SNO Collaboration), Direct Evidence for Neutrino Flavor Transformation from Neutral-Current Interactions in the Sudbury Neutrino Observatory, *Physical Review Letters* **89**(1): 011301 (2002), https://doi.org/10.1103/PhysRevLett.89.011301.

[4] P. Adamson *et al.* (MINOS Collaboration), Improved Search for Muon-Neutrino to Electron-Neutrino Oscillations in MINOS, *Physical Review Letters* **107**(18): 181802 (2011), https://doi.org/10.1103/PhysRevLett.107.181802.

[5] K. Abe *et al.* (T2K Collaboration), Indication of Electron Neutrino Appearance from an Accelerator-Produced Off-Axis Muon Neutrino Beam, *Physical Review Letters* **107**(4): 041801 (2011), https://doi.org/10.1103/PhysRevLett.107.041801.

[6] Y. Abe *et al.* (Double Chooz Collaboration), Indication of Reactor $\bar{\nu}_e$ Disappearance in the Double Chooz Experiment, *Physical Review Letters* **108**(13): 131801 (2012), http://dx.doi.org/10.1016/j.phpro.2014.12.071.

[7] F.P. An *et al.* (Daya Bay Collaboration), Observation of electron-antineutrino disappearance at Daya Bay, *Physical Review Letters* **108**: 171803 (2012), https://doi.org/10.1103/PhysRevLett.108.171803.

[8] J.K. Ahn *et al.* (RENO Collaboration), Observation of Reactor Electron Antineutrino Disappearance in the RENO Experiment, *Physical Review Letters* **108**(19): 191802 (2012), https://doi.org/10.1103/PhysRevLett.108.191802.

[9] K. Abe *et al.* (T2K Collaboration), Observation of Electron Neutrino Appearance in a Muon Neutrino Beam, *Physical Review Letters* **112**: 061802 (2014), https://doi.org/10.1103/PhysRevLett.112.061802.

[10] Y. Abe *et al.* (Double Chooz Collaboration), Improved measurements of the neutrino mixing angle θ_{13} with the Double Chooz detector, *Journal of High Energy Physics* **086**(10) (2014), http://dx.doi.org/10.1007/JHEP10(2014)086 Erratum-ibid. [11].

[11] Y. Abe *et al.* (Double Chooz Collaboration), Erratum to: Improved measurements of the neutrino mixing angle θ_{13} with the Double Chooz detector, *Journal of High Energy Physics* **074**(02) (2015), http://dx.doi.org/10.1007/JHEP02(2015)074.

[12] F. Ardellier *et al.*, Letter of Intent for Double-CHOOZ: a Search for the Mixing Angle θ_{13}, *arXiv:hep-ex/0405032* (2004).

[13] F. Ardellier *et al.*, Double Chooz: A Search for the Neutrino Mixing Angle θ_{13}, *arXiv:hep-ex/0606025* (2006).

[14] S. Schoppmann, Statistical Methods for the Interpretation of Recent Results in Neutrino Physics, *Master's thesis*, Rheinisch-Westfälische Technische Hochschule Aachen, 2012.

[15] R. Halleux, J. Vandersmissen, A. Despy-Mayer and G. Vanpaemel, *Histoire des Sciences en Belgique, 1815-2000*, La Renaissance du Livre, Bruxelles, 2 edition, 2001, 109–121.

[16] C.L. Cowan Jr., F. Reines, F.B. Harrison, H.W. Kruse and A.D. McGuire, Detection of the Free Neutrino: a Confirmation, *SCIENCE* **124**: 103–104 (1956), http://dx.doi.org/10.1126/science.124.3212.103.

[17] K.A. Olive *et al.* (Particle Data Group), Review of Particle Physics, *Chinese Physics C* **38**: 090001 (2014), http://dx.doi.org/10.1088/1674-1137/38/9/090001.

[18] G. Danby, J.-M. Gaillard, K. Goulianos, L.M. Lederman, N. Mistry, M. Schwartz and J. Steinberger, Observation of High-Energy Neutrino Reactions and the Existence of Two Kinds of Neutrinos, *Physical Review Letters* **9**(1): 36–44 (1962), https://doi.org/10.1103/PhysRevLett.9.36.

[19] K. Kodama *et al.* (DONUT Collaboration), Observation of tau neutrino interactions, *Physics Letters B* **504**: 218–224 (2001), http://dx.doi.org/10.1016/S0370-2693(01)00307-0.

[20] B. Pontecorvo, Mesonium and Antimesonium, *Soviet physics, Journal of Experimental and Theoretical Physics* **6**: 429–431 (1958), reproduced and translated from [22].

[21] B. Pontecorvo, Inverse Beta Decay and Nonconservation of Lepton Charge, *Soviet physics, Journal of Experimental and Theoretical Physics* **7**: 172–173 (1958), reproduced and translated from [23].

[22] B. Pontecorvo, Мезоний и антимезоний, Журнал Экспериментальной и Теоретической Физики **33**: 549–551 (1957).

[23] B. Pontecorvo, Обратное β-процессы и несохранение лептонно заряда, Журнал Экспериментальной и Теоретической Физики **34**: 247–249 (1958).

[24] Z. Maki, M. Nakagawa and S. Sakata, Remarks on the Unified Model of Elementary Particles, *Progress of Theoretical Physics* **28**(5): 870–880 (1962), http://dx.doi.org/10.1143/PTP.28.870.

[25] S. Gasiorowicz, *quantum physics*, volume 1, John Wiley and Sons, Inc., 1974.

[26] D.H. Perkins, *Introduction to High Energy Physics*, volume 3, Addison-Wesley Publishing Company, Inc., 1987.

[27] J.A. Thomas and P.L. Vahle, editors, *Neutrino Oscillations - Present Status and Future Plans*, World Scientific Publishing, 2008.

[28] G. Mention, Étude des sensibilité et bruits de fond de l'expérience Double Chooz pour la recherche du paramètre de mélange leptonique θ_{13}, *PhD thesis*, Université Claude Bernard Lyon 1, 2005, `https://tel.archives-ouvertes.fr/tel-00010528`.

[29] H. Nunokawa, S. Parke and J.W.F. Valle, CP Violation and Neutrino Oscillation, *Progress in Particle and Nuclear Physics* **60**: 338–402 (2007), `http://dx.doi.org/10.1016/j.ppnp.2007.10.001`.

[30] O. Mena and S. Parke, Unified Graphical Summary of Neutrino Mixing Parameters, *Physical Review D* **69**(11): 117301 (2004), `https://doi.org/10.1103/PhysRevD.69.117301`.

[31] S. Parke, What is Δm^2_{ee}?, *Physical Review D* **93**: 053008 (2016), `https://doi.org/10.1103/PhysRevD.93.053008`.

[32] S. Abe *et al.* (The KamLAND Collaboration), Precision Measurement of Neutrino Oscillation Parameters with KamLAND, *Physical Review Letters* **100**(22): 221803 (2008), `https://doi.org/10.1103/PhysRevLett.100.221803`.

[33] B. Aharmim *et al.* (SNO Collaboration), Combined analysis of all three phases of solar neutrino data from the Sudbury Neutrino Observatory, *Physical Review C* **88**: 025501 (2013), `https://doi.org/10.1103/PhysRevC.88.025501`.

[34] G. Bellini *et al.* (Borexino Collaboration), Precision Measurement of the Be7 Solar Neutrino Interaction Rate in Borexino, *Physical Review Letters* **107**: 141302 (2011), `https://doi.org/10.1103/PhysRevLett.107.141302`.

[35] R. Wendell *et al.* (Super-Kamiokande Collaboration), Atmospheric neutrino oscillation analysis with subleading effects in Super-Kamiokande I, II, and III, *Physical Review D* **81**: 092004 (2010), `https://doi.org/10.1103/PhysRevD.81.092004`.

[36] P. Adamson *et al.* (MINOS Collaboration), Combined analysis of ν_μ disappearance and $\nu_\mu \rightarrow \nu_e$ appearance in MINOS using accelerator and atmospheric neutrinos, *Physical Review Letters* **112**: 191801 (2014), `https://doi.org/10.1103/PhysRevLett.112.191801`.

[37] M.H. Ahn *et al.* (K2K Collaboration), Measurement of neutrino oscillation by the K2K experiment, *Physical Review D* **74**(7): 072003 (2006), `https://doi.org/10.1103/PhysRevD.74.072003`.

[38] K. Abe *et al.* (T2K Collaboration), Measurement of Muon Antineutrino Oscillations with an Accelerator-Produced Off-Axis Beam, *Physical Review Letters* **116**: 181801 (2016), `https://doi.org/10.1103/PhysRevLett.116.181801`.

[39] Double Chooz Collaboration, 2009 power plant site, http://www.dchooz.org/DocDB/cgi-bin/private/DocumentDatabase, 2009, Double Chooz Internal Document 1037-v1.

[40] Central Intelligence Agency, The World Factbook 2012, https://www.cia.gov/library/publications/the-world-factbook/index.html, 2012.

[41] M. Vivier, Double Chooz geodetic survey: report and results, http://www.dchooz.org/DocDB/cgi-bin/private/DocumentDatabase, 2015, Double Chooz Internal Document 6286-v1.

[42] Double Chooz Collaboration, CATS, http://doublechooz.in2p3.fr/Private/Working_Groups/Analysis/DC-IV/CATS/, 2016, Double Chooz Internal Document.

[43] D. Lhuillier, Reactor $\bar{\nu}_e$ spectra, 2015, Seminar of the RWTH Aachen Particle Physics DFG Graduate School.

[44] Nobelprize.org. Nobel Media AB 2014, Energy from Matter, http://www.nobelprize.org/educational/physics/energy/fission_2.html, 2016.

[45] H. Gomez, Muon background studies for shallow depth Double - Chooz near detector, http://www.dchooz.org/DocDB/cgi-bin/private/DocumentDatabase, 2015, Double Chooz Internal Document 6006-v1.

[46] M. Ishitsuka, New Results of Double Chooz, in *51st Rencontres de Moriond EW Session*, 2016.

[47] C. Bauer *et al.*, Qualification tests of 474 photomultiplier tubes for the inner detector of the Double Chooz experiment, *Journal of Instrumentation* **6**: P06008 (2011), http://dx.doi.org/10.1088/1748-0221/6/06/P06008.

[48] S. Wagner, Ionization Quenching by Low Energy Electrons in the Double Chooz Scintillators, *Master's thesis*, Ruprecht-Karls Universität Heidelberg – Max-Planck-Institut für Kernphysik, 2010.

[49] C. Aberle, C. Buck, F.X. Hartmann and S. Schönert, Light yield and energy transfer in a new Gd-loaded liquid scintillator, *Chemical Physics Letters* **516**: 257–262 (2011), http://dx.doi.org/10.1016/j.cplett.2011.09.067.

[50] A. Givaudent, Near detector measures of the Outer Veto, private communication, 2015.

[51] E. Blucher, L.L. Camilleri, E. Conover, M. Dierckxsens, A. Franke, C. Mariani, A. Norrick, M. Toups and L.A. Winslow, OV electronics and test, http://www.dchooz.org/DocDB/cgi-bin/private/DocumentDatabase, 2011, Double Chooz Internal Document 1400-v3.

[52] M. Dracos and L. Kalousis, The Inner Veto Light Injection System, http://www.dchooz.org/DocDB/cgi-bin/private/DocumentDatabase, 2010, Double Chooz Internal Document 1772-v3.

[53] P. Wahnon, Absolute light level measurements of the Light Injection Calibration System (LICS), http://www.dchooz.org/DocDB/cgi-bin/private/DocumentDatabase, 2010, Double Chooz Internal Document 1652-v1.

[54] I. Ostrovskiy, Guide tube IRR, http://www.dchooz.org/DocDB/cgi-bin/private/DocumentDatabase, 2009, Double Chooz Internal Document 887-v1.

[55] M. D'Agostino, J. Reichenbacher, M. Goodman, J. Busenitz and Z. Djurcic, Z-axis Deployment System IRR, http://www.dchooz.org/DocDB/cgi-bin/private/DocumentDatabase, 2011, Double Chooz Internal Document 2419-v2.

[56] R. Brun and F. Rademakers, ROOT – An object oriented data analysis framework, *Nuclear Instruments and Methods in Physics Research A* **389**(1–2): 81–86 (1997), http://dx.doi.org/10.1016/S0168-9002(97)00048-X.

[57] K. Amako *et al.*, Geant4 developments and applications, *IEEE Transactions on Nuclear Science* **53**(1): 270–278 (2006), http://dx.doi.org/10.1109/TNS.2006.869826.

[58] S. Dazeley *et al.*, Generic Liquid-scintillator Anti-Neutrino Detector (GenericLAND) Geant4 simulation, http://neutrino.phys.ksu.edu/~GLG4sim/.

[59] A. Cabrera, DCRoSS, http://www.dchooz.org/DocDB/cgi-bin/private/DocumentDatabase, 2007, Double Chooz Internal Document 3773-v1.

[60] M. Fechner, CT Production Architecture, http://www.dchooz.org/DocDB/cgi-bin/private/DocumentDatabase, 2008, Double Chooz Internal Document 217-v1.

[61] P. Vogel and J.F. Beacom, Angular distribution of neutron inverse beta decay, $\overline{\nu}_e + p \rightarrow e^+ + n$, *Physical Review D* **60**: 053003 (1999), https://doi.org/10.1103/PhysRevD.60.053003.

[62] P. Novella, The Antineutrino Energy Structure in Reactor Experiments, *Advances in High Energy Physics* **2015**: 364392 (2015), http://dx.doi.org/10.1155/2015/364392.

[63] K. Wisshak, F. Voss, F. Käppeler, K. Gruber, L. Kazakov, N. Kornilov, M. Uhl and G. Reffo, Stellar neutron capture cross sections of the Gd isotopes, *Physical Review C* **52**: 2762–2770 (1995), https://doi.org/10.1103/PhysRevC.52.2762.

[64] D.L. Sastry and S. Jnanananda, Slow neutron capture gamma rays from samarium and gadolinium, *Journal of Scientific Instruments* **41**: 497–500 (1964), http://dx.doi.org/10.1088/0950-7671/41/8/303.

[65] R.E. Bell and L.G. Elliott, Gamma-Rays from the Reaction $H^1(n,\gamma)D^2$ and the Binding Energy of the Deuteron, *Physical Review* **79**(2): 282–285 (1950), https://doi.org/10.1103/PhysRev.79.282.

[66] Y. Abe *et al.* (Double Chooz Collaboration), First measurement of θ_{13} from delayed neutron capture on hydrogen in the Double Chooz experiment, *Physics Letters B* **723**: 66–70 (2013), http://dx.doi.org/10.1016/j.physletb.2013.04.050.

[67] Y. Abe *et al.* (Double Chooz Collaboration), Measurement of θ_{13} in Double Chooz using neutron captures on hydrogen with novel background rejection techniques, *Journal of High Energy Physics* **01**: 163 (2016), http://dx.doi.org/10.1007/JHEP01(2016)163.

[68] A. Remoto, Correlated background and impact on the measurement of θ_{13} with the Double Chooz detector, *PhD thesis*, Université de Nantes, 2012, https://tel.archives-ouvertes.fr/tel-00821629.

[69] G.A. Sawyer and M.L. Wiedenbeck, Decay Constants of K^{40}, *Physical Review* **79**(3): 490–494 (1950), http://dx.doi.org/10.1103/PhysRev.79.490.

[70] Y. Abe *et al.* (Double Chooz Collaboration), Characterization of the Spontaneous Light Emission of the PMTs used in the Double Chooz Experiment, *Journal of Instrumentation* **11**: P08001 (2016), http://dx.doi.org/10.1088/1748-0221/11/08/P08001.

[71] Oracle Corporation, My Structured Query Language (MySQL), http://dev.mysql.com/doc, 2016.

[72] A. Franke, Migration of DC MySQL to a High-Availability Implementation, http://www.dchooz.org/DocDB/cgi-bin/private/DocumentDatabase, 2011, Double Chooz Internal Document 1945-v3.

[73] A. Franke, Guide to Administering the DC High-Availability MySQL Service, http://www.dchooz.org/DocDB/cgi-bin/private/DocumentDatabase, 2011, Double Chooz Internal Document 1980-v4.

[74] A. Franke, Implementation of Periodic Backups of DC MySQL, http://www.dchooz.org/DocDB/cgi-bin/private/DocumentDatabase, 2011, Double Chooz Internal Document 2138-v4.

[75] S. Schoppmann, *User and Expert Manual of the Double Chooz Databases in the 2 Detector Setup*, http://www.dchooz.org/DocDB/cgi-bin/private/DocumentDatabase, 2014, Double Chooz Internal Document 5723-v13.

[76] F. Yermia, Shift Leader Report, http://www.dchooz.org/DocDB/cgi-bin/private/DocumentDatabase, 2014, Double Chooz Internal Document 5826-v1.

[77] Centre de Calcul de l'Institut National de Physique Nucléaire et de Physique des Particlues, RDMS, 2016.

[78] Y. Abe *et al.*, The waveform digitiser of the Double Chooz experiment: performance and quantisation effects on photomultiplier tube signals, *Journal of Instrumentation* **8**: P08015 (2013), http://dx.doi.org/10.1088/1748-0221/8/08/P08015.

[79] The Double Chooz Analysis Group, Internal Note of DC-III Electron Antineutrino Disappearance Analyses Using Energy Spectrum, http://www.dchooz.org/DocDB/cgi-bin/private/DocumentDatabase, 2014, Double Chooz Internal Document 5162-v23.

[80] A. Stüken, Estimation of the systematic uncertainties of the measurement of the neutrino mixing angle θ_{13} related to the trigger system of the Double Chooz Experiment, *PhD thesis*, Rheinisch-Westfälische Technische Hochschule Aachen, 2013, http://nbn-resolving.de/urn:nbn:de:hbz:82-opus-48019.

[81] D. Lhuillier, Error Propagation in the Prediction of Antineutrinos Spectra, http://www.dchooz.org/DocDB/cgi-bin/private/DocumentDatabase, 2011, Double Chooz Internal Document 2671-v3.

[82] A. Onillon, Prédiction des taux de fission des cœurs de Chooz et estimation des incertitudes associées dans le cadre de l'expérience Double Chooz, *PhD thesis*, Ecole des Mines de Nantes, 2014, https://tel.archives-ouvertes.fr/tel-01082405.

[83] Y. Declais *et al.*, Study of reactor anti-neutrino interaction with proton at Bugey nuclear power plant, *Physics Letters B* **338**: 383–389 (1994), http://dx.doi.org/10.1016/0370-2693(94)91394-3.

[84] Th.A. Mueller *et al.*, Improved Predictions of Reactor Antineutrino Spectra, *Physical Review C* **83**: 054615 (2011), https://doi.org/10.1103/PhysRevC.83.054615.

[85] G. Mention, M. Fechner, Th. Lasserre, Th.A. Mueller, D. Lhuillier, M. Cribier and A. Letourneau, Reactor antineutrino anomaly, *Physical Review D* **83**: 073006 (2011), https://doi.org/10.1103/PhysRevD.83.073006.

[86] K. Schreckenbach, H.R. Faust, F. von Feilitzsch, A.A. Hahn, K. Hawerkamp and J.L. Vuilleumier, Absolute measurement of the beta spectrum from 235-U fission as a basis for reactor antineutrino experiments, *Physics Letters B* **99**: 251–256 (1981), http://dx.doi.org/10.1016/0370-2693(81)91120-5.

[87] V. Sibille, Lithium rate estimates, http://www.dchooz.org/DocDB/cgi-bin/private/DocumentDatabase, 2016, Double Chooz Internal Document 6561-v1.

[88] V. Sibille, Cosmogenic background status and strategy, http://www.dchooz.org/DocDB/cgi-bin/private/DocumentDatabase, 2016, Double Chooz Internal Document 6631-v1.

[89] K. Kale, A. Meregaglia and G. Pronost, Preliminary Correlated Background Estimate, http://www.dchooz.org/DocDB/cgi-bin/private/DocumentDatabase, 2016, Double Chooz Internal Document 6489-v1.

[90] A. Meregaglia and G. Pronost, Correlated BG fits and rates, http://www.dchooz.org/DocDB/cgi-bin/private/DocumentDatabase, 2016, Double Chooz Internal Document 6508-v2.

[91] J.M. López Castaño, Accidental BG for Moriond, http://www.dchooz.org/DocDB/cgi-bin/private/DocumentDatabase, 2016, Double Chooz Internal Document 6530-v4.

[92] J. Haser, Neutron Detection Uncertainties in the θ_{13} Analysis of the Double Chooz Experiment, *PhD thesis*, Ruprecht-Karls Universität Heidelberg – Max-Planck-Institut für Kernphysik, 2015, http://nbn-resolving.de/urn:nbn:de:bsz:16-heidok-184329.

[93] C.S. Levin and E.J. Hoffman, Calculation of positron range and its effect on the fundamental limit of positron emission tomography system spatial resolution, *Physics in Medicine and Biology* **44**(3): 781–799 (1999), http://dx.doi.org/10.1088/0031-9155/45/2/501.

[94] E. Brun *et al.*, TRIPOLI-4®, CEA, EDF and AREVA reference Monte Carlo code, *Annals of Nuclear Energy* **82**: 151–160 (2015), http://dx.doi.org/10.1016/j.anucene.2014.07.053.

[95] H. Almazán, Detection systematics: Cf method – Status & Strategy, http://www.dchooz.org/DocDB/cgi-bin/private/DocumentDatabase, 2016, Double Chooz Internal Document 6637-v1.

[96] A. Cabrera, DC-IV Definition (MORIOND summary tables), http://www.dchooz.org/DocDB/cgi-bin/private/DocumentDatabase, 2016, Double Chooz Internal Document 6571-v3.

[97] A. Meregaglia, BG Veto Inefficiency, http://www.dchooz.org/DocDB/cgi-bin/private/DocumentDatabase, 2016, Double Chooz Internal Document 6556-v1.

[98] V. Sibille, J.-C. Barrière and T. Lasserre, Weight measurements in the Double Chooz experiment, http://www.dchooz.org/DocDB/cgi-bin/private/DocumentDatabase, 2016, Double Chooz Internal Document 6683-v2.

[99] R. Carr, Measurements of Electron Antineutrino Disappearance in the Double Chooz Experiment, *PhD thesis*, Columbia University, 2015, http://dx.doi.org/10.7916/D8W37VNN.

[100] R. Carr and K. Crum, Gd-III in CUfits Preliminary fit results, http://www.dchooz.org/DocDB/cgi-bin/private/DocumentDatabase, 2014, Double Chooz Internal Document 5501-v2.

[101] T. Konno and T. Matsubara, Final Fit in Cluster-Japan, http://www.dchooz.org/DocDB/cgi-bin/private/DocumentDatabase, 2012, Double Chooz Internal Document 3532-v1.

[102] P. McCullagh and J.A. Nelder, *Generalized Linear Models*, Chapman & Hall/CRC, Boca Raton, London, New York, Washington D.C., 2 edition, 1989.

[103] S.S. Wilks, The Large-Sample Distribution of the Likelihood Ratio for Testing Composite Hypotheses, *The Annals of Mathematical Statistics* **9**(1): 60–62 (1938), http://dx.doi.org/10.1214/aoms/1177732360.

[104] R.A. Fisher and F. Yates, *Statistical tables for biological, agricultural and medical research*, volume 6, Oliver and Boyd, Edinburgh, 1963.

[105] G. Yang, A coherent reactor correlation and SF estimate using the 2RM, http://www.dchooz.org/DocDB/cgi-bin/private/DocumentDatabase, 2016, Double Chooz Internal Document 6573-v1.

[106] H. Minakata, H. Nunokawa, S.J. Parke and R. Zukanovich Funchal, Determining neutrino mass hierarchy by precision measurements in electron and muon neutrino disappearance experiments, *Physical Review D* **74**: 053008 (2006), https://doi.org/10.1103/PhysRevD.74.053008.

[107] P. Huber, M. Lindner and W. Winter, Simulation of long-baseline neutrino oscillation experiments with GLoBES: (General Long Baseline Experiment Simulator), *Computer Physics Communications* **167**(3): 195–202 (2005), http://dx.doi.org/10.1016/j.cpc.2005.01.003.

[108] P. Huber, J. Kopp, M. Lindner, M. Rolinec and W. Winter, New features in the simulation of neutrino oscillation experiments with GLoBES 3.0: (General Long Baseline Experiment Simulator), *Computer Physics Communications* **177**(5): 432–438 (2007), http://dx.doi.org/10.1016/j.cpc.2007.05.004.

[109] A. Franke, A Method for Propagating Reference Spectrum Uncertainties Based on MultiSims, http://www.dchooz.org/DocDB/cgi-bin/private/DocumentDatabase, 2011, Double Chooz Internal Document 2315-v1.

[110] W. Dahmen and A. Reusken, *Numerik für Ingenieure und Naturwissenschaftler*, Springer-Verlag, Berlin, Heidelberg, 1 edition, 2006.

[111] N. Higham, Computing the nearest correlation matrix – a problem from finance, *IMA Journal of Numerical Analysis* **22**: 329 – 343 (2002), https://doi.org/10.1093/imanum/22.3.329.

[112] Y. Abe *et al.* (Double Chooz Collaboration), Direct measurement of backgrounds using reactor-off data in Double Chooz, *Physical Review D* **87**(1): 011102(R) (2013), https://doi.org/10.1103/PhysRevD.87.011102.

[113] F. James and M. Roos, Minuit – a system for function minimization and analysis of the parameter errors and correlation, *Computer Physics Communications* **10**(6): 343–367 (1975), http://dx.doi.org/10.1016/0010-4655(75)90039-9.

[114] M. Ishitsuka, T. Matsubara, S. Schoppmann and G. Yang, Mock-data validation macro, http://www.dchooz.org/DocDB/cgi-bin/private/DocumentDatabase, 2016, Double Chooz Internal Document 6545-v9.

[115] G. Yang, Update on the Rate+Shape fit, http://www.dchooz.org/DocDB/cgi-bin/private/DocumentDatabase, 2016, Double Chooz Internal Document 6459-v2.

[116] M. Ishitsuka, Status of N+F fit, http://www.dchooz.org/DocDB/cgi-bin/private/DocumentDatabase, 2016, Double Chooz Internal Document 6536-v1.

[117] C. Buck, A.P. Collin, J. Haser and M. Lindner, Investigating the Spectral Anomaly with Different Reactor Antineutrino Experiments, *arXiv:1512.06656 [hep-ex]* (2015).

[118] P.R. Kampmann, Vergleich von Gadolinium- und Wasserstoffdaten für die Bestimmung des Neutrinomischungswinkels θ_{13} mit dem Double-Chooz Experiment, *Master's thesis*, Rheinisch-Westfälische Technische Hochschule Aachen, 2016.

[119] C. Buck, H. Almazán and J. Haser, Cf data in GC, http://www.dchooz.org/DocDB/cgi-bin/private/DocumentDatabase, 2016, Double Chooz Internal Document 6630-v1.

Acknowledgement

I thank the Deutsche Forschungsgemeinschaft (DFG) for supporting my work as a member of the graduate college 1675 “Teilchen- und Astroteilchenphysik im Lichte von LHC” and my working group via the SBH WI 2152. In particular, I thank the Professors Achim Stahl and Christopher Wiebusch for supporting my application to the graduate college and for supervising my thesis.

I thank the many members of the Aachen Double Chooz working group, having supported me in discussion, counsel and ideas on many occasions. Special thanks go to Ilya Bekman being of the utmost help on uncountable occasions.

I thank the members of the Double Chooz collaboration for their support and their collaboration. Special thanks go to Dr. Tsunayuki Matsubara and Guang Yang for their collaboration on the oscillation analysis. Furthermore, I thank Dr. Didier Kryn and Dr. Michel Obolensky for their support during the commissioning of the data handling system.

Final thanks go to my parents continuously supporting me now throughout three decades as well as to my girlfriend Katja being an invaluable source of support and motivation.

*

Ich danke der Deutschen Forschungsgemeinschaft (DFG), die diese Arbeit als Teil des Graduiertenkollegs 1675 „Teilchen- und Astroteilchenphysik im Lichte von LHC“ unterstützt hat, sowie die Aachener Double Chooz Arbeitsgruppe durch SBH WI 2152 unterstützt. Insbesondere danke ich den Professoren Achim Stahl und Christopher Wiebusch, die meine Aufnahme ins Graduiertenkolleg ermöglicht haben und mich bei dieser Doktorarbeit betreut haben.

Ich danke den vielen Mitgliedern der Aachener Double Chooz Arbeitsgruppe, die mir wiederholt durch Diskussionen, Rat und Ideen geholfen haben. Spezieller Dank gilt Ilya Bekman, der bei unzähligen Gelegenheiten seine außerordentliche Hilfsbereitschaft gezeigt hat.

Ich danke den Mitgliedern der Double Chooz Kollaboration für ihre Unterstützung und ihre Zusammenarbeit. Besonderer Dank gilt Dr. Tsunayuki Matsubara und Guang Yang für ihre Zusammenarbeit bei der Oszillationsanalyse. Im Weiteren danke ich den Dres. Didier Kryn und Michel Obolensky für ihre Mithilfe während der Inbetriebnahme des Datenverarbeitungssystems.

Abschließender Dank geht an meine Eltern, die mich nunmehr seit drei Jahrzehnten unterstützen, sowie an meine Freundin Katja, die eine unschätzbare Quelle an Unterstützung und Ansporn ist.